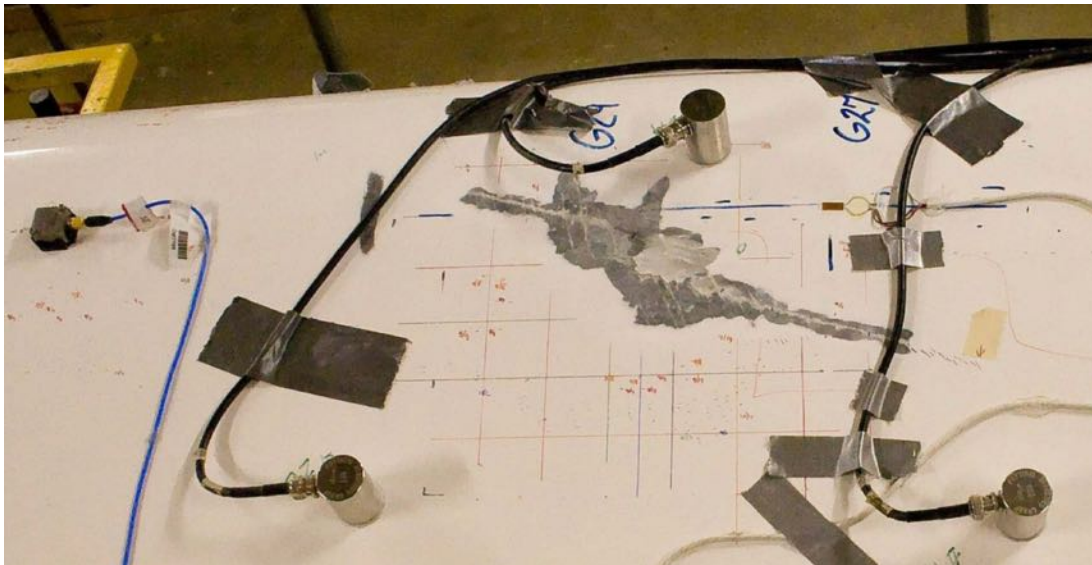


An International
Forum For
The AE Science
and Technology

JOURNAL OF ACOUSTIC EMISSION

Vol.37/January-December 2020

Editors: M.A. Hamstad (AEWG) and G. Manthei (EWGAE)



Sandia's TX-100 Turbine Blade Testing

Endorsed by
AEWG
and
EWGAE

Published by
Acoustic Emission Group
Encino, CA USA
©2020 Acoustic Emission Group

Journal of Acoustic Emission
Volume 37 (2020)

Contents

Tutorial

- 37-001 Alan G. Beattie, Acoustic Emission Testing of Structures using Source Location
1 – 85
- 37-086 R. Vidya Sagar and Swarnangshu Ghosh, Relating Damage Assessed by Using
Intensity Signal Analysis of Acoustic Emission with Surface Strain in Concrete and Ultrasonic
Pulse Velocity in Reinforced Concrete Beams under Monotonically Increasing Load
86 - 108

Selected Papers from the Proceedings of E-GLEA-10

Jose Ruzzante and Antolino Gallego, Topical Editors

- 37-S001 Basgall A., Ferrari, G., and Gómez, M.P., Neural Networks applied to the
monitoring of drilling processes in geological material samples, J. Acoust. Emiss. **37**, 2020, S1-
S10
- 37-S011 Bonelli Toro, A. G., Gómez M. P., Machine learning applied to acoustic emission
for tool wear classification during milling of composite materials, J. Acoust. Emiss. **37**, 2020,
S11-S20
- 37-S021 Groth, E. B., Shumacher, G., Idzi J., Rojo Tanzi, B. N., Clarke, T. G. R., Lima, T.
R. S. and Jacques, R. C., Acoustic emission numerical analysis applied to structural health
monitoring of laminar structures (Guided waves), J. Acoust. Emiss. **37**, 2020, S21-S29
- 37-S030 da Silva, D.S., Groth, E.B., Walter, J.S., Lutckmeier, F., Zuglian, G. F., Jaques, R.
C., de Lima, T.R.S. and Clarke, T.G., Study of fiber Bragg gratings (FBG) as acoustic emission
sensor to inspect and monitoring fiber-glass reinforced polymers (FGRP) degradation, J. Acoust.
Emiss. **37**, 2020, S30-S37
- 37-S038 Veca, A. C., Valse, N., Ruzzante, J., Albalat, A., Marino, A., and Reyes Reyes,
M. V., Autonomous acoustic system for passive acoustic monitoring of cetaceans, J. Acoust.
Emiss. **37**, 2020, S38-S54.
- 37-S055 Zitto, M.E., Sassano, M.P., Muszkats, J.P., Filipussi, D.A., and Piotrkowski, R.,
Energy and shannon entropy in acoustic emission signals for damage evaluation in andesite rock,
J. Acoust. Emiss. **37**, 2020, S55-S64
- 37-S065 López Pumarega, M. I., Ruzzante, J. E., and Gómez, M. P., La Emisión Acústica,
su Historia en la Argentina, J. Acoust. Emiss. **37**, 2020, S65-S76. (in Spanish)

Contents of the Proceedings of E-GLEA 10 (Índice)

Cover photographs: D. T. Griffith, G. Smith, M. Casias, S. Reese, and T. W. Simmermacher,
Sandia Report, SAND2005-6454, 2006 and A.G. Beattie (37-001).

Acoustic Emission Testing of Structures using Source Location

Alan G. Beattie

Sandia National Laboratories, Albuquerque, NM

Abstract

This is a tutorial article and covers the physical principles encountered in the field of acoustic emission (AE). This is followed by instrumentation and signal analysis methods. The second half is devoted to structural AE testing that relies on source location methods with detailed presentation of case histories. Three test setup examples and results on fiber-reinforced wind turbine blades and pressure vessels are provided.

Keywords: physical principles, instrumentation, signal analysis methods, source location, fiber-reinforced wind turbine blades, pressure vessels.

Foreword

The use of acoustic emission (AE) techniques in both non-destructive testing (NDT) and research and development has expanded rapidly since its first real investigation by Kaiser [1] over seventy years ago. It was recognized early that one might be able to triangulate to the source of an emission by detecting the same sound wave at several different sensors. An early successful usage of triangulation in an actual NDT test was reported by Green [2] in 1966 on a hydrotest of a Saturn S-II propellant tank. Since then the art of acoustic emission source location has rapidly expanded. Part of this expansion has been pushed by the many advances in the field of personal computers. The technology has changed from simple analog systems to sophisticated digital systems. A premium has been placed on acquiring data and using universal type programs, included in the commercial systems, to analyze the data. These programs are a marvelous advance over the first analysis programs included in the early source location systems but they cannot cover all of the possible types of analysis in the field of acoustic emission testing.

The author has been using AE techniques at Sandia National Laboratories in a wide variety of applications for most of the last forty years. Many of these applications required the development of specialized testing and/or analysis techniques. Obviously, as in any new field, not all worked, but a general approach was slowly developed. This monograph will describe in considerable detail the testing and analysis techniques developed in two areas: Wind Energy and Small Pressure Vessels. These applications use multiple sensors to perform acoustic emission source location. All involve analysis of the digital data. When the programs included in the early commercial systems were not readily adaptable for the analysis, custom programs in FORTRAN were written. As the field has evolved, many of the techniques of these programs have been incorporated in the software furnished with the commercial systems. However, the details of the commercial software are hidden in executable files. A few of the Sandia developed FORTRAN programs are included to illustrate the methods and assumptions used in AE programs. These are working programs and can be used with necessary minor adaptations to fit a test. No apologies are made for using FORTRAN. It is one of the easier languages, in which to follow the workings of a code. And it is still used despite the decline and death of many computer languages in the last fifty years.

This monograph first covers a general discussion of acoustic emission and AE sources. It then goes into a general discussion of the properties of acoustic waves in materials. This is the basic

background, which one should have to understand what is occurring in an acoustic test, either ultrasonics or acoustic emission. It is included to aid readers, who are new to the field of acoustics in solids, and can serve as reference material for others. Briefly covered are acoustic waves in solids including different acoustic modes, reflection and refraction of waves, attenuation, superposition and dispersion of waves, resonance effects and other phenomena, which will be encountered in an AE test. There is also a discussion of sensors, couplants, preamplifiers and other topics involved in performing an AE test. There is a brief section on AE source mechanisms and one on various parameters of AE waveforms, which are used in most commercial systems. All of this material was covered in an early review article [3] and makes no pretense of being new or different. It is hoped that the most useful parts of the monograph will be the discussions of the design, execution and analysis of several types of AE tests. No two tests are ever identical but the general methodology is widely applicable.

Selected Reading List from J. of Acoustic Emission (JAE). (These are available for download at www.aewg.org. Download the volume needed; e.g., get vol. 22 for Tensi article.)

H.M. Tensi, The Kaiser Effect and Its Scientific Background, J. AE, 2004, **22**: S1-S16.
T.F. Drouillard, A History of Acoustic Emission, J. AE, 1996, **14**: 1-34.

Chapter 1 Introduction to Acoustic Emission

Acoustic emission (AE) is the study and practical use of acoustic waves generated by a material subjected to an external stress. The actual use of the phenomena in technology dates back to early miners, who exited a mine when the rocks or supporting timbers started groaning. Tin cry when a tin bar was bent was known soon after the production of metallic tin. In 1947, C.S. Barrett [4] mapped a low temperature phase transition in Lithium-Magnesium alloys by sticking a phonograph needle into the crystal and recording the output as the temperature was changed. J. Kaiser investigated the signals produced by samples undergoing tensile testing and discovered the *Kaiser effect*, that no signals were generated by a sample upon the second loading until the previous maximum load was exceeded. After Kaiser's thesis was published in 1950, several groups started investigating the phenomena for possible use in testing structures. In the early 1960's, Allen Green and a group at Aerojet Corp. started using acoustic emission in the testing of Saturn Rocket propellant tanks. They used a form of triangulation using the arrival times of the acoustic pulse at several AE sensors. This was the direct precursor of the work that is described in this paper.

Acoustic emission is the generation of an acoustic wave by the rapid change in the stress state of some region in the material. This is usually caused by the application of an external stimulus to the material. The material can be a solid, liquid, gas or plasma and the external stress can be applied mechanically, thermally, magnetically, etc. The only requirement is that the stress change is rapid enough that some energy is transmitted to the surrounding material and dissipates as an acoustic wave. On a macroscopic scale, this definition includes earthquakes and thunder and on a microscopic scale, it includes the fracture of crystallites and martensitic phase transformations. The most important characteristic of the phenomena is that the occurrence of the burst of energy is completely determined by the local conditions, the local stress field and the physical state of the region. The result of this is that the exact time that the energy burst occurs cannot be determined beforehand. Not only is the time of occurrence indeterminate, but also the exact details of the released energy. In general, the event generating the emission is irreversible. Neither a ruptured geologic fault nor a fractured crystallite in a metal plate will heal spontaneously.

Once the acoustic wave is generated, it then travels throughout the material and can be detected at considerable distances from its point of origin. As it travels from its source to the point of detection, it is subjected to all the characteristics and variations of its acoustic path. Its energy is attenuated by geometric spreading and scattering by both microscopic and macroscopic variations in the structure of the material as well as other kinds of attenuations, which may be present. Its frequency content is generated by the source and modified as it travels the acoustic path. The primary information carried by the wave is the time of arrival and the acoustic energy detected at each sensor on the structure. The excitation of the sensor indicates that something happened in the specimen at a specific time. The amplitude gives an indication of the level of the disturbance. The apparent location of the source and all other characteristics of the detected signal are modified by the characteristics of the acoustic path to each sensor as well as the characteristics of each sensor. The result is that while in a highly controlled laboratory experiment, a reasonable estimate can be made of the characteristics of the emission source, in a test on an actual structure, we are limited to what are basically statistical estimates from multiple emissions to tell us what is happening in the specimen. Statistical analysis is not generally used in the study of acoustic emissions, but the state of the specimen as well as the location coordinates of the sources are inferred from averages of calculated values from multiple emissions.

Acoustic energy is ubiquitous. It travels through all materials where there is an interaction between atoms. Only a hard vacuum does not transmit acoustic energy. The distance that an acoustic signal can travel depends on its initial amplitude and the attenuation of the material that comprises the object or path to the object. This is an advantage in that an AE test can cover an entire structure and not just a small region of it. It is a disadvantage in that many acoustic signals, which have nothing to do with the test, can be present and detected. Acoustic isolation of the test object is highly desirable. Most AE testing filters out acoustic signals at frequencies below 20 kHz, thus ignoring background noise and verbal communication in the test area.

Finally, an AE test occurs in real time. The test does not find preexisting defects but detect (or flaw) growth as it occurs. If the stress application simulates the conditions, which test structure is designed to experience in actual operation, serious acoustic emission will indicate pathological flaws, which could lead to failure of part or all of the structure. The amount of emission seen and the locations of the emission sources will depend both on the design of the structure and the materials used in its fabrication. An example is the bending of a strip of glass and a strip of fiber reinforced plastic (FRP) with identical dimensions. The strip of glass would likely give a single high amplitude burst of emission just at failure while the FRP would show a period of low-level emissions followed by a few higher-level emissions and then one or more high amplitude emissions as the strip started to fail and then tore apart or snapped. The interpretation of the emissions that are detected is the job of the test engineer. The value of the information obtained from a test is determined first by the design of the test and then by the analysis of detected emission. On complex structures both the test design and interpretation are seldom simple. It is the purpose of this monograph to aid the test engineer in both areas.

1.1 Sources of Acoustic Emission:

Acoustic emissions are acoustic waves generated by a rapid change in the stress state of a region in a material. Acoustic waves are one of two non-electromagnetic methods of transmitting energy through a material. The other method is thermal diffusion. A difference between the two is that thermal diffusion involves direct energy transfer between individual atoms while an acoustic wave transfers energy by a cooperative motion of atoms. An acoustic wave can be as simple as a

pressure pulse in a gas or liquid or as complicated as the many modes of transmission in a bounded solid. The generation of an acoustic wave almost invariably involves a region of atoms instead of a single atom.

The most common acoustic waves are sound waves in air and water. These are produced by vibration of a surface such as the vocal apparatus of an animal, a leaf in the wind or the diaphragm of a speaker. These sources are quasi-continuous, involving a modulated vibration of an interface between the generating region and the transmitting medium. Another type of acoustic wave is generated by a sudden disturbance in or on the material itself. The disturbance can be described as a transient event and produces a transient acoustic wave. Such a transient wave is what we define as *acoustic emission*. It may have the form of a single damped wave with a complex frequency content or appear as many small transient events, which sum into quasi-continuous noise. Its primary characteristics are that it is generated in the medium which transmits it and it is transient in nature. Any sudden movement of a group of atoms at velocities near the sound velocity in a material can produce a transient acoustic wave. The apparent quasi-continuous signals, which are often seen, are generated by the overlap of many transient events instead of a continuous vibration of a surface. Figure 1 shows waveforms from a transient event (often called burst emission) and from a superposition of many transient events (continuous emission). The long decay of the transient event is produced by reflections of the original wave in the complex metal specimen (and within the sensor used).

The size of the region generating an emission can vary from a small row or plate of atoms moving into a new crystal position during a martensitic phase transition to a fracture in a subduction zone between two continental plates. The energy released in an AE event will be, very roughly, proportional to the volume of the source. The energy range of these waves ranges from smaller than an electron volt to the energy contained in a thunder clap or that of the recent earthquakes in Japan and Chile. The frequencies of these waves are generally related inversely to the volume of the generating region, ranging from a few mHz for earthquakes to several MHz in fine grain metals. An important characteristic of acoustic emission in solids is that the fracture of the region occurs when the local stress tensor exceeds the strength of the region for that tensor. In other words, the exact time when the emission occurs is strictly dependent upon the local conditions. In a metal, for example, the precise environment of every crystallite will be different and the fracture of one crystallite or the boundary between two crystallites will make small changes in the local stress tensors in the other crystallites. This complete dependence upon the local conditions means that it is impossible to predict the exact time that any one emission will occur or what the time interval between any two emissions will be. Acoustic emissions occur randomly in time. The parameters of the detected emission depend not only on the characteristics of the emission source but also upon the characteristics and geometry of the medium between the source and sensor, and upon the characteristics of the sensor and the couplant between sensor and medium. The signal characteristics detected by different identical sensors located at various positions on a specimen will often have large variations for a single emission. The more complex the medium, in which the AE is generated and transmitted, the more likely there will be large differences between detected signals from the same AE at different sensors. The combination of random origination in time and lack of duplicate signals are fundamental characteristics of AE. As such, they have a profound effect on the type of analysis used on the detected emissions.

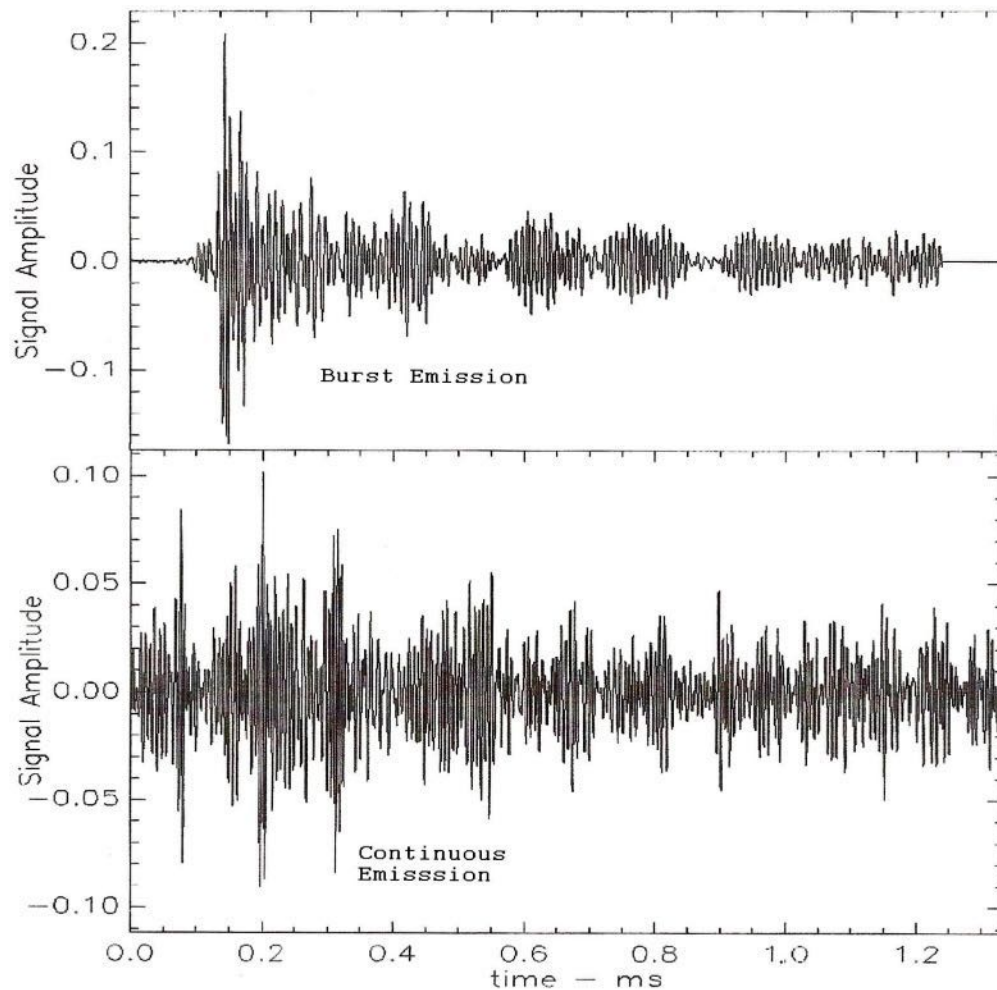


Figure 1 Examples of burst emission and continuous emission from a high-strength aluminum alloy.

In structural metals, both intergranular and transgranular cracking of metal crystallites can generate low level acoustic emission. Emission will also be generated at inclusions both by fracture of the inclusion and the breaking of the bonds between the inclusion and metal. Crack growth where at least several crystallites are involved can generate emission of moderate to large amplitudes. The presence of corrosion on a metal surface can be detected by the fracture of brittle corrosion byproducts while active corrosion can generate emission from bubble formation and collapse. In high stress environments, twinning can occur in some metals like Mg and Ti and this can produce emission. Creep deformation in metals may involve the movement of dislocations. However, the creep rate in structural materials under normal usage is usually far too slow to generate AE useable for flaw detection except at the tertiary stage where creep cracks develop. Creep also causes the cracking of brittle oxide films. These creep-induced cracks can be detected.

Source mechanisms in FRP include; matrix cracking, debonds between the matrix and fibers, fiber fracture and crack propagation, and delamination. These source mechanisms can all be activated by the application of an external stress. Based upon the idea that the emission amplitude is related to the volume of the source, matrix cracking should produce the lowest amplitude emission, followed by matrix-fiber debonding. Fiber breakage would be louder still, partly due to the amount of energy released by the fracture of a high strength fiber. Finally, crack propagation, which includes all three of the previous mechanisms, would produce the highest amplitude emissions. This

appears to generally be the case, but trying to quantify it as a general rule has never worked well. This is probably because FRP is usually laid up by hand and never comes close to the structural uniformity of a well annealed metal. As a general rule, the first loading of an FRP structure will generate AE at loads well below the strength of the structure. The most likely cause of this emission is local regions with high residual stresses which developed during the curing process. These stresses are relieved by matrix cracks in the FRP during the first loading. They have little effect on the strength of the FRP and the emission usually stops before the design loads are reached. This emission is seldom seen upon reloading. Another source of emission in FRP structures is often seen during cyclic loading. This emission appears in the middle ranges of the cyclic load where the rate of change in applied stress is highest, instead of at the peak loads. It appears to be caused by friction between small regions in the structure, which are not bonded. This type of emission can be present during the entire cyclic load test. However, it does not correlate with structural damage in the test object. Structural damage is associated with emission, which occurs near the peak loads, especially during the rising load.

The above discussion shows that most AE mechanisms involve a permanent change in the micro structure of the material. Once a micro-fracture occurs, it will not happen again unless there is some sort of healing mechanism occurring. Therefore, acoustic emission appears irreversible. The Kaiser effect, where the re-stressing of a specimen will not generate AE until the previous load level has been exceeded, is caused by this irreversibility. The Kaiser effect holds very well for the immediate re-stressing of a metal specimen but not so well for composites. The problem is that the reapplication of an external stress does not necessarily take the specimen along the same micro-stress path. One often sees emission on subsequent loadings at loads lower than previously reached. The ratio of the load value when emission starts on subsequent loadings over the maximum value of the previous loading is known as the *Felicity ratio* and it is an indicator of possible damage induced by the previous loading. Many NDT tests of FRP structures apply the test load in a series of steps, returning to zero between each step. The appearance of Felicity ratios much less than unity is a good indication that significant damage has occurred.

Selected Reading List from JAE Articles

C.R. Heiple and S.H. Carpenter, Acoustic Emission Produced by Deformation of Metals and Alloys - A Review: Part I and II, J. AE, **6**: 177-204, 215-237, 1987.

M.A. Hamstad, A Discussion of the Basic Understanding of the Felicity Effect in Fiber Composites, J. AE, **5**: 95-102, 1986.

K. Ono, Structural Integrity Evaluation Using Acoustic Emission, J. AE, **25**: 1-20, 2007.

T.J. Fowler, J.A. Blessing, P.J. Conlisk and T.L. Swanson, The MONPAC System, J. AE, **8**: 1-8, 1989.

M.R. Gorman, Modal AE Analysis of Fracture and Failure in Composite Materials, and the Quality and Life of High Pressure Composite Pressure Vessels, J. AE, **29**: 1-28, 2011.

Chapter 2 Acoustic Waves in Solids

Acoustic emissions are vibrational waves generated in materials. They travel through the material and are detected by a sensor of some type. In plasmas, liquids and gases, the wave motion is usually simple and the sensor can be immersed in the material. In solids, the wave usually travels through the material until it reaches a surface. There a sensor detects the surface motion produced by the wave. Wave motion in solids can be far from simple. Solids have boundaries and the

interaction of waves and the boundaries will depend upon the acoustic properties and the geometry of the solid. Acoustic wave motion is a cooperative movement of the atoms in a material. The simplest type of acoustic wave occurs when a shell of material around a region is suddenly compressed by a disturbance in the region. This compression can be either negative or positive, such as a bubble imploding or exploding. The material in this shell experiences a change in its density. This density change is then passed to the next shell by coupling between the atoms. The density in the first shell then rebounds, usually going past the original value of the density to a smaller density change in the opposite direction. This variation in the density is transmitted to the next shell and so on, throughout the material. The speed with which the disturbance propagates is determined by the strength of the coupling between the atoms or molecules of the material and the density of the material. This type of wave is known as a compressional wave and occurs in all materials, solids, liquids, gases and plasmas. As materials become more rigid and ordered, more types of waves are possible and the introduction of boundaries in a material will introduce other complications into the wave motion. However, all wave motion is based upon the cooperative movement of groups of atoms. This is in contrast to thermal energy where the motion of adjoining groups of atoms is not coupled and the energy is transferred between individual atoms or molecules. Heat transfer is a diffuse flow of motional energy through the material and involves much higher frequencies than seen in acoustic emission.

2-1 Characteristics of Acoustic Waves:

Much of the complexity seen in AE signals is generated as the wave travels through the medium. Any understanding of AE signals requires knowledge of the characteristics of acoustic waves. The place to start is the properties of the medium, through which the wave travels. All materials are collections of atoms. The atoms are held together by attractive forces but also prevented from approaching each other too closely by short range repulsive forces. The superposition of these forces results in an equilibrium position for the atom where it has its lowest energy and therefore the most stable configuration of the material. In crystals, long range forces between the atoms result in defined locations for these equilibrium positions. The result is a crystal structure. In a glass or a liquid, the structure is amorphous but there is an approximate distance between atoms resulting in a uniform density. In a liquid, only the density is defined, the ability of the atoms to change positions is measured by the viscosity of the liquid and can range from very low to very high. A glass is just a liquid with extremely high viscosity. A gas can be thought of as a liquid with low viscosity and a density, which is defined by its container. The acoustic properties of a material depend upon the density of the material and the long-range coupling constants between the atoms of the material. The viscosity in solids causes the attenuation effect on the acoustic properties [5].

The long-range correlations in an acoustic wave result in many atoms in a small region being displaced in the same direction from their equilibrium positions. This displacement is a local strain in the crystal. The strain is a dynamic one as its direction and magnitude are constantly changing as the atoms move. When the atomic motion is pseudo-oscillatory, so is the dynamic strain. An acoustic wave is an oscillating strain moving through a material. Because stress and strain are always directly related in a material there is also an oscillating stress field. Therefore, an acoustic wave can be described as either a dynamic stress field or strain field in a material.

2-1-1. Wave Motion:

The most familiar depiction of a wave is a sinusoidal curve such as shown in Fig. 2a. The amplitude oscillates between positive and negative limits at a fixed rate, known as the frequency and the curve extends indefinitely. This curve can equally well be plotted as a function of space or

time. In a medium, a wave has both a spatial and a time component. An equation for such a curve is

$$Y = A \sin (\omega t - kx) \tag{2-1a}$$

where A is the amplitude, ω (called angular frequency) is 2π times the frequency, f , and k (called wavenumber) is 2π over the wavelength, λ . The frequency, f , wavelength, λ , and wave velocity, v , are related by

$$v = \lambda \cdot f. \tag{2-1b}$$

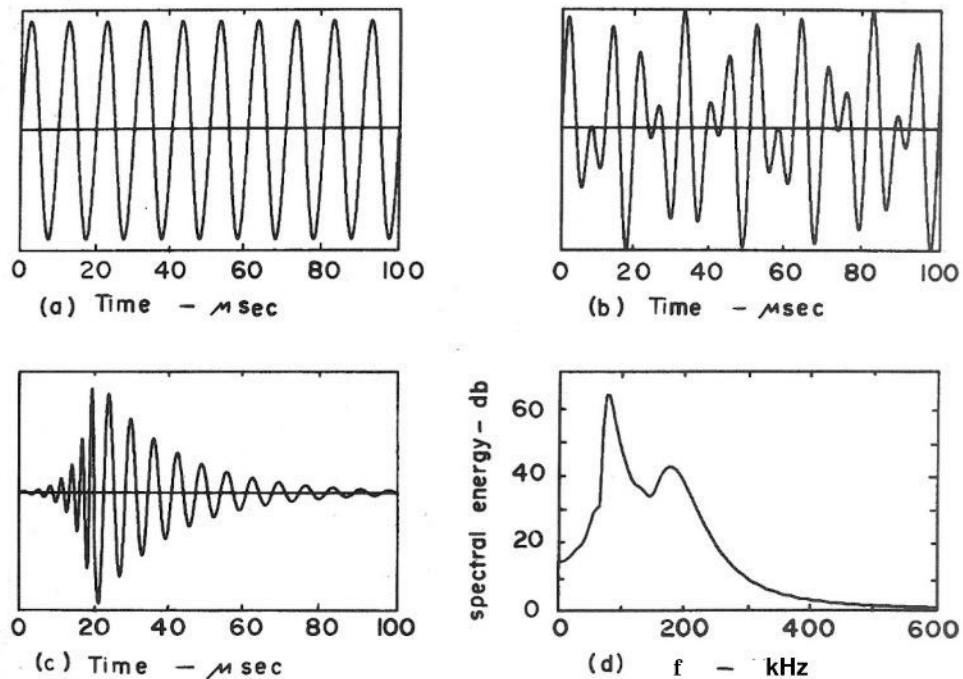


Figure 2 (a) simple sine wave, (b) sum of two sine waves, (c) transient wave, (d) spectrum of transient wave.

The wave described in eq. (2-1a) propagates in one direction only. In three dimensions, the wave front, which is a surface of constant phase for the wave, is a plane perpendicular to the X axis. Such a wave is known as a plane wave. Most waves originating at a point in an extended medium initially have a spherical wave front. However, at some distance from the point of origin, the spherical surface will approximate a plane over a small area. For simplicity, in the rest of this discussion, plane waves will be assumed.

If two waves exist in a medium simultaneously, their amplitudes will add algebraically. Fig. 2b shows the sum of two waves

$$Y = A_1 \sin \omega_1 t + A_2 \sin \omega_2 t \tag{2-2}$$

where only the time component is plotted for clarity. One can, in this fashion, represent a complex wave form as a sum of simple waves. It has been long known that any arbitrary function, which does not contain a discontinuity, can be represented by an infinite sum of sinusoidal curves known as a Fourier series. One form of such a series can be written as

$$f(t) = A_0/2 + \sum A_n \sin(n\omega_n t + \alpha_n) \quad (2-3)$$

where the A_n is the amplitude of the n -th sine curve, ω_n its angular frequency and α_n its phase. There is no restriction that the curve or wave form represented by the Fourier series be continuous. A transient wave such as that shown in Fig. 2c can be described by a Fourier series. One very useful method of analyzing a wave is to look at its frequency components. A plot of the amplitude of the frequency components, A_n in eq. (2-3), against the frequency f is known as the frequency spectrum of the wave. Fig. 2d shows the frequency spectrum for the wave shown in Fig. 2c, indicating two peaks exist at 80 and 170 kHz.

3-1-2. Acoustic Media:

An acoustic wave only exists in a material, whether it is a solid, liquid, gas or plasma. Its velocity is determined by the characteristics of the material. The stronger the force between neighboring atoms, the more closely coupled will be their motion. On the other hand, the larger the mass of the atoms, the more force must be applied for the same acceleration. Because a wave is a synchronized movement of a large number of atoms, it is actually the density of the material, ρ , rather than the mass of the individual atoms which governs wave motion. Thus, the wave velocity should be directly proportional to the atomic restoring force between the atoms or molecules and inversely proportional to the density. The actual relationship is

$$v_i = (C_i/\rho)^{0.5} \quad (2-4)$$

where v_i is the velocity for the i -th type of wave and C_i is known as the elastic constant for that type of wave. The elastic constant is a measure of the strength of the coupling between atoms for that particular kind of motion. Different relative motions of the atoms will have different values of the elastic constant. Another property of the material is the characteristic acoustic impedance. This is defined as

$$Z_i = \rho v_i = (\rho C_i)^{0.5}. \quad (2-5)$$

The reflection and transmission of acoustic waves at an interface depend upon the characteristic acoustic impedances of the two materials. Acoustic velocities, acoustic impedances and densities for some materials often seen in AE tests are given in Table 1.

Table 1 Acoustic velocities and impedances for longitudinal, shear and Rayleigh (surface) waves for several materials

Material	V_l	V_s	V_r	ρ	Z_l	Z_s	Z_r
Aluminum	6.42	3.04	2.87	2.70	17.30	8.20	7.70
Brass	4.70	2.11	1.99	8.60	40.60	18.30	17.10
Steel	5.94	3.25	3.03	7.80	46.50	25.40	23.60
Nylon	2.62	1.07	1.01	1.11	2.86	1.18	1.12
Lucite	2.68	1.10	1.04	1.18	3.16	1.30	1.23
Water	1.50	-	-	1.00	1.50	-	-
Air	0.33	-	-	0.00123	0.0004	-	-

Velocities are in units of mm/ μ s, densities are in units of Mg/m³, acoustic impedances are in units of kg/m² μ s (= MPa·s/m = Mrayl).

2-2 Types of Acoustic Waves:

The path traced out by a particle under the influence of an acoustic wave can generally be represented by an ellipse with one of its axes oriented along the direction of travel of the wave. The type of wave is determined by the relationship between the particle motion and the direction of travel of the wave for bulk materials. For materials with boundaries, the exact details of the wave motion will be determined by the materials properties, the geometry of the material and the frequencies of the acoustic wave.

Waves traveling through an extended medium (one whose dimensions are much larger than the acoustic wavelength) are called bulk waves. There are two types of pure bulk waves called longitudinal (compressional) and shear (transverse) waves. In both these waves, the minor axis of the elliptical atomic paths collapses toward zero, resulting in an approximate linear oscillatory motion. Longitudinal waves are waves where the average of this motion over a region in the material is parallel to the direction of wave propagation and shear waves have the average motion perpendicular to the direction of propagation. (It should be noted that the motion of atoms around their equilibrium position is very complicated with much higher frequency components than acoustic waves. The acoustic waves are averages over a very large number of atoms in the lattice. The average acoustic motion will be ellipses around the lattice position but there is no requirement that the axes of the ellipse correspond to symmetry directions in the lattice). These waves are illustrated in Figs. 3a and 3b. Since the relative motions of the particles in these two waves are different, the elastic constants and therefore the wave velocities also differ. Generally, the shear velocity is slightly greater than one half of the longitudinal velocity. Waves often have both shear and longitudinal components. However, these components each travel at their own velocity. In a non-attenuating, non-dispersive medium (v is independent of f), a transient wave, sampled at some distance from its point of origin, may appear to be two separate waves, one longitudinal and one shear. This is illustrated in Fig. 4. The anisotropy of the coupling forces between atoms at the surface of a bounded solid will produce additional types of waves. A surface wave has its maximum amplitude at the surface of the solid with its amplitude decreasing with distance from the surface. The plane of the particle motion ellipse can be either parallel (Love waves) or perpendicular (Rayleigh waves) to the surface. However, because most AE sensors detect motion perpendicular to the surface, the parallel component is seldom seen. The velocity of Rayleigh waves is slightly lower than the shear velocity. If the solid is bounded by two surfaces so that it is a plate and the thickness of the plate is on the order of a few acoustic wavelengths or less, plate waves (Lamb waves) can occur. A plate wave is essentially two synchronized surface waves which can be synchronized either symmetrically or anti symmetrically. Particle motions in Rayleigh waves and plate waves are illustrated in Fig. 5.

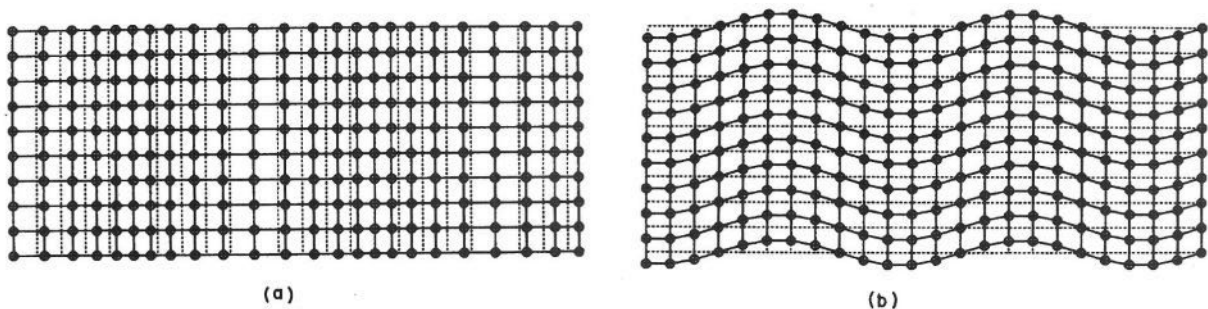


Figure 3 Particle displacement for bulk acoustic waves, (a) compressional wave, (b) shear wave.

Bulk waves, surface waves and plate (Lamb) waves are the most important types of waves seen in the field of acoustic emission. However, these are not the only types of waves which can be found in solids. In general, bounded solids of moderately symmetrical geometry can support unique types of waves.

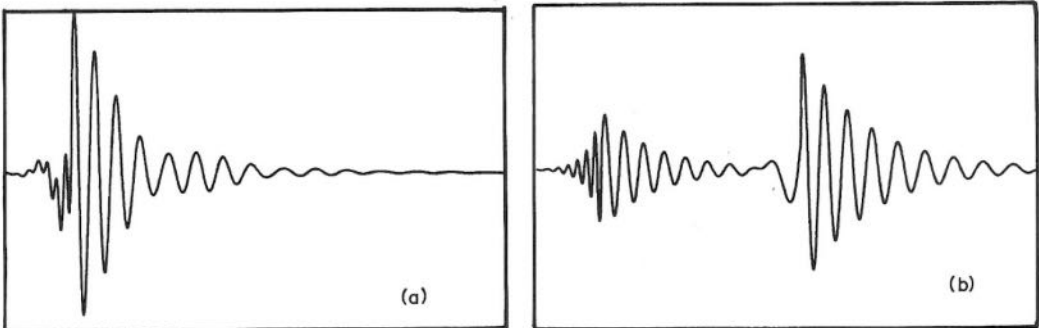


Figure 4 Waveform with compression and shear wave. (a) at origin, (b) some distance from origin.

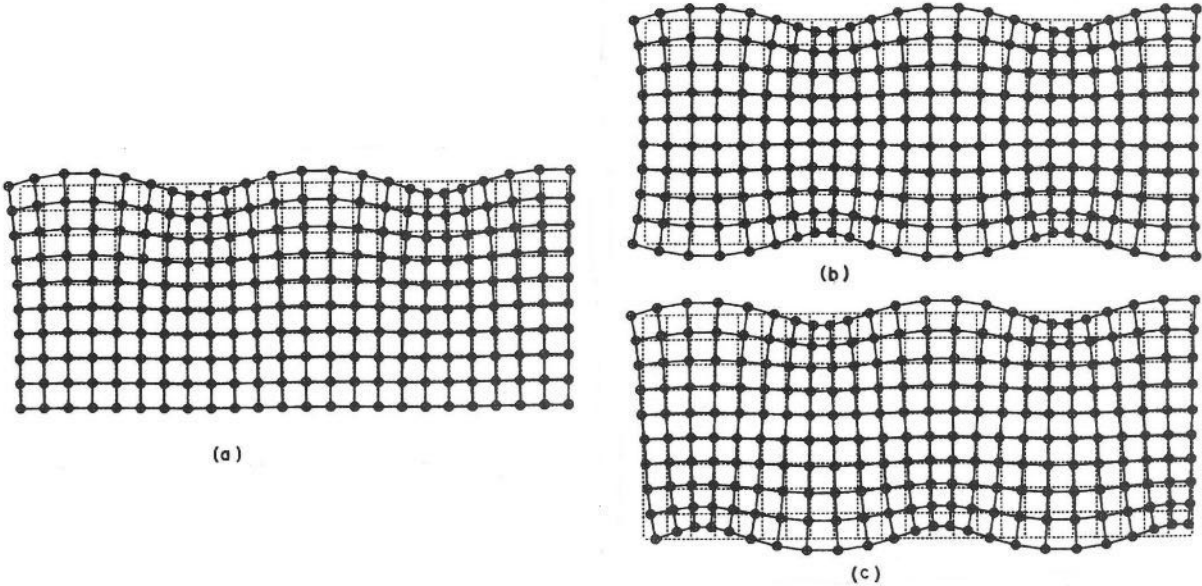


Figure 5 Particle displacements for acoustic waves. (a) Rayleigh wave. (b) Plate (Lamb) wave, first symmetric mode, S_0 . (c) Plate (Lamb) wave, first antisymmetric mode, A_0 .

2-3 Dispersion and Group Velocity:

The velocity defined in Eq. 2 is the phase velocity. For unbounded media and surface waves on a single surface, this velocity is the only wave velocity and it is independent of frequency. However, all waves traveling in bounded media, where the physical dimensions are within an order of magnitude of the acoustic wavelength, are dispersive, that is, the phase velocity is a function of frequency. This is illustrated in Fig. 6 where the frequency dependences of the velocities for symmetric and anti-symmetric plate waves are shown. Dispersion would have little effect on continuous waves. However, acoustic emissions are packets of waves, which can be thought of as a superposition of continuous waves, as shown in eq. (2-3). If each wave train, making up the packet, travels at a different velocity, the wave packet will change shape as it travels through the medium. The result is that the same AE signal may look quite different when detected by the same sensor

at different positions. Energy in a wave packet, does not travel at the phase velocity, but at the group velocity. The phase velocity can be defined by rewriting eq. (2-4) as

$$v_p = \omega/k \tag{2-6}$$

while the group velocity is defined as

$$v_g = d\omega/dk. \tag{2-7}$$

In the absence of dispersion, these are the same velocity, but in most bounded solids the group velocity will be less than the phase velocity. This can have real effects in AE when one is attempting source location by measuring the differences of arrival times at two or more sensors. One can also get interesting results when trying to compute the locations of AE sources by using a phase velocity for a thin sheet of metal.

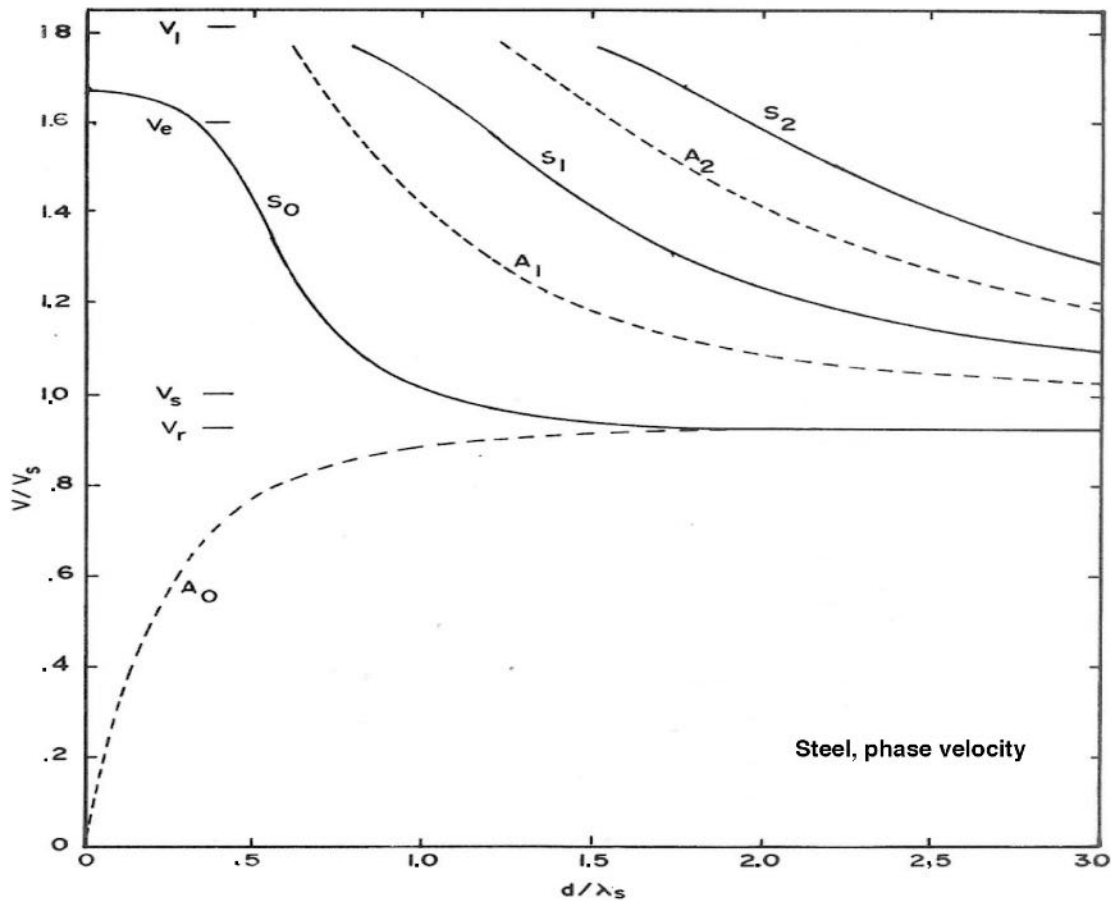


Figure 6 Phase velocities for six different plate wave modes (S_0 , S_1 , S_2 , A_0 , A_1 , and A_2) plotted against the ratio of plate thickness to shear wavelength. Plotted for steel with a Poisson's ratio of 0.28. The longitudinal, extensional, shear and Raleigh wave velocities are shown as v_l , v_e , v_s and v_r .

2-4 Attenuation:

A wave packet is generated with a well-defined energy. As the packet propagates away from its source, the energy content will remain constant in the absence of any dissipative mechanisms.

However, if the wave front of the packet is expanding, the energy per unit area on the wave front must decrease so that the total energy on the wave front is conserved. The rate of this decrease will depend upon the geometry of the medium. In three dimensions, the energy per unit area will decrease as the square of the distance from the source while in two dimensions, it will decrease linearly with this distance. If the packet is confined to one dimension, as in propagation down a rod, the energy per unit area will be independent of the distance from the source. Normally, when thinking about acoustic waves, one assumes a plane wave traveling in only one dimension. Therefore, this geometrical effect on the wave packets energy is ignored. However, in an acoustic emission test, where neither the location of the source nor, often, the geometry of the sample is under the control of the investigator, this geometrical effect should be considered in any attempt to measure the energy of the generated wave packet. The attenuation of a plane wave arises from dissipative mechanisms or scattering as the wave propagates. In a homogeneous medium, these losses usually occur as a fixed percentage of the wave packet energy per unit length of travel. Mathematically, this is an exponential decrease in the wave amplitude with distance and can be expressed as

$$A = A_0 \exp(-\alpha x) \quad \text{or} \quad A = A_0 \exp(-\beta t), \quad (2-8)$$

where α is an attenuation constant per unit length and β is an attenuation constant per unit time. The two constants are related by the acoustic velocity, $\beta = \alpha v$. Both forms of the attenuation constant are seen in the literature. Knopoff [5] showed that α is related to the viscosity (η) of the Kelvin-Voigt solid by

$$\alpha = \omega^2 \eta / 2vE', \quad (2-9)$$

in terms of angular frequency ω , the acoustic velocity v and the elastic constant E' .

There are many types of acoustic attenuation mechanisms and most have some form of frequency dependence. Fortunately, in the normal acoustic emission frequency range of 50 kHz to 1 MHz, both the frequency dependence and the magnitude of many of these attenuation mechanisms are small in metallic structural materials. However, in composites and geological materials, the attenuation can be a severely limiting factor in AE tests, often restricting the useable frequency range to 100 kHz and below.

2-5 Interfaces; Reflection, Transmission and Mode Conversion:

If a plane wave strikes a surface between two materials with different acoustic impedances, part of the wave will be reflected and part transmitted. The intensities of the reflected and transmitted components are given by:

$$A_t = 4Z_1 Z_2 / (Z_1 + Z_2)^2 \quad (2-10a)$$

$$A_r = ((Z_1 - Z_2) / (Z_1 + Z_2))^2 \quad (2-10b)$$

where the Z 's are the acoustic impedances of the materials. It should be noted that these equations are symmetrical; it does not matter which medium the wave is traveling in when it hits the interface. The differences in acoustic impedances can result in large differences in the acoustic intensities transmitted through interfaces. For example, the transmitted intensity of longitudinal waves is 78% for a steel-aluminum, 12% for a steel-water and 0.004% for a steel-air interface.

When a plane wave strikes the interface, the angles of the reflected and transmitted waves are governed by Snell's law

$$\sin \theta_1/v_1 = \sin \theta_2/v_2 \quad (2-11)$$

where θ_1 is the angle of incidence or reflection, θ_2 is the angle of refraction, and the v_i are the velocities in the materials. In eq. (2-11), a transmitted velocity is positive and a reflected one, negative. The particle motion anywhere on a wave front of a plane wave is the same. It wants to remain the same even when the wave passes an interface. However, at an interface the direction of propagation will change even though the particle motion does not. For a wave perpendicular to the surface ($\theta_1 = 0^\circ$), this results in a phase change of 180° in the relative motion of the particle to the wave direction. This does not change the character of the wave. For non-perpendicular angles of incidence, the reflected and transmitted waves will have both longitudinal and shear components (unless the particle motion is parallel to the interface) because of the change in the angle between the particle motion and the propagation direction. This is illustrated in Fig. 7. The process of generating both modes of bulk waves upon reflection or refraction is known as *mode conversion*. In acoustic emission, where there is no control of the wave path, the almost inevitable result of mode conversion is that the wave reaching the sensor is composed of both longitudinal and shear components, no matter what its original polarization was. In most situations, surface waves are also present. Since mode conversion occurs at almost every reflection, it is an almost continuous process as the wave propagates in a bounded medium. Because of this continuous transformation between modes traveling at different wave velocities, the transient waveform will lengthen in time as it travels instead of dividing into separate longitudinal and shear components as shown in Fig. 4 earlier.

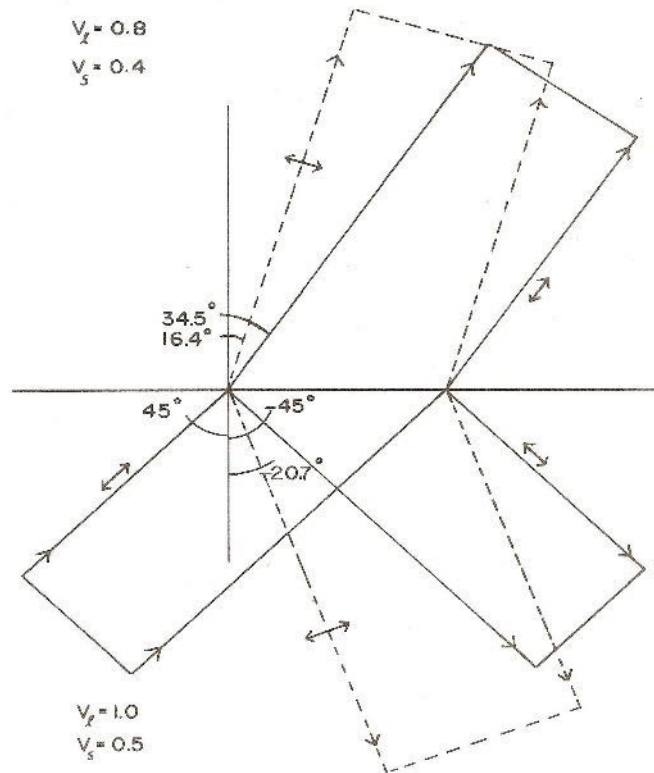


Figure 7 Reflected and transmitted waves across an interface. The incident wave is a longitudinal wave with an angle of incidence of 45° . The double arrows show the direction of particle motion associated with each wave.

2-6 Resonance:

The phenomenon of resonance occurs when there are reflected waves and regular geometries. For example, place a plate of a material between two other materials such as a steel plate submerged in water. When an acoustic wave is directed at it, there will be transmitted and reflected waves at each interface. Figure 8a shows how the waves will bounce back and forth in the plate. The number of reflections will depend both on the acoustic impedances of the steel and water and upon the attenuation in the steel. If the plate thickness is one half of a wavelength, as shown in Fig. 8b, each reflected wave will be in phase and the strains will algebraically add. If there are a great many reflections, the peak strain can reach a very high level. If there are only a few reflections, the frequency of this wave need not be exactly that of a half wavelength to get some reinforcement but the greater the number of reflections, the narrower will be the allowed frequency range at maximum strain and the larger this maximum strain will be. This is illustrated in Fig. 8c. The sharp high amplitude peak is said to have a high Q where Q is related as the ratio of energy stored per cycle to the energy dissipated per cycle. This increase of the stress or strain level in a material at a half- λ thickness is known as a resonance and f_0 is the resonant frequency. From Fig. 8b, we see that at resonance, the average strain throughout the plate is a maximum. Resonances can occur anywhere that a regular geometry allows acoustic waves to reflect in such a way that the strains from several reflections of the wave are superimposed. In piezoelectric materials, such as quartz and LiNO_3 , very high Q resonances allow precise generation of single frequency waves.

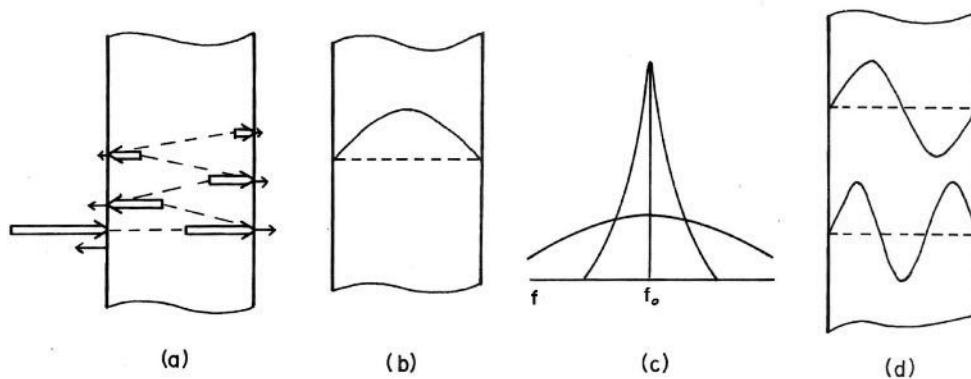


Figure 8 Reflected and transmitted waves inside a plate immersed in water. (a) Successive reflections have been displaced for clarity. (b) Strain in a plate one half wavelength thick at $f = f_0$. (c) amplitude as a function of frequency in the plate for high and low Q materials. (d) Strain in the plate of (b) at $f = 2f_0$ and $f = 3f_0$.

Selected Reading List from J. AE and Open Access Paper

W. H. Prosser, M. R. Gorman and D. H. Humes, Acoustic Emission Signals in Thin Plates Produced by Impact Damage, *J. AE*, 1999, **17**, 29-36.

K. Ono, A Comprehensive Report on Ultrasonic Attenuation of Engineering Materials, Including Metals, Ceramics, Polymers, Fiber-Reinforced Composites, Wood, and Rocks, *Appl. Sci.* 2020, **10**, 2230; doi:10.3390/app10072230. Values of v_1 and α of 300+ materials are tabulated.

Chapter 3 Detection of Acoustic Emission

3-1 Sensors:

A sensor is a device, which generates an electrical signal when it is stimulated by an acoustic wave. The exact relationship between the characteristics of the wave and those of the signal will depend upon both the sensor and the wave. An ideal sensor would produce a voltage-time curve identical to the amplitude-time curve of the wave at the point where the sensor is located. No sensor approaches this ideal although for certain types of acoustic waves, laser interferometry will come close. Many available sensors operate quite well for specified types of waves over limited ranges of parameters. Because of the wide range of frequencies and different acoustic modes contained in most AE signals, the choice of a sensor is usually not critical in detecting AE. However, the optimal choice of a sensor will always improve the data and may be the difference between a successful or unsuccessful test or experiment where low amplitude emissions are involved. AE sensors can be based upon several physical principles. The signals can be generated by electromagnetic devices such as phonograph pickups, by capacitive microphones, by magnetostrictive devices, by piezoelectric devices and by the use of laser interferometers to detect the surface displacement of the sample. For use in NDT applications, most of AE sensors are piezoelectric and the rest of this discussion will be limited to such devices.

3-2 Piezoelectricity:

Piezoelectricity [6] is the name given to the coupling between strain and electric polarization, which occurs in many crystals. It is a geometrical effect and occurs only in materials, which lack a center of crystal symmetry. This is not a severe restriction as 21 of the 32 classes of crystal structure lack a center of symmetry. In such crystals, a strain will shift the centers of positive and negative charge distribution so that they no longer coincide. This produces an electric dipole moment throughout the crystal. The polarization of a crystal is defined as the dipole moment per unit volume. When a polarization exists in a non-conducting crystal, electric charges will appear on certain surfaces. Conducting electrodes on these surfaces allow the measurement of the charge, which is directly proportional to the strain. The effect is symmetric in that application of charges to the electrodes changes the strain. Since the stress field and the strain field in a material are directly related, the piezoelectric effect can equally be defined as the coupling between the stress and the polarization in a crystal. The exact stress or strain, which is measured (or generated), can be chosen by a careful selection of the crystal surfaces to deposit electrodes (usually done by vacuum deposition). A characteristic, which is highly desirable in a measurement, is linearity. Piezoelectricity more than meets this requirement. A single crystal sensor appears linear over more than nine orders of magnitude.

Initially, all piezoelectric devices were made from single crystals. The most useful of these were quartz, Rochelle salt and ammonium dihydrogen phosphate. Later, a class of materials known as ferroelectrics (piezoelectric materials, which have a polarization even in the absence of a strain) were investigated and methods were discovered, in which ceramics made of ferroelectrics, could be given a uniform direction of polarization similar to that found in a piezoelectric crystal. It became possible to produce ferroelectric ceramics with many properties superior to piezoelectric single crystals. The result has been that almost all AE sensors are made from ferroelectric ceramics of various types. The most common one is lead zirconate-titanate, often referred to as PZT.

3-3 Size Effects:

An infinitesimal piece of piezoelectric material with many different sets of electrodes totally imbedded in a sample would come close to the ideal sensor. However, when we scale up the piezoelectric to manageable size, put on one set of electrodes and place it on the outside surface of the sample, we rapidly depart from that ideal. The physical size of the sensor leads to two main effects. The first is resonance and the second is strain averaging. Both can become important when the physical dimensions of the sensor approach or exceed the wavelength of the acoustic wave. Since the output of a piezoelectric crystal is proportional to the strain, and to the average strain for a crystal of finite dimensions, the maximum output of a sensor occurs at its resonant frequencies. The fundamental resonate frequency of a plate occurs when the plate thickness is one-half wavelength ($\lambda/2$) as shown in Fig. 8b. The reflected wave is in phase with the incident wave at the surface and the strains add. If the frequency is increased until there is one full wavelength in the crystal there will again be strain re-enforcement due to the reflected waves. However, we can see in Fig. 8d that while the strain level may be very great at this frequency, $2f_0$, the average strain over the crystal exactly cancels so that the output of the sensor is zero. Increasing the frequency to $3f_0$, we see 1.5λ in the crystal, re-enforcement again occurring, and the average strain over two-thirds of the crystal cancelling but the average strain over that last third being a maximum. The result is that a piezoelectric sensor will have a maximum output whenever the thickness, d , is

$$d = (2n - 1) \cdot \lambda / 2 \quad (3-1)$$

and no output when

$$d = n \cdot \lambda \quad (3-2)$$

Thus, a sensor can be operated either at its fundamental frequency, f_0 , or its odd harmonic frequencies nf_0 , n being odd. The Q of the transducer depends only on the number of reflections in the sensor and therefore the Q is independent of the harmonic at which the sensor is operating as long as the material of the sensor does not show a frequency dependent attenuation. The sensor will always have an output at frequencies below the fundamental frequency, f_0 . At frequencies less than about $3f_0/4$, the resonance will have no effect and the output will be essentially independent of frequency. In reality a material cannot be strained in one dimension without producing strains in other directions as shown in Fig. 9a. Many AE sensors use this to get a maximum response. The piezoelectric element is in the shape of a squat cylinder (a round disk). A wave with a vertical displacement on the cylinder face will excite the radial resonance. This resonance will then give a large output signal. This type of sensor is a very sensitive detector of acoustic emission. However, it should not be used to measure the frequency spectrum nor the actual wave form of the acoustic wave since this cross coupling of vibration modes can give a distorted representation of the wave.

Piezoelectricity is quite complex and a large part of its history in acoustics has been a search for particular crystal orientations where only certain strains will generate charge on a pair of electrodes. Modern AE sensors, made of polarized ferroelectric ceramics, also suffer from multiple resonances. However, because the ceramics have an intrinsically low Q neither the peaks nor valleys are especially sharp. Thus, most sensors have a broad but highly "colored" spectral response curve as shown in Fig. 9b.

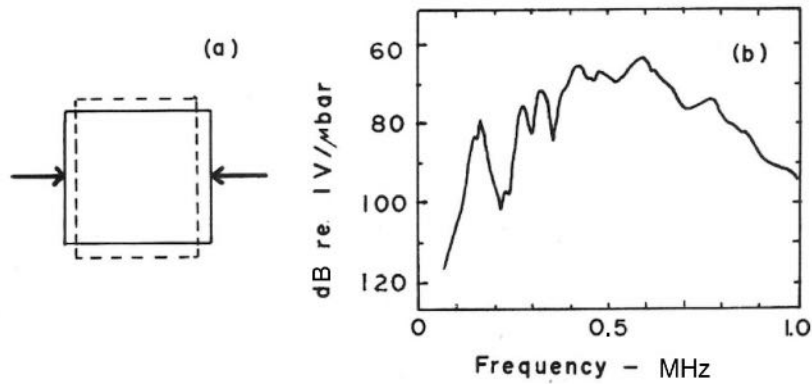


Figure 9 (a) Deformation of a material showing multi-axial strain resulting from uniaxial force. (b) spectral response of an AE sensor.

There is another important aspect of strain averaging by a sensor. This is known as the aperture effect [10a]. Fig. 10a shows a block with a sensor mounted on it. If the sensor is excited with a compressional wave moving perpendicular to its surface, the entire sensor face will move in phase and, excluding resonances, the average strain in the sensor will be independent of frequency. Next look at a Rayleigh wave which is traveling parallel to the sensor face and has the particle motion perpendicular to the sensor face. In this case, the strain distribution in the transducer will vary as a function of distance along the wave. Fig. 10b shows the strain variation where the diameter of the sensor is less than $\lambda/2$. Here, the output is still proportional to the amplitude of the wave. In Fig. 10c, we see the case where the diameter of the sensor is larger than the wavelength. In this case, for every complete wave-length under the sensor, the strain averages to zero. Only the extra fraction of the wavelength under the sensor contributes to its output. This averaging essentially reduces the effective area of the sensor and the higher the frequency, the greater the reduction. Another effect is that at certain frequencies, dependent upon the shape of the sensor and the acoustic velocity of the sample, the total strain averages to zero. These effects can be expressed in terms of the Bessel function [10a] and are illustrated in Fig. 10d where the response for this type of surface wave is plotted for a sensor with a flat response to compressional waves perpendicular to its face. It is obvious that the high frequency response of such a sensor is going to depend drastically upon the angle of incidence, with which the wave strikes the sensor. This averaging effect depends upon the acoustic wave-length in the material. Therefore, the sensor response not only is going to vary with frequency and angle of incidence, but it is going to vary when used with different materials. The best answer to this problem is to make the sensor physically small. For steel, a 3-mm diameter sensor should work reasonably well below 500 kHz. The inevitable tradeoff is that the smaller sensor has a lower capacitance and thus, as will be discussed later, a reduced effective sensitivity. Another approach has a more complicated polarization geometry than a simple disk polarized between its faces. Some sensors of this type are commercially available and the reader should contact the various manufacturers for details and specifications (the geometry and materials in such sensors are often treated as trade secrets).

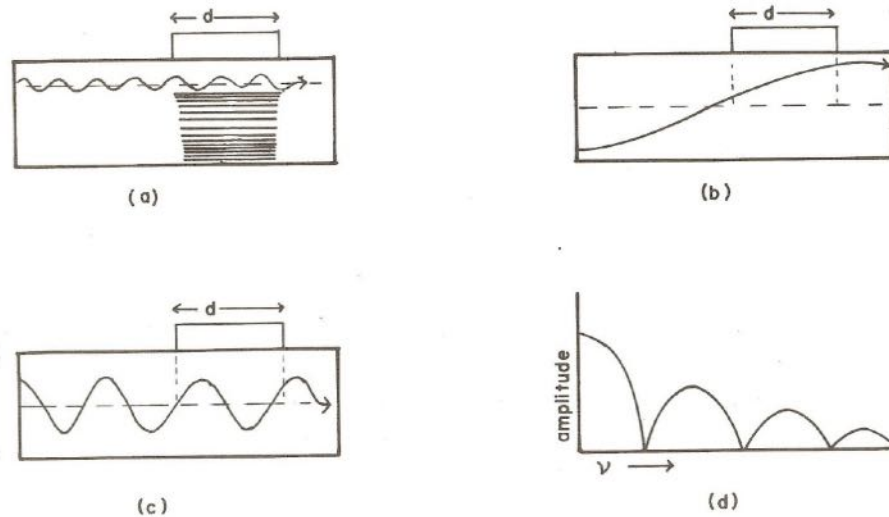


Figure 10 (a) block with sensor mounted, compressional wave hits perpendicular to sensor face and Rayleigh wave travels parallel to face. (b) Strain in on blocks surface from Rayleigh wave with wavelength much longer than sensor diameter. (c) Strain on surface from Rayleigh wave-length shorter than sensor diameter. (d) Sensor output as a function of frequency of Rayleigh waves with equal amplitudes [10a].

3-4 Couplants:

To this point, it has been assumed that the sensor has simply been placed on the surface of the material containing the acoustic wave. When this is tried, you find that the sensor produces no or a very weak signal. If a thin layer of a fluid is placed between the sensor and the surface, a much larger signal is obtained. The use of some type of couplant is essential for the detection of low-level AE signals. Physically, this can be explained by looking at the acoustic wave as a pressure wave transmitted across two surfaces in contact. On a microscopic scale, the surfaces of the sensor and the material are quite rough so that only a few spots actually touch when they are in contact. Stress is force per unit area and the actual area transmitting a force is very small. If the microscopic gaps are filled with a fluid, the pressure will be uniformly transferred between the surfaces. For a shear wave with a variable strain component parallel to the surfaces, again very little strain will be transferred between the surfaces because of the few points in actual contact. In this case, filling the gaps with a low viscosity liquid will not help much since such a liquid will not support a shear stress. However, a high viscosity liquid or a solid will help transmit the parallel strain between surfaces. The purpose of a couplant is to insure good contact between two surfaces on a microscopic level.

Much is written about couplants for both ultrasonics and AE and much of this is either wrong or misleading. One basic problem is in using the terms bond and couplant interchangeably, a practice of which many people, including the author, have been guilty. Strictly, a couplant is any material, which aids the transmittal of acoustic waves between two surfaces, while a bond is a couplant, which physically holds the sensor to the surface. Water is a couplant and cured epoxy resin is a bond. Many problems have come about from using a bond in an inapplicable way. If a rigid bond is used to attach a sensor to a sample, which elastically deforms during the test, the normal result is a broken bond and poor or no sensitivity to the acoustic wave. Similarly, in an experiment where the temperature is changed appreciably, the use of a rigid bonding material can lead to

broken bonds due to differential thermal expansion between the sensor and the sample. Bonding agents, then, must be chosen with great care, and the primary emphasis put upon the compatibility of the materials under the test conditions. Usually, if the bond will hold the sensor on, it will be an adequate couplant. For a compressional wave, any fluid will act as a couplant. A highly viscous fluid will transfer some shear stress across the boundary, which may or may not be an advantage. The author tested a large number of couplants with compressional waves [7]. Almost all couplants showed an increase in the signal strength over no couplant of 30 ± 2 dB. The variation was little more than the uncertainty of the measurement. The most practical rule is to use as a couplant, a thin layer of any viscous fluid, which wets both surfaces. The sensor should be held against the surface with some pressure furnished by magnets, springs, tape, rubber bands, etc. The secret is to use as thin a layer as possible. If a rigid bond is used, there must be minimal differential expansion between the two surfaces.

A flexible bond can be used. Over the years, the author has had excellent results with GE Silicone II sealant. It is available as a clear household glue, which will set up within about 12 hours when used between a 25-mm diameter sensor and a metal or plastic surface. In one test, a perpendicular sinusoidal acceleration of about 100 G produced no bond failures using this glue. It is quite flexible and a sensor can be removed from a surface by sliding a knife blade or wood chisel between the sensor and the surface. In Table 2, a few commonly used couplants are listed along with the temperature range where they can be used [6,7].

Table 2 Some common acoustic emission couplants and the approximate temperature range where they can be used.

Couplant	Approximate Temperature Range
Dow Corning V-9 Resin	$\sim -40^{\circ}\text{C}$ to 100°C
High Vacuum Stop Cock Grease	$\sim -40^{\circ}\text{C}$ to 200°C
Ultrasonic Couplants	Room Temperature
Petroleum Gel	Room Temperature
Dow Corning 200 Fluid	-273°C to -70°C and -30°C to 200°C
Dental Cement	$\sim 0^{\circ}\text{C}$ to $\sim 50^{\circ}\text{C}$
50 % Indium – 50 % Galium mixture	$\sim 20^{\circ}\text{C}$ to 700°C
GE Silicone II	5°C to 200°C

3-5 Temperature Effects:

The temperature dependence of piezoelectricity is complicated and a detailed discussion of its effect on sensors is beyond the scope of this article [5]. However, there are certain effects which can lead to problems when a sensor is used at different temperatures. First, ferroelectric materials [8], such as the PZT ceramics, have a temperature (the Curie temperature), above which the material transforms to another, and usually non-ferroelectric, phase. Taking a ferroelectric sensor through the Curie temperature will remove the polarization, destroying the piezoelectric properties of the sensor, and may shatter the ceramic as well. Ferroelectric sensors will usually work well up to temperatures within 50°C of the Curie temperature, if the other materials in the sensor can stand the temperature. The Curie temperatures of PZT ceramics lie between 300 and 400°C .

Ferroelectric ceramics are polycrystalline. Each crystallite may have one or more ferroelectric domains in it. These domains are regions where the spontaneous polarization is all in one direction. This polarization can only be along certain directions in the crystal structure. When the ceramic is

polled, these domains are aligned as closely as the crystal orientation allows to the direction of polarization. Because of the random orientation of the crystallites, there are always going to be a fair number where there may be several possible orientations of the domain, which are almost equally close to the direction of polarization in the ceramic. Small strains may be enough to cause the domain to change orientation. Such a flip of a domain may cause a very small change in the polarization of the sensor. However, this change is the same order of magnitude as the change caused by a small acoustic wave. In general, it is impossible to distinguish an electric signal caused by a flipped domain from one caused by AE. The strain necessary to produce a domain flip can come from changing the temperature of a sensor. Thus, changing the temperature of a ceramic sensor can produce signals, indistinguishable from AE, which arise in the sensor and not the sample. Empirically, the temperature change necessary to produce appreciable amounts of these domain flip signals is around 100°C in PZT. This effect does not prevent ferroelectric ceramic sensors from being used at different temperatures but thermal equilibrium should be achieved before data is taken. If one wishes to measure AE while changing temperature, it is recommended that ferroelectric ceramics only be used for temperature deviations of less than 100°C. To measure AE over larger temperature deviations, a sensor made of a single crystal, such as quartz or lithium niobate should be used.

3-6 Sensor Sensitivity - Effects of Cables:

The sensitivity of a sensor is governed by the intrinsic sensitivity of the piezoelectric material, the dimensions of the piezoelectric element and the design and materials used in its case. Practically, one receives from a manufacturer a measured response curve to a standard signal and the capacitance of the sensor. This curve is often presented as if it were independent of the measurement technique. However, the sensitivity of a sensor will always depend, in part, upon the equipment with which it is used. The open circuit voltage produced by a sensor is a property of the piezoelectric element and is

$$V_o(S) = Q(S)/C_o, \quad (3-3)$$

where Q is the charge produced by a strain S and C_o is the capacitance of the sensor. When connected to a preamplifier, the actual voltage across the input resistor of the preamplifier (if the input resistance is large) is

$$V(S) = Q(S)/(C_o + C_c + C_i) \quad (3-4)$$

where C_c is the cable capacitance and C_i is the input capacitance of the preamplifier. AE sensors usually have a capacitance that falls between 100 and 1500 pF. Preamplifier input capacitances range between 20 and 40 pF. The capacitance per unit length of coaxial cables depends upon the cables' impedance with approximate values of 100 pF/m for 50-ohm cable, 66 pF/m for 75-ohm cable and 50 pF/m for 95-ohm cable. To see the range of this reduction in sensitivity assume an input capacitance of 30 pF and 1.5 m of 50-ohm cable. For a sensor with a capacitance of 100 pF, the output voltage would be $V = 0.356V_o$ or a decrease in sensitivity of 9 dB. A sensor of 1600 pF capacitance would have $V = 0.9 V_o$, a decrease in sensitivity of 1 dB. Thus, the loss in sensitivity can be appreciable for low capacitance sensors. Since most of the extra capacitance comes from the cable, it is a good practice to keep the length of the cable between the sensor and preamplifier as short as possible. This is also a problem for small sensors as the capacitance is directly proportional to the area of the disk.

Presently, most sensor manufacturers provide sensors with integral preamplifiers to prevent this cable effect. However, electronic components have a lower temperature tolerance than piezo-electric ceramics. Typical allowable temperature is from -50 to 100°C .

3-7 Sensor Sensitivity - Effect of Preamplifier Noise:

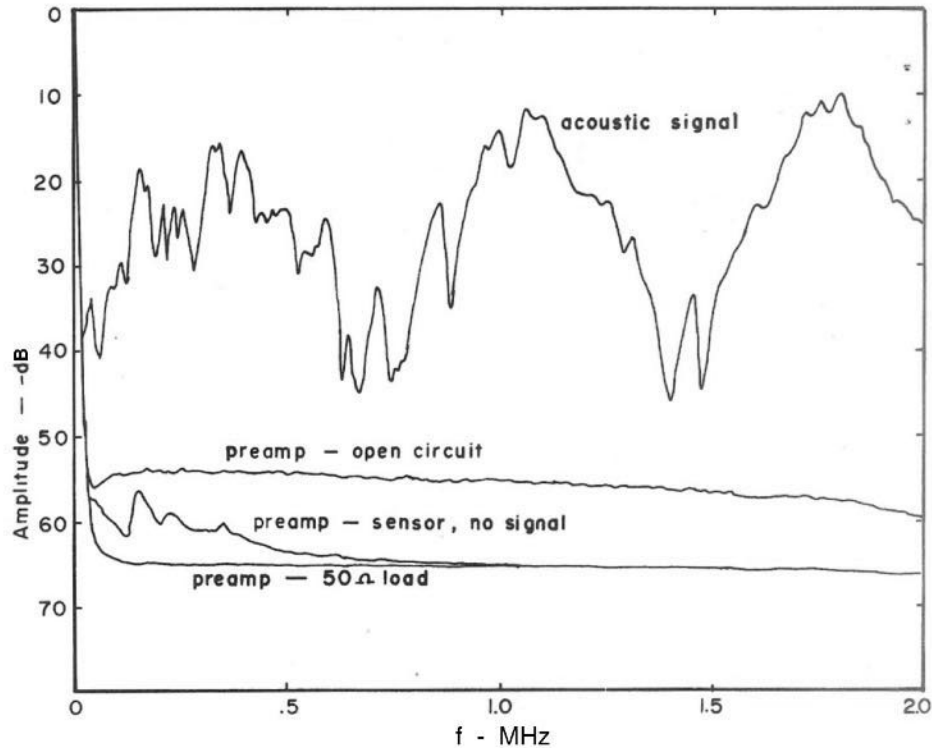


Figure 11 Frequency response of sensor-preamplifier combination. The top is the signal response and the rest are no signal responses with the preamp input circuit open, sensor only or 50-ohm load only.

The spectral response curve of a sensor-cable-preamplifier combination to an AE signal is shown in Fig. 11. Also shown are three response curves of the preamplifier without an AE signal. The exact shape of the spectral response of a sensor to an AE signal will depend to some extent on the preamplifier input characteristics and on the cable capacitance. Too much cable capacitance will tend to short out the high frequencies relative to the low frequencies. Different preamplifiers will give different response curves even with the same cable-sensor combination, although the difference is small between most commercial acoustic emission preamplifiers. The use of preamplifiers not designed for AE can have an appreciable effect on a sensor's spectral response characteristic as the input impedance can be as low as $50\ \Omega$.

The three preamplifier spectral response curves in Fig. 11 are, from the top down, the open circuit response, the response with cable and sensor in the absence of an AE signal and the response of the preamplifier with the input shorted with a $50\text{-}\Omega$ resistor. The noise in a shorted preamplifier is generated by current fluctuations in the first amplification device. If the input is not shorted, the noise can be regarded as being generated by current fluctuations in the input resistor. The root-mean-square (rms) noise voltage for such a resistor is given by [9]

$$V_n^2 = 4kTR\Delta f \tag{3-5}$$

where k is the Boltzmann's constant, T is the absolute temperature, R is the resistance and Δf is the bandwidth of the preamplifier. If the input stage of the preamplifier is open, R is the input resistance of that stage but if there is a sensor connected, R is some equivalent resistance. The capacitance of the sensor and cable will tend to decrease the higher noise frequencies. The peaks in the sensor curve in Fig. 11 are caused by the mechanical resonances of the sensor raising the impedance of the sensor cable combination at the resonant frequencies. The noise level of a pre-amplifier is commonly specified by the manufacturers as the output rms voltage, V_o , divided by the gain, G , when the input is shorted.

$$V_s = V_o/G. \quad (3-6)$$

The noise contributed by the sensor-cable combination can be estimated from eq. (3-5). A value of 295 K should be used as the temperature and the output impedance of the sensor-cable combination used as the equivalent resistance, R . This output impedance can easily be measured by a simple circuit. A variable resistance in parallel with the preamplifier input is reduced until the preamplifier output is one-half the level with no parallel resistor. The output impedance of the sensor cable combination is then equal to the input impedance of the preamplifier, which is essentially the value of the parallel resistor network formed by the preamplifier input resistance and the value of the variable resistor. For most AE sensors this impedance will be between 50 and 1000 Ω . Equation (3.5) can be rewritten

$$V_n = 0.004 (Z_o \Delta f)^{0.5} \quad (3-7)$$

where Z_o , the sensor impedance, is in $k\Omega$ and Δf is in Hz. The approximate noise voltage of the preamplifier-sensor-cable combination will be

$$V_{\text{noise}} = (V_s^2 + V_n^2)^{0.5}. \quad (3-8)$$

This noise voltage is measured by an rms voltmeter, which measured heating power of random signal. It assumes that the noise voltage is flat over the bandwidth, Δf . In Fig. 11, we saw that this is not strictly the case and that the noise level at certain frequencies may be 6 to 8 dB higher than the rest of the bandwidth. As long as the AE signals contain a large range of frequencies, this should not matter but if they are confined to one narrow frequency band and are at relatively low level, the noise peaks may present problems.

3-8 Sensor Calibration:

All manufacturers furnish calibration curves with their sensors. The currently accepted units for Rayleigh waves are dB referenced to 1 volt per meter per second. Many manufacturers will also furnish a calibration to normally incident compression waves with units of dB referenced to 1 volt per μbar . The acoustic signal used to calibrate the sensors is either a surface wave or a compression wave. A typical calibration curve for the compression waves is shown in Fig. 11. Calibration curves for the same transducer will not be the same for calibrations in Rayleigh velocity (meters/sec) or in pressure (μbar) because these were measured for different incident wave modes. For Rayleigh waves, the wave motion is parallel to the surface, while compression waves move perpendicular to the surface. Another reason is that pressure is proportional to strain, which is related to the surface displacement while velocity is related to the time derivative of surface displacement. For a constant frequency, the relationships for a given wave mode are

$$V_{\text{displacement}} \approx D \sin \omega t \quad (3-9)$$

$$V_{\text{velocity}} \approx d/dt (D \sin \omega t) = D \omega \cos \omega t \quad (3-10)$$

where D is the surface displacement and V is the surface velocity. For the compressional wave mode, for example, the velocity calibration curve is approximately the pressure calibration curve multiplied by the frequency. This tends to make the velocity curve seem flatter since it does not fall off as fast at higher frequencies. In selecting a sensor, one should have some idea of both the frequency range and the type of waves to be expected. Calibration curves can then be compared provided that they are for the same type of source and the same units.

The National Institute of Standards and Technology (NIST) [10] developed a sensor calibration for Rayleigh waves. This involves a point displacement in the center of a large steel block to produce the wave. The sensor is placed close enough to the source (100 mm) to allow a differentiation between the direct wave and reflected waves from the edge or the bottom of the block. The output of the sensor is digitized and the frequency spectrum of the received wave is calculated. This spectrum is compared to that of a reference sensor placed at a comparable position on the block. The reference sensor is a capacitive sensor, which is sensitive only to the average displacement of the block surface produced by the Rayleigh wave. This calibration is valid only for waves traveling on the surface of the block with a displacement perpendicular to the surface of the block. These are the most common waves seen in AE testing. Furthermore, the calibration is strictly valid only for steel or other materials with the similar acoustic impedances to steel. However, the NIST calibrations do give a valid comparison of the characteristics of different sensors. For the testing of most structures, the frequency and sensitivity characteristics of the sensors given by the NIST calibrations are more than adequate. However, any attempt to determine AE source characteristics from waveforms detected by routine AE sensors should include a far deeper study into the relationship between acoustic waves and piezoelectric sensors than is given here. Current studies [11] indicate that the shape of the wave front, the angle of incidence of the displacement to the surface of the sensor and even the construction details of the sensor can affect the output waveforms of the sensor.

Selected Reading List from J. AE Papers

K. Ono. Through-Transmission Characteristics of AE Sensor Couplants, J. AE, 2017, **34**: 1-11, 2017.

K. Ono, Receiving Sensitivities of Acoustic Emission Sensors: A data compilation, J. AE, 2019, **36**, 1-8.

Chapter 4 Instrumentation

4-1 Acoustic Emission Systems:

Acoustic emission instrumentation has changed drastically in the last sixty years. The basic detector of acoustic waves is still a piezoelectric sensor and a preamplifier. Analysis instrumentation was initially an amplifier, an oscilloscope and an electronic counter. Computerized systems were then developed where signal parameters such as signal arrival time, rise time, peak amplitude, duration etc. were measured with analog circuits. These allowed the calculation of the locations of AE sources as well as more sophisticated displays and methods of analysis. However, they were limited by both the relatively slow processing speeds and small memories of the early computers and the need for separate analog circuits for the detection of each desired AE parameter. Current computer systems are much faster and have far greater memory capacity. Instead of analog circuits for the AE signal parameters, they directly digitize the signals from the preamplifiers. This allows the use of any possible signal parameters in the analysis, for which one can write a code. A commercial system may list twenty or more possible signal characteristics. In practice, however, the analysis of AE signals is often confined to using digitized versions of the old analog parameters.

Besides speed and versatility, the new computer technology has resulted in much smaller AE systems. Twenty-four channel systems, which started out requiring at least a full instrumentation rack, now consist of three eight channel PCIe cards and a notebook computer. Eight channels on a single card is currently a reasonable limit. This limit is partly determined by the number of coaxial connectors that one can fit on the input of a card and partly by the amount of circuitry still required for each channel. At present, most systems still require coaxial cables between the circuit boards and the sensor-preamplifier combinations. There are some systems, which use rf broadcast connections to the sensors, but these are not yet common. Therefore, in the rest of this paper, a notebook computer with a separate box containing multi-channel digital cards and coaxial cables to the sensors is assumed. Eight channel cards are not quite as versatile as four or two channel cards – limitations being a slower maximum digitization rate and shorter maximum lengths for digitized signals. However, these superior capabilities of the smaller cards are more important in laboratory experiments than in field tests.

There have been a large number of commercial AE systems manufactured. Systems, which digitize the AE signals have been available since the mid-1990s. Three major manufactures selling in the United States have been Physical Acoustics Corporation, Vallen Systeme and Digital Wave Corporation. Other systems have been produced in many countries, Japan, China, Russia, England and Israel, to name a few. All of these systems perform the same basic functions although they may use different nomenclature and methods of analysis. This paper will be based upon the operation of Physical Acoustic Corporation (PAC) systems [12], with which the author is most familiar. It is hoped that the ideas expressed here will be fairly easy to apply to other systems.

4-2 System Operation:

The basic measurement in a multi-channel AE system is the system time. This starts when the test starts and stops when it ends. It uses a 4.0 MHz clock in the PAC systems giving a time resolution of 0.25 μ s. Every time a sensor detects a signal, the exact time of arrival in test time is recorded. Every channel of the system is independent, thus if a strong electromagnetic noise signal hit the system, every channel could record the same arrival time. Each channel also has its own clock, which starts when the trigger threshold of that channel is first crossed. The channel clock

runs until the programmed maximum signal length is reached. This is used to determine the signal rise time and the signal length. Each channel has a set *PDT* (peak definition time). When the signal amplitude reaches a maximum and starts to decline, the card notes the time and maximum amplitude, then waits an additional *PDT* to see if the previous signal amplitude is exceeded. If it is, the *PDT* clock is reset and the measurement continues. If there is no higher amplitude signal within the *PDT*, the previous amplitude is the peak amplitude and the time from the signal start is defined as the signal rise time. As the signal continues, the card always records the time of the last threshold crossing. If there is no further crossing within the *HDT* (hit definition time), the last recorded time defines the signal length. After the *HDT* has been reached, the card waits until the *HLT* (hit lockout time) expires. At this point, the card is reset and ready to acquire the next signal. The *HLT* time prevents the channel from treating a reflection of the first signal as a new emission. However, an excessively long *HLT* time can prevent the capture of rapidly occurring emissions. In most AE tests, the exact values of these three times are not important, but the values of the settings should be considered, especially if a high average repetition rate with short emissions is expected. Simultaneously with these time measurements, the card is also digitizing the signal and storing it, if waveforms are desired.

Both the time measurements and the digitization of the emission waveform start when a preset threshold is exceeded. The digitization runs until a preset number of samples is exceeded. The digitizer is actually running continuously with the samples sweeping through the memory. When the card is triggered, the card stores the number of words set for the record length but it starts the record some time (say 50 to 200 μs) before the trigger occurred. In this manner one has a record of the waveform including 50+ μs before the original trigger time. Thus, the actual start of the waveform can be examined, if necessary, to determine how accurately the first threshold crossing defines the leading edge of the signal. The signal length is defined by the last time that the signal crosses the threshold. However, signals are often longer than the set digitized word length. Therefore, the signal length is usually measured from the system clock, not from the digital record. The rise time and peak amplitude can just as well be measured from the digitized signal as from the system clock.

The shift from analog to digital AE systems was made possible by advances in signal digitizers. When the first computerized AE systems were designed the available signal digitizers ran at speeds up to one MHz and had eight bit words. With a sign bit, an 8-bit word gives a precision of one part in 128. This gives a dynamic range of 42 dB, a little over two orders of magnitude. Modern systems have signal digitizers, which run up to 40 MHz and have 16-bit words, which, at one part in 32,768, gives them a dynamic range of 90 dB or four and a third orders of magnitude. This performance is more than adequate for the usual AE test. Most engineering materials have relatively high acoustic attenuations at frequencies above 1 MHz. The acoustic attenuation of plastics and composites restricts useable emissions to below 500 kHz. The dynamic range of AE signals from structural tests is usually somewhat less than 80 dB between the background noise level and the largest signal detected. The current digitizers thus have a satisfactory performance for most AE testing. One limiting factor is the number of words in a digital signal record. The record length is chosen when designing the test, subject to a hardware limit, which is usually between 4,000 and 16,000 words. For high digitization rates and large signals, the digital signal is often truncated before it drops into the background noise. This is not usually a major problem as most of the energy in the transient signals occurs at the beginning of the record with the latter part of the transient consisting of a low amplitude exponential decay into the background noise.

The limitation on the digitation rate is set by the frequency of the AE signals emitted by the specimen. The frequency content of the signals is usually determined by the materials used in the specimen. The upper frequency of an AE event will be governed by the size of the region involved and the speed with which the movement occurs. On a microscopic scale, this can lead to quite high frequencies. However, in tests involving structural materials, the detected frequencies will depend on the attenuation characteristics of the materials involved. For metals such as aluminum, steel and titanium, frequencies up to 1 MHz are often detected. For lead and copper, maximum detected frequencies will be no more than 500 kHz and for plastics and composites, the maximum detected frequencies will be about 200 kHz. This does not mean that higher frequencies will not be present, only that they will be minor components of the larger amplitude signals. This combined with the *Nyquist criteria* (which states that the digital record must have at least two samples per wavelength of the highest frequency recorded to avoid inherent distortion) suggests that sampling rates of 2.0 MHz for plastics and composites and 10 MHz for metals are as high as is needed. The penalty for signals containing frequencies higher than half the Nyquist frequency is that these higher frequency components are aliased, folded back, into the lower frequency range. In the worst cases, this can result in gross distortions of the original signal. If a lower sampling frequency is used, the low-pass filters in the system should be set for considerably less than the Nyquist frequency.

It was mentioned that several AE parameters were described and used from early days of AE, when signal shapes were confined to the face of an oscilloscope. To facilitate the discussions of AE testing in this paper several of the terms and parameters are listed with definitions and discussions of their usefulness.

An **AE hit** is defined as a transient signal from a sensor which rises above the detection threshold received at an AE channel.

Its **arrival time** is the time when the hit signal first exceeds the detection threshold.

The **detection threshold (V_t)** is set during the hardware set up. It is the value (in dB above 1.0 μ V) at which that channel will detect a signal and trigger the signal digitizer. Normally all channels in the test have the same detection threshold but if during a test a channel develops a noise problem, it can be raised so that the channel only sees larger signals. The detection threshold is limited by the background noise in the system. If there is no acoustic noise in the specimen, the limit will be, at best, the noise level in the preamplifier. From equation (3-5), it is seen that the noise signal in the input of the preamplifier is proportional to the square root of the input impedance, the absolute temperature and the band width. For AE preamplifiers and sensors, this noise voltage will vary between, very roughly, 5 and 15 μ V. This would suggest that for a quiet specimen, a detection threshold of 30 dB (32 μ V) would be reasonable. (The AE Halon Bottle tester uses a 25-dB threshold with a narrow bandwidth and the bottle is enclosed in a metal oven, which helps reduce external rf noise)

An **AE event group** is defined as a number of hits from different sensors, which occur within a preset time window. Every hit is checked to see if it is in an event group or starts one. This time is set in the hardware during set up and determined by the test engineer. An example is a multi-channel test of a sphere. To prevent several hits from the same channel, the time window is set at the time an AE signal with the shear velocity (the slowest wave) takes to travel half way around the sphere. Any signal that occurs after this time, measured from the first hit in the group, will not be included in the group.

An **AE located event** is defined as an event group, for which the system program can calculate a location on the specimen from the arrival times in the event group.

A **cluster** is a group of located events, which occur in a defined region in the specimen. The area or volume of the cluster can either be defined in the post-test analysis or defined in the system program, which allows the system to identify the cluster in real time. The AEWin software can be

set to identify clusters of different sizes and monitor them as to size or count content but not absolute energy content.

Figure 12 shows a typical AE signal with several defined signal parameters. Obvious are:
the **signal duration (τ_s)**, which is defined as the time between the first and last threshold crossing,
the **signal peak amplitude (marked A_+)**, the largest amplitude of the signal and is usually given in dB in reference to $1 \mu V$,
the **signal rise time (τ_+)**, which is defined as the time between the first crossing and the time of the signal peak amplitude.

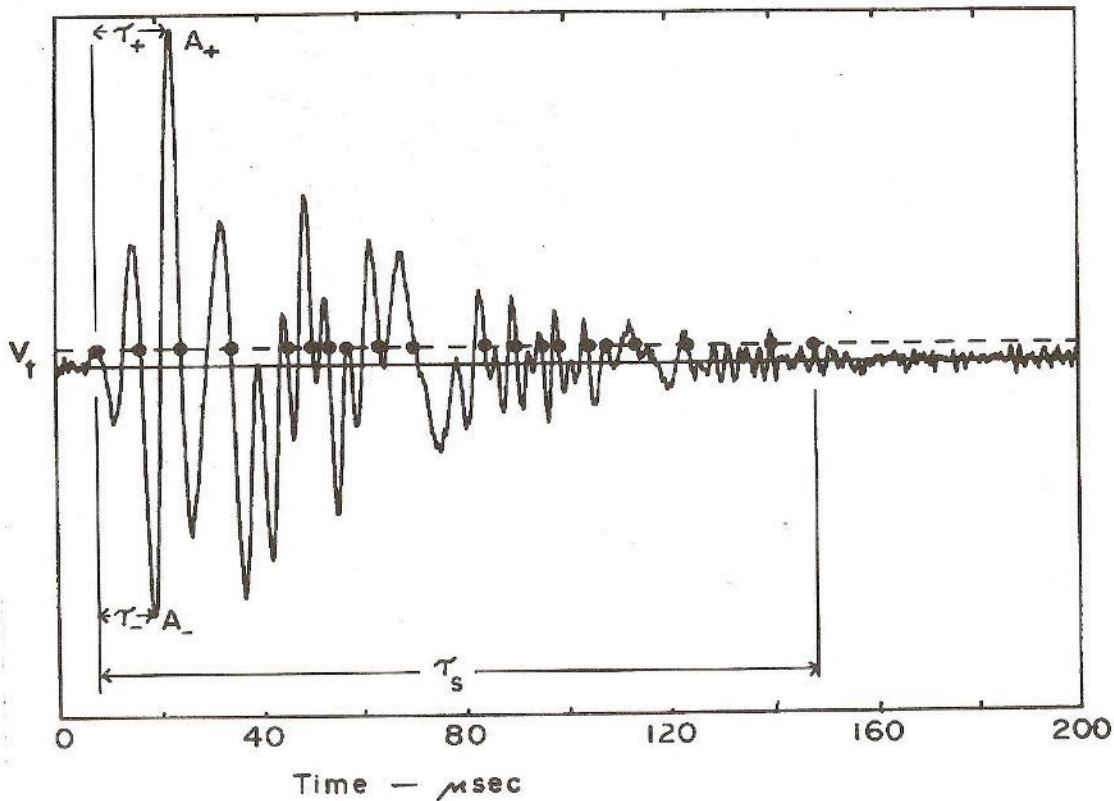


Figure 12 AE signal showing the AE count (the number of crossings of the trigger threshold, $n = 20$), the risetime τ_+ , the peak amplitude A_+ and the signal duration τ_s .

For long signals, such as a large impact on a piece of aluminum, the time it takes for the signal to damp down to below the detection threshold is far longer than the longest digital record available can hold. A very short signal of $<50 \mu s$ indicates that the signal is probably an electrical noise spike and not an AE signal while a signal length greater than 10 ms suggests either a frictional origin or a very low attenuation for the AE signal. The peak amplitudes are a good indicator of how strong the emissions are. Peak amplitudes below 40 dB are very weak for most tests and peak amplitudes above 70 dB often are indications of some damage in the specimen. From Fig. 4b which shows the time difference between peaks of an ideal signal containing both compressional and shear waves, it would appear possible to determine how far a signal had travelled from the signal rise time. Unfortunately, real AE signals are seldom that simple. The rise time parameter does have another use. If a channel is re-armed slightly after a signal has reached it, the resulting waveform is usually a decaying wave. In such cases, the rise time it often registers is the time from when the

threshold is crossed to the first oscillatory peak. For normal signals the rise time will be several wavelengths long. Therefore, if the rise time is short, less than 10 to 15 μs , the channeled triggered in the middle of a signal and the registered arrival time for that channel is probably wrong. All the data from that signal can be ignored unless it is a very large amplitude signal. If a signal has a very long rise time, especially greater than half the signal length, it is almost certainly not a transient and such an AE signal can also be ignored. The signal rise time is the main indicator, which can indicate whether the received signal is actually from a transient event in the sample or it is distorted or extraneous.

The **AE count** (the number of dots in Fig. 12, $n = 20$) was one of the first parameters used in the AE field. It is simply the output of an electronic counter applied to an AE signal. Every time the signal crosses a preset threshold in one direction (decreasing or increasing) a count is registered. If this count is plotted continuously, it gives a history of the emission from the specimen. If a count per unit time is plotted, one has a history of the rate of emission. It is one of the simplest and most useful measures of AE. It is also almost impossible to directly relate it to any physical parameter. The AE count depends upon the detection threshold, characteristics of the sensor, the gain and bandwidth of the preamplifier, the quality of the acoustic coupling and the characteristics and geometry of the specimen. The one thing which can be said for the AE count from an AE signal is that if the signal has only a single count, it is probably electronic noise. An AE signal almost always contains several oscillations.

The **signal energy** is easy to define but hard to measure with an analog circuit. It can be defined as the integral of the voltage squared vs time curve over the signal length. The problem with an analog measurement is the dynamic range of the signals. If an AE test has a dynamic range of 80 dB, which is relatively common, then the energy range of those signals will cover at least eight orders of magnitude or 10 μV to 1 kV. Analog circuits with such a dynamic range were not available. If AE signals all had the same signal characteristics then it might be possible to design analog circuitry to measure the energy. But AE signals come in a wide variety of shapes and sizes in the same test. For a digitized signal the signal energy is defined as

$$E = (\Delta t/R) \cdot \sum_i V_i^2(t) = (\Delta t/R) \cdot A_s \quad (4-1)$$

where Δt is the sample width in seconds, R is the resistance in ohms, $V_i(t)$ is the sample amplitude in volts and the summation is over T , the total signal length in seconds. A_s is the summation of the squares of the sample voltages. For a Physical Acoustics Corp. system, this E is called the absolute energy in units of 10^{-21} J (or atto J) by multiplying with a constant, 9.31×10^{-4} . If the constant is changed to 6.70×10^{-6} , the energy is given units of MeV (million electron volts), a unit the author finds more useful. The one problem with this measurement is that it only covers the digitized signal length. If the transient signal is longer, the calculated energy will be somewhat less than the actual signal energy. However, most of the signal energy in a transient is near the beginning of the digital record. The small percentage of the signal energy lost by truncating the signal is insignificant compared to the other uncertainties in the measurement of the signal energy.

It must be stressed that while the signal energy is given in physical units, it is not the actual energy of the emission, only the energy converted by the piezoelectric sensor. The actual emission energy was radiated throughout the specimen and only that actually hitting the face of the sensor is measured. The energy detected by the sensor is strongly affected by the distance between the source and the sensor. In the analyses in this paper, the absolute energies from the three nearest sensors to the emission source are summed to give a better estimate of the actual strength of the source. This sum is what is graphed as energy in the analysis chapters.

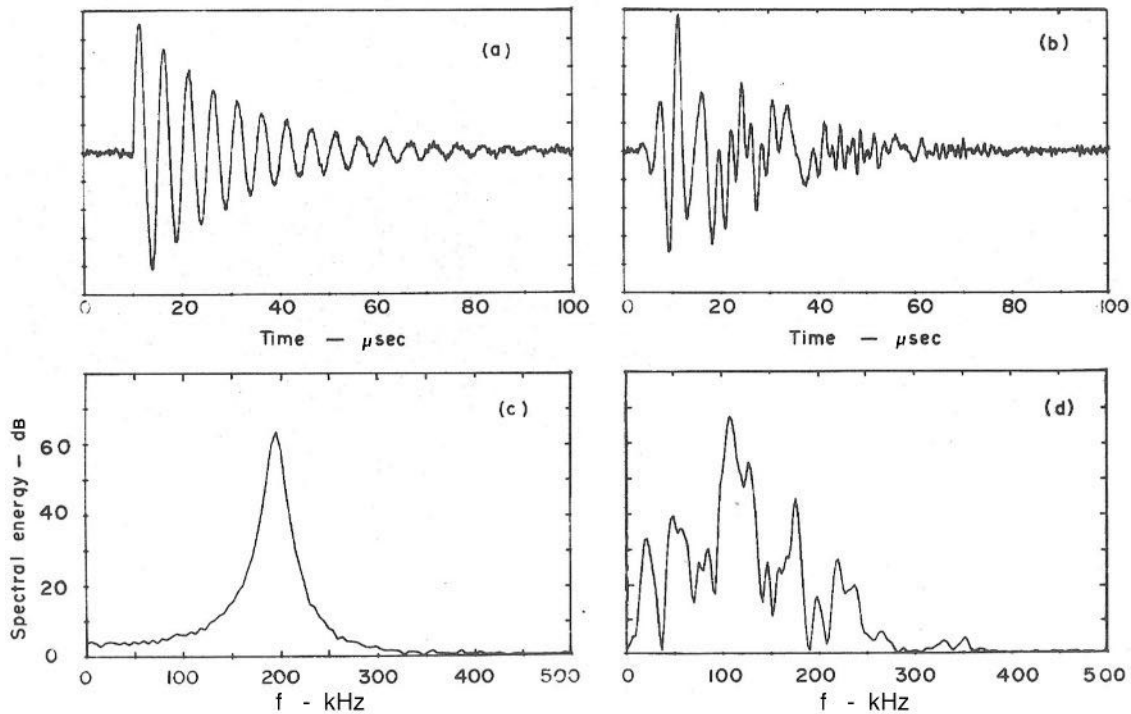


Figure 13 The spectra (c) of a damped sine wave (a) and (d) of an AE signal (b).

The last signal “parameter” which is useful to calculate from the digitized waveform is the **Signal Spectrum**. This is a Fourier transform of the digitized signal. The spectrum of the signal (Fig. 13b) is shown in Fig. 13d. In theory, one should be able to learn a lot about the characteristics of the source from the spectrum. In practice a back calculation to the actual characteristics of the source is almost impossible. The reason is that for the calculation, one needs to know the response function of the sensor for the exact combination of acoustic waves, which excites it. Also needed is the response function of the specimen for all the acoustic paths of the generated acoustic waves, which reach the sensor. There have been attempts to back calculate the sensor response function in the laboratory but these are very far from an actual test. The topic of the detailed interaction of acoustic waves and sensors has been explored in recent papers by Ono et al. [11]. This work has shown that the subject is far more complicated than was originally thought. The author was a far stronger advocate of spectral analysis in AE thirty years ago than he is now.

4-3 Noise suppression:

One of the major problems in AE testing is unwanted noise. Noise can be defined as any signal detected by the AE system, which is not a desired response to the applied stimulus. This includes all types of electronic interference and acoustic signals not produced by the stimulus as well as undesired responses to the applied stimulus. In the past, electronic noise has been a major problem. The defining electrical characteristics of AE signals are: random occurrence in time, random frequencies, amplitudes and durations and waveforms whose sole common characteristic is that they are transients. Even transient signals, if they occur fast enough, can be superimposed and appear as an apparent continuous signal. The response to such electrical noise has been improved shielding on sensors and preamplifiers, using double shielded coaxial cable when needed and much improved filtering in system power supplies. This has eliminated much interference from radio and television stations, ignition systems on internal combustion engines and extraneous signals on input power lines. However, such problems as ground loops in the AE cables and multiple and

poorly connected power grounds in the work facility are often encountered. Almost any industrial area can have unexpected sources of electrical noise, which would not be a problem if one were not looking for wideband signals down to the 10- μ V level.

AE signals occur randomly and have no definite characteristics except their transient origin so many traditional electronic methods of noise reduction are not possible. Narrow bandwidth electronics, any type of frequency locks and predetermined time windows either do not work or eliminate real emission signals. Frequencies below 20 kHz are avoided for good reason. Most AE signals, with the exception of earthquakes, contain adequate energy above 20 kHz. It is desirable to be able to converse during a test and there is no need to detect the normal acoustic background of a shop. Radio and TV stations were once a problem but using good coaxial cables and shielding on both preamplifiers and sensors has almost eliminated their interference. Modern systems have very good filters on their power supplies but there are still situations in industrial locations where noise on the input power lines is suspect. When suspected radio frequency noise is still detected even when the sensors are in a sealed can filled with foam or, better yet, a vacuum and there is still noise, one good rule is to ground everything even remotely connected to the system. Still, it is possible to spend years chasing that randomly occurring signal with little success.

Electromagnetic signals, as they are detected, are usually short, often with a single spike with a length of a few μ s or less. Most acoustic signals have several oscillations at least. Filtering out all signals with only one count usually does not remove any important AE signals. Another useful filter is the signal duration. Assuming that an AE signal has over three cycles of the dominate frequency, one could filter out any signals shorter than 10 μ s for a frequency of 300 kHz or 50 μ s for a frequency of 60 kHz. These two filter times have worked well for the Halon Bottle tester and FRP tests.

Another problem is unwanted acoustical noise. Any two surfaces, which are in contact and have the slight movement between them, can generate relatively large acoustic signals and such signals can travel long distances in metals. Impacts on surfaces can generate large signals. A rain storm hitting a railroad track a quarter of a mile from the sensor has been seen. Any test involving motion, such as rotation of a bearing or cycling of a wind turbine blade is going to have some continuous type acoustic signals. For a good bearing, the normal signals will be below the 20-kHz low-pass filter in the signal channel. Any bearing signals that pass this filter may indicate problems with the bearing. In fatigue cycling of FRP, such as a wind turbine blade, large noise signals are often seen. If they are plotted against where they appear in the loading cycle, many appear in the middle of the cycle where the load is changing the fastest. This suggests that there may be some small regions of the blade, which are rubbing together during the loading. On the other hand, signals from defects in the part usually appear during the rising load at or near the peak. This is where flaw growth signals should be found. Current AE systems contain provisions for an electronically controlled *time gate*. Using the load signal as input to this gate, it can be set so that the system only accepts data during part of the load cycle. In wind turbine blade fatigue tests, this gate is open for only the top 10 % of the load. This has worked well at filtering unwanted signals. Almost no signals have been seen as the load decreases from 100 % to 90 %.

A final comment about noise signals is that no detected signal should be removed from a data set as being noise until one has a good idea of its origin. Every acoustic signal is produced by some mechanism. In any real test, that mechanism should be identified and understood before a signal is discarded. Often signals can be attributed to noise only after their locations have been graphed.

Chapter 5 Setting up the Test and Emission System

Acoustic emission tests are performed for a variety of reasons. In this monograph, only tests of structures are considered. There are three basic types of structural tests:

1. **Proof tests** where the object of the test is to prove that the structure is sound up to a proof load.
2. **Failure tests** where the object is to find at what load the structure starts to fail.
3. **Fatigue tests** where a cyclic load is applied to the structure to obtain some idea as to what the working lifetime of the structure is.

AE monitoring of a proof test will indicate whether the proof load itself is producing any damage in the structure. In tests to failure, whether static or cyclic, AE monitoring can indicate whether it is a sudden or a prolonged failure and if there are several other regions, which are starting to fail when the main failure takes place. Such monitoring can also provide some information on the mechanisms of the failure.

The design of an AE test involves tradeoffs in both the physical set up of the test and in the type of analysis to use. Most of the time the geometry and construction of the specimen and the method of applying the test stress will simplify the choices. Other limitations will be the characteristics of the AE system, the number of channels in the system and the sensors available. For clarity, various topics will be discussed separately although in a real test, they all interact to some degree.

5-1 Test Assessment:

The first step in setting up an AE test of a structure is a study of the design and function of the structure. What is its function? How well does it appear designed for that function? What is the test designed to determine? Does the proposed loading duplicate the stresses seen in actual usage? An AE test can only detect growing flaws. They must be activated the same way in the test as in normal operation. If mechanism for the test load does not correspond to the normal operation of the structure, the value of the test is questionable. The loading rate must also be considered. If the rate is too fast, the emission can swamp the instrumentation, too slow and the test can take forever. Finally, what are the structural materials? Is the AE test operator familiar with them or not? If not, is there literature available which could provide information such as previous AE tests on the material? Or, are there samples, which could be tested? Of all these questions, the most important are how the load is applied and the material properties. Only then should the choice of sensors and sensor location be determined.

5-2 Acoustic Properties of Materials:

Structural materials can be divided into categories; Metals, ceramics, glasses and composites. Composites include both metal-metal and fiber reinforced plastic materials (FRP). Metals are generally crystalline, composed of many small crystallites (grains) of random orientations and different compositions. On a macroscopic scale, metals are relatively homogeneous. The acoustic wavelengths for the frequencies normally used in AE testing are much larger than the crystallites. Thus, the acoustic properties of metals are averages over large number of crystallites and will be independent of frequency and direction of propagation. These bulk properties, both acoustic velocities and impedances, are homogeneous with a single compressional and a single shear velocity. Acoustic attenuations, however, arise from a large number of mechanisms and cannot be so easily characterized. Ceramics are similar to metals in that on a microscopic scale, they are composed of

randomly oriented crystallites, but with some porosities. Glasses have an amorphous structure with an average density and coupling coefficient between atoms. Both have bulk acoustic properties similar to metals. They differ from metals in that both are quite brittle and tend to fracture suddenly when their elastic limit is reached. Metals are ductile to some degree and undergo inelastic deformation before fracture appears. Plastics are seldom used by themselves as critical structural materials. They could be classified as very ductile glasses and are usually one component of composites. Composites differ from metals in being composed of several materials, which are segregated into distinct substructures. In general, these substructures are larger than metallic crystallites which results in acoustic properties that are not homogenous. The different materials have different mechanical and acoustic properties. The bulk velocities of composites are anisotropic and can show definite frequency effects. One difference often seen in composites is that the elastic limit is not as abrupt as in ceramics or metals. Composites can experience a very long period between the load where the elastic limit is reached and the failure load. There have been fatigue tests on wind turbine blades where the composite matrix in the blade skin started to turn to powder before structural failure occurred.

5-3 Acoustic Emission Frequencies:

The acoustic frequencies generated by AE signals cover a wide spectral range, from much less than one Hz in earthquakes to well over a MHz in metals and ceramics. Typically, AE testing restricts itself to a low frequency cutoff of about 20 kHz and a high frequency cutoff dependent upon the material being examined. The low frequency cutoff is usually set so that it excludes much environmental noise produced in a test area, such as voices, machinery noise and other environmentally produced acoustic noises. The upper limit is usually determined by the material and the test objective. Typical frequency ranges of 100 to 500 kHz are used in ceramics and metals and 20 to 100 kHz in composites. The choice is often determined by what sensors are available. If locational accuracy is wanted, higher frequency sensors are suggested.

5-3 Simple Attenuation and Velocity Measurements:

Because of the variation of acoustic properties with both material and geometry, it is advisable to measure the acoustic velocities and attenuations in the actual test specimen. The following procedure can give a reasonably accurate measurement. Mount two of the test sensors to be used on the specimen in an area free of welds, variations in specimen thickness and other features, which could interfere with the acoustic transmission path. The distance between the sensors should be between 200 mm for composites and 1000 mm for metals. Make five pencil-lead breaks (PLBs) about 5 to 10 cm away from each of the sensors. The breaks should be approximately on the line between the sensors. This procedure is designed to have at least similar acoustic waveforms exciting the two sensors. Record the arrival times and absolute energies for each PLB. The velocity is the difference in arrival times over the distance between sensors and the attenuation is ten times the log ($\text{energy}_2/\text{energy}_1$) over the distance. The averages of the two number sets should give reasonable values for the velocity and attenuation for that path. The trigger threshold used for the measurements should be about the same as is to be used in the test. The velocity value will probably have a smaller variation than attenuation value. For composites, the velocity and attenuation should be measured in at least three directions, along the main fiber axis, perpendicular to that axis and 45 degrees between the two. A variation in the velocity between the two perpendicular axes of 10 % or less may not make much difference in source location accuracy, so an average of the three velocities can be used. However, a difference of 30 % or more can make a large difference so an anisotropic velocity calculation should be considered. If this is necessary, velocity measurements

should be made every 10° on the specimen. A FORTRAN program using an anisotropic velocity is included in the Appendix. Programs, which can use an anisotropic velocity in locations, may also be included in the system software.

5-4 Sensor Layout:

The object in most AE structural tests is to cover all significant regions where failures could occur. It is important to cover the areas of interest so that all parts of the area are within acoustic range of at least three sensors. Where the areas are separated, multiple location programs can be used. Where it is desirable to display adjoining areas separately, such as the upper and lower surfaces of a wing or turbine blade, common sensors can be used in separate programs (check in the system instruction manual for the correct settings to use common sensors in separate location programs). The easiest starting point for laying out sensors is to start with an overall sensor pattern such as interlocking triangles or interlocking rectangles. The triangular pattern covers somewhat more area per sensor while the rectangular pattern has a somewhat greater probability of at least four sensors hits by an emission, desirable for an over-determined data set. Once the overall pattern is set, the actual locations can be determined from the features of the surface. Not only is it not necessary to adhere rigorously to the starting geometric layout, it is helpful for the actual locations of the sensors to differ somewhat from the geometric points. When using a nonlinear least-squares program to locate the sources, having several sensors lying on a straight line encourages location artifacts.

An important parameter in setting up a test is the acoustic attenuation of the specimen surface. This will suggest the maximum sensor separation. The attenuation should be measured, if the value is not already known. For accurate location with an approximation calculation, an over-determined data set would have at least four hits per event for 2D location or five hits per event for 3D location. Therefore, the sensor spacing must be small enough to allow sensors outside of the immediate triangle around an intense source to be excited. A rule of thumb is that the maximum distance between two sensors should have an acoustic attenuation between 30 and 40 dB. Thus, an attenuation of 0.1 dB/mm would suggest a maximum separation of 400 mm while an attenuation of 0.01 dB/mm could have a separation of 4 m on average between sensors on a triangle. This maximum distance is a goal, not an absolute requirement. Any attenuation measurement on a composite should not be believed to better than on order of magnitude because of differences in acoustic scattering with different construction layouts of the components.

5-5 AE System Setup:

The setup of the AE system consists of two parts, the AE acquisition parameters and the real time graphs. The acquisition parameters include the trigger threshold, the timing parameters, possibly the gain and the channel bandwidth and waveform settings. The trigger threshold is set in dB above $1.0 \mu\text{V}$ out of the sensor. It can be either a fixed value or a fixed value above the background noise level, a so-called floating threshold. A floating threshold is not recommended for multichannel tests. It is hard enough to get hit data sets from multiple sensors, which all trigger at approximately the same point on the waveforms without having the threshold of each sensor bouncing up and down. The fixed threshold should be set a few dB above the trigger level of the noise level of specimen. All sensors should have the same trigger level. Occasionally during a test, the noise level of one channel will increase to the point of continually triggering the channel. When this happens, the trigger level can be raised for that channel. However, AE events located using that

channel will have a greater location error. For a very high energy event, the absolute energy value is probably still valid even though the location is more uncertain.

The timing parameters PDT, HDT and HLT in PAC systems, are not critical for most tests. PDT, the peak definition parameter, is often set at 200 μ s. This parameter helps measure the rise time, which ranges between 50 and 1000 μ s for emission in an FRP test. One use of the rise time is to help filter out hits, which have started just before the channel was activated. Hits with rise times of less than a few cycles of the waveform are suspect. HDT, the hit definition time, helps determine when the hit has ended. The standard value of 800 μ s seems reasonable. HLT, the hit lockout time determines how soon the channel can re-arm after a hit has ended. Most tests with relatively slow load increase rates show repeated events on a channel with spacings of at least several milliseconds. A re-arm gap of 1 or 2 ms has seldom produced a recognized problem. However, a gap of 20 ms could start missing data. The **max duration** setting should be set higher than the longest duration expected to be seen in the test. For FRP, a setting of 10 ms should be long enough. For metals such as aluminum and steel, a value of 50 ms or longer may be needed to include the full signal length of high amplitude hits.

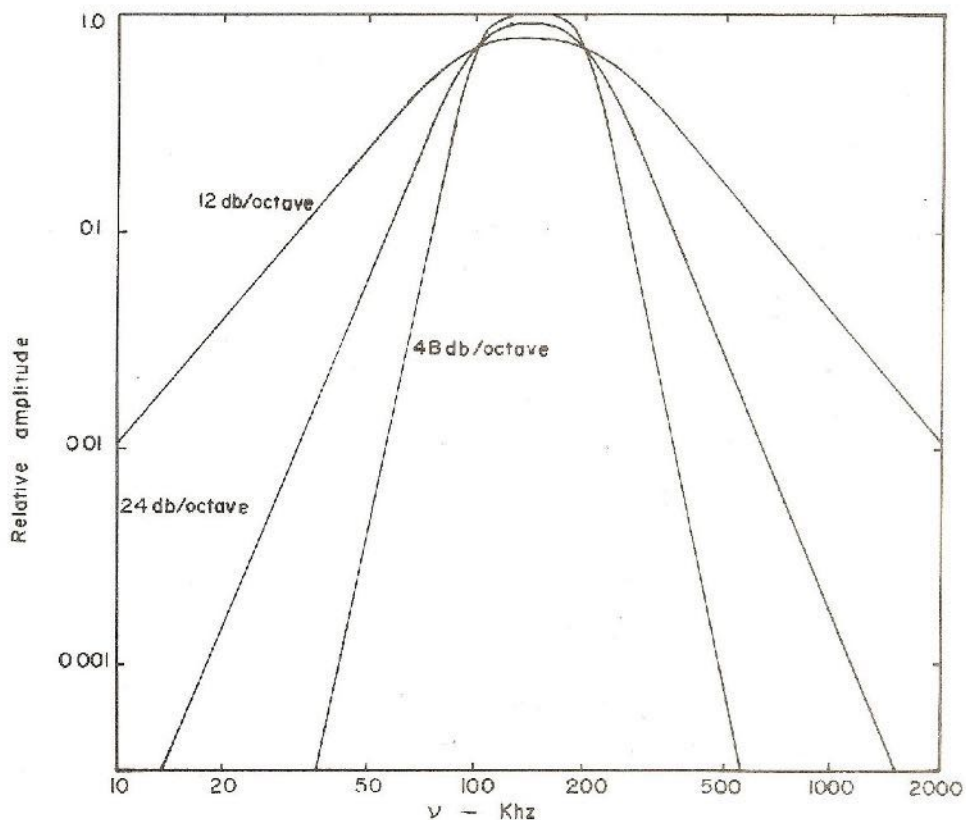


Figure 14 Electronic bandpass characteristics of different filters as a function of frequency.

Most of the gain is in the preamplifier and is often fixed. With 90 dB of dynamic range in the system, the typical preamplifier gain of 40 dB is usually adequate. Additional gain on the computer board seems redundant. The band width should be chosen to eliminate most room noise and any truly high frequency noise (1 MHz +). It must be remembered that the upper and lower band width figures are for the knees of the curve as shown in Fig. 14. A large amplitude signal with energy outside of that bandwidth will still pass appreciable energy through the filter.

Waveform settings are the digitization rate and the number of words in a sample. The digitization rate should be 1 to 2 MHz for composites and 4 to 6 MHz for metals. The problem with high digitization rates is that more words are needed for the same length sample. Current PAC eight channel boards are limited to 4000-word samples, which allows a 4-ms sample at 1 MHz, but only a 1.33-ms sample at the boards maximum sampling rate of 3 MHz. Another problem is that a hit on an AE system uses only about 30 bytes of memory to store it in the computer while a 4000-word waveform takes over 8 k-bytes of memory. If there are many low-amplitude emissions detected, data files, which include waveforms, can rapidly become unmanageable. For example, a 5-megabyte file will contain about 500 hits with 4000-word waveforms or up to 200,000 hits without waveforms. A fatigue test of a composite structure near the failure point can record those 200,000 hits in little more than one minute.

Another useful feature of an AE system is front-end filters. These can be invaluable in a noisy environment. They automatically exclude hits that fall outside of preset windows for signal parameters. The most useful that I have found are the AE count, the signal duration and for source location, the rise time. A count of one for a hit is usually meaningless – a simple excursion of a background noise spike above the threshold. Such hits have low amplitudes and durations. They may not appear very often and the only problem is that they may lock the channel out for the duration of the HLT time. However, some electrical equipment can generate short, intense rf spikes. A little oxide on a coaxial connector or a minor cut in a cable shield may enable the cable to act as antennas for the preamp inputs. If they occur at harmonics of 60 cycles, they can completely lock out a channel. A front-end filter eliminating all hits with one count can be very useful and have almost no effect on the detection of real emission.

A front-end filter rejecting signals with durations of less than three wavelengths of the dominant frequency seen in the test can remove other forms of electrical noise, which are short transients. The rationale for this is that most AE signals contain considerably more than three oscillations. Filtering out signals of less than 50 μ s in FRP tests or 10 μ s in the Halon bottle tester has worked very well. Filtering out signals with rise times of less than a few wavelengths during location tests can remove signal, which have started before the channel trigger was reset. These signals, while they are real emissions, have arrival times, which, at best, confuse the location algorithms. While such filters are useful, they should be used with restraint.

One essential parameter for any load test is an electrical signal proportional to the load. With a direct hydraulic load drive, there is a load cell and the hydraulic controller will have signal from the load cell. This may or may not be easily available to the AE system but it is necessary. Where no load signal is available, such as a resonance fatigue test, a signal from a strain gauge located in a region where the strain is a linear function of the load, can be used. The gauge can be calibrated by applying a static load to the blade. Note that in a resonance test, regions far from the point where the oscillating load is applied may not be in phase with the load signal.

On a proof test or load-to-failure test, the background noise level is usually constant and independent of load. The real filtering need is to set the trigger threshold a few dB above the noise level. However, in fatigue tests, there can be a large amount of noise generated where the load is low but the rate of change of the load is high. Any structural damage due to the load should occur near the maximum load. These other emissions may be due to rubbing friction in the specimen and have nothing to do with induced damage. They can be greatly reduced by operating the system in the voltage-time-gate mode using the load signal as the reference. Most load induced flaw signals occur when the load is within 5% of its maximum value. By using the voltage-time-gate to shut

out the system unless the load is above 90 to 95 % of its maximum value most of this noise will be ignored. As a proof of the premise, almost all of the emission occurs on the rising or the peak load. Almost nothing is seen as the load falls from 100% to 90% of its maximum. A word of caution. In a resonance fatigue test, the signal driving the voltage-time-gate should be provided from the area of the specimen where failure is expected. The displacement signal from an area far from the driving load can have a considerable phase difference from that of the driving load. The other alternative is to filter out only signals near the maximum change in the driving load.

5-6 Example of Setup:

The best way to illustrate an AE test setup is to go through a simulation setup. The specimen will be a 9-m long FRP wind turbine blade. This blade was designed at Sandia, named Blade System Design Study (BSDS) blade and tested at the National Wind Technology Center, Boulder, CO. Acoustic velocities along the length of the blade of $3.0 \text{ mm}/\mu\text{s}$ and of $2.4 \text{ mm}/\mu\text{s}$ along the chord will be assumed, For this example, the velocity variation with angle will be that programmed in the AEWin 2D Anisotropic program. Separate location calculations for the compression and tension side of the blade will be used. It will be assumed that the majority of the damage produced in the blade will occur between 0.5 and 3.5 m, as seen in the majority of 9-m long blade tests. The sensor lay out is shown in Fig. 15. It consists of 6 rows of 4 sensors each surrounding the blade every 0.5 m along the blade. The first row is on the chord at 0.5 m from the root. For consistency, the sensor number sequence is started with #1 placed on top of the shear web at station 0.5 m on the compression side of the blade. The sensors are then placed in rows, numbered clockwise looking from the end of the blade, on blade stations every 0.5 m. The 2nd, 4th and 6th rows are rotated 45 degrees from the top of the shear web. The chord measurements for the sensors on the two sides are referred to the positions of the top and bottom of the shear web. The convention used is that the measurement is positive toward the leading edge and negative toward the trailing edge on both sides of the blade. The sensors in front are placed as close to being on the leading edge as possible and those on the rear are placed either on the top or bottom of the trailing edge surface, as is convenient. Measurements of the trailing edge positions of the sensors should be either to the center of the sensors face or the point on the other side of the blade directly below the sensor's center. All sensor positions should be measured to the nearest mm if possible. Actual errors of a few mm are usually not important to the overall test.

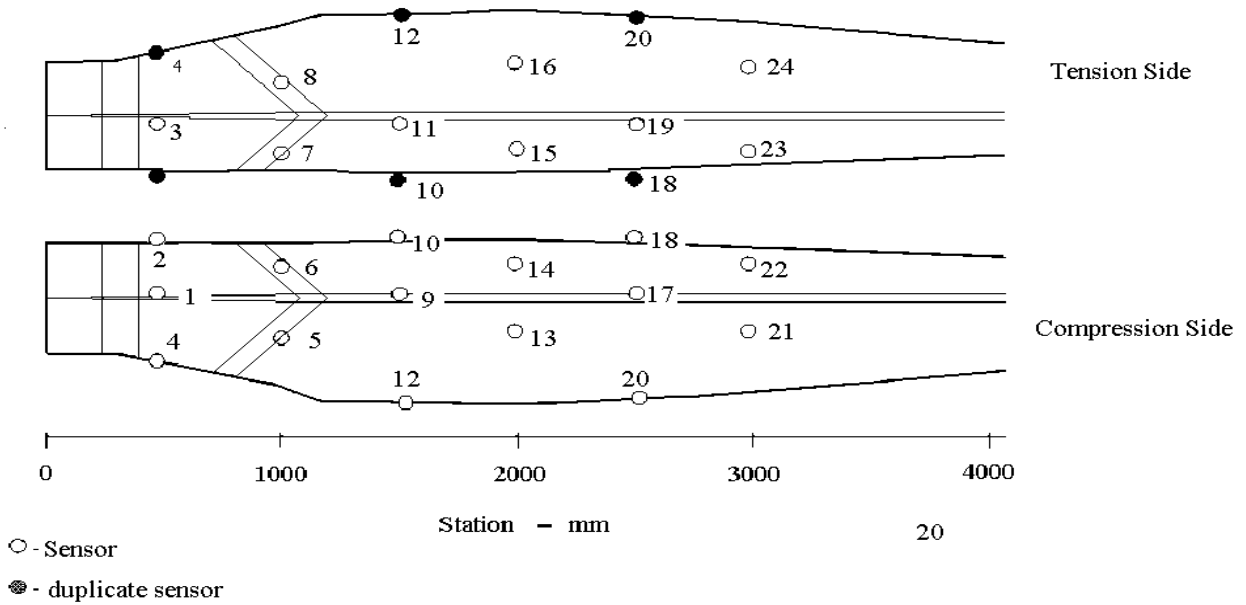


Figure 15 Layout diagram of 24 sensors on the BSDS wind turbine blade.

Next, the location programs can be set up. The compression side will use the following sensors: 1, 2, 4, 5, 8, 9, 10, 12, 13, 16, 17, 18, 20, 21, and 24. The tension side will use sensors: 2, 3, 4, 6, 7, 10, 11, 12, 14, 15, 18, 19, 20, 22 and 23. Unless the shear web is perpendicular to both surfaces, the leading and trailing edge sensors may have slightly different location values on the two surfaces. Using the AEWIn program, set up two channel groups, compression and tension, and enter the sensor numbers of the groups into the computer. Set the location type for each group to *2D anisotropic* then click the *set all points* button for each group. This allows the edge sensors to be used in the calculations of both sides. Then set the HLT parameter to 0.0 for both groups. This allows Hits to occur at the same time for both location groups. Go to the *location setup view* and enter the sensor locations. Notice that in the AEWIn software, the two velocities v_x and v_y are entered in different tables; the v_x in the general location set up table and the v_y in the sensor view table.

The next item is to setup the real time graphs on the computer. Most of the more useful graphs are discussed in some depth in Chapter 7. For a single load test, a graph of the summation of the AE count as a function of load is probably the most useful. Then come location graphs for both sides, summation of absolute energy for located events graphs for both sides, AE hits vs. sensor graph and distribution graphs for both hits and events vs. peak amplitude. In a fatigue test, a scatter point graph of the parametric voltage for each hit vs time along with a similar graph for counts per hit can be useful both to see how well a load filter is working and to monitor the overall emission rate. A note of caution, an AE system has a capability to generate a huge number of graphs. Each of these graphs needs memory and computational power. It is quite possible to greatly slow down the system by setting up too many graphs. Modern computers are quite fast but too many simultaneous graphs can leave the system far behind the test in real time. Conservatively, a dozen real time graphs should be about the maximum used. Many more graphs can be used in replay, but at a cost of a rapidly increasing replay time per file.

Finally, there is the problem of multiple files. AEWin allows the specification of maximum file size and whether the files are separate or a continuation. A 5 to 10 Mbyte file size is convenient for analysis and transporting. The author has found that separate files are easier to handle than continued files. Separate files are easily grouped together with an AEWin utility to make one large file when needed. If the files are recorded in continued mode, the continuing time base can make the individual files more cumbersome to analyze.

Chapter 6 Source Location

The main function of an AE test is to identify flaw growth in a structure as it undergoes an increasing or continuing stress. Ideally, the test should both locate the flaws and describe their growth rate as the stress level increases or the stress state continues in time. On simple structures a single AE sensor can report how the structure itself is behaving. However, complex structures will have many possible flaw sites. If it is large or constructed of multiple materials or materials with high acoustic attenuations, there will be many structures, which cannot be monitored by a single sensor. Thus, most of the growth in the field of AE in the last 40 years has been in the design of multi-sensor systems and their analysis techniques. The focus of these techniques has been the location of AE sources on large structures. Starting with the early work of Green et al. at AeroJet Corp., a primary structure of interest was pressure vessels. Now, almost any structure that experiences changes of stress in normal operation is a candidate for AE testing and most of these tests involve source location.

The basic idea in source location is to cover a surface with a network of sensors. If one can determine the arrival times of an AE signal at several sensors, then, knowing the acoustic velocity, it is possible to triangulate back to the location of the source of that emission. The idea is simple but there are already several assumptions that have been made. First, an isotropic material is assumed so that there is one acoustic velocity. Second, the shortest path between the flaw and the sensor can be determined. Third, the AE signal is simple and its exact time of arrival can be measured. And fourth, the resulting set of nonlinear equations can easily be solved.

The assumption of an isotropic material for a metal pressure vessel seems safe. However, a single known velocity and a known acoustic path may not be. The shortest distance between a flaw and a sensor may go through or around a vessel penetration or a weld. The change in the acoustic path may be small but it is real. The acoustic velocity in a plate is not a constant but is a function of frequency (cf. Fig. 6 for plate wave velocity). The geometry and speed of the fracture of the flaw is unknown. There may be several frequencies and an unknown polarization in the excited acoustic wave. As it travels toward the sensor, the frequency and polarization components of an acoustic wave can change with distance. The result is that the waveforms detected at the different sensors may be quite different from each other. The amplitude of the wave that first crosses the trigger level of the electronics will not always occur at the same portion of the waveform. Again, there will be variations in the triggering time of each sensor from what would be predicted by whatever model is being used in the analysis.

The equations for the distance between two points on a surface are nonlinear even for a flat plane. To locate a point on a plane, one has two unknowns. However, in an AE experiment, one records arrival times of the acoustic wave at the sensors, but in order to know distances, the starting time of the wave must be known. Therefore, to triangulate the location of an AE source, one has three unknowns, the two coordinates of the source on the plane and the time that the emission was generated by that source. One problem with sets of nonlinear equations is there are at least several

solutions to the set of equations if there is any solution. Real experimental data is full of small uncertainties. Triggering on slightly different parts of the waveform at different sensors as well as minor path differences from those predicted by the model can give data sets, which have strange solutions or no solutions. Further, analytic solutions to even an exact set of nonlinear equations do not come easily, if at all.

Another major problem is that many structures have varied geometries and may be multiply connected. One can get analytic solutions for the shortest path between two points for planes and spherical surfaces. One can also combine these two types of surfaces into cylinders with hemispherical end caps. Beyond these shapes, one has to approximate. Large surfaces, which have gradual curves, can be approximated by planes. An aircraft wing or wind turbine blade can be approximated by either two independent surfaces or one surface folded down the middle. Large curved surfaces can be approximated by a group of joined plates. The beauty of AE testing is that exact modeling of a surface is not necessary. Even if the model is far from a one-to-one approximation of the actual surface, all emission from one spot on the surface should be located at one place on the model. While the location on the model may be some distance from the corresponding point on the structure, the important fact is that all the emissions that were located at that point actually originated from the same location on the structure. Thus, a grouping or cluster of points on the model corresponds to an actual location on the structure. While the two locations may differ, the fact that there is an active flaw at a point on the structure is real. If the exact location of the flaw is needed, one can inject signals into the structure at various points until the same arrival sequence at the different sensors is found.

A way around the problem of analytical solutions is to use a numerical approximation. One type is known as nonlinear least-squares fitting routines. Such a calculation starts from a trial solution. In an AE calculation, this is usually a point inside the triangle formed by the first three sensors hit. The routine starts with this trial solution and calculates the travel times of the wave from that point to the sensors. It then takes the sum of the squares of the differences between the calculated travel times and measured arrival times for each sensor. If the sum is not zero, it will make small shifts in the trial solution and from the changes in the sum, estimate what a better trial solution would be. This iteration is repeated until the sum either reaches zero (a real solution) or a minimum (the best estimated solution). Because the trial solution was essentially a best guess from the physics of the test, the solution arrived at is usually the most probable location of the source. Often, a nonlinear least-squares routine will calculate a goodness of fit parameter, which is an estimate of how good the answer may be. Because of errors in the data, it is always possible to get solutions, which are located well off the surface of interest. If the fitting parameter is reasonable and the solution lies within the bounds of the sensor network, one can assume that the solution is the most probable location of the source. An over-determined data set, using hits from additional sensors outside the triangle of the first three hits, will generally improve the accuracy of the calculation. However, using more than six to eight sensors starts to degrade the calculation because the traveling waveforms have often lost most of their relationship to the original waveform and the triggering point may have little correlation to that of the initial waveform. Thus, the measured time of flight may have little to do with the actual acoustic velocity.

Another approximation usually used in source location is that the acoustic velocity is isotropic. This is usually not the case for composites and may not be the case for metallic structures if they are made of plates with different thicknesses. A nonlinear least-squares program has the capability of using anisotropic velocities. A routine, which uses the velocity distribution, shown in Fig. 33, is included in the Appendix. Because of the large amount of variation in AE data from composites,

small anisotropies in the velocity are not that important. However, if the anisotropy in the velocity is greater than 10 %, using it in the location calculation may improve the fit. An anisotropic velocity routine is available in AEWin software has a fixed angular dependence of the velocity. In many, but not all, composites, this should give adequate results.

An **AE cluster** is a group of emission sources, which occur near the same location on the structure. Current commercial AE programs include various methods for detecting and defining such a cluster. The importance of a cluster cannot be over-emphasized. A growing flaw will generate a series of emissions. The actual source of these emissions may be a very localized source, such as the tip of a growing crack or a more diffuse source, such as a patch of corrosion. Because of minor errors in the measured arrival times, both types of sources can appear as a cluster of sources over a small but definite area. It is up to the designer of the test to define a cluster. The usual definition is at least some number of located sources occurring in a defined area on the surface of the specimen. It is often easier to define the clusters during or after the test. The most important characteristic of a cluster is, first, that it exists. The presence of a cluster indicates that there is a specific region on the specimen, which is generating acoustic emission. The second is the size of the cluster. This can either be the number of events or the amount of an AE parameter contained in the cluster. Most commercial programs allow the system to grade the clusters based on either the number of events contained or amount of the parameter measured. The third is the behavior of the cluster with increasing stress. The sum of the number of events in the cluster plotted against stress or time can give strong indication as to whether that cluster is produced by a flaw undergoing steady state, i.e. controlled growth, or uncontrolled growth leading to failure of the specimen. If the emission is fairly uniform such that the variation of the AE count or peak amplitude is not much over an order of magnitude, the number of located events in the cluster is an adequate measure of its growth. However, if the variation is large, as occurs in composites, a plot of the absolute energy of cluster members is a better measure of its behavior. Unfortunately, at least with PAC AEWin software, plots of the absolute energy of a cluster as a function of load or time are not available.

The author has been using a nonlinear least-squares fitting routine in data analysis since the mid-1970's. It was used by several physicists at Sandia at the time and was applied to AE analysis. The name of the routine is NRL but over the last 35 years in the course of many moves, all references to its origins have been lost. The program is the foundation of the current analysis techniques and a FORTRAN listing of the location program, which was used on the Sandia Sensor Blade test is in the Appendix. This program can locate emission sources and plot the locations with the absolute energy of each color coded as to order of magnitude. It can also plot the absolute energy of the sources located in a cluster as a function of load or time. These graphs have been very useful in trying to analyze the results of BSDS wind turbine blade structural tests. A discussion of nonlinear least-squares programs, with examples, is given in "Numerical Recipes in FORTRAN" [13].

Selected Reading List from J. AE Articles

- K. S. Downs and M. A. Hamstad, Correlation of Regions of Acoustic Emission Activity with Burst Locations for Spherical Graphite/Epoxy Pressure Vessels, *J. AE.*, 1995, **13**, 56-66.
A. Wanner and M.R. Gorman (eds.), *Materials Research with Advanced Acoustic Emission Techniques*, *J. AE*, 1996, **14**. Twelve papers from a Workshop at Schloss Ringberg, Germany.
M. Ge, Analysis of Source Location Algorithms, Part 1 and 2, *J. AE*, 2003, **21**, 14-28, 29-51.

Chapter 7 Analysis

The primary purpose of an AE test on a structure is the detection and monitoring of flaws, which affect the integrity of the structure. An AE test is by definition not a nondestructive test as the detected emissions are produced by irreversible changes in the material under test. However, the sensitivity of an AE test is usually high enough to detect flaws long before they reach a severity level, which will affect the strength of the structure.

A flaw can be defined as any defect or error in a structure, which can affect the strength or well-being of the structure while it is in normal use. For the field of AE, the term flaw will refer only to flaws, which are influenced by the working loads on the structure. A flaw such as a cracked step in the ladder leading to a crane is serious, but is not influenced by the load hoisted by the crane. The growth of a flaw, as influenced by the load, can roughly be divided into three categories; **controlled flaw growth**, **uncontrolled flaw growth** and **catastrophic flaw growth**.

As an example, take a piece of metal composed of many random crystallites. Micro-flaw growth can involve either the fracture of a crystallite, the fracture of a boundary between two crystallites, the fracture of a boundary between a crystallite and an inclusion in the metal or the fracture of the inclusion. All of these cases will have a stress level where an applied stress tensor will cause a fracture. To be accurate, there will probably be several stress levels where different stress tensors will cause a fracture of the same crystallite. The fracture of a single crystallite will usually rearrange the stress tensors on the surrounding crystallites. This rearrangement may leave the surrounding micro-stress tensors essentially unchanged or change the micro-stress level on some crystallites to some degree. An increase in a micro-stress level may be enough to fracture other crystallites. In such a case, an avalanche to macro-fracture can be the end result. Whatever the result, it is totally dependent upon the local stress environment and local material environment. There is no way of predicting the exact stress level or the exact location of the first or any other micro-fracture.

Controlled flaw growth will occur when the fracture or group of fractures does not produce a rearrangement of the local stress fields, which causes further fractures. The emission rate will remain relatively constant or even drop as the stress level is increased. A decrease in the rate usually means that there were a relatively small number of regions where built-in higher micro-stress levels were left from the manufacturing process. When these have all fractured, the emission rate will decrease until the fracture stress level of more serious flaws is reached. Such regions where the micro-stress levels are significantly higher than the mean are often found in new FRP structures and seldom in metal structures. In their absence, most AE tests start out with no emission (above background noise level) and then proceed into a controlled flaw growth regime with a relatively steady emission rate over some range of applied external stress. When the emission rate starts to increase with stress, uncontrolled flaw growth has started.

In **uncontrolled flaw growth**, the micro-fractures generally produce an increase in the local stress fields of the surrounding regions. As the external stress field is raised, the rate of emissions increases. This rate increase may be slow at first but then tends toward an exponential increase. If the exponential increase is not stopped, the test will rapidly proceed to the failure at the flaw. If the load increase is slow, there usually will be enough time in this uncontrolled flaw growth region to stop the test and prevent a serious failure. This is one of the prime purposes of many AE tests.

In **catastrophic failure**, the exponential increase in flaw growth may be quite rapid. The speed of the failure is a property of the material. In brittle fracture, there is little or no AE preceding the failure. A typical example is the fracture of glass. An AE test may tell when a small glass part in a structure breaks but it will seldom give advanced warning of brittle fracture.

Analysis of an AE test consists primarily of looking for the occurrence of AE and then measuring the rate of that emission with respect to the change of the test stress level. In structures where multi-channel tests are used, the location of the emission and the measurement of the emission rate for each located area is the goal. An analysis can either be done in real time if the prevention of structural failure is the test objective or in post-test analysis. Real-time analysis depends primarily on an operator's experience and knowledge. It can become interesting, especially where the loading involves large energy levels, and can probably only be learned by experience.

Acoustic emission tests can be divided into two types, depending upon the loading. The first type has a single load to either a test load or failure. The load may be applied continuously or in steps. In FRP tests, the steps may be separated by returns to a zero load between each step. This allows a determination of the Felicity ratio at the beginning of each step. In a continuous load with steps, the load hold between steps allows the determination of how fast the emission stops as the load increase stops. As a specimen nears failure, the emission will often continue for a period of time after the hold starts. When the emission does not stop during the hold period, that is a good time to declare the test over and reduce the load, unless the object of the test is to actually fail the specimen. The second type of loading is the fatigue test. The load is periodically cycled over a fixed load range. This range may be constant over the test but often it is increased after predetermined cycle intervals. The test may be monitored continuously or the AE system can be activated only at near peak loads with a voltage-controlled gate. The practice of detecting emissions only at peak loads restricts the observed emission sources to those produced by actual flaw growth and eliminates frictional sources, which are at a maximum during the periods of rapid load change. In fatigue tests, there is usually an interval where the emission rate from flaw growth increases slowly with time. However, there can be exceptions to this rule. The author has analyzed one fatigue test where the failure occurred quite suddenly and only extensive post-test analysis revealed some pre-failure emission.

7-1 Test Graphics:

Analysis of a test in real time is up to the operator of the AE system. The operator is totally dependent upon the graphs, which have been set up on the system. In the early days of AE testing, two of the most important instruments of the test setup were the oscilloscope and the audio channel. The scope would show the output of one AE channel. One could get a good idea from the scope of how rapidly the emission was occurring, its amplitude and the general shape of the emission bursts. Non-emission noise signals showed up immediately. Impending failure of the specimen was quite evident as the whole scope would light up. The audio channel would use a beat frequency to bring the main AE frequencies into the audio range. An experienced operator could obtain additional information about the status of the test from changes in the audio amplitude and frequency. From these instruments and an x-y recorder, which plotted summed AE counts against load or time, an experienced operator could give a good picture of what was happening in the test.

Currently, the AE systems are digital and the oscilloscope and audio instrumentation is missing. They are replaced by real time graphs on the computer screen. The following displays are useful in both real time and post-test analysis.

7-1-1: AE parameters vs. load or time graphs

A graph of the AE hits, events, counts or absolute energy versus the load or time is essential. The author prefers the graph of the cumulative hits etc. over the graph of the rate of hits etc. because it is easier to visually differentiate a cumulative graph than to visually integrate a rate graph. The parameter vs. time graph is the classic graph, which has been used almost from the start of AE testing. The choice of which AE parameter is used will depend on what is expected out of the test. AE hits or counts will show all detected AE with counts being more sensitive to the intensity of the emission. An AE events count is sensitive to emission from actual flaws but may miss regions where only one or two sensors are activated. Counts or absolute energy per event will give the most information about the state of flaw growth but can become confusing when there are multiple flaws. A rate of absolute energy per load interval graph is probably the most useful but must be confined to post-test analysis since it requires a knowledge of the total behavior of all clusters.

Changes in the slope of the cumulative graph indicate changes in the AE rate. A steady rate in the absence of external noise indicates controlled flaw growth while an increasing rate indicates uncontrolled flaw growth. When the slope of the curve appears to increase toward an exponential, or shows a distinct knee, structural failure is usually approaching. Figure 16 shows a steady emission rate in Fig. 16a and an increasing emission rate in Fig. 16b. These are graphs of the number of located events as a function of temperature (load) in two Halon Bottle tests. Both bottles failed the test but for different reasons. In Fig. 16a, the number of AE events in a cluster exceeded a preset maximum and in Fig. 16b, both the slope of the event vs temperature curve for a cluster and the number of events in the cluster exceeded preset maxima. The test in Fig. 16b was terminated early by the computer program to prevent catastrophic failure.

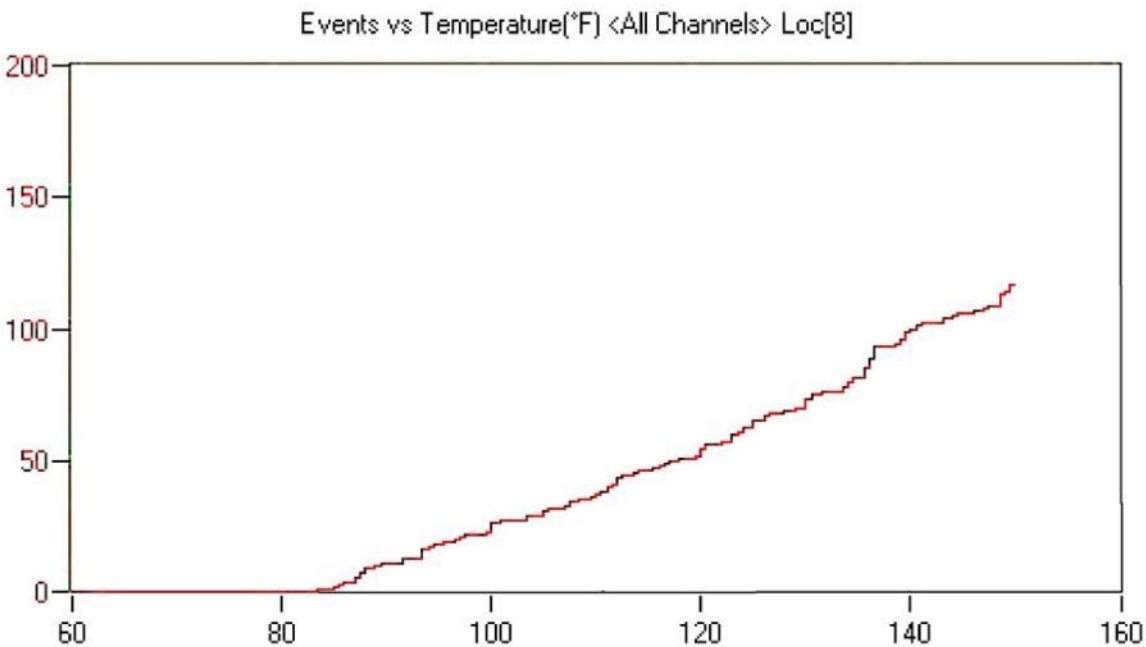


Figure 16a Stable flaw growth in Halon bottle.

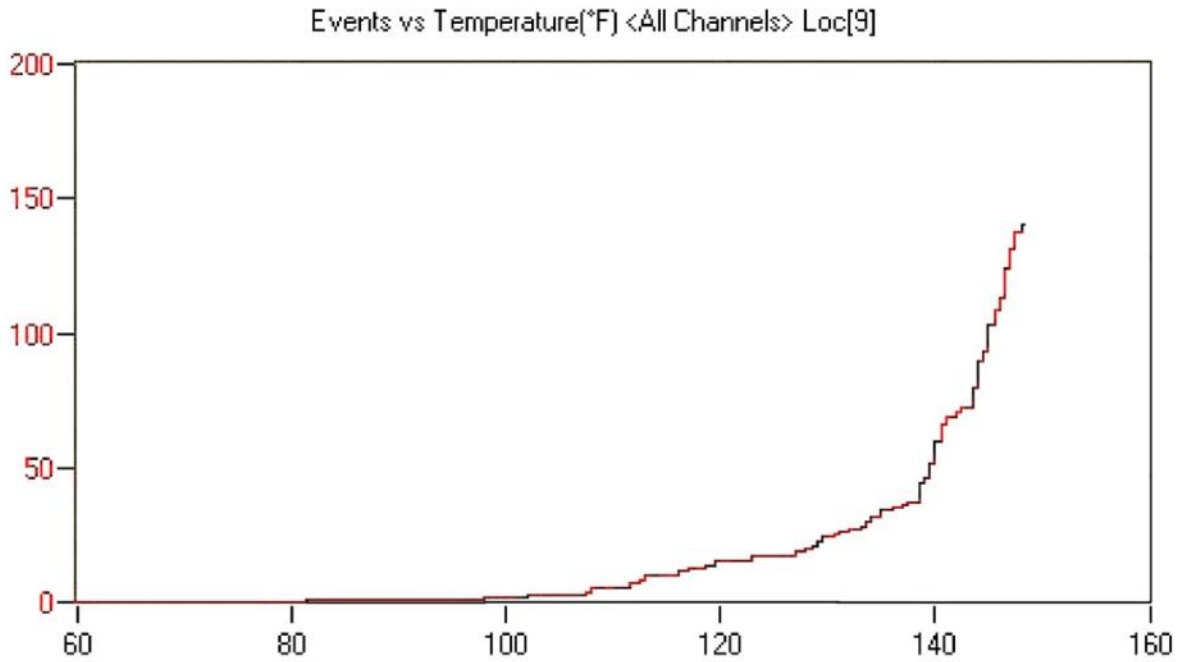
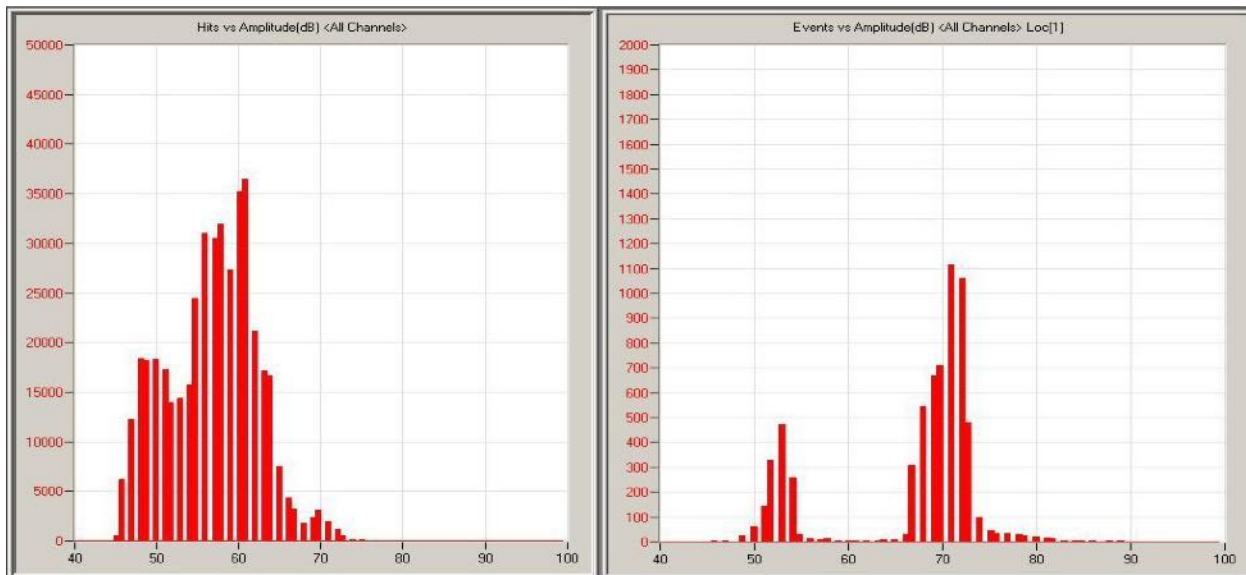


Figure 16b Transition from stable flaw growth to unstable flaw growth in a Halon bottle.

7-1-2: Peak amplitude distributions

Graphs of the peak amplitude distributions of AE hits and events are useful. Figures 17a and 17b show peak amplitude distributions of a small portion of the BSDS blade fatigue test. The AE hit distribution shows most of the hits were below 65 dB peak amplitude while the events fell into two groups, one near 54 dB and one near 71 dB. There were a large number of hits compared to the number of located events for each peak. However, there were many more events per hit near 71 dB than near 54 dB. This implies the growth of two different flaws, which should be apparent from a location graph. A location graph (see Figure 19) shows low amplitude events located above sensor 3 and the high amplitude events located around sensor 5.



Figures 17a and b Amplitude distributions of hits and events from the same BSDS data.

7-1-3: A bar graph of the number of hits per channel.

Figures 18a and 18b show a linear and a log plot of the hits per channel of the same data as shown in Fig. 17. The linear plot Fig. 18a shows that channel 13 is receiving most of the hits. It is so dominant that most of the other sensors appear inactive. Using a log plot of the same data, Fig. 18b, we see that is not the case and that only sensors 11, 15, 21 and 23 appear totally inactive while sensors 6, 17 and 22 have only a few hits. It also appears that the part of the structure covered by sensors 14 thru 24 is showing very little emission. This data was from a fatigue test, so a temporary

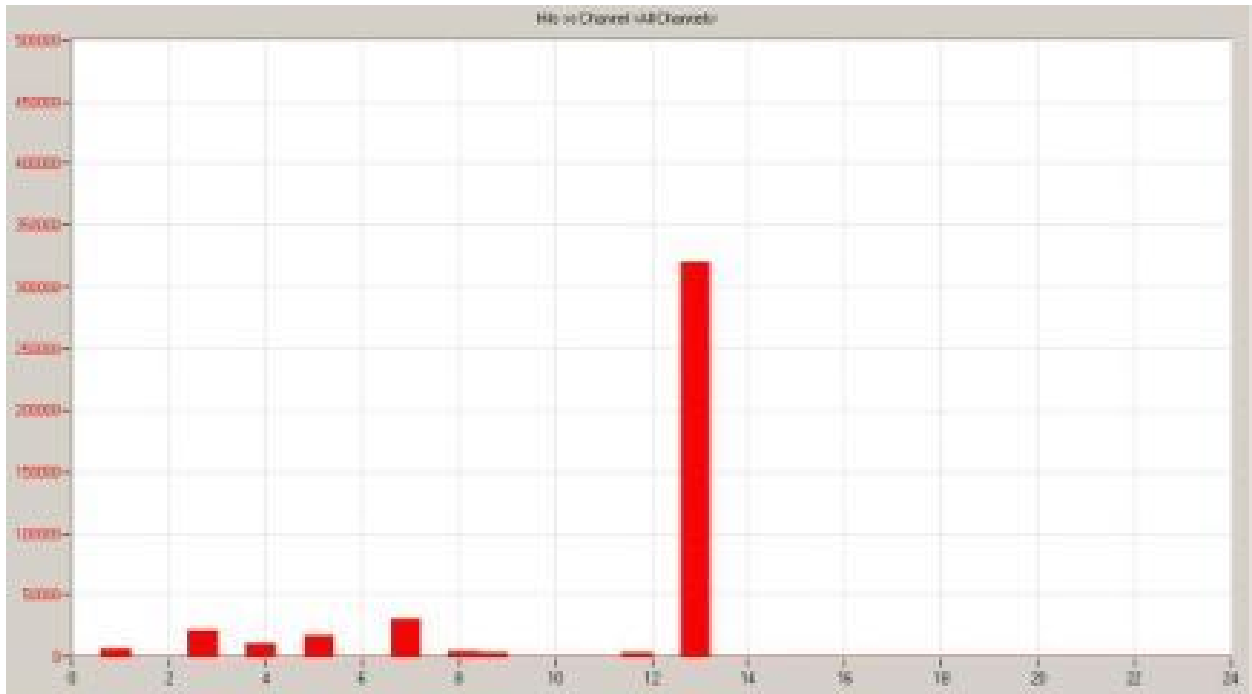


Figure 18a Hits vs Channel: linear scale.

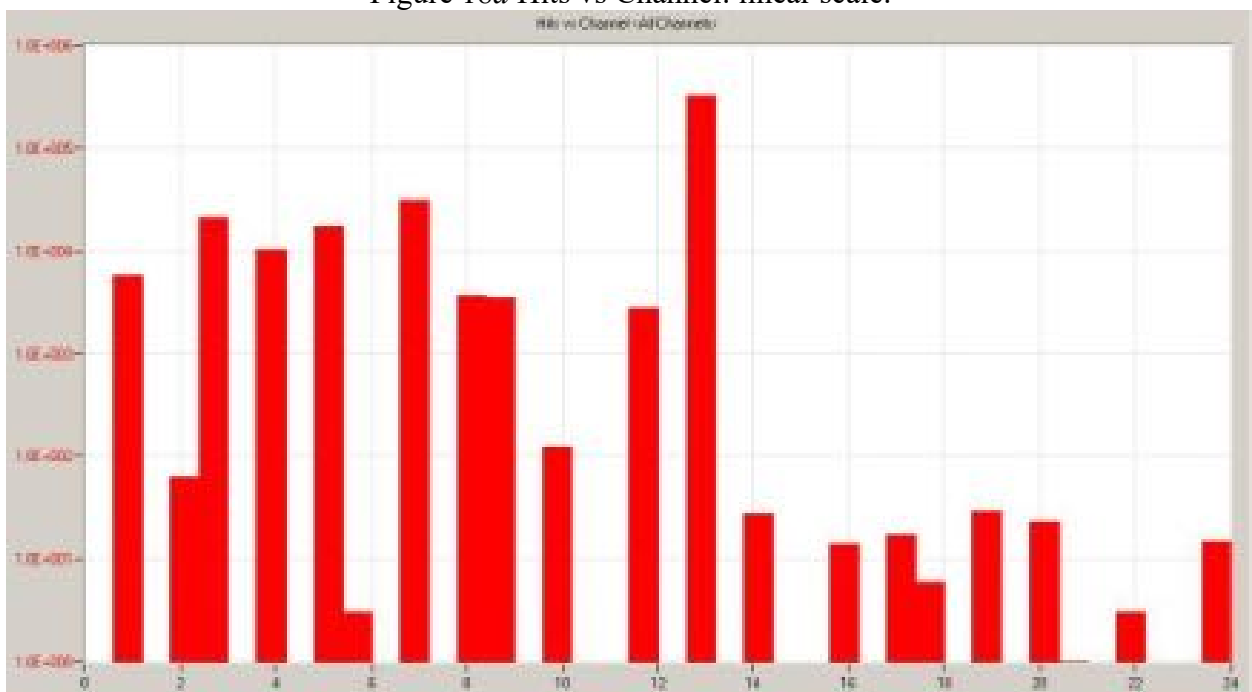


Figure 18b Hits vs Channel: logarithmic scale.

stoppage of the loading did not affect the test. The low amplitude channels were tested with PLBs shortly before this data set was recorded. All channels tested good except channel 11. It was determined that the electronics on channel 11 were not working but the sensor was and the sensor at position 11 was connected to channel 13, which had a very low activity, and the switch was inserted to the layout file. Whether the excess signals seen on channel 13 in Fig. 18 was caused by this switch is not known. However, the data in Fig. 18 and resulting PLB tests did show that the lack of emission from sensors 14 to 24 was real and not an electronic problem.

7-1-4: Location graphs in real time.

These graphs plot the calculated location of each event as it occurs. The location calculation can be setup as a single graph or multiple graphs. The graphs setup for the system monitor probably will not have a one to one correspondence to the structure.

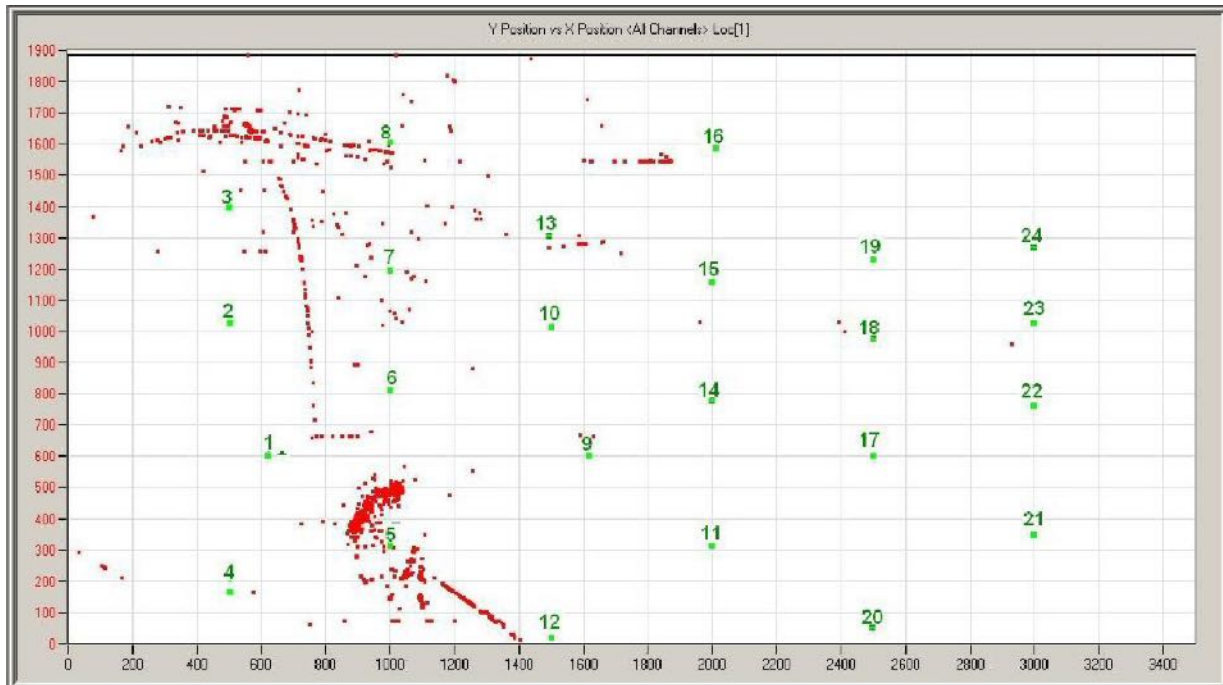


Figure 19 Location graph of data from BSDS wind turbine blade fatigue test.

This is not very important for real time monitoring. Usually most emissions originating in one region on a structure will have their calculated locations in a similar region on a graph even though the two regions may have somewhat different locations on the structure. The appearance of a cluster of events on a real time graph indicates a growing flaw and the behavior of the events with load will define how serious the flaw is, even if the calculated location appears to be vague.

Figure 19 is a location graph of the BSDS wind turbine blade fatigue test for 15,000 cycles early in the next to last loading level for the test. This representation assumes that the leading edge of the blade is straight and that the blade surface is opened flat out on either side of it. Sensors 2, 10 and 18 are located on the leading edge with sensors 1, 9 and 17 on the spar cap on the low-pressure side and sensors 3, 13 and 19 located on the spar cap of the high-pressure side of the blade. Sensors 4, 12 and 20 are located at the trailing edge. The blade surface has been distorted but this this representation allows one to see the whole blade surface at one time. The distinct straight lines in Fig. 19 are artifacts often seen in tests involving source location. Straight lines are

often artifacts of the calculation while curved lines often arise from RF interference. Both may be caused by beat frequency interference signals, which are locked to the load frequency. They may appear to be acoustic in origin but the regular patterns often seen in the data indicate that are not signals from a growing flaw. They are usually seen events, which only contain three hits. As a rule, AE from a flaw is random in occurrence. Any regular patterns seen in the raw data either imply signals with non-flaw origins or events along a structural feature.

Another point that should be mentioned in setting up location graphs like Fig. 19. Software based upon nonlinear least-squares fitting of the data can use information from any number of sensors up from the minimum necessary for the geometry of the calculation. For a surface, the minimum number of sensors is three. There will usually be more 3-sensor events than 4-, 5- or 6-sensor events, just because of the normal variation in amplitudes of the events. A 3-sensor event on a surface usually implies an exact calculation. The location graph Fig. 19 was calculated using all events containing 3 to 6 sensors. If the calculation had been restricted to 4 to 6 sensors, the straight lines and most of the well filled in curved lines in Fig. 19 disappear. However, the cluster around sensor 5 and the scattered points above sensor 3 remain.

7-1-5: A scatter point graphs

A scatter point graph as a function of time or the load value for each hit and an accompanying scatter point graph of the AE count for each hit are also used. These graphs are useful for fatigue tests. In a fatigue test, flaw growth is only going to occur at or near the peak load. However, in a complex structure, such as a wind turbine blade, there are often areas in the blade where apparent frictional emission is generated. This emission is usually most intense at the mid-load region, where the actual change in the load is a maximum. If the load is offset such that one peak of the cycle is at the normal zero load of the specimen, then the maximum load is at the opposite peak of the cycle. By using a voltage-controlled gate to only accept data at the top 10 % of the load, one can greatly reduce the amount of data being collected. If the load is not offset, one may want to accept data from both the positive and negative load peaks. (One caution, in a resonant fatigue test, the load signal from one position on the blade may be out of phase with the displacement at the location of a flaw. The gate must be set so that it includes the displacement peaks at the flaw positions, even if it means accepting larger data files.)

Figure 20 shows the AE count and load curves for one data file from a test, which had a large amount of emission occurring throughout the entire load cycle. The recorded data was restricted to the AE hits, which occurred in the upper peak of the load cycle from a load value of 2.2 to 2.6 volts. The AE count curve (top) shows the times when more energetic emission was occurring and show that the gaps where the AE system was paused because other data was being taken were not falling into periods of high emission rates. In this test, there was a large number of signals during every cycle of the loading but locatable emission was still occurring only every few cycles. The use of a voltage-controlled gate can reduce the number of unwanted signals collected by a factor of 5 or more. By pausing the AE system when other interfering data is being collected, the ability to collect exact cycle data is removed. However, by knowing the time interval of the gaps and when they occurred, the ability to plot emissions as a function of number of cycles is not lost.

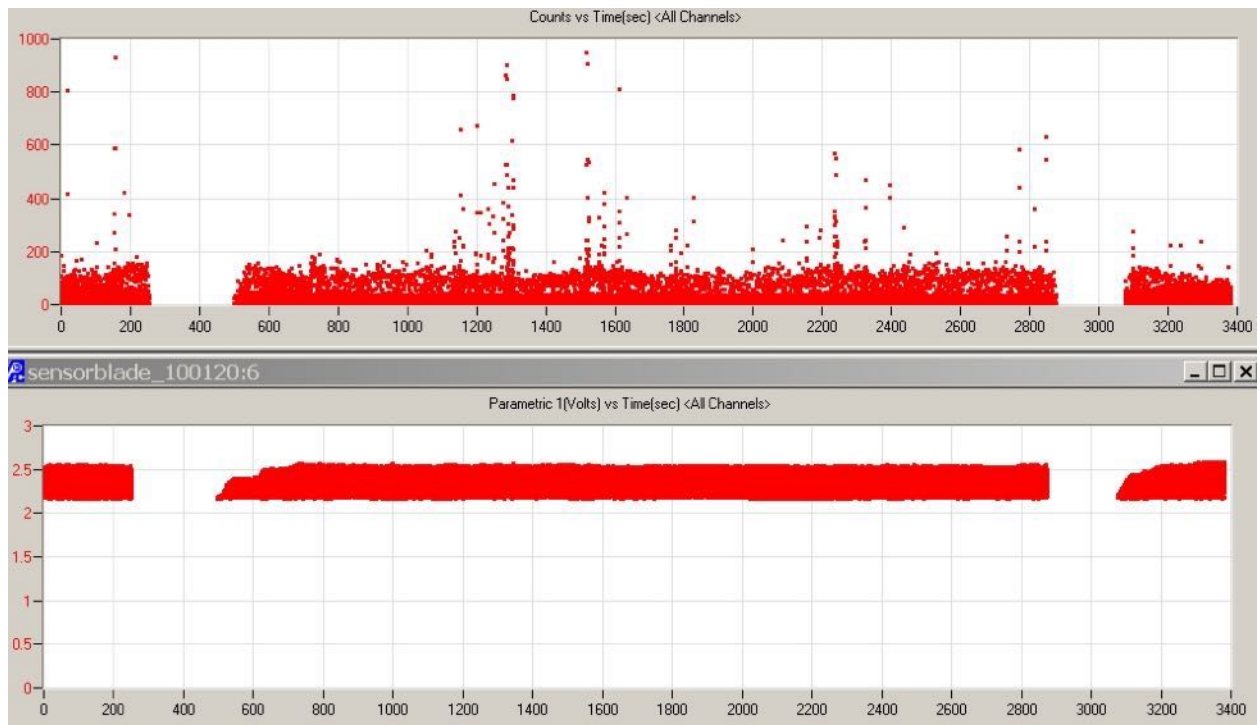


Figure 20 Scatter point plots of AE counts (top) and load parameter (bottom) for period of a blade fatigue test. The data was accepted only with load parameter values of higher than 2.20 V. The two breaks were where the AE system was paused while other ultrasonic tests were being run on the blade.

There is one more procedure which can be useful in determining what signals are produced by actual flaw growth and which result from some other mechanism during a fatigue test. A wind turbine blade fatigue test applies a large amount of force and motion to a blade and it is sure that not all of the acoustic signals are produced by material failures. Since AE is a result of random processes, it is of value to look at the output of such a process. An easy experimental example is the melting of an ice cube in a glass of water. As each crystallite of ice melts, it changes the local stress fields in the ice cube. This results in a continuing micro cracking in the ice cube and a steady generation of acoustic emission. Plotting the distribution of the absolute energies from the emissions produced by a melting ice cube gives the curve shown in Fig. 21. While there are many more emissions at the low energy end of the curve, all energy values appear represented. With 7500 emissions, almost every energy value between 0 and 200 units has at least one burst. There are no peaks in this energy distribution nor are there any gaps. We expect AE from flaw growth to have this general distribution of energies.

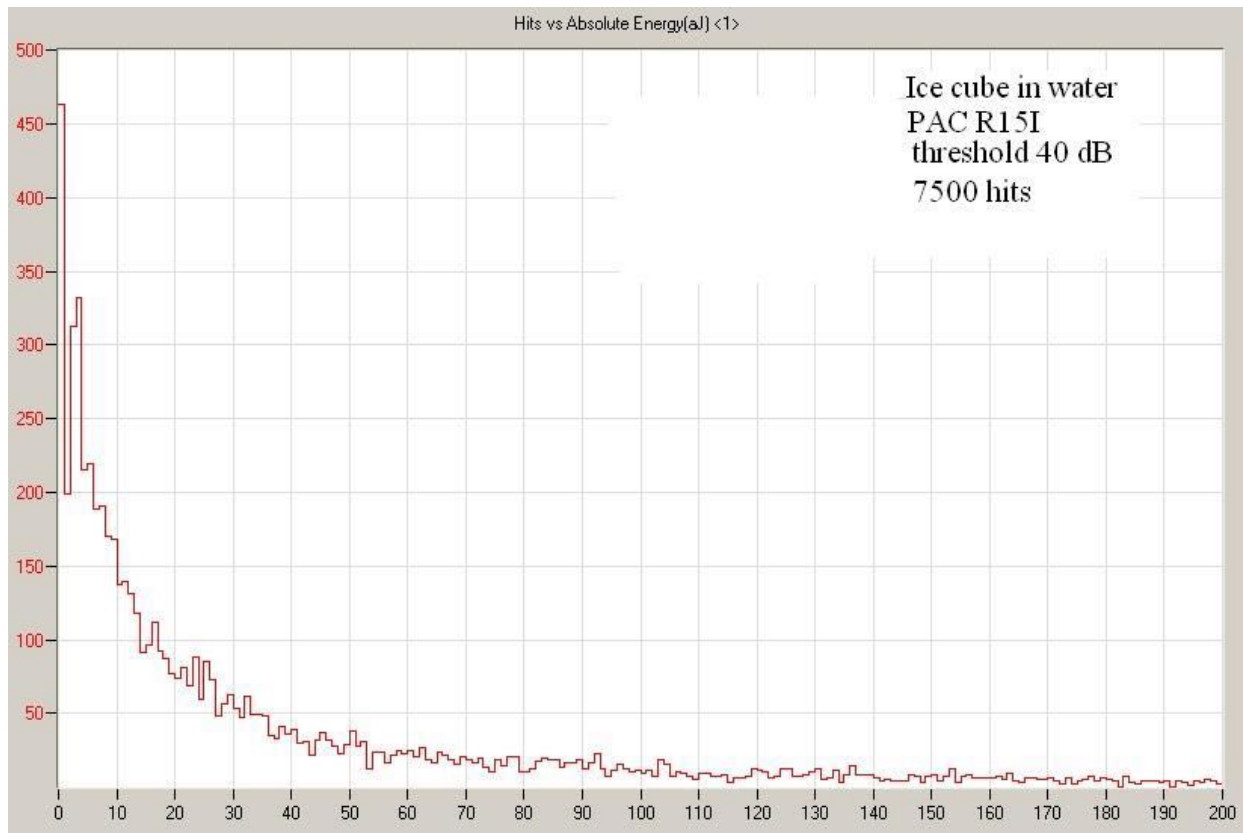


Figure 21 Distribution of signal absolute energies from emissions generated by melting ice cubes.

Now look at Fig. 22. This shows the distribution of energies from five sensors spanning two built-in flaws in a wind turbine blade undergoing fatigue testing. Channels 17 and 21 follow the distribution seen in the ice cube emission. Channels 18 and 20 have more structure but still show a broad distribution of emission energies. Even channel 23, which had very little emission, does show a broad distribution of energies. There is no indication from this data that this is not real emission produced by structural failures in the blade. However, at the root end of this blade where the strength of the blade is much higher, data from the same set showed a large amount of emission located in one area of the blade surface. This is seen in Fig. 23 and is distributed in a strange pattern of curved lines, which had nothing to do with the blade structure. Sensors 1 and 5 are located on the opposite side of the blade from sensors 2 and 6. The energy distribution from the six sensors in the root region is shown in Fig. 24. While sensor 6, which was adjacent to the drive fixture, shows an energy distribution similar to the ice cube, sensors 1 thru 4 show all the energies that were detected by each sensor to lie within a narrow energy band. Those AE signals appear to be produced by some other mechanism than flaw degradation. The conclusion here is that while the signals from sensor 6 were probably produced by small relative movements between the blade surface and the drive fixture, located emissions using data from sensors 1 thru 4 were complete artifacts produced by signals excited by the motion of the fatigue driving mechanism. When the located emissions do not appear to make sense, either from a strange location or strange distributions on the blade, this type of analysis can be very useful.

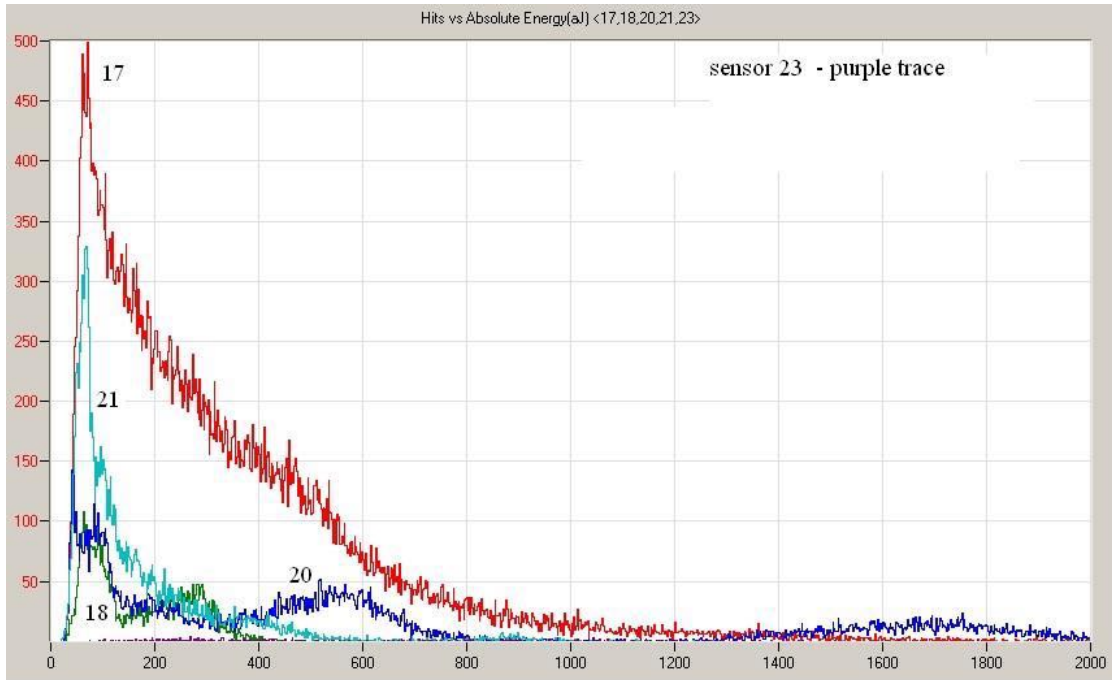


Figure 22 Energy distributions from five sensors near built-in flaws in blade.

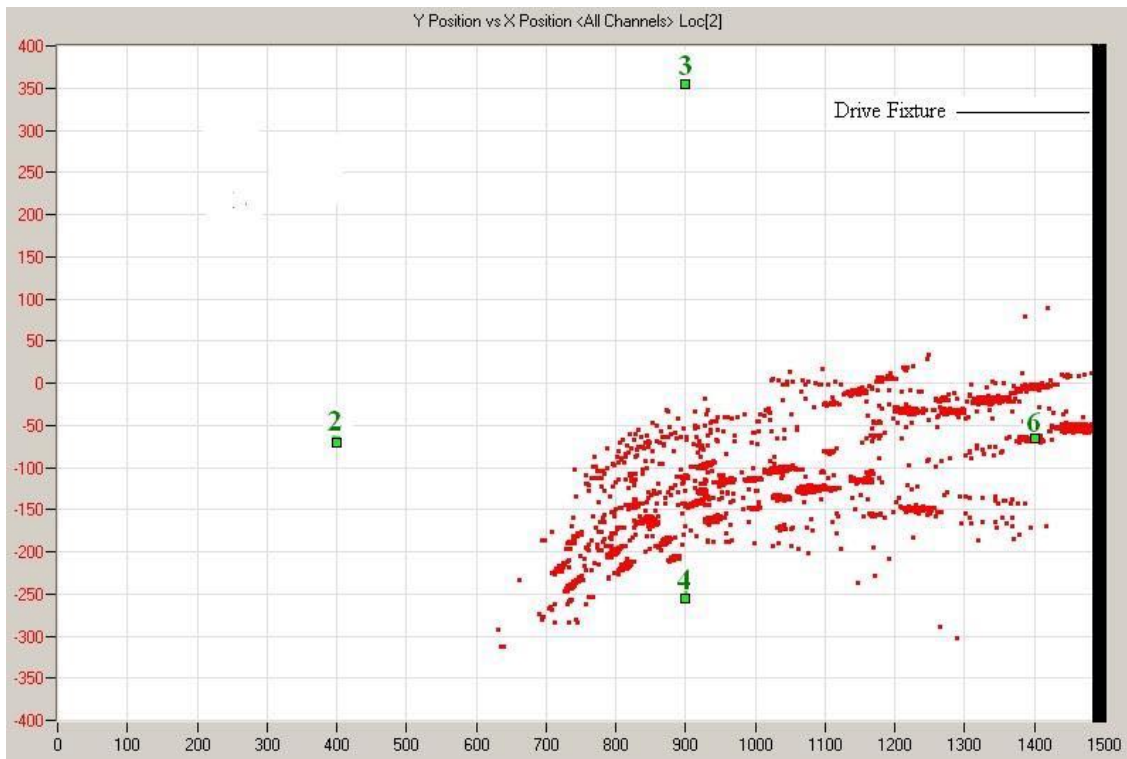


Figure 23 Apparent flaw locations on high-pressure surface of blade root near drive fixture.

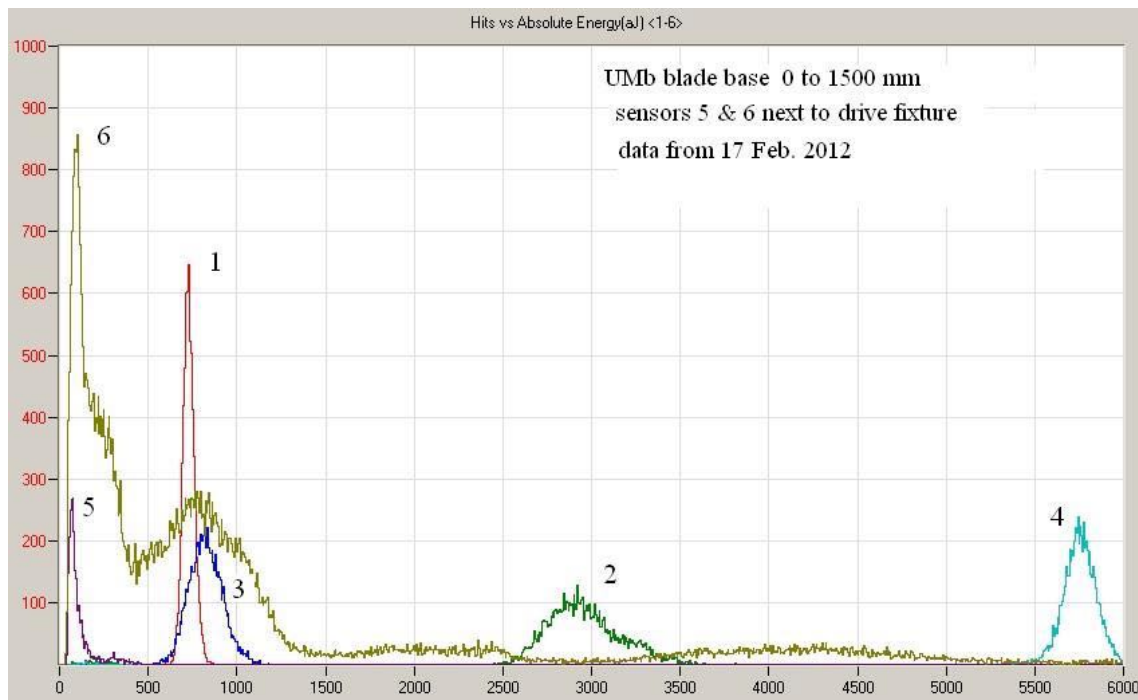


Figure 24 Energy distributions for six sensors on the root of blade. Same data as seen in Fig. 23.

These are the main graphs that the author considers useful to the operator running the test. On a fatigue test, he has often set up graphs of absolute energy rate vs time for both sides of the blade. Unfortunately, there has seldom been a significant difference in the two graphs and so there is no recommendation for such graphs unless there is a real expectation that different regions of the structure will be affected differently by the increasing load or cycle count.

7-2 Post Test Analysis:

The first step in post-test analysis should be a critical review of all the data collected during the test. It is usually valuable to create a time line of the loading sequence and when all events occurred during that sequence. At the point where the emission starts, replay that data and look at the listing display. If there are a large number of 3-hit locations, look at the delta times or arrival time differences. If these delta times are almost identical for many of the hits and/or the hit durations or hit energies are very similar for the different located events, the events are probably not generated by flaws. In a fatigue test, any hits or events, which occur regularly in phase with the load signal, will seldom be produced by flaw growth, even if they occur at the load peaks. Microscopic flaw growth depends upon the local material environment. Regular crack advancement during a recurring load will only be seen near failure, if at all.

It is often useful to combine several sequential files into one larger file, which covers a single time sequence. AEWin has a “link separate data files” utility, which works well. One word of caution, AEWin slows down the replay drastically when the file is too large. If the test is a single loading of a structure and there were pauses during the loading, look for when the emission did not stop instantly with a loading pause. This is an early indication of flaw growth and indicates where one should start looking for locatable events.

Most of post-test analysis consists of trying to determine where the flaws were and what their behavior under stress was. During the time of the test, one is limited to the graphs which were implemented for the test and for the current time period. The number of real time graphs is limited by the speed and capacity of the computer. However, there is no such limitation in post- test and number of possible graphs available in current AE software is very large. The start of the post-test analysis should use the original real time graphs to replay the test. After that, other graphic analysis should be used as appears desirable.

Unfortunately, there are some analyses, which are often not available. A group of source location programs evolved over the author’s career in the practice of AE testing. An example is the FORTRAN program discussed in Chapter 6 and listed in the Appendix. One technique used is to color code the located emissions on a graph with respect to their absolute energy. Another is to define specific locations on a location graph as clusters and then to plot a graph of AE parameter versus time or load for each cluster. AEWin does show clusters but does not allow the freedom to choose an arbitrary size or location for each cluster nor does it allow the plotting of an arbitrary AE parameter such as the absolute energy of the event for members of the cluster. Finally, AEWin does allow for anisotropic acoustic velocities but specifies a single shape of the anisotropy. In at least the TX blades, the acoustic surface velocity anisotropy was unique to the blades. In many AE tests the results are not ambiguous and the commercial programs can produce acceptable results. However, most of the AE testing at Sandia has been analyzed with variations of the listed FORTRAN program and they are used in the following example.

Figure 25 is very similar to Fig. 19. It uses the same data, but covers many more cycles of the next to last load block. The figure shows four areas that appear to have clusters starting. This data is shown here so that the incipient clusters can be identified. Figure 19 shows the located events on the tension side of the blade during the last loading of the test. As can be seen, there is so much located emission that the original clusters are hidden.

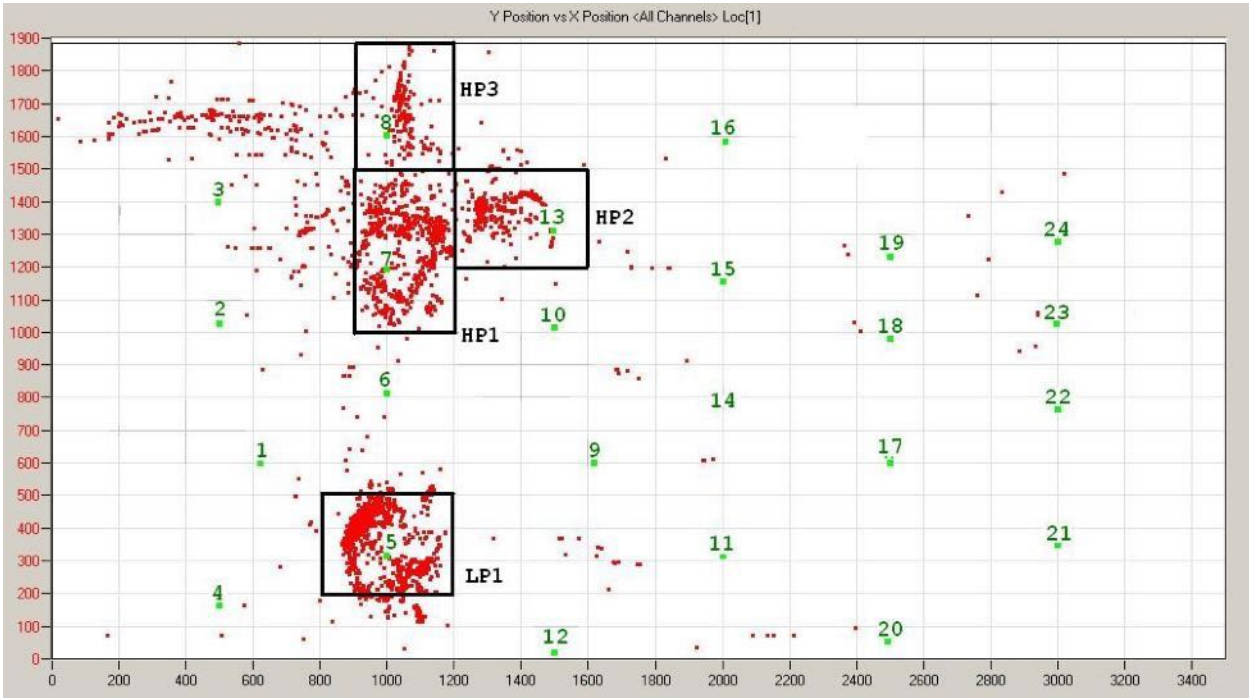


Figure 25. Location graph the next to last load block from extended data set of Fig. 19 showing locations of incipient clusters.

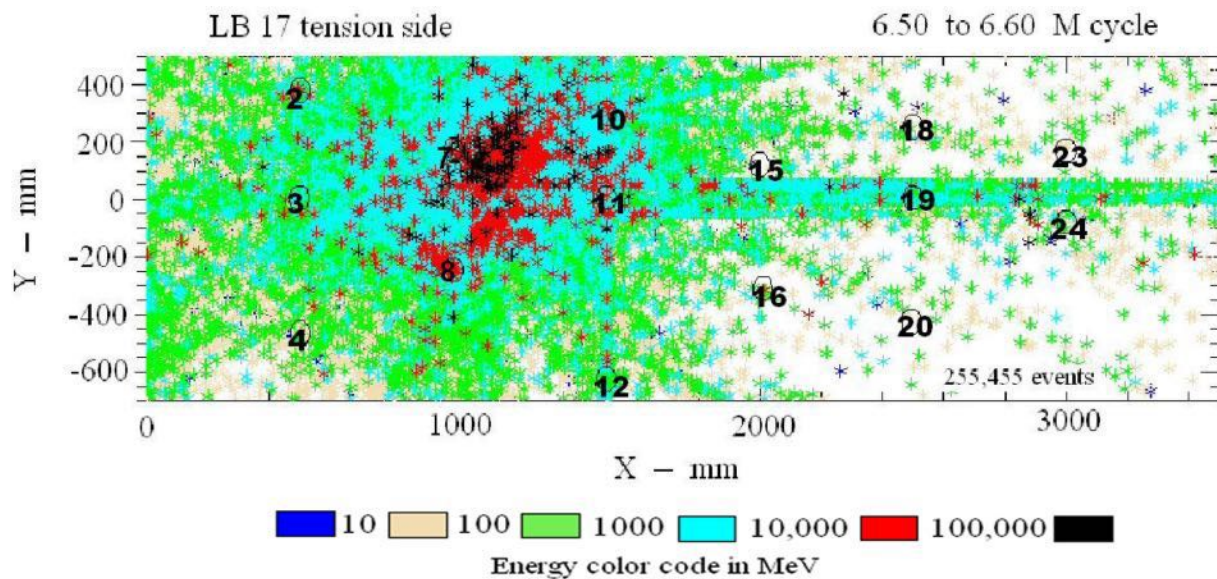


Figure 26 Location graph of tension side of blade during last loading. The view is an inverted image of the top half of Fig. 25. Absolute energies of events are in MeV and the color code is given at bottom. The location conventions of the graph are that the shear web position is zero chord on both sides of the blade. Positive values are toward the leading edge and negative values are toward the trailing edge.

Figure 27 shows the total energy vs cycle graphs for the four clusters seen in Fig. 25. The cluster on the low-pressure (compression) side of the blade shows a decreasing slope as the test moves toward failure. This was the major cluster on the low-pressure side of the blade and shows that the failure was confined to the high-pressure (tension) side of the blade. Most of the energy release was in cluster HP1 surrounding sensor 7. The major failure appears to have started at about 73,000 cycles. The emission rapidly increased until around 90,000 cycles where it becomes almost constant until failure. The interesting feature of the failure is that this rapid increase in the energy release rate is seen in all three clusters on the high-pressure side. Furthermore, there are indications in all three clusters that the energy release rate slowed down just before failure. When the 12,000 cycles were examined in detail, it was found that the release rate where the failure occurred was little different than the release rate of the front high-pressure surface of the blade from 500 to 1500 mm. The conclusion reached was that whole front surface of the blade between 500 mm and 1500 mm was failing and that the actual fracture could have occurred anywhere on that surface. This blade appeared to be without any serious flaws, most of the surface being of uniform strength and the actual failure position occurred almost randomly on the blade. The graphs in Figures 26 and 27 were made with the author's FORTRAN programs. Further details of this test are given in Chapter 9.

To sum up. The post-test analyses are the most important part of an AE test. In most cases, the customer is less interested in the test details and analysis as long as the methods are believable. What is important is the information which the AE gives about the test. If a test is not taken to actual failure, what is the location of the worst flaw and an estimation of how close the specimen was to failure? Or on a proof test, were there any signs of flaw growth at all during the test and was the test sensitive enough to see minor flaw growth. Fine details of the analysis are often not needed in a final test report but the estimate of the health of the specimen is all important.

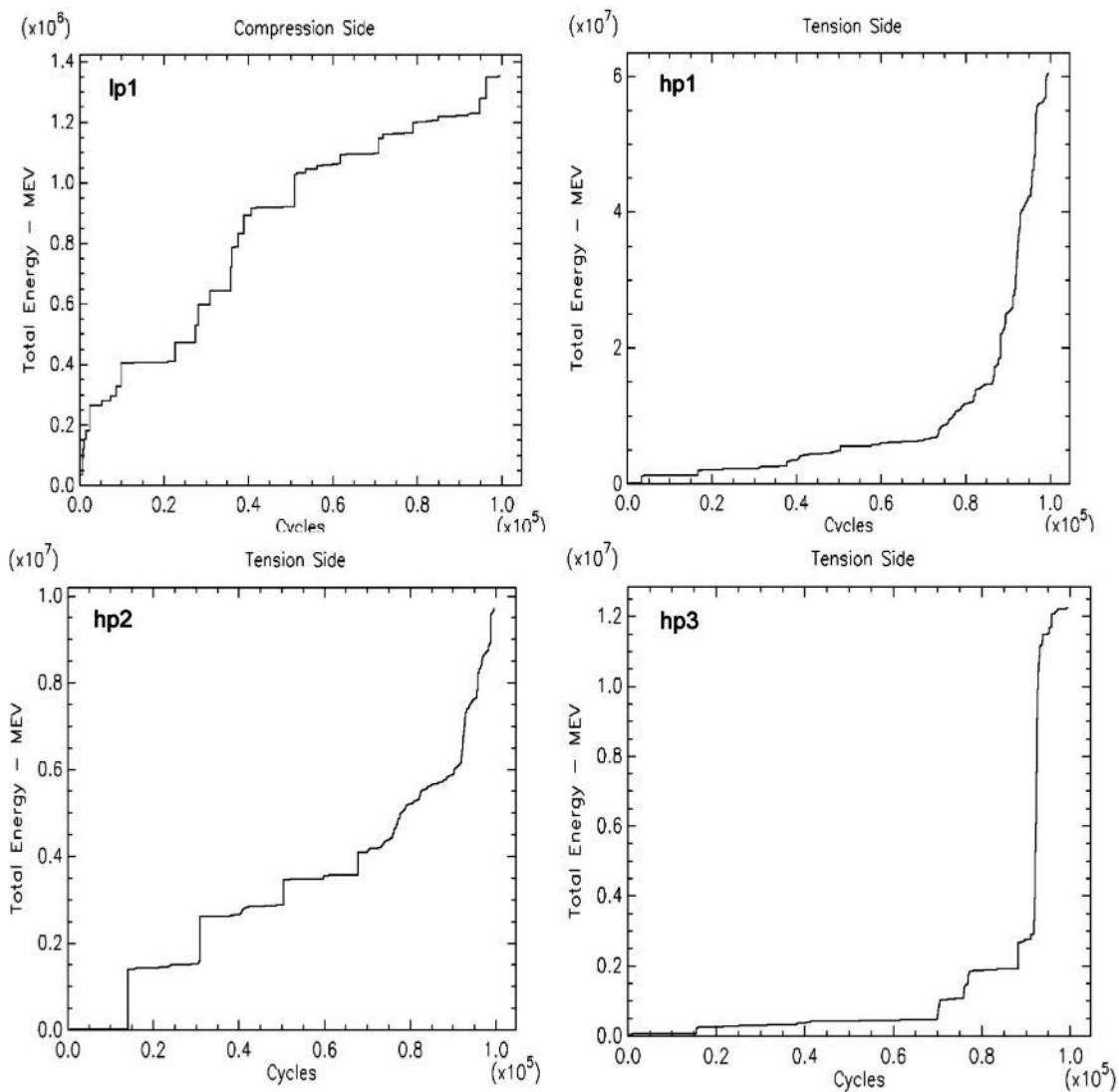


Figure 27 Total energy vs cycle graphs for four clusters for the last load value of the BSDS blade fatigue test.

Selected Reading List from JAE and Open Access Papers

- P.R. Blackburn, Acoustic Emission from Fatigue Cracks in Chrome Molybdenum Steel Cylinders, *J. AE*, 1988, **7**, 49-56.
- M. J. Peacock, Acoustic Emission Monitoring of a Large Pressure Vessel during a Pneumatic Re-qualification Test, *J. AE*, 1989, **8**, 11-20.
- S. Hewerdine, ICI's Perspective on Acoustic Emission Monitoring, *J. AE*, 1989, **8**, 21-24.
- R.K. Miller, R.G. Tobin, D.J. Gross and D.T. Tran, A Summary of Experiences with MONPACT™ Testing by the MQS/Dunegan Testing Group, *J. AE*, 1989, **8**, 25-30.
- P.T. Cole, MONPAC - Condition Monitoring for Static Plant - Case Histories, *J. AE*, 1989, **8**, 31-34.
- H.-A. Crostack and P. Böhm, Monitoring of a Pressure Vessel (ZB2) by means of Acoustic Emission, *J. AE*, 1990, **9**, 29-36.
- K. S. Downs and M. A. Hamstad, Correlation of Regions of Acoustic Emission Activity with Burst Locations for Spherical Graphite/Epoxy Pressure Vessels, *J. AE*, 1995, **13**, 56-66.

D. Kouroussis, A. Anastassopoulos, P. Vionis and V. Kolovos, Unsupervised pattern recognition of acoustic emission from full scale testing of a wind turbine blade, *J. AE.* 2000, **18**, 217-223.

V. Godinez, S. Vahaviolos, R.D. Finlayson, R.K. Miller, and M.F. Carlos, Improved source location methods for pressure vessels, *J. AE.* 2000, **18**, 272-279.

A. Sato et al., Development of Abnormality Detection Technology for Electric Generation Steam Turbines, *J. AE.* 2001, **19**, 202-208.

M. Takemoto, H. Cho and H. Suzuki, Lamb-Wave Acoustic Emission For Condition Monitoring Of Tank Bottom Plates, *J. AE.* 2006, **24**, 12-21.

K. Ono, Review on structural health evaluation with acoustic emission. *Appl. Sci.* 2018, **8**, 958; doi:10.3390/app8060958.

Chapter 8 TX Blade Fatigue Test

Next three chapters present three test cases in detail. The first example of an AE test setup and analysis is the fatigue test of the TX blade [14]. This was a 9-m wind turbine blade with a special skin designed to rotate the tip angle of incidence as the load on the blade increased. The modification was a single layer of carbon fibers on the skin surfaces, which were oriented at 20° from the axis of the blade. The first TX blade was subjected to a static load test to obtain structural characteristics of the blade. That blade failed near the 1-m station on the low-pressure surface. There was also significant AE activity on the high-pressure side near the root and on both surfaces near the 4.6-m station where the internal shear web with its accompanying spar caps ended. These results suggested local stress concentrations at these locations. Previous fatigue tests on this type and size of wind turbine blade had been carried out with a hydraulic actuator driving the free end of the blade up and down. However, the actuator had to be both powerful and have a large stroke. For this test, the blade was firmly fixed at the base, a static load was placed near the tip and a hydraulic fixture driving two moderate weights up and down was mounted on a saddle about 1.6 m from the base of the blade. The resonant frequency of the first flap mode of the blade was measured and the two weights were driven up and down at this frequency. At resonance, the tip of the blade had a large amplitude swing. To conform with previous tests, the blade was tested with the low-pressure side down and a weight mounted towards the end of the blade. This weight was adjusted so that the actual load on the low-pressure side was always positive. With this geometry, the failure was expected to be similar to that of the static test, occurring around 1 to 2 m from the base on the low-pressure side of the blade.

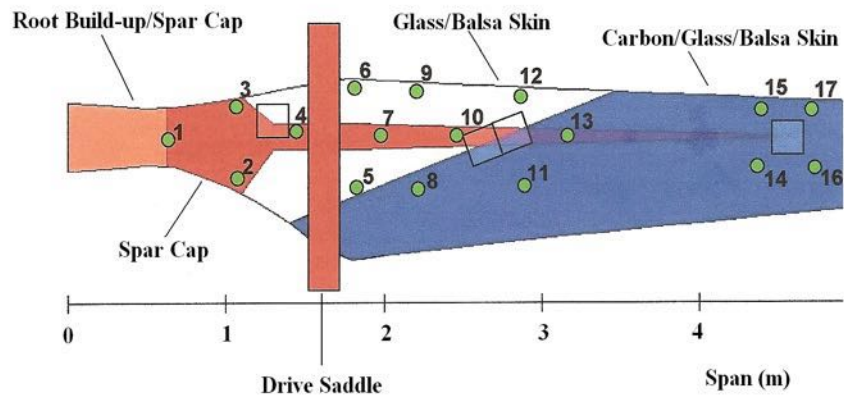
A 24-channel PAC DISP system using AEWIn software was used for data acquisition. The sensors were PAC R6I, which contain a built-in preamplifier. Their response covers the bandwidth of 30 to 150 kHz, peaking around 60 kHz. The load signal was taken from a dedicated strain gauge mounted on the surface of the blade near the driving actuators. It was calibrated with a dead weight test load and the output amplified and fed to the DISP system. The decision about which areas of the blade to monitor was based upon the results of the static test of the TX blade. Locations of the sensors, the driving fixture position and construction details of the blades upper and lower surfaces are shown in Fig. 28. The low-pressure surface from 500 mm to 3500 mm was instrumented with 13 sensors. This array covers the region where failure had occurred in many of the previous 9-m blade tests. Finite element analyses of the blade had indicated the possibility of problems around the abrupt end of the shear web at 4.6 m. An array of four sensors was placed on the low-pressure side of the blade centered around 4.6-m station and an array of three sensors was centered around 4.6 m on the high-pressure surface. Finally, an array of four sensors was located on the high-pressure side of the blade just inboard of the driving fixture. These placements were based upon

our estimation that the failure would be on the low-pressure side of the blade but because we had not previously monitored a blade driven into resonance, we should cover all bases. The sensors were bonded, as usual, with GE Silicone II adhesive. The sensor placement coordinates were referenced to the inboard end of the blade and the approximate center line of the blade as defined by the center of the spar cap above and below the internal shear web. Acoustic velocities were measured on the skin behind the shear web both perpendicular and parallel to the shear web. These velocities were quite close to each other at 3.1 mm/ μ s parallel and 2.9 mm/ μ s perpendicular and were used in the setup of the AEWin software. They were close enough together that there was no hesitation to use 3.0 mm/ μ s in the location software, which assumed an isotropic acoustic velocity. The collected data set included AE hit, arrival time, sensor number, rise time, AE count, signal duration, signal peak amplitude and signal absolute energy. During most of the test, waveform data was collected. The digitization rate was 2.0 MHz and the first 2 ms of each wave was digitized and recorded. Almost all of the AE signals were shorter than 2 ms because of the high attenuation of the blade skin.

The test was monitored by several NDT methods besides AE. This required the AE system to stop taking data when the other methods were in use. At least two of the other systems generated acoustic waves in the blade. Because of these gaps, the cycle counting feature of the software could not be employed. All cycle data had to be obtained from the NREL operators log and the time data from the AE system (start, stop and running times). The inclusion of the waveform data created huge data files. (one hit contained 28 bytes of data without waveforms and about 8.1 kbytes including waveforms). They were sent by TCP over the internet in batches of one hundred 5 Mbyte files at a time. Toward the end of the test, the waveform acquisition was stopped and each 5 Mbyte file then contained about 16,135 hits instead of 600 hits with waveforms.

The test results were far from what had been expected. After minor emission on the few initial cycles, almost all the emission seen came from the region around the end of the shear web at 4.6 m. The majority was from the high-pressure surface. Sensor 19, which was approximately over the end of the web, showed almost continuous low-level emission from the first cycle. It was thought at first to be rubbing noise but the waveform and its location near the peak load of each cycle indicated that it was probably real emission. By the time the test reached 2 Mcycles, a surface crack was developing near sensor 19. This became quite noticeable as can be seen in Fig. 29. In the post-test analysis, it was found that data from just three sensors did not give very good location graphs. The two sensors, 15 and 17, while on the other side of the blade, were just past the leading edge and were often hit in the hit sequence data. Their inclusion into the calculation much improved the location graphs. Figure 30 shows the final calculated source locations from the same time period as the picture in Fig. 29. The absolute energy per cycle for the emissions within the triangle formed by sensors 18, 19 and 20 was calculated from 3 to 4 Mcycles and is shown in Fig. 31. The peak between 3.78 and 3.81 Mcycles indicates where a major fracture of the blade occurred. The damaged blade continued to disintegrate until the test was stopped at 4 Mcycles to prevent the blade from complete failure, which might harm the testing apparatus.

Bottom View – Compression Side – Low Pressure Side



Top View – Tension Side – High Pressure Side

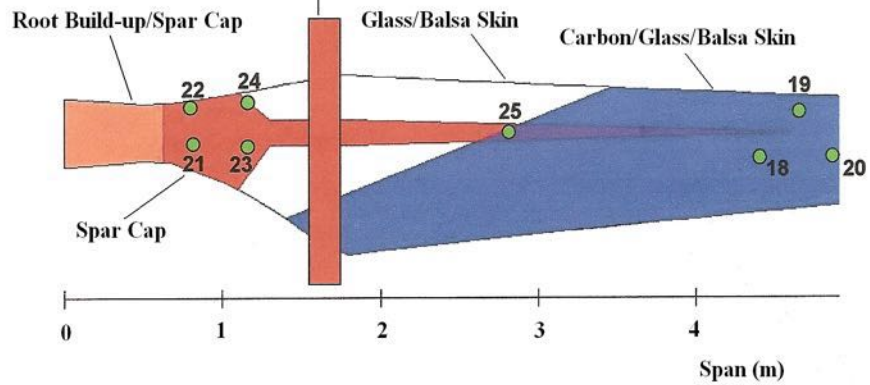
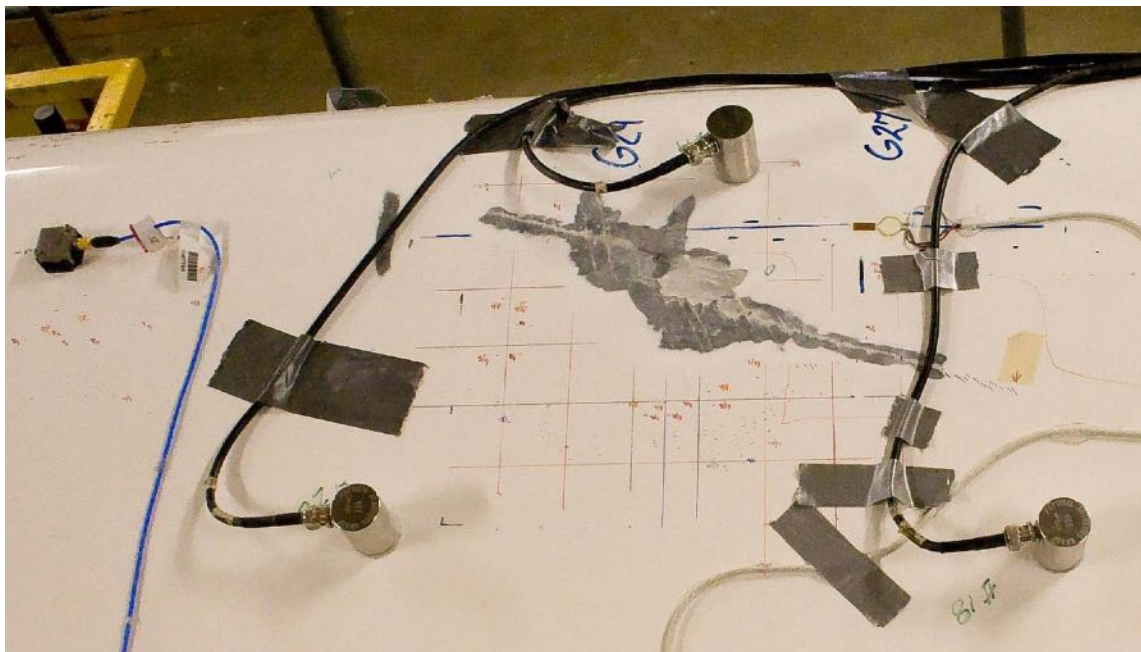


Figure 28 Construction diagram and sensor layout for TX Blade fatigue test.



Figures 29. Picture of surface crack on tension side of blade around 2 Mcycles.

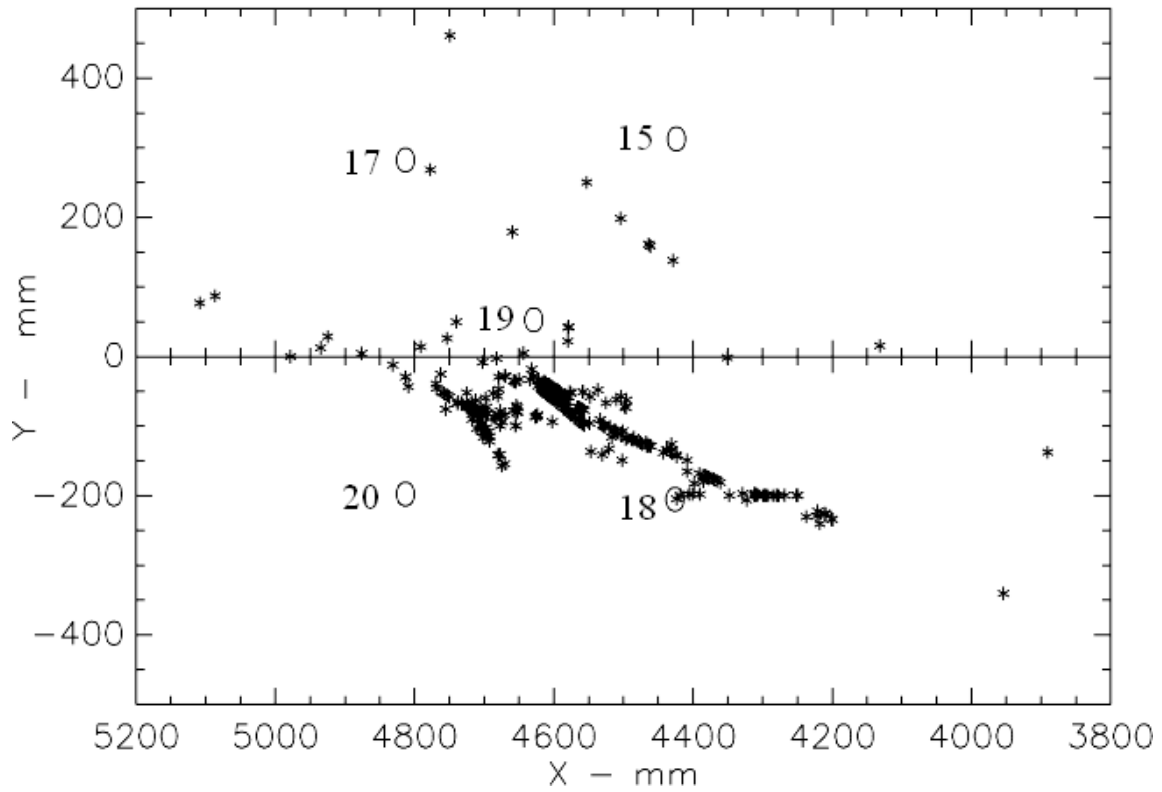


Figure 30. Final source location calculation of same area of blade around 2 Mcycles.

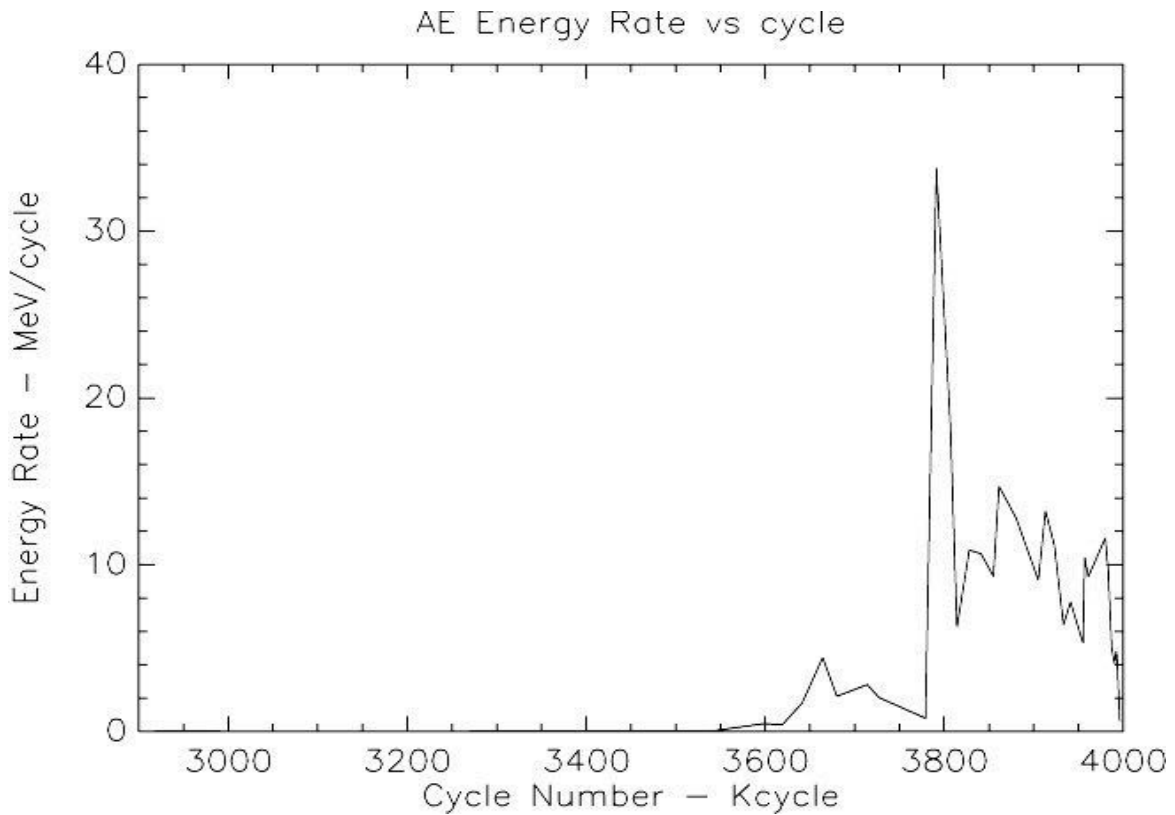


Figure 31 Energy rate from tension side of blade near end of shear web showing peak when major damage started.

A FORTRAN program was written by the author to include an anisotropic acoustic velocity in the calculation. A 1-m section of the TX Blade, which had been broken in the static test, was obtained. An initial velocity measurement had shown that the parallel and perpendicular velocities were fairly close to each other. However, off the major axes there appeared to be a much larger variation in the acoustic velocities. It was decided to make an accurate measurement of the velocities. PLB measurements were made of the velocity in the section skin behind the shear web. An average value for the velocity was calculated every 10°. The result for the velocity is shown in Fig. 32. This result is quite dramatic considering that the diameter of the carbon fibers in the surface layer of the blade is almost microscopic. It appears that most of the energy in the Rayleigh wave created by the PLB must be contained in the surface interface with the air. The effect of the 20° orientation of the fibers dominates. In order to include this information in the location program, an analytic function that fits this velocity data was devised. It is included on the accompanying disk as a subroutine. The graph in Fig. 30 was generated by this program.

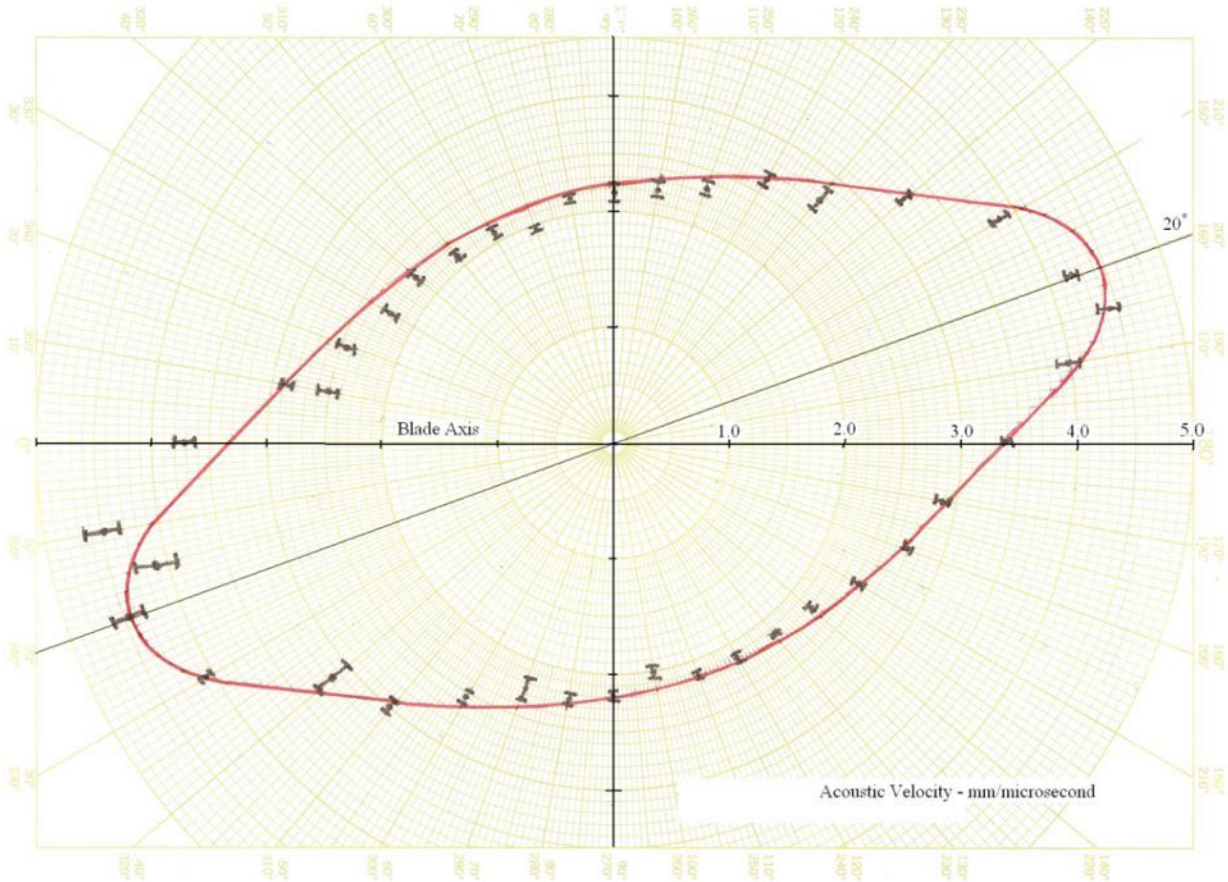


Figure 32 Measured acoustic velocity of TX blade as function of angle from blade axis.

This test showed that accurate AE source location is possible on an FRP structure if enough sensors and an accurate measurement of the velocity are available. Adding some filtering and color coding the energies of the events improved the location graph shown in Fig. 33 over that shown in Fig. 30. This graph pins down the location of the major flaw although visually the first graph agrees better with the visual damage. The major conclusion of the AE test was that the only problems seen in the blade structure were in the stressed regions where the shear web abruptly ended. There was strong evidence that load level at the start of the test was already producing minor damage in these regions.

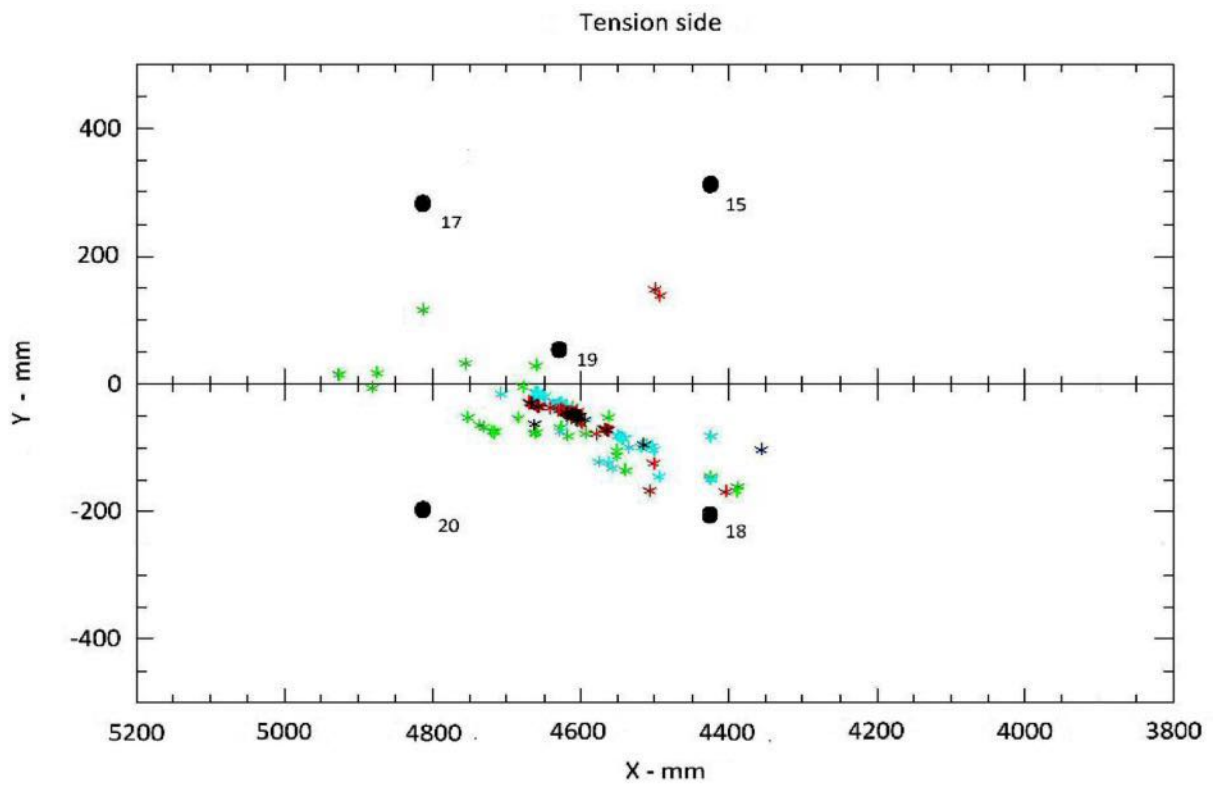


Figure 33 Same data as Fig. 30, with filtering. Color code black $>10^5$ MeV, red $> 10^4$ MeV.

Chapter 9 Example, BSDS blade

The next example of a test setup and analysis is the fatigue test of the BSDS blade [15]. The BSDS design is a 9-m blade, which incorporates flatback airfoils in the inboard section of the blade. These airfoils give the blade a thick, structurally efficient geometry. Cross sections of the blade at 0.5 and 1.0 m are shown in Fig. 34. Not shown in the figure is the shear web down the center of the blade with carbon fiber reinforced spar caps on the top and bottom of the web. The fatigue test was performed using a hydraulic cylinder to apply single point cyclic loading to the blade in both the flap and edge orientations. The loads were applied to a saddle located at a station 5.0 m from the base of the blade. Loading frequencies started at 1.5 Hz and had to be slowly decreased as the load was increased. The final load frequency was 0.65 Hz.

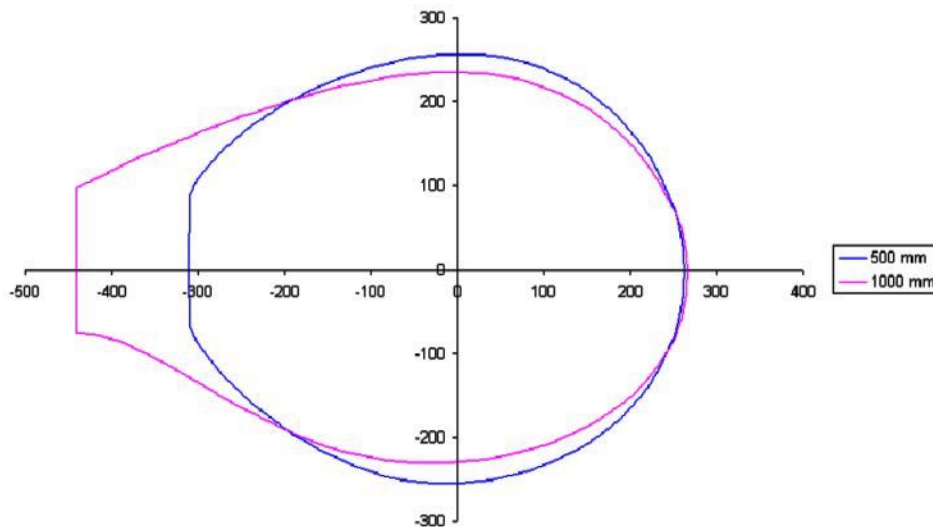


Figure 34 Flat-back airfoils of BSDS blade for stations 500 and 1000 mm.

A static test of a BSDS blade was conducted and acoustically monitored. That blade proved to be considerably stronger than previously tested 9-m blades. The static load was distributed through two wiffel trees to three fixtures on the blade. The inboard fixture was located at approximately station 3 m. The failure occurred at a load of about 4.9 kN at a location between the inboard and second fixtures. This was unexpected so the stub of the blade was reloaded and soon failed near station 2 m during the first reload step. Acoustic emission from the first test indicated the start of failure around a 4.3-kN load on the compression side of between stations 2 and 2.6 m. There were no sensors beyond station 2.6 m on the first static test so there was no data from the region of the first failure. The second loading was without AE instrumentation due to severe budget restrictions. On the first loading, one sensor was mounted on the tension side of the blade over the shear web at station 0.97 m. It recorded about an order of magnitude more detected acoustic energy during the test than the sensor mounted approximately above it on the compression side of the blade.

The static tests indicated that there was appreciable AE from both the compression and tension sides of the blade and that failure could occur beyond station 3 m although a longer-term hold at 4.3 kN, could have led to failure on the compression side between stations 2.5 and 3 m. The decision was made to monitor the whole surface of the blade between station 0.5 m and station 3 m. It was thought that the blade failure outside of station 3 m may have been due to the distributed load applied to the outer end of the blade during the first static test and that single point fatigue loading would probably cause failure inboard of station 3 m. A pattern of 24 sensors in six rows of four sensors each was decided upon. The first row would be at station 0.5 m with a sensor above and

below the shear web with the other two placed on the leading and trailing edges. The next row would be at station 1 m and would be rotated 45° around the center of the blade. This pattern would continue out to station 3 m. This is the pattern described in the Setup chapter and is shown in Fig. 15.

At the time of this test, it was not known that the AEWIn software could run two programs simultaneously when both layouts contained the same sensor, but used different locations of the sensor in the programs. In order to display the entire surface of the blade and use the leading and trailing edge sensors for calculations on both sides of the blade, the AE system was set up in cylindrical mode, but with the actual sensor locations inserted. It was hoped that this would warp the cylinder surface into a form equivalent to the blade. This appeared possible since the different airfoils and construction made the blade much closer to a tube than the other 9-m blades. It would also allow the author to set up his own programs for separate graphs of the tension and compression sides of the blade. This approach appeared to work fairly well although it is recommended that separate programs be used for the two sides of a blade in future tests.

The data collected by the AE system consisted of the sensor number, the arrival time of the wave at that sensor, the amplitude of the load at the instant of arrival at each sensor, the log of the peak amplitude of the wave, the rise time and duration of the transient wave, the AE count and the true energy of the waveform generated by the sensor. The digitized waveform was recorded for some of the early data, but as was found in the TX test, the information obtained did not appear worth the huge increase in the amount of data it would have produced. Other system settings were the same as in the TX test. The load signal was again taken from a strain gauge mounted on the blade and calibrated with static loads. This signal was used to drive a voltage-controlled window to allow the system to acquire data only when the load signal was over 90 % of the peak load. Front-end filtering in place during the data acquisition removed all hits with a single count or a duration less than 50 μ s.

The acoustic velocity was measured to check for anisotropy. Surprisingly the velocity was measured to be isotropic at 2.5 mm/ μ s in the skin beyond 1.5 m from the base of the blade. Near the base of the blade, the velocity varied from 4.40 mm/ μ s along the blade axis to 2.85 mm/ μ s perpendicular to the blade axis. The spar caps had a velocity of 4.6 mm/ μ s along the blade axis but were too narrow to worry about the velocity perpendicular to the axis. These velocities were used in the FORTRAN programs. In the data acquisition with the cylinder program, a velocity of 2.6 mm/ μ s was used.

The test was run first for 1 Mcycles in the normal flap mode. The blade was then rotated and another 1 Mcycles in an edge mode where the motion was parallel to the chord of the blade. No significant emission was seen in either of 10 % percent increases in the load were made, first at ½ Mcycle increments and then at ¼ Mcycle increments. This was continued until the blade finally failed at level of 418 % of the initial load. This failure occurred at 6.6 Mcycles. During most of the test, random hits were seen but no located events appeared until 4.945 Mcycles. For a short time, events were seen on the tension side of the blade. These soon stopped but resumed at 5.165 Mcycles and located events on the tension side were continuously seen until failure. On the compression side, located events did not appear until 5.85 Mcycles and then continued until failure.

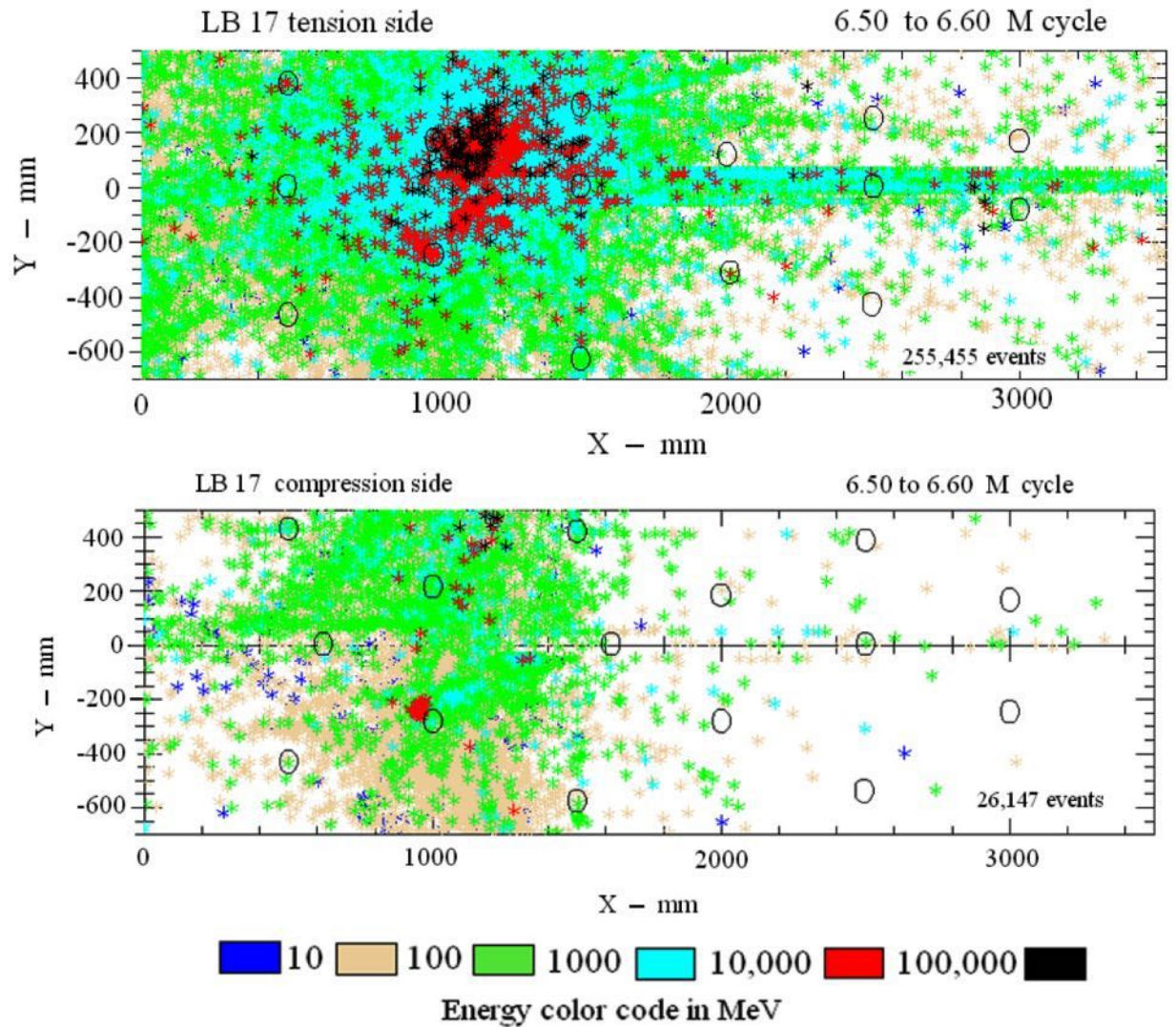


Figure 35 Location graphs for the tension and compression sides of the blade on the last 200 cycles of the test.

Test results were complex. There was far more emission from the tension side of the blade. Figure 35 shows the location graphs for both tension and compression sides of the blade for the last 100 cycles of the test. Essentially the whole tension side of the blade from the base to around station 2 m was emitting. A very broad area from the shear web to the leading edge of the blade and station 1 to 1.3 m appeared to be failing. The compression side shows much less emission with the very large emissions up near the leading edge. (the three sensors at the top of both graphs are the same.) There is one tight cluster on the compression side located very close to sensor 5. This cluster was seen for the last 300 cycles but did not seem to grow. The energy emission rates showed a relatively constant rate of about 20 MeV per cycle for the clusters on the compression side over the last 300 cycles. On the other hand, on the tension side of the blade, the energy release rate started at roughly 10 MeV per cycle and ended at around 10,000 MeV per cycle. The conclusion from these results is that a minor flaw appeared on the compression side of the blade and emitted steadily throughout the rest of the test. However, it showed no sign of growth and appeared to have no effect on the blade failure.

The data from the tension side of the blade showed a steady growth over the entire side between the base and station 2 m. Figure 23 shows the total energy released over the last 100 kcycles from the main cluster regions on both compression and tension sides of the blade. Most of the energy on the tension side was released in the last 12 kcycles. From the broad distribution of high energy emissions seen in Fig. 35, the question becomes: was this failure a growing tear or was it a broad failure over the tension surface? Figure 36 is a plot of the energy released, over the last 12 kcycles, from the whole tension surface in this region and the energy released from the smaller area containing most of the high energy events. They both have a steady slope indicating that the whole surface area was failing and that the crack seen after the test was just part of that general failure.

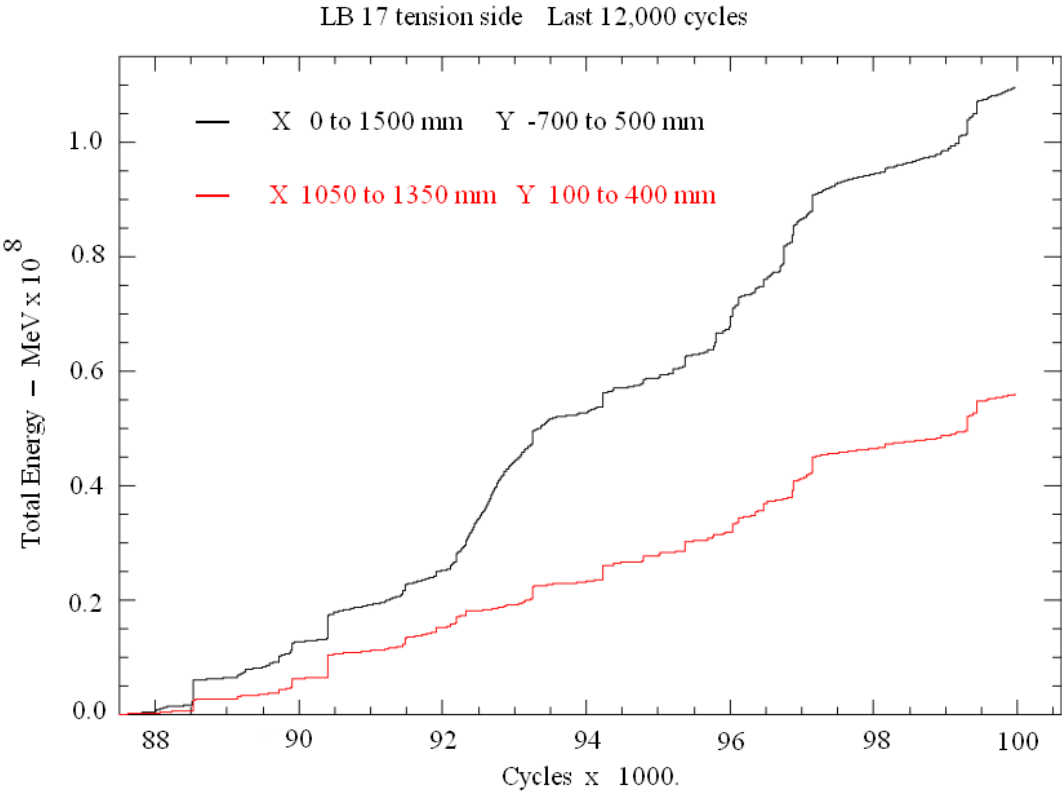


Figure 36 Total energy released on tension side during the last 1200 cycles from the entire end of the blade and just from the failure region

The conclusion reached from the AE data was that the BSDS blade had no major flaws and that the failure occurred when material in an entire region of the blade reached the end of its fatigue life.

Chapter 10 Example, Halon Bottle Tester

The last example to be reviewed is Acoustic Emission Halon Bottle Tester [16]. This is a commercially available system that was developed at Sandia National Laboratories. The problem to be solved was how to perform a non-destructive test on commercial aircraft Halon fire extinguisher bottles. These bottles are spherical metal containers with diameters ranging from 102 to 380 mm. They are filled with Halon-1301 and over-pressured with Nitrogen gas to around 4.13 MPa. After filling, the fill port is welded shut. When needed, a squib charge is fired, breaking a rupture disk, releasing the Halon gas into the cargo hold or engine compartment. The only accepted method of testing these hermetically sealed bottles was cut them open, empty them and hydrostatically

overpressure them in a water bath in order to measure their expansion, elastic and inelastic. After passing, the bottles are refilled with Halon and resealed. This procedure is expensive, time consuming and has the potential to leave the bottle in a worse position than before the test. It is also insensitive. Most of the recent test failures occurred when the bottle exploded in the water bath. Sandia answered an industry request to develop a better test method. Experiments showed that over-pressurizing these bottles by heating them in an industrial oven was possible and that some of them produced detectable low-level AE when heated to around 66°C. These results showed the feasibility of developing an acoustic emission test for such bottles. The author developed and designed a commercial AE Halon bottle tester with the cooperation of the Air Transport Association, the bottle manufactures, Federal Express and Physical Acoustics Corp. (PAC). A commercial system built by PAC has been in use at American Airlines for the last 20 years.

The AE test method used was the location of the sources on the sphere and the determination of whether they were grouped in clusters. The location algorithm was based on spherical geometry, which meant that the important variable between the bottles was the radius of the sphere. A fixture was designed, Fig. 38, which held the bottle and let six sensors be moved in and out along radii of a sphere. The sensors are pressed against the bottle wall by springs. They were mounted 90° apart at the six poles of the sphere. With this arrangement, we could use the same fixture and analysis program for all of the different sized bottles. This fixture was designed to fit into an industrial oven. The source location program was similar to that described in the chapter on source location.

The sensors used were the PAC nano 30. They are small, 8-mm diameter and 7.4-mm high and have maximum sensitivity between 200 and 400 kHz. A 250 to 600 kHz bandpass filter was used in an external preamplifier. The high frequency was chosen for two reasons. First: good location accuracy was desired. Second: it was found that AE signals in the bottle wall could excite acoustic waves in the liquid Halon. These would bounce around inside the bottle for relative long times compared to an AE signal in the bottle wall. The acoustic waves usually had frequencies below 100 kHz. By going to frequencies between 300 to 400 kHz, these waves are completely ignored by the system. As the sensors are a permanent part of the fixture an attempt was made to dry couple them to the bottles. A thin disk of hard rubber is glued to their wear plate. This helps the sensor to conform to the slight curvature of the bottle and makes good contact. When things work right, this is an adequate acoustic coupling, but in a production environment, a thin film of grease improved the coupling. The AE signals in the bottles are relatively weak. The trigger threshold was set as low as possible. With a preamplifier gain of 40 dB, a trigger threshold of 25 dB was used. With these gain and bandpass settings, the noise level of the system starts triggering at 22 dB. A full set of AE parameters, including waveforms, were taken but by the end of the development stage, only the arrival times at the sensors and the temperature of the bottle wall were used in the analysis, so the waveforms were dropped from the data sets.

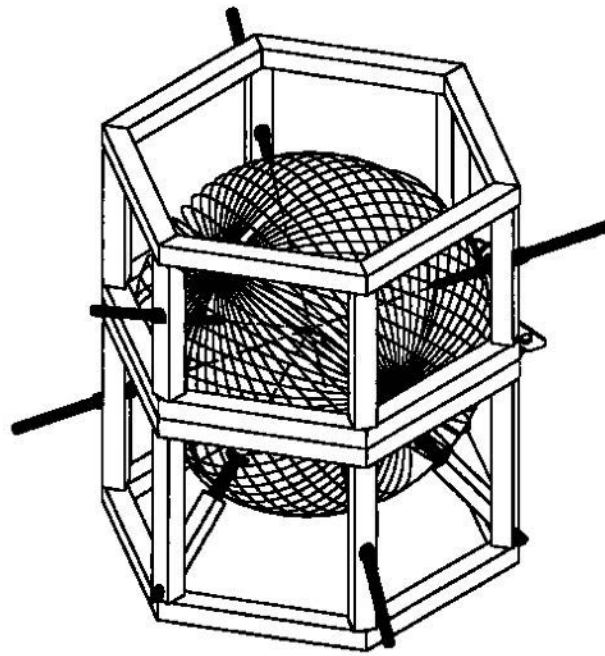


Figure 37 Acoustic Emission Halon Bottle Tester, fixture for spheres 102 to 410-mm diameter.

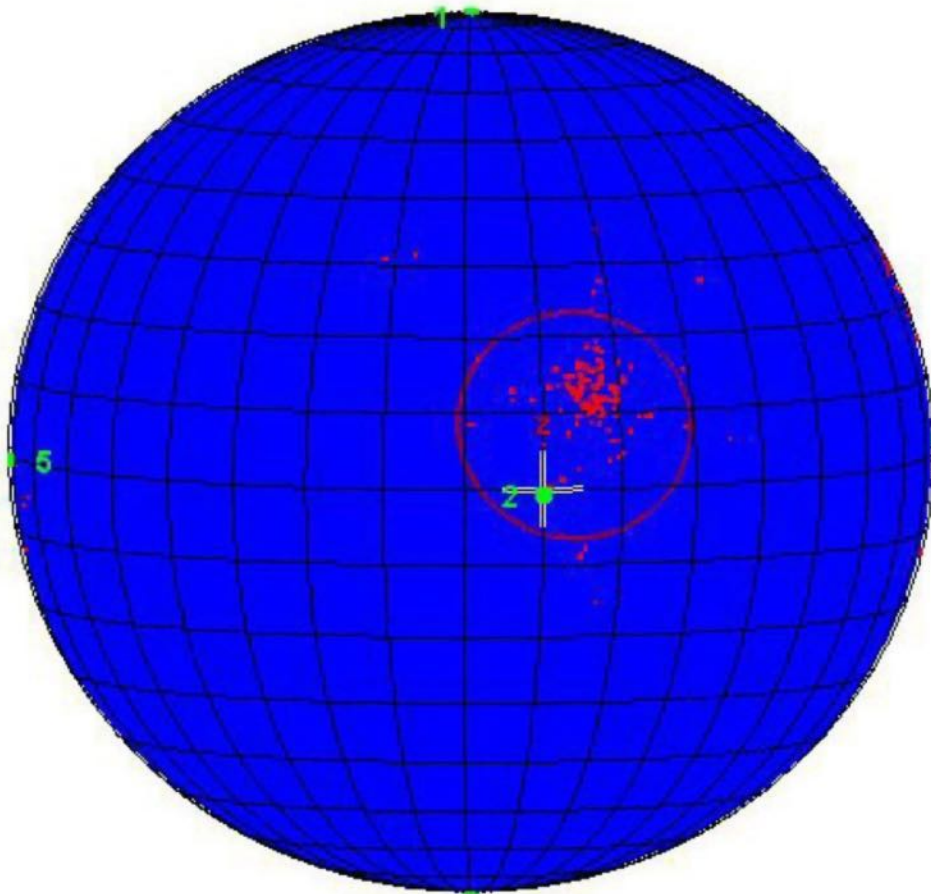


Figure 38 Diagram of Halon Bottle showing located events and cluster outline. This bottle failed the test badly with 156 events in the cluster but no sign of uncontrolled flaw growth.

The first step in the test is to load the bottle in the fixture. There is no preferred orientation of the sphere. The actual orientation in the fixture will vary between bottles as the operator searches for a position where none of the sensors touch welds, ports, mounting lugs or stick on labels. Once the bottle is in the fixture and the system turned on, the program takes over. An automatic sensor test (AST) is performed and if all sensors are not adequately coupled the program stops and requests that coupling be checked. The problem may be that the sensor spring tensions are too uneven or the bottle is not centered in the fixture. After adjustment, another attempt is made. The program will not continue until the coupling meets the programs specifications. Here is where a little grease on the sensor pad can help. When ready, the program starts the oven heaters and the AE monitoring. An AE event is when four sensors are hit within a specified time. This time is 20 % longer than it takes for a flexural wave to go half way around the sphere. The program attempts to locate the source using the extensional velocity (2.05 mm/ μ s). If that does not work, the flexural velocity (1.18 mm/ μ s) is tried. No attempt is made to use different velocities for different sensors. If the source is located, it is then checked for proximity to another source. If it is closer than a 15° arc of a great circle of the bottle, it is declared a member of a cluster. The center of the cluster is defined as the average position of all of the members of a cluster. After a cluster is defined the program first checks for membership in all defined clusters then looks for another cluster to be defined. Figure 38 shows a display of such a cluster on a sphere.

The problem for the analysis of this data became how to grade the clusters. In the development of the system, 206 bottles of all sizes had been tested. Some showed no hits but most had a few hits and maybe one small cluster. An extensive analysis suggested that an important measure was the number of events in a cluster. The significant signature of the cluster was the distribution of those events as a function of temperature (which is linearly connected to internal pressure). A strictly empirical observation was that a suspect cluster had 18 or more events occurring above 43°C. If the events showed a pseudo exponential behavior, then the bottle was on its way to failure. Later we added two other criteria. If the cluster contained 36 or more events above 43°C, the bottled was declared failed, no matter what the temperature dependence of the cluster events was and if the cluster had over 70 events and showed the exponential behavior, the system would be stopped and the bottle allowed to cool before being removed and scrapped. After the American Airlines system had been running a few years, data from another 400 bottles was added to the original 206 and the whole set was reanalyzed. No reason was found to change these criteria. The decision on whether cluster was growing too fast was a simple algorithm. The number of events in the cluster which occurred between 54°C and 75°C was divided by the number of cluster events occurring between 43°C and 54°C. If this ratio was 3.0 or greater, the bottle failed. The bottle failure rate was about 5 % for the initial run including the American Airline bottles, some of which were up to 30 years old. After almost all of the bottles had been tested once, the failure rate dropped to 1 % or less.

The rationale behind the AE test was to find incipient cracks in the bottles. The first flaw found was a small piece of tungsten in a weld on a bottle. At American Airlines several of the failed bottles were cut open. Almost all were found to have a round area on the inside where there was surface etching. Wall thickness measurements of these areas showed a decrease in thickness up to 25% in the worst case. The explanation of these areas goes as follows. Most bottles are stored or installed in the same position. A small amount of corroding agent, if denser than the liquid Halon, will settle to the bottom. Over a long period of time, it will corrode a circular area whose diameter depends upon the depth of the pool. The corroding agent is thought to arise from the slow reaction between the Halon and traces of water in it. The most likely products of such a reaction are hydrofluoric and hydrobromic acids. The bottles are mostly stainless steel so the corrosion is a slow

process. Microscopic examination shows etching of the surface with exposure of subsurface grains. The AE is produced either by flaking of corrosion products or intergranular cracking, which have been partially exposed. This mechanism explains the very low amplitude of emission, which is seen.

A final note. The system has been a success. American Airlines has estimated a saving at its bottle shop of over a million dollars a year since it has replaced the Hydrostatic test with the Acoustic Emission Halon Bottle Tester.

Selected Reading List from J. AE

P. Ouellette, S.V. Hoa and L. Li, A Procedure for Acceptance Testing of FRP Balsa Wood Core Pressure Vessels, J. AE, 1990, **9**, 37-44.

Acknowledgments

The author would like to acknowledge the encouragement and support of Mark Rumsey to write this monograph. The experimental work described was supported directly and indirectly by the Sandia National Laboratories Wind Energy Department. Much of the testing was conducted at the National Wind Technology Center near Boulder, Colorado where the aid and advice provided by Scott Hughes, Mike Jenks, Jeroen van Dam, and Mike Desmond was invaluable. Finally, Mike Desmond, Dale Berg, Didem Ozevin, and Alex Rinehart reviewed in detail the draft version and greatly improved the presentation.

References

- [1] J. Kaiser. *Untersuchungen uber das Auftreten Gerauschen beim Zugversuch. (A Study of Acoustic Phenomena in Tensile Tests)*, PhD Thesis. Technische Hochschule of München. Munich Germany, 1950, (in German); translated to English UCRL-Trans-1082(L).
- [2] A.T. Green. "Stress Wave Detection: Saturn S-II". NASA-CR-61161, Final Report. Aerojet-General Corporation, Sacramento Calif. Dec 1966. [NTIS: X67-18378]
- [3] A.G. Beattie. "Acoustic Emission, Principles and Instrumentation", J. Acoust. Emiss. 1983, **2**, 96-128.
- [4] C.S. Barrett. "A Low Temperature Transformation in Lithium". Physical Review, 1947, **72**(3), 245.
- [5] Knopoff, L. Q, Review on Geophysics, 1964, **2**, 625-660.
- [6] a) W.G. Cady. *Piezoelectricity*, Vol. 1 & 2, Dover Publications, NY. 1946, 2018. b) W.P. Mason. *Piezoelectric Crystals and Their Application to Ultrasonics*, van Nostrand Co. Princeton 1950
- [7] a) A.G. Beattie. "Acoustic Emission Couplants I: the ASTM Survey". J. Acoust. Emiss. 1983, **2**, 67. b) A.G. Beattie, J.A. Barron, R.S. Algers and C.C. Feng. "Acoustic Emission Couplants II: Coupling Efficiencies of Assorted Materials". J. Acoust. Emiss. 1983, **2**, 69.
- [8] Wikipedia, "Ferroelectricity"
- [9] D.A. Bell. "Noise", in *Handbook of Electronic Engineering*, L.E.C. Hughes and F.W. Holland, Chemical Rubber Co. Cleveland OH, 1967
- [10] a) D. Eitzen and F.R. Breckenridge, AE Sensors and their Calibration, NDT Handbook, 2nd ed., vol. 5, 1987, pp. 126-130. b) F.R. Breckenridge, "Acoustic Emission Transducer Calibration by Means of the Seismic Pulse", J. Acoust. Emiss. 1982, **1**, 87.

- [11] a) K. Ono, Calibration Methods of Acoustic Emission Sensors, *Materials*, 2016, **9**, 508; doi:10.3390/ma9070508. b) K. Ono, Rayleigh Wave Calibration of Acoustic Emission Sensors and Ultrasonic Transducers, *Sensors*, 2019, **19**, 3129; doi:10.3390/s19143129.
- [12] “AEWin Software, Installation, Operation and User’s Reference Manual”, Mistras Group, Princeton Junction, NJ
- [13] W.H. Press, S.A. Teukolsky, W.T. Vetterling and B.P. Flannery, *Numerical Recipes in Fortran*, 2nd ed. Cambridge University Press, 1992.
- [14] M.A. Rumsey, J.R. White, R.J. Werlink, A.G. Beattie, C.W. Pitchford, J. van Dam “Experimental Results of Structural Health Monitoring of Wind Turbine Blades” <<http://windpower.sandia.gov/asme/AIAA-2008-1348.pdf>>, 2008.
- [15] D. Berry, T. Ashwill. “Design of 9-Meter Carbon-Fiberglass Prototype Blades: CX-100 and TX-100,” SAND2007-0201 September 2007.
- [16] A.G. Beattie, ‘An Acoustic Emission Tester for Aircraft Halon-1301 Fire Extinguisher Bottles’, *J. Acoust. Emiss.*, 1997, **15**: 63.

Appendix

A FORTRAN program listing which reads an AEWIn data file from the fatigue test of the Sandia Sensor Blade fatigue test is given in this appendix. The program was compiled in Fortran 77 by an Absoft compiler and includes the use of PLplot graphics routines. It analyzes data for locations on the compression side of the blade. Brief notes on this program follow.

The program starts with the measured positions on of all the sensors the blade. It then has a list of sensors on the tension side of the blade, which are not used in this calculation, since this program is for the compression side of the blade. The data is then read in from a binary .DTA file. The file is searched for the byte sequence, which defines the start of the AE data. When this is found, the file is rewound and then positioned at the start of the data. The program then looks for hit data with the hit parameters that are recorded in this test. A different set of parameters on a test would require changes in this sequence. The parameters in this sequence are the test time, sensor number, (if the sensor is in the exclusion list, it goes to the next hit), rise time, count, duration, amplitude, absolute energy and load. There is also some filtering using rise time and duration in this section (which can be omitted). The next step is to search for hits that fall in the same time window. It accepts event hit sequences with from 3 or 4 hits to a maximum of 14 hits. The sensor number is matched to the sensor position coordinates and a trial solution found. Here, the trial solution is the averaged coordinates of the first three sensors hit. This starts the nonlinear least-squares program in the center of the triangle of the first hit sensors. The delta times for the event set are calculated and the least-squares program called. If the goodness of fit parameter, RSQ, is between 0.7 and 1.0 the solution is kept. It is then matched to the energy of the event (the sum of the absolute energies of the first three sensors hit) and checked to see if the solution lies within the selected boundaries on the blade. (On the first run of the program, the boundaries are set for the entire instrumented compression side surface of the blade. On later runs the coordinates of clusters found on the first run can be used). After sorting the solution for its energy, a location graph routine is called. On succeeding runs, an energy vs number of cycles graph can be called for a cluster.

The only part of the nonlinear least-squares program (NLR), which pertains to the blade, is the subroutine, FCDEMT. This routine calculates the sensor delta times for each trial solution. It uses the sensor coordinates in the chosen geometry (planar, spherical, cylindrical with end caps) and a model for the acoustic velocities. The model in this program goes from a higher velocity at station 0 mm to a lower constant velocity at station 1000 mm and beyond. It also includes a higher velocity in the spar cap. At the end of this program, another version of FCDEMT is included, which corresponds to the measured velocity in the TX blade shown in Figure 32.

Program SSENCMP

```
Program ssencmp
c This program searches a SAMOS data file for the sandsen blade c fa-
c  tigue test and reads the hit data.
c It calculates the AE source locations for the compression
c surface using the measured velocity, and graphs the locations

real*8 rtim,dtim,tim,const,ttim(24)
BYTE indaset(200000),tster(9),id,itm
BYTE buf2(50000),rlen(2),benr(4),dup(10000)
CHARACTER*1 buf(10000)
Integer*4 isen(15),iris(15),icnt(15)
Integer*4 idur(15),iamp(15),idu
real*4 load(15),tenr,param(2),w(6),td(6)
      Dimension gy(15),dy(30000),gx(30000)
CHARACTER*4 tst
CHARACTER*2048 test
EQUIVALENCE (indaset,test),(tenr,benr)
EQUIVALENCE (tst,tster),(len,rlen),(id,idd)
EQUIVALENCE (buf,dup)
Character*40 name
Common /zot/xsen(6),ysen(6),pi
common /zat/senx(24),seny(24),nsn(9)
common /zut/x1(20000),y1(20000),x2(250000),y2(250000),
+ x3(150000),y3(150000),x4(150000),y4(150000),x5(13000),y5(13000),
+ x6(5000),y6(5000),nn1,nn2,nn3,nn4,nn5,nn6

! coordinates of all sensors -- nsn -sensors not used on this
! side of the blade
Data senx/46.,83.,0.,81.,500.,0.,0.,500.,995.,
+ 993.,0.,1020.,1460.,0.,0.,1475.,2080.,2055.,0.,
+ 2060.,2473.,0.,0.,2488./
Data seny/0.0,255.,0.,-341.,140.,0.,0.,-140.,-35.,
+ 280.,0.,-280.,140.,0.,0.,-285.,-36.,385.,0.,-610.,
+ 195.,0.,0.,-278./
Data nsn/3,6,7,11,14,15,19,22,23/
const=2.5d-7

tster(1)=#07 ! byte sequence just before data starts
tster(2)=#00
tster(3)=#80
tster(4)=#00
tster(5)=#00
tster(6)=#00
tster(7)=#00
tster(8)=#00
tster(9)=#00

print *, 'Enter the name of the input File'
Read(*,1000)name

1000 Format( A40)

dtim=0.001200 ! event determination time gate
Open(1,file=name,form='binary',status='old')
```

```

Read(1) (indaset(I), I=1, 50000) ! start reading binary data file
num=index(test,tst)
print *,num
rewind(1)
read(1) (buf2(i), i=1, num)
do 10 i=1, 50
read(1) itm
if(itm.ne.0) then
  rlen(1)=itm
  go to 19
end if
10 continue

nrej=0
noffbld=0
n=0
in=0
nev=0
nn1=0
nn2=0
nn3=0
nn4=0
nn5=0
nn6=0
pi=3.1415927

20 continue

read(1, err=512) rlen(1)
19 read(1, err=512) rlen(2)
read(1, err=512) id
if(idd.ne.1) then
  read(1, err=512) (buf2(i), i=1, len-1)
  go to 20
else
  read(1, err=512) (buf(i), i=1, len-1)
end if

iflg=0
rtim=0. !read hit parameters must agree with layout set up

do 25 i=1, 6
25 rtim=rtim+(256.**(i-1))*ICHAR(buf(i))
tim=rtim*const
msen=ICHAR(buf(7))
do 40 i=1, 9
if(msen.eq.nsn(i)) goto 20
40 continue
nflg=0
mris=ICHAR(buf(8))+256*ICHAR(buf(9))
if(mris.le.5) go to 20
mcnt=ICHAR(buf(10))+256*ICHAR(buf(11))
idu=0
do 27 i=1, 4
27 idu=idu+(256.**(i-1))*ICHAR(buf(i+11))

```

```

mdur=idu
if(mris.ge.mdur/2) go to 20
mamp=ICHAR(buf(16))
do 28 i=1,4
28 benr(i)=dup(i+16)
enr=tenr*6.7041e-6
mpr=ICHAR(buf(22))+256*ICHAR(buf(23))
if(mpr.le.32767)then
  par=mpr/32767.
else
  par=(mpr-65536)/32767.
end if
aload=10.*par
n=n+1
in=in+1
if(in.eq.1)then
! determine event members
  ttim(in)=tim
  isen(in)=msen
  iris(in)=mris
  icnt(in)=mcnt
  gy(in)=enr
  idur(in)=mdur
  iamp(in)=mamp
  load(in)=aload
  go to 20
else
  if(tim.le.ttim(1)+dtim)then
    ttim(in)=tim
    isen(in)=msen
    iris(in)=mris
    icnt(in)=mcnt
    idur(in)=mdur
    iamp(in)=mamp
    gy(in)=enr
    load(in)=aload
    nflg=1
    if(in.eq.14) go to 50 !accept no more than 14 his in event
    go to 20
  else
    if(in.lt.4)then ! 3 hits min lt, 4 hits min le
      go to 35
    else
      in=in-1
      iflg=1
      go to 50
    end if
  end if
end if
35 ttim(1)=tim
isen(1)=msen
iris(1)=mris
icnt(1)=mcnt
idur(1)=mdur
iamp(1)=mamp
gy(1)=enr
load(1)=aload
do 31 i=2,14

```

```

    ttim(i)=0.
    isen(i)=0
    iris(i)=0
    icnt(i)=0
    idur(i)=0
    iamp(i)=0
    gy(i)=0.
31  load(i)=0.
    in=1
    go to 20
50 continue
    if(isen(2).eq.20)then ! sensor 20 was not working in this test
    in=0
    go to 20
    end if
    if(in.gt.3) in=3
    do 55 i=1,in
    xsen(i)=senx(isen(i))
55  ysen(i)=seny(isen(i))
    nparm=2
    ndata=in-1
    parm(1)=(xsen(1)+xsen(2)+xsen(3))/3.0 !starting loc estimate
    parm(2)=(ysen(1)+ysen(2)+ysen(3))/3.0
    do 67 i=1,6
67  w(i)=1.0 ! weighting factors for calc not used here
    do 69 i=2,in
69  td(i-1)=(ttim(i)-ttim(1))*1.e6 !delta times

    CALL NLR(ndata,nparm,td,parm,w,rsq)

    if(rsq.ge.0.7) then !accept results with fit parm down to 0.7
    go to 80
    end if
    nrej=nrej+1
    if(iflg.eq.1) go to 35
    in=0
    go to 20
80 continue
    x=parm(1) ! answers
    y=parm(2) ! accept window on blade
    if(x.lt.650..or.x.gt.950..or.y.gt.250..or.y.lt.-50.) go to 90
    energy=gy(1)+gy(2)+gy(3)
    If(energy.lt.10.)then ! ignore events with very low energy
    in=0
    go to 20
    end if

    nev=nev+1
    write(*,600)nev,ttim(1),x,y,rsq,energy,in,load(1),
+   (isen(i),i=1,3)
600  format(i6,2x,f11.4,' x =',f5.0,' y =',f5.0,' r =',f4.2,
+   2x,f11.2,x,i2,x,f4.2,x,3i2)
    ! sort as to energy for graph
    if(energy.lt.10.) then
    nn1=nn1+1
    x1(nn1)=x
    y1(nn1)=y

```

```

      go to 85
    else if(energy.lt.100.)then
      nn2=nn2+1
      x2(nn2)=x
      y2(nn2)=y
    else if(energy.lt.1000.)then
      nn3=nn3+1
      x3(nn3)=x
      y3(nn3)=y
      go to 85
    else if(energy.lt.10000.)then
      nn4=nn4+1
      x4(nn4)=x
      y4(nn4)=y
      go to 85
    else if(energy .lt.100000.)then
      nn5=nn5+1
      x5(nn5)=x
      y5(nn5)=y
      go to 85
    else
      nn6=nn6+1
      x6(nn6)=x
      y6(nn6)=y
    end if
85 continue

      gx(nev)=ttim(1)          ! * 1.86 to convert to cycles
      dy(nev)=energy

      go to 91
90 noffbld=noffbld+1
91 if(iflg.eq.1) go to 35
      in=0
      go to 20

512 continue
      write( *,1010)n,nev,nrej,noffbld
1010 format(i8,' hits, events =',i6,' rej =',i6,'off blade =',i6)

! CALL grafel(gx,dy,nev)      !energy graph
print *,nn1,nn2,nn3,nn4,nn5,nn6
CALL cgraf                    !location graph
END

SUBROUTINE FCDEMT(T,XY) !arrival time calculation, used in NLR
COMMON /zot/xs(6),ys(6),pi
COMMON /WNLGPH/PAD(2754),k
DIMENSION XY(2)
x=XY(1)
y=XY(2)
xo=x-xs(1)
yo=y-ys(1)
xk=x-xs(k+1)

```

```

yk=y-ys(k+1)
cso=abs(xo/((xo**2+yo**2)**0.5))
csk=abs(xk/((xk**2+yk**2)**0.5))
d0=(xo**2+yo**2)**0.5
dk=(xk**2+yk**2)**0.5

if(x.le.500.) v=4.0
if(x.gt.500.and.x.le.1000.)then
  v=2.55+((1000.-x)/500.)*1.45

else
  v=2.55
end if
  v0=v
  vk=v
  ! velocity varies with distance from base
if(abs(y).le.75..and.abs(ys(1)).lt.75.) then
  if(abs(y).le.25..and.abs(ys(1)).lt.25.) then
    v0=7.0
  else
    va=7.0-v
    v0=v+va*(cos(((abs(y)-25.)/50.)*pi)/2.+0.5)
  end if
end if

if(abs(y).le.75.and.abs(ys(k+1)).lt.75.) then
  if(abs(y).le.25..and.abs(ys(k+1)).lt.25.) then
    vk=7.0
  else
    vb=7.0-v
    vk=v+vb*(cos(((abs(y)-25.)/50.)*pi)/2.+0.5)
  end if
end if
T=dk/vk-d0/v0 !calculated arrival times
RETURN
END

! SUBROUTINE NLR non-linear least squares routine

SUBROUTINE NLR(ND,NPARG, DAT, PARM,WEIGHT,RSQ)
DIMENSION BS(25),BA(25),YMF(550),P(25),AX(25,25),B(25)
DIMENSION DAT(1),PARM(1),WEIGHT(1)
COMMON /WNLGPH/ Y(550),YP(550),X(550,2),WT(550),UWP,N,K,M,I
COMMON/WNLGDB/ A(25,25),AY(25,25),DB(25),SA(25),G(25),XLL,
1XKDB,GMA,ZTA,JCL,IFDPO,IFWT
C ..... INITIALIZATION AND DATA INPUT .....
NTM = 0
N=ND
DO 1000 I=1,N
Y(I)=DAT(I)
WT(I)=WEIGHT(I)
1000 CONTINUE
K=NPARG
DO 1020 I=1,K
B(I)=PARM(I)
1020 CONTINUE
903 FORMAT(F1.0,F10.0,F10.0)

```

```

M=1
NITR=26
IY=0
IFWT=1
IFDPO=1
XNK = N-K
KEND=2
ITR = 0
JCL = 0
XKDB = 1.0
IF (IFWT.EQ.1) GO TO 24
DO 20 I=1,N
20 IF(WT(I).EQ.0.0) WT(I)=1.0
24 CONTINUE
C ..... DUB IN CRITICAL-VALUE CONSTANTS (CHANGEABLE IN SUBZMT).
DEL = 1.0E-5
EPS = 1.0E-5
FF = 4.0
GMC = 45.0
TAU = 0.001
XL = 0.01
ZTA = 1.0E-31
CALL GETPHI (B,PHI)
GO TO 62
C ..... PTP MATRIX, ITERATIONS, AND TESTS FOR FIT .....
60 ITR = ITR+1
IF (NITR.GT.1) NITR=NITR-1
XKDB = 1.0
62 DO 64 I=1,K
G(I) = 0.0
BS(I) = B(I)
DO 64 J=1,K
64 A(I,J) = 0.0
C ..... FIND PARTIALS, EITHER ESTIMATED OR ANALYTIC
DO 82 I=1,N
CALL FCDEMT (F,B)
YP(I) = F
YMF(I) = Y(I)-F
DO 68 J=1,K
DBW = B(J)*DEL
IF(DBW .EQ. 0.) DBW=DEL
TWS = B(J)
B(J) = B(J)+DBW
CALL FCDEMT (FWS,B)
B(J) = TWS
68 P(J) = (FWS-F)/DBW
C ..... MAKE PARTIALS MATRIX
80 DO 82 J=1,K
G(J) = G(J)+YMF(I)*P(J)
1*WT(I)
DO 82 L=J,K
A(L,J) = A(L,J)+P(L)*P(J)
1*WT(I)
82 A(J,L) = A(L,J)
PHIZ = PHI
IF(XNK .EQ. 0.) XNK=1.0
SE = SQRT(PHIZ/XNK)

```

```

DO 86 I=1,K
DO 86 J=1,K
86 AX(I,J) = A(I,J)
C ..... SAVE SQUARE ROOTS OF DIAGONAL ELEMENTS
DO 98 I=1,K
  if(A(i,i).lt.0.) A(i,i)=0.0
SA(I) = SQRT(A(I,I))
IF (SA(I).EQ.0.0) GO TO 94
G(I) = G(I)/SA(I)
DO 92 J=1,K
92 A(I,J) = A(I,J)/SA(I)
GO TO 98
94 G(I) = 0.0
DO 96 J=1,K
  A(I,J) = 0.0
96 A(J,I) = 0.0
98 CONTINUE
DO 104 J=1,K
  IF (SA(J).EQ.0.0) GO TO 102
DO 100 I=1,K
100 A(I,J) = A(I,J)/SA(J)
102 A(J,J) = 1.0
DO 104 I=1,K
104 AY(I,J) = A(I,J)
C ..... WRITE TEST PARAMETERS AND FIND INITIAL INCREMENTS
CALL GETDBS (BS,B,XL,PHI,JUMP)
IF(JUMP.EQ.1) GO TO 700
C ..... EPSILON TEST
DO 170 J=1,K
  IF (ABS(DB(J)/(ABS(B(J))+TAU)).GE.EPS) GO TO 172
170 CONTINUE
GO TO 700
C ..... MAXIMUM NO. OF ITERATIONS (FORCE OFF) TEST
172 IF (NITR.NE.1) GO TO 171
GO TO 700
C ..... DETERMINE PARAMETERS FOR NEXT ITERATION
171 IF (XL.LE.1.0E-08.AND.PHI.LE.PHIZ) GO TO 60
XLS = XL/10.0
CALL GETDBS (BS,BA,XLS,PHI1,JUMP)
IF(JUMP.EQ.1) GO TO 700
IF (PHI1.GT.PHIZ) GO TO 176
XL = XLS
PHI = PHI1
DO 174 J=1,K
174 B(J) = BA(J)
GO TO 60
176 IF (PHI.LE.PHIZ) GO TO 60
178 XL = 10.0*XL
180 CALL GETDBS (BS,B,XL,PHI,JUMP)
IF(JUMP.EQ.1) GO TO 700
IF (PHI.LE.PHIZ) GO TO 60
IF (GMA.GE.GMC) GO TO 178
XKDB = XKDB/5.0
C ..... GAMMA EPSILON TEST
DO 182 J=1,K
  IF (ABS(DB(J)/(ABS(B(J))+TAU)).GE.EPS) GO TO 180
182 CONTINUE

```

```

C C
C ..... CONFIDENCE LIMITS AND DATA OUTPUT .....
700 IF (JCL-1) 702,10,701
701 CONTINUE
702 CONTINUE
C ..... CALCULATE R SQUARED
SSY = 0.0
SW = 0.0
CHISQ = 0.0
DO 707 I=1,N
SSY = SSY+Y(I)*WT(I)
707 SW = SW+WT(I)
SW = SSY/SW
SYG = SSY
SSY = 0.0
DO 708 I=1,N
708 SSY = SSY+(Y(I)-SW)**2
    if(ssy.eq.0.)ssy=0.0001
RSQ = 1.0-PHIZ/SSY
BL=B(K)
C ..... FIND AND WRITE PTP INVERSE.
CALL GJRMIX (AX,25,K,ZTA,MSNG)
IF (MSNG.EQ.2) GO TO 10
KST = 1
711 KEND = KST+4
IF (KEND.GT.K) KEND=K
IF (KEND.EQ.K) GO TO 713
KST = KST+5
GO TO 711
713 DO 715 J=1,K
IF (AX(J,J).GE.0.0) GO TO 715
GO TO 10
715 SA(J) = SQRT(AX(J,J))
C ..... FIND AND WRITE PARAMETER CORRELATION MATRIX.
DO 720 I=1,K
DO 718 J=I,K
WS = SA(I)*SA(J)
IF (WS.GT.0.0) GO TO 716
AX(I,J) = 0.0
GO TO 718
716 AX(I,J) = AX(I,J)/WS
718 AX(J,I) = AX(I,J)
AX(I,I) = 1.0
720 SA(I) = SA(I)*SE
KST = -9
721 KST = KST+10
KEND = KST+9
IF (KEND.GT.K) KEND=K
IF (KEND.LT.K) GO TO 721
C ..... FIND AND WRITE PARAMETER ERRORS AND SUPPORT PLANES.
WS = K
DO 750 J=1,K
B(J) = BS(J)
750 CONTINUE
C ..... NONLINEAR CONFIDENCE LIMITS
PC = PHIZ*(1.0+FF*WS/XNK)
XNK = 2.0*(PHIZ-PC)

```

```

DO 780 J=1,K
ITR = 1
DO 764 L=1,2
SPL = 1.
B(J) = BS(J)+SPL*SA(J)
CALL GETPHI (B,PHI)
IF (PHI.LT.PC) GO TO 756
DO 754 IY=1,9
SPL = SPL/2.0
B(J) = BS(J)+SPL*SA(J)
CALL GETPHI (B,PHI1)
IF (PHI1.LT.PC) GO TO 762
754 CONTINUE
GO TO 760
756 DO 758 IY=1,3
SPL = SPL+1.
B(J) = BS(J)+SPL*SA(J)
CALL GETPHI (B,PHI1)
IF (PHI1.GE.PC) GO TO 762
758 CONTINUE
760 ITR = ITR+L
GO TO 764
762 WS = SPL-1.0
  if(ws.eq.0.) ws=0.001
OPL = 2.0*((PHIZ+PHI1/WS)/SPL-PHI/WS)
OPU = (PHI*SPL-PHI1/SPL)/WS-PHIZ/SPL*(SPL+1.0)
B(J) = BS(J)+(SQRT(OPU**2-OPL*XNK)-OPU)*SA(J)/OPL
CALL GETPHI (B,PHI)
BA(L) = B(J)
G(L) = PHI
764 CONTINUE
780 B(J) = BS(J)
790 CONTINUE
800 CONTINUE
C C
10 CONTINUE
  DO 3000 I=1,K
  PARM(I)=B(I)
3000 CONTINUE
  RETURN
924 FORMAT(5X,19H... FORCE OFF AFTER,I5,10H ITERATION,A1)
END

```

```

SUBROUTINE GETPHI (B,PHI)
C THE SUBROUTINE CALLED BY THIS SUBPROGRAM IS
C FCDEMT
DIMENSION B(25)
COMMON /WNLGPH/ Y(550),YP(550),X(550,2),WT(550),UWP,N,K,M,I
PHI = 0.0
UWP = 0.0
DO 302 I=1,N
CALL FCDEMT (F,B)
FMYQ = (Y(I)-F)**2
PHI = PHI+FMYQ*WT(I)
302 UWP = UWP+FMYQ
RETURN

```

END

```

SUBROUTINE GETDBS (BS,B,XL,PHI,JUMP)
C THE SUBROUTINES CALLED BY THIS SUBPROGRAM ARE
C GJRMIX, GETPHI
DIMENSION B(25),BS(25)
COMMON /WNLGPH/ Y(550),YP(550),X(550,2),WT(550),UWP,N,K,M,I
COMMON /WNLGDB/ A(25,25),AY(25,25),DB(25),SA(25),G(25),XLL,
1XKDB,GMA,ZTA,JCL,IFDPO,IFWT
JUMP = 0
XLL = 0.0
DTG = 0.0
GTG = 0.0
DO 202 I=1,K
DO 201 J=1,K
201 A(I,J) = AY(I,J)
202 A(I,I) = A(I,I)+XL
CALL GJRMIX (A,25,K,ZTA,MSNG)
IF (MSNG.EQ.1) GO TO 204
JCL = 1
GO TO 602
204 DO 210 I=1,K
DB(I) = 0.0
DO 208 J=1,K
208 DB(I) = DB(I)+A(I,J)*G(J)
IF(DB(I) .EQ. 0.) GO TO 210
  if(SA(i).eq.0.) SA(i)=0.0001
DB(I) = DB(I)/SA(I)*XKDB
DTG = DTG+DB(I)*G(I)
GTG = GTG+G(I)**2
XLL = XLL+DB(I)**2
210 B(I) = BS(I)+DB(I)
XLL = SQRT(XLL)
IF (K.EQ.1) GO TO 214
IF(GTG .EQ. 0) GO TO 602
CGM = DTG/(XLL*SQRT(GTG))
JGM = 1
IF (CGM.GT.0.0) GO TO 212
JGM = 2
CGM = ABS(CGM)
212 if(cgm.ge.1.0) cgm=0.99
GMA = 57.2957795*(1.5707288+CGM*(-0.2121144+CGM*(0.074261-CGM*
10.0187293)))*SQRT(1.0-CGM)
IF (JGM.EQ.1) GO TO 216
GMA = 180.0-GMA
IF (XL.LT.1.0) GO TO 216
JCL = 2
GO TO 602
214 GMA = 0.0
216 CALL GETPHI (B,PHI)
IFDPO=1
IF (IFDPO.NE.1) GO TO 600
RETURN
602 JUMP = 1
600 RETURN
END
```

```

SUBROUTINE GJRMIX (A,N,IM,EPS,MSING)
DIMENSION A(N,N),B(25),C(25)
INTEGER P(25),Q(25)
C .. DETERMINATION OF THE PIVOT ELEMENT.

MSING = 1
DO 10 K=1,IM
PIVOT = 0.0
DO 20 I=K,IM
DO 20 J=K,IM
IF (ABS(A(I,J)).LE.ABS(PIVOT)) GO TO 20
PIVOT = A(I,J)
P(K) = I
Q(K) = J
20 CONTINUE
IF (ABS(PIVOT).LE.EPS) GO TO 40
C .. EXCHANGE OF THE PIVOTAL ROW WITH THE KTH ROW.
IF (P(K).EQ.K) GO TO 80
DO 70 J=1,IM
L = P(K)
Z = A(L,J)
A(L,J) = A(K,J)
70 A(K,J) = Z
C .. EXCHANGE OF THE PIVOTAL COLUMN WITH THE KTH COLUMN.
80 IF (Q(K).EQ.K) GO TO 90
DO 100 I=1,IM
L = Q(K)
Z = A(I,L)
A(I,L) = A(I,K)
100 A(I,K) = Z
C .. JORDAN STEP.
90 DO 110 J=1,IM
IF (J.NE.K) GO TO 130
B(J) = 1.0/PIVOT
C(J) = 1.0
GO TO 140
130 B(J) = -A(K,J)/PIVOT
C(J) = A(J,K)
140 A(K,J) = 0.0
110 A(J,K) = 0.0
DO 10 I=1,IM
DO 10 J=1,IM
10 A(I,J) = A(I,J)+C(I)*B(J)
C .. REORDERING THE MATRIX.
DO 155 M=1,IM
K = IM-M+1
IF (P(K).EQ.K) GO TO 170
DO 180 I=1,IM
L = P(K)
Z = A(I,L)
A(I,L) = A(I,K)
180 A(I,K) = Z
170 IF (Q(K).EQ.K) GO TO 155
DO 150 J=1,IM
L = Q(K)

```

```

Z = A(L,J)
A(L,J) = A(K,J)
150 A(K,J) = Z
155 CONTINUE
GO TO 151
C .. WRITE MESSAGE IF MATRIX IS SINGULAR.
40 CONTINUE
MSING = 2
151 RETURN
END

```

! GRAPHICAL ROUTINES USE PLplot graphics library

```

SUBROUTINE grafel(eld,enr,nev)

dimension xx(100000),x(200000),y(200000),eld(1),enr(1)
do 10 i=1,nev
10 xx(i)=eld(i)
do 20 i=1,nev

x(2*i-1)=xx(i)
x(2*i)=xx(i)
y(2*i+1)=enr(i)+y(2*(i-1))
y(2*i)=enr(i)+y(2*(i-1))
20 continue
y(1)=0.
x(2*nev+1)=xx(nev)
ymax=1.05*y(2*nev)
xmin=0. ! xmax=1.05*eld(nev)
xmax=xx(nev)*1.05 ! xmin=0
call plinit()
call plcol0(15)
call plenv(xmin,xmax,0.0,ymax,0,0)
call pllabb('Time - Sec','Total Energy - MEV',
+ ' Compression Side')
nn=2*nev
Call plline(nn,x,y)
Call plend
return
end

SUBROUTINE cgraf
dimension mclr(6),snx(15),sny(15)
common /zat/senx(24),seny(24),nsn(9)
common /zut/x1(20000),y1(20000),x2(250000),y2(250000),
+ x3(150000),y3(150000),x4(150000),y4(150000),x5(13000),y5(13000),
+ x6(5000),y6(5000),nn1,nn2,nn3,nn4,nn5,nn6

data mclr/14,9,3,11,1,15/ ! colors - salmon,blue,green,cyan,red,
! black

n=0
do 10 i=1,24
do 9 j=1,9

```

```

    if(i.eq.nsn(j))go to 10
9  continue
    n=n+1
    snx(n)=senx(i)
    sny(n)=seny(i)
10 continue
    call plinit()

    call plcol0(15)
    call plschr(0.,1.0)
    call plenv(650.,950.,-50.,250.,1,1)
    call pllalab('X - mm','Y - mm','compression side')

    call plcol0(mclr(1))
    call plpoin(nn1,x1,y1,42)

    call plcol0(mclr(2))
    call plpoin(nn2,x2,y2,42)

    call plcol0(mclr(3))
    call plpoin(nn3,x3,y3,42)

    call plcol0(mclr(4))
    call plpoin(nn4,x4,y4,42)

    call plcol0(mclr(5))
    call plpoin(nn5,x5,y5,42)

    call plcol0(mclr(6))
    call plpoin(nn6,x6,y6,42)

    call plcol0(15)
    call plschr(0.,3.)
    call plpoin(15,snx,sny,79)

    call plend
    return
end

```

SUBROUTINE FCDEMT for TX blade:
Contains acoustic velocity calculated for Figure 32.

```

SUBROUTINE FCDEMT(T,XY)
COMMON /zot/xs(5),ys(5)
COMMON /WNLGPH/PAD(2754),k
DIMENSION XY(2)
pi=3.14159265
of20=0.3490659
x=XY(1)
y=XY(2)
xo=x-xs(1)
yo=y-ys(1)
xk=x-xs(k+1)
yk=y-ys(k+1)
cso=acos(xo/((xo**2+yo**2)**0.5))
csk=acos(xk/((xk**2+yk**2)**0.5))

```

```

if(yo.gt.0.0) then
  ango=cso-of20
else
  ango=cso+of20
end if
if(yk.gt.0.0) then
  angk=csk-of20
else
  angk=csk+of20
end if
if(xo.lt.0.0) ango=pi-ango
if(xk.lt.0.0) angk=pi-angk
if(ang<of20) then
  v0=2.10+2.40*exp(-(2.3851*ango)**2.0)
else
  v0=2.10+2.40*exp(-(2.4062*abs(ang))**1.15)
end if
if(ang<of20) then
  vk=2.10+2.40*exp(-(2.3851*angk)**2.0)
else
  vk=2.10+2.40*exp(-(2.4062*(angk))**1.15)
end if
d0=(xo**2+yo**2)**0.5
dk=(xk**2+yk**2)**0.5
T=dk/vk-d0/v0
RETURN
END

```

Relating Damage Assessed by Using Intensity Signal Analysis of Acoustic Emission with Surface Strain in Concrete and Ultrasonic Pulse Velocity in Reinforced Concrete Beams under Monotonically Increasing Load

R. Vidya Sagar¹ and Swarnangshu Ghosh²

¹Department of Civil Engineering, Indian Institute of Science, Bangalore-560012, India (rvsagar@iisc.ac.in), ²Department of Civil Engineering, National Institute of Technology, Surathkal -575025, India (swarnangshughosh.171cv146@nitk.edu.in)

Abstract

This article reports on the assessment of damage state of reinforced concrete (RC) beams using the intensity signal analysis (ISA) based on acoustic emission (AE) testing. The influence of shear reinforcement in RC beams on damage developed was studied. There are few AE based studies related to distinguishing the damage (accumulation of microcracks) due to tensile and shear cracking in RC beams. The aim is to relate the surface strain in concrete and the corresponding damage as the load is increased monotonously. The damage developed in RC beams was represented with five levels namely Level - A (indication that insignificant AE has been detected in the region), Level - B, Level - C, Level - D, and Level - E (major defects detected and use of RC structural member is not recommended). The surface strain in concrete reached its maximum value quickly in shear failure. The AE sensor (s) present in the location where severe damage occurred, recorded higher number of AE signals than the other sensors. At the same location, ultrasonic pulse velocity decreased considerably. The surface strain in concrete reached its maximum value at the same region. The results reported in this article may be an improvement related to the knowledge on ISA of AE to monitor damage in RC structures.

Keywords: Damage, reinforced concrete, strain, shear failure, ultrasonic pulse velocity

1. Introduction

Generally, for non-destructive testing of reinforced concrete (RC) structures, visual inspection is a preliminary method which engineers use *in-situ*. There are chances of occurrence of subjective and potentially inaccurate assessments with regards to decisions on a structure's damage status, *in-situ*. It can thereby pose doubts about safety and in some cases can lead to structure's failure or sudden collapse. In general, damage can be defined as accumulation of microcracks in a reinforced concrete structure. To determine whether the RC structure is suitable for its designed use, it is often necessary to assess damage in the same after 30 - 35 years. From the recorded acoustic emission (AE) waveforms or parameters, it is possible to identify the AE source location (s), type of cracks (tensile/shear), characterisation of the cracks (micro/macro), and to assess the status of damage in the existing RC structures, in real time [1-5].

1.1 Brief Literature Review

Researchers introduced several AE-based techniques or methods to assess damage level in RC structures (both in laboratory and *in-situ*) by using AE waveforms or AE signal parameters [6]. Fowler *et al.* [7, 8] introduced intensity signal analysis (ISA) of AE to assess the damage status in fiber reinforced polymers. Researchers attempted to study the application of ISA of AE for real

time damage monitoring of members in concrete bridges [9,10]. Shahidan *et al.* [11] studied the type and level of damage using RA-AF analysis and ISA based analysis of AE, where

RA = (Rise time, RT)/(Peak amplitude of an AE signal) and

Average frequency (AF) = (AE counts)/Duration.

An RC portal frame was tested in the laboratory and ISA of AE was implemented to study the damage process [12]. To date most of the studies on ISA of AE are related to damage assessment in RC structures. The influence of shear reinforcement on damage in RC beams when subjected to static loading using ISA of AE has not been studied extensively. Also, by connecting the surface strain in concrete and damage assessed by using ISA of AE, the confidence on this approach increases.

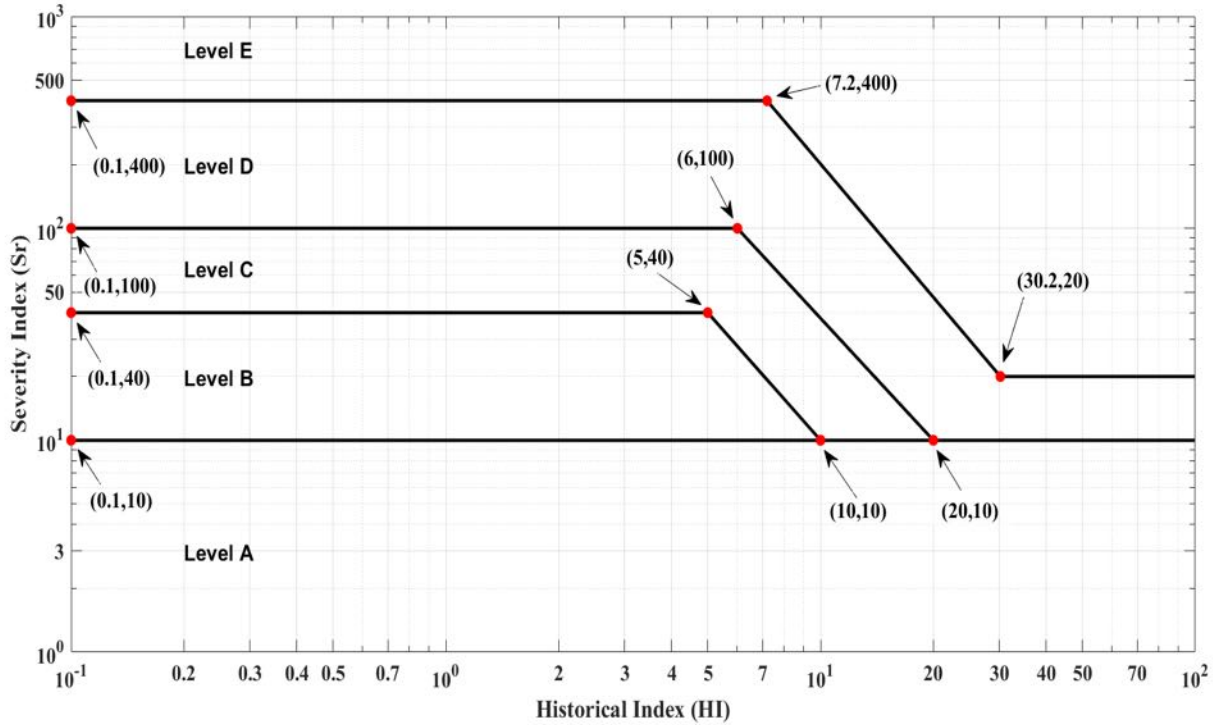


Fig. 1. Schematic representation of various levels of damage in Intensity Signal analysis of Acoustic emission; Level A: no damage; Level B: damage detected; Level C: Minor damage; Level D: Major damage; Level E: Severe damage [7, 9 - 11].

1.2 Acoustic Emission based Intensity Signal Analysis

The ISA of AE is a mathematical method for evaluating the damage in both composite and RC structures in laboratory and *in-situ* [7-10]. It results in damage level in RC structure as shown in Fig. 1. The details about the damage intensity levels recommended by ISA of AE are given in Table 1. This approach uses an AE parameter, namely, signal strength (picovolt-s), which is the time integral of absolute signal voltage. AE energy (Volt-s) is the area under rectified signal envelope. AE absolute energy (aJ) is the square of signal voltage at the sensor before amplification, divided by 10 kΩ impedance [3, 4, 13]. Signal strength is derived from Eq. 1, and is therefore proportional to AE energy.

$$\text{Signal Strength} \propto \sum_{FTC}^{LTC} (|V_i| \Delta t) \quad (1)$$

where *FTC* is the first threshold crossing, *LTC* is the last threshold crossing of an AE waveform, V_i are the successive readings of the signal voltage and Δt is the time interval between them. Two AE indices namely historical index (*HI*) and severity index (S_r) are used in ISA of AE. *HI*

Table 1. Damage classification based on AE intensity levels [8, 10].

AE intensity levels	Observation on the test specimen during the experiment	Indication	Recommendations
A	Insignificant acoustic emission generated.	No damage	-
B	Minor surface defects such as cracking due to corrosion.	Damage detected	Note for reference in future tests.
C	Defects appeared.	Minor damage	Requires follow-up evaluation. Evaluation may be based on further data analysis or complementary non-destructive examination.
D	Significant defect developed.	Major damage	Requires follow-up inspection.
E	Major defect developed.	Severe damage	Requires immediate shut-down and follow-up inspection.

determines the change of AE signal strength rate. Particularly, it measures the slope change of the curve plotted between cumulative signal strength and time [9, 11].

$$HI = \frac{N}{N-K} \frac{\sum_{i=K+1}^N S_{oi}}{\sum_{i=1}^N S_{oi}} \quad (2)$$

where N is number of the AE hits, S_{oi} is signal strength of the i^{th} hit, K is an empirical constant based on the material used to cast the test specimen. Severity index (S_r) is the mean signal strength among the largest numerical value of AE signals.

$$S_r = \frac{1}{J} \sum_{m=1}^J S_{om} \quad (3)$$

where J is an empirical constant based on test specimen material, S_{om} is the signal strength of the m^{th} hit where the order of m is based on magnitude of the signal strength. For concrete, K and J are related to N as shown in Table 2 [10, 11].

Table 2. The relation between values of N , K and J for concrete [10].

N and K values		J (constant)
N (number of hits recorded by each channel)	K (constant)	
< 50	0	0
$50 < N < 200$	$N-30$	50
$200 < N < 500$	$0.85N$	
$N > 500$	$N-75$	

Table 3. Geometrical and steel reinforcement details of the RC beams.

Specimen	28 - day Compressive strength of concrete cube (MPa)	Dimensions (mm)			Span (mm)	Shear stirrups	Loading Rate (mm/s)	Test duration (minutes)	Location coordinates at which surface strain was recorded in concrete at section near to			Type of failure
		Length	Depth	Width					Left Support (Section - I)	Mid span (Section - II)	Right Support (Section -III)	
RF1	21.6	2440	250	150	2240	2 legged 8Φ	0.0035	151.9	x = 50 mm y = 125 mm	x = 1120 mm	x = 2170 mm	Flexure
RF2	18.2	2440	250	150	2240	2 legged 8Φ	0.0089	113.1		y = 125 mm	y = 125 mm	Flexure
RS1	18.5	2340	250	150	2140	Nil	0.0400	6.7		x = 1170 mm	x = 2070 mm	Shear
RS2	23.7	2340	250	150	2140	Nil	0.0050	58.2		y = 125 mm	y = 125 mm	Shear

Table 4. AE sensor location coordinates (2D - planar) mounted on the RC test beams.

Specimen	Number of AE Sensors mounted	Sensor location coordinates (2D- Planar) (mm)									
		Ch-4		Ch-5		Ch-6		Ch-7		Ch-8	
		X	Y	X	Y	X	Y	X	Y	X	Y
RF1	5	1200	200	685	50	1755	50	150	200	2290	200
RF2	5	1200	200	685	50	1755	50	150	200	2290	200
RS1	5	1200	200	685	50	1755	50	150	200	2290	200
RS2	5	1220	50	685	175	1755	175	150	75	2290	75

Table 5. Total AE parameters recorded during fracture process in the test specimens.

Specimen	Peak load (kN)	In-service design load (kN)	Load at which first crack appeared (kN)	Total AE parameters								
				Hits					Absolute Energy (aJ)	Ring down counts (RDC)	Energy (Volt-s)	Signal Strength (picovolt-s)
				Ch-4	Ch-5	Ch-6	Ch-7	Ch-8				
RF1	87.38	58.25	36.60	625726	3170928	804123	445436	301931	2.34×10^{10}	7.20×10^7	5.05×10^7	3.30×10^{11}
RF2	78.40	52.26	31.36	4250	2364938	256049	291828	61886	1.12×10^{10}	2.71×10^7	3.48×10^7	2.24×10^{11}
RS1	71.40	47.60	28.50	98668	77754	41316	67762	64001	3.75×10^{10}	1.62×10^7	1.70×10^7	1.13×10^{11}
RS2	80.10	53.40	32.10	1375	60374	37821	157597	1644	2.20×10^9	2.42×10^6	2.27×10^6	1.48×10^{10}

1.3 Aim of the study

RC beams, with and without shear reinforcement, were tested in laboratory to study the damage by using ISA of AE. The results of this experimental study may result in a better understanding about the damage which occurred due to tensile failure and shear failure. During tensile failure of RC beams, vertical cracks appear at the location where maximum bending moment is developed, and diagonal shear cracks appear near the supports when the beam reaches yielding and collapse stages. Also, the surface strain in concrete is connected with the damage level. The outcome of the study may be useful to identify the damage accumulated in RC structure under static loading. Subsequently, the engineer can plan for the implementation of suitable retrofitting methods (to extend the life span for further usage) to the RC structure.

2. Experimental program

2.1 Materials

Four RC beams with rectangular cross-section were tested in laboratory under monotonously increasing loading and simultaneously the generated AE during fracture process in the same were recorded. Ordinary Portland cement, river sand, coarse aggregate (20 mm) and water were used to cast the test specimens in the laboratory. The 28-day compressive strength of the concrete used to cast the RC beam specimens are given in Table 3.

2.2 Test specimen

The steel reinforcement details, geometrical details (dimensions) of the test specimens are given in Fig. 2. The cross-sectional area of tensile steel reinforcement in each RC beam specimen is 276.32 mm². All RC beams (Specimen - RF1, Specimen - RF2, Specimen - RS1 and Specimen - RS2) were tested under monotonously increasing loading and the loading rate is mentioned in Table 3. Specimens RF1 and RF2 were cast with the same batch of concrete, but specimens RS1 and RS2 were cast with different batches of concrete. The RC beams were cast in wooden moulds and the specimens were demoulded after 24 hours. The RC beams were cured with water for 28 days. Steel stirrups as shear reinforcement were provided in two test specimens (RF1 and RF2). The spacing of the steel stirrups in RF1 and RF2 were 160 mm. The other two specimens (RS1 and RS2) which did not have shear reinforcement were also tested. These two RC beams specimens were tested in order to distinguish the damage computed using ISA of AE in the absence of shear stirrups.

2.3 Test setup

The experimental setup consisted of a servo-controlled hydraulic machine of 1200 kN capacity with a data acquisition facility. All RC beam specimens were tested in Structures Laboratory, Department of Civil Engineering, Indian Institute of Science, Bangalore, India, under four-point bending. The longitudinal surface strain in concrete at (i) close to left support [Section - I], (ii) mid-span [Section - II], (iii) close to right support [Section - III] at mid height of the beam were measured manually with a Demec gauge over 99 mm gauge length, at different time intervals during testing. The location coordinates where the surface strain in concrete were recorded are shown in Table 3.

2.4 AE monitoring setup

The AE signal parameters were recorded using an eight channel AE monitoring system during the fracture process of the RC beams. Resonant type differential AE sensors (57 kHz) with preamplifier gain of 40 dB were used. High vacuum silicon grease was used as coupling agent to

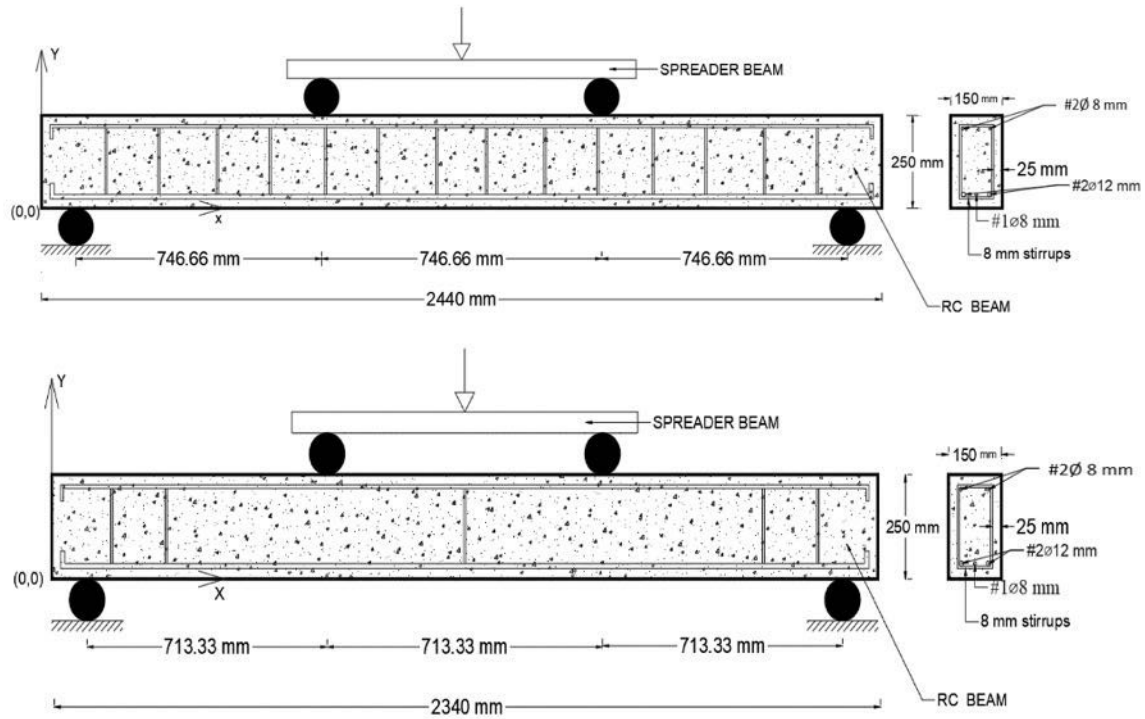


Fig. 2. Schematic diagrams of (a) simply supported RC beam having shear reinforcement (top); (b) simply supported RC beam without shear reinforcement (bottom).

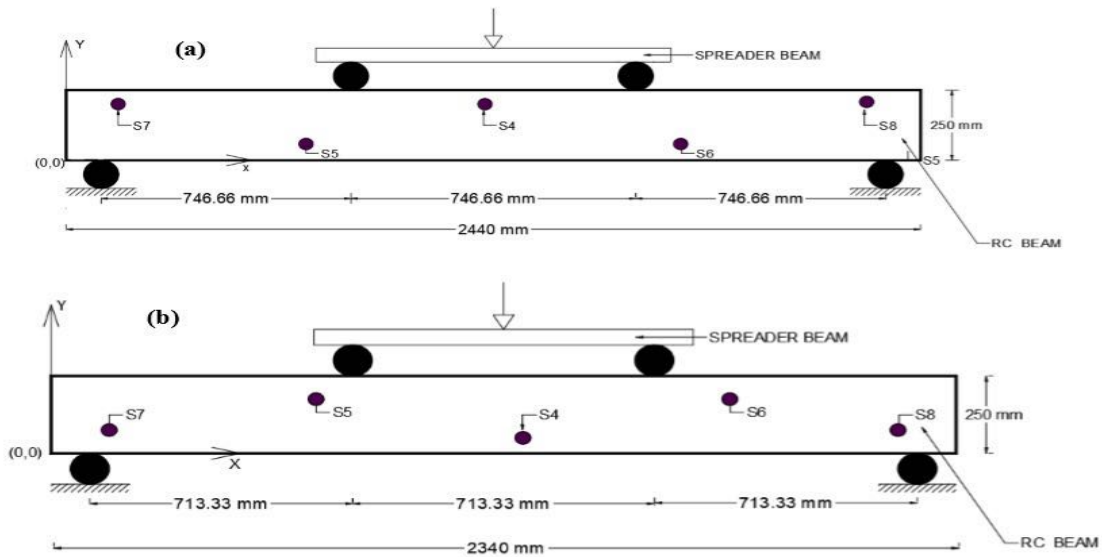


Fig. 3. Schematic diagram of AE sensors on RC beams (a) RF1, RF2, RS1. (b) RS2 (The small black circles on the surface of the beams represent the sensors).

mount the sensor on the RC beam specimen. A gum tape was used to tie the AE sensor to the test specimen at the desired location. A fixed threshold of $39 \text{ dB}_{\text{AE}}$ was set to screen out surrounding noise. AE system monitoring parameters namely peak definition time of $200 \mu\text{s}$, hit definition time of $800 \mu\text{s}$ and hit lockout time of $1000 \mu\text{s}$ were set. The sensor locations on test specimen are shown schematically in Fig. 3. The frequency bandwidth of the preamplifier operating connected with AE sensors was 20 kHz-1200 kHz. The AE sensor had a good sensitivity and frequency response over the range of 35 kHz-100 kHz. As per calibration chart of each AE sensor supplied

by the manufacturer of the AE system, authors concluded that sensors had good sensitivity and nearly the same response. The 2D planar location (X and Y coordinates) of the AE sensors on the RC beam specimens are given in Table 4. The preamplifier gain was set to 40 dB and the sampling rate was 1 MHz. The total AE energy released was calculated by summing up the AE energy recorded by the channels used. The study on AE event locations (or source locations) has not been attempted.

2.5 Ultrasonic Pulse Velocity (UPV) Measurement

Ultrasonic pulse velocities were recorded in the RC beams before and after testing using PUNDIT (Portable Ultrasonic Non-Destructive Digital Indicating Tester) equipment. Transducers of 54 kHz frequency were used. To ensure the proper transmission of the ultrasonic pulse between transmitter and receiver, petroleum grease was used as a coupling agent between the concrete surface and face of each transducer. Both the front and back surfaces (2D plane) of the RC beam were represented with a grid consisting of 3 rows and 23 columns to measure the UPV. Direct transmission arrangement method was used to record the UPV across the RC beam. The path length was 150 mm. However, the corrections to the UPV recordings due to influence of steel reinforcement were not included.

3. Results and Discussion

3.1 AE characteristics of RC beams under monotonously increasing load

It is known that AE is a phenomenon where transient elastic stress waves are generated during fracture process in solids. The AE waveform parameters namely absolute energy, counts, signal strength, hits, AE energy recorded during the fracture process in RC beams are shown in Table 5. The influence of shear reinforcement on load carrying capacity can be observed from Fig. 4. The specimen (RF2) having shear reinforcement exhibited elasto-plastic behaviour during monotonously increasing loading. However, specimen RS2 exhibited brittle failure after reaching peak load and failed suddenly. In the same figure, the variation with time for specimen RS2 and RF2 can be observed. And also, a constant bending moment and zero shear force are observed in the mid span as shown in Fig. 5. Fig. 6a shows the variation of cumulative AE hits with time for beams RF2 and RS2. A larger number of AE hits were generated for tensile failure than shear failure. The reason could be attributed to a greater number of micro-cracks which occurred in the specimen with shear reinforcement, than in the specimen without shear reinforcement. Fig. 6b and Fig. 6c shows the variation of cumulative signal strength recorded by all the AE sensors with time for beams RF1 and RS1 respectively. From Fig. 6b it can be observed that the cumulative signal strength curve increased linearly till failure of the specimen RF1 (with shear reinforcement). The cumulative AE signal strength curve in Fig. 6c is divided into five regions namely 0 - a₁, a₁ - a₂, a₂ - a₃, a₃ - a₄, and a₄ - a₅. In the first region, there is no rise in the cumulative signal strength curve indicating fracture process has not begun. In the region a₁ - a₂, there is a rise in the cumulative signal strength curve which indicates minor cracking has started. Towards the end of this interval from 190 s, there is a steep rise in the curve which might indicate commencement of macrocracking. From a₂ - a₃, the rise was linear. In the region a₃ - a₄, when the load was approaching the peak, the rate was very high indicating the higher generation of AE signals during the collapse. In the last region, the curve rose linearly till failure. The load also suddenly dropped without warning. Even though the load carrying capacity is almost equal for specimens RF1 and RS1, but the cumulative signal strength is higher for specimen RF1 than RS1 which indicates that specimen RF1 has more capacity to absorb strain energy during fracture process. The reason could be due to the presence of shear reinforcement. Fig. 7a and b show the variation of AE energy with time for specimens RF2 and RS2. At the instant in which specimen RF2 started yielding,

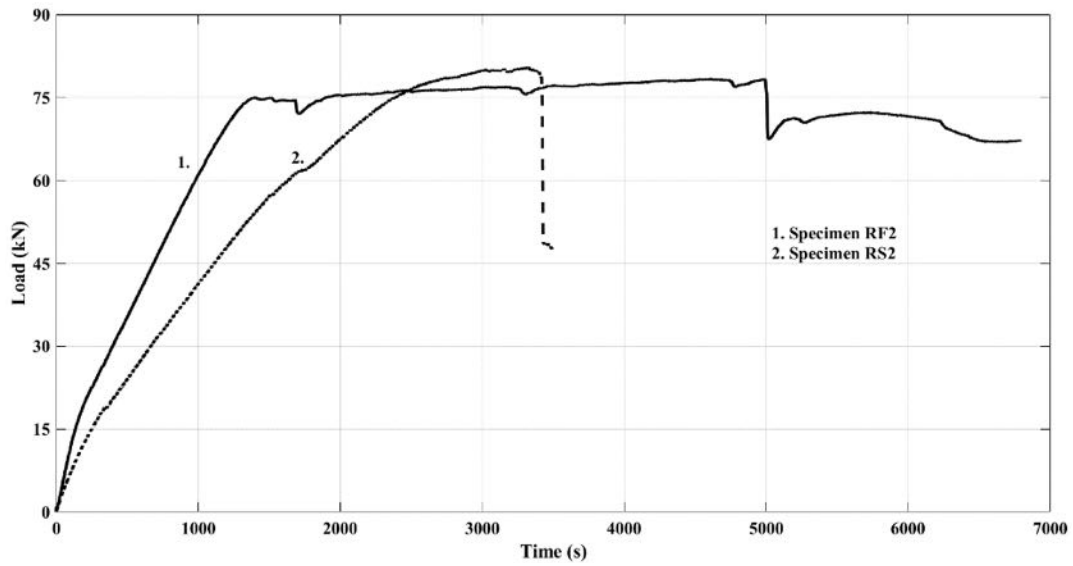


Fig. 4. Load variation with time for RC beams RF2 and RS2.

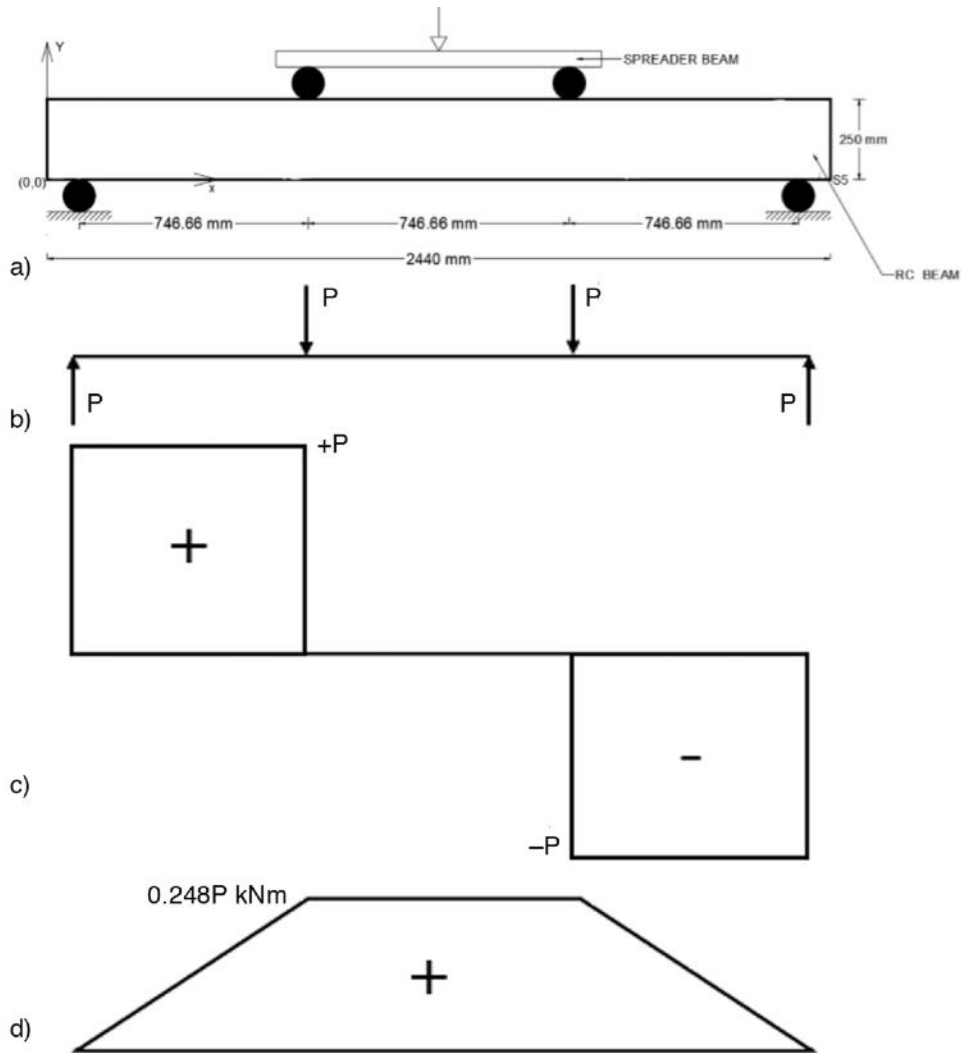


Fig. 5. (a) Schematic diagram of RC beam; (b) Free body diagram; (c) Shear Force diagram; (d) Bending Moment diagram of the RC beam [P refers to arbitrary load acting on the beam].

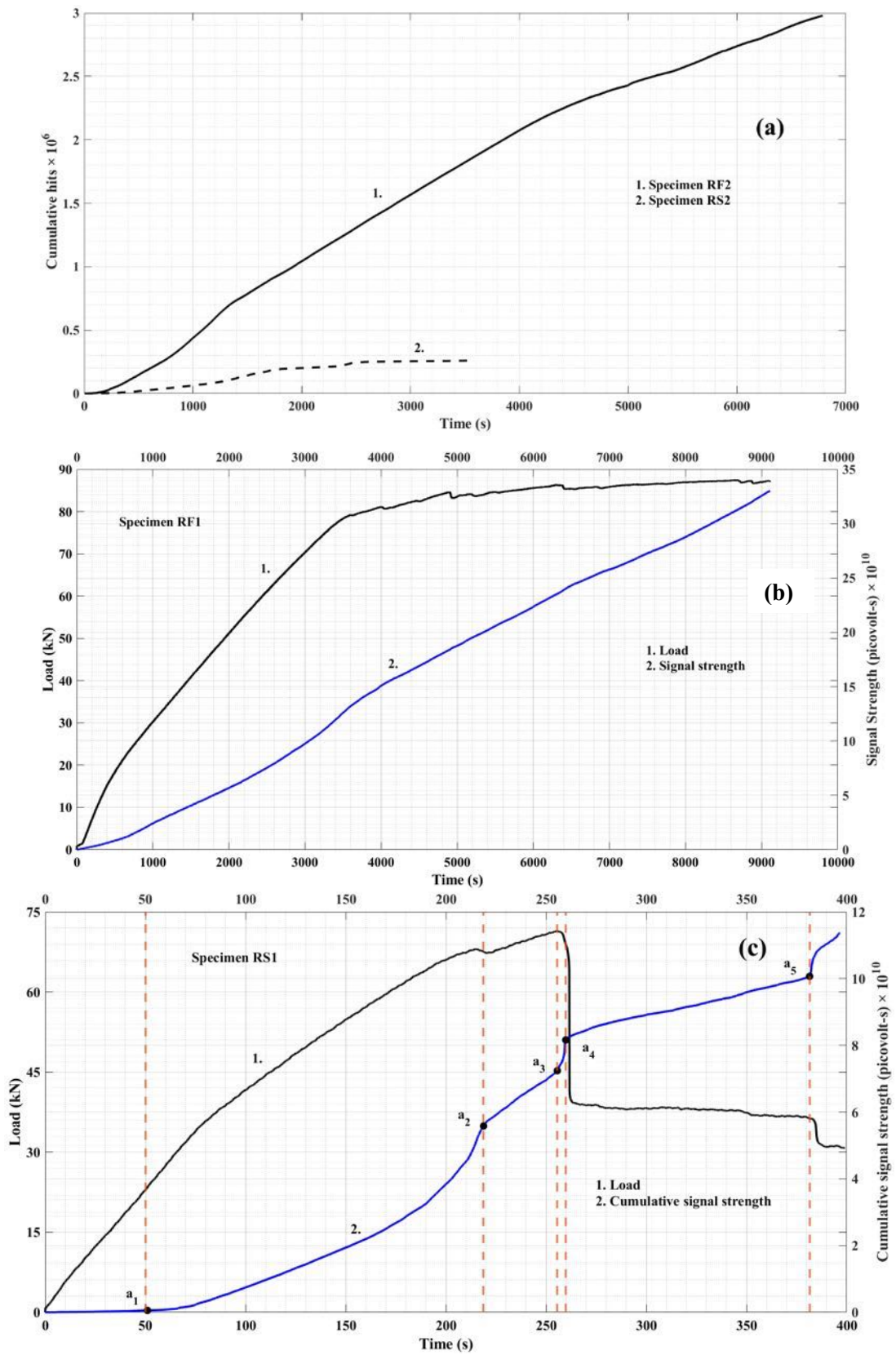


Fig. 6. (a) Cumulative AE hits versus time for specimens RF2 and RS2; (b) Variation of AE signal strength with load and time for specimen with shear reinforcement; (c) Variation of AE signal strength with load and time for specimen without shear reinforcement.

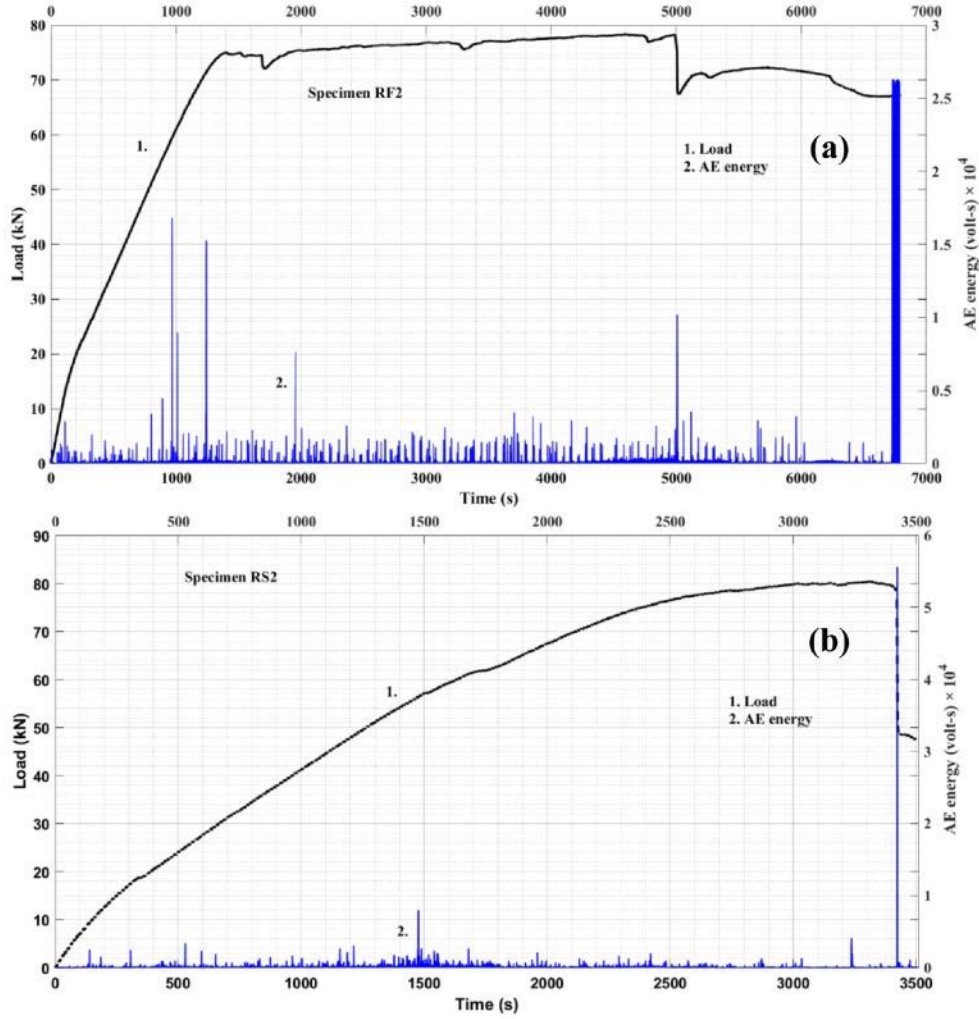


Fig. 7. Variation of load with AE energy for (a) Specimen RF2; (b) Specimen RS2.

considerable AE energy (1.5×10^4 volt-s) is released. However, after yielding, the specimen withstood loading till 6900 s, but didn't collapse. At collapse, very high AE energy (2.56×10^4 volt-s) signals were released. But in case of specimen RS2, the elastoplastic behaviour was absent and higher energy signals (5.5×10^4 volt-s) were released at collapse.

3.2 Damage assessment in RC beams with shear reinforcement using ISA of AE

By following [10, 11], a MATLAB program was developed to compute HI and S_r indices. The total number of AE hits recorded during fracture process in specimen RF2 were separated channel-wise to execute ISA of AE. The loading stages are divided into 4 intervals namely 0 - $0.2P_{max}$, 0 - $0.5P_{max}$, 0 - $0.8P_{max}$ and 0 - P_{max} , where P_{max} indicates peak load. Subsequently, the AE hits for each channel are separated from N_{total} (N_{total} refers to total number of hits recorded from 0 - P_{max}). The first loading stage (0 - $0.2P_{max}$) and the hits corresponding to this stage are considered. By using Table 2, the expression $\sum_{i=K+1}^N S_{oi}$ is computed. The values of K and J are then computed based on N . This is followed by computing the expression $\sum_{i=1}^N S_{oi}$. The values of HI and S_r are then calculated by following Eq. 2 and Eq. 3 respectively. In fact, S_r is the mean of the first fifty AE signal strength values of hits of the corresponding interval arranged in descending order. The same process should be repeated for the other loading stages namely 0 - $0.5P_{max}$, 0 - $0.8P_{max}$ and

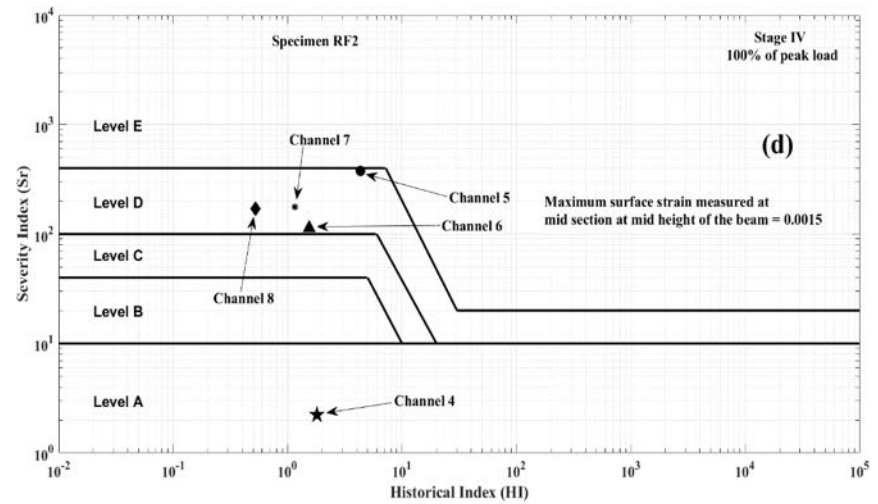
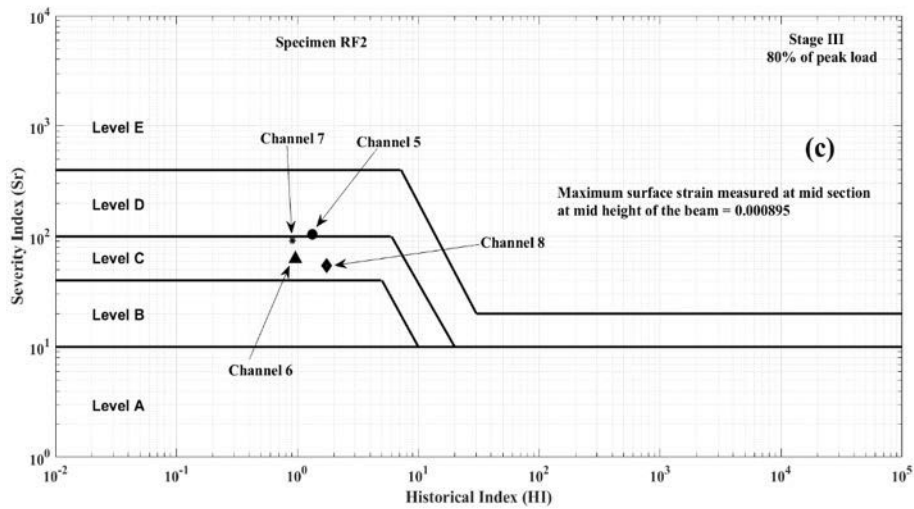
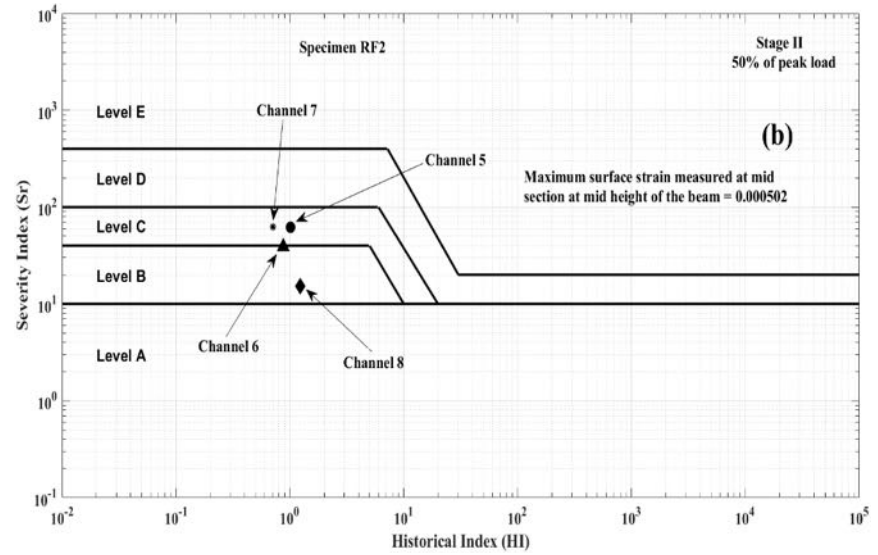
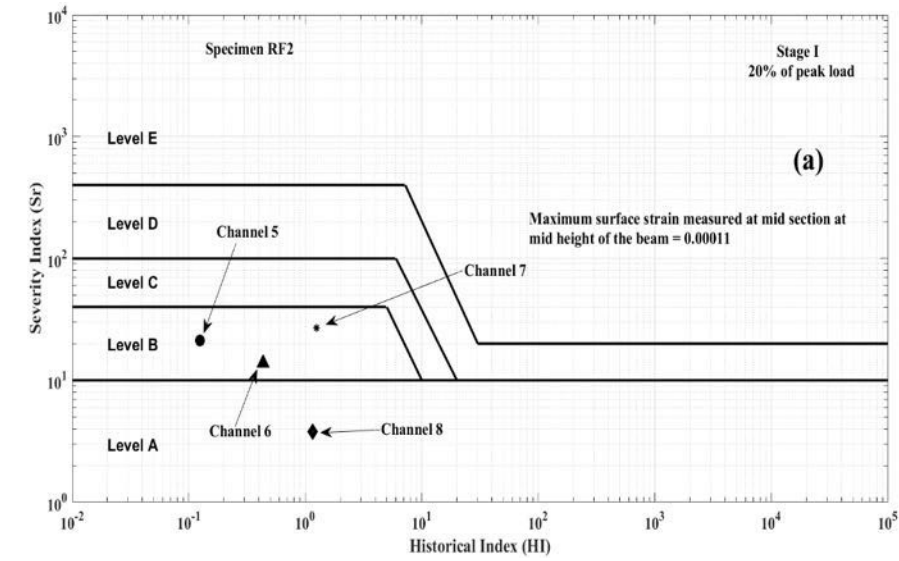


Fig. 8. Intensity signal analysis of AE up to (a) 20%; (b) 50%; (c) 80%; (d) 100% of peak load for specimen RF2.

0 - P_{max} . After computing HI and S_r for each loading interval, a log-log graph between HI and S_r is plotted and five levels of damage are introduced.

The AE indices HI and S_r are computed for the generated AE. By following IS 456-2000, the *in-service* design load for the beam RF2 is 52.26 kN [14]. From Fig. 8a, it can be observed that Channel - 5, Channel - 6 and Channel - 7 fall in Level - B at 20% of peak load which indicates minor surface defects whereas Channel - 8 falls in Level - A. The maximum surface strain in concrete recorded at mid-span (Section - II) at this level of loading is 0.00011 as shown in Fig. 8a. Upon increasing the loading level to 50% of peak load, Channel - 5 and Channel - 7 now moved to Level - C and Channel - 8 moved to Level - B as shown in Fig. 8b. The reason could be the fracture process is relatively more severe compared with previous level of loading (0 - 20% of peak load). The surface strain at this level at Section - II is 0.000502. At 80% of peak load, Channel - 5 just reached Level - D which indicates major damage in its vicinity and the other channels were at Level - C as shown in Fig. 8c. The surface strain at mid-span (Section - II) at this load level is 0.000895. Upon reaching the peak load, as can be observed from Fig. 8d, Channel - 4 reached Level - A indicating no damage in its surrounding whereas the other channels reached Level - D indicating major damages occurring in various locations of the beam and need follow up inspection. The strain at peak load at Section - II is 0.001523. Even though Channel - 4 is at mid-span, it didn't record noticeable number of AE signals because the AE sensor got detached from the test specimen in the middle of the experiment. Figure 9a shows variation of load with surface strain for RF2. The crushing of concrete at mid-section can be observed from Fig. 9b. The UPV in

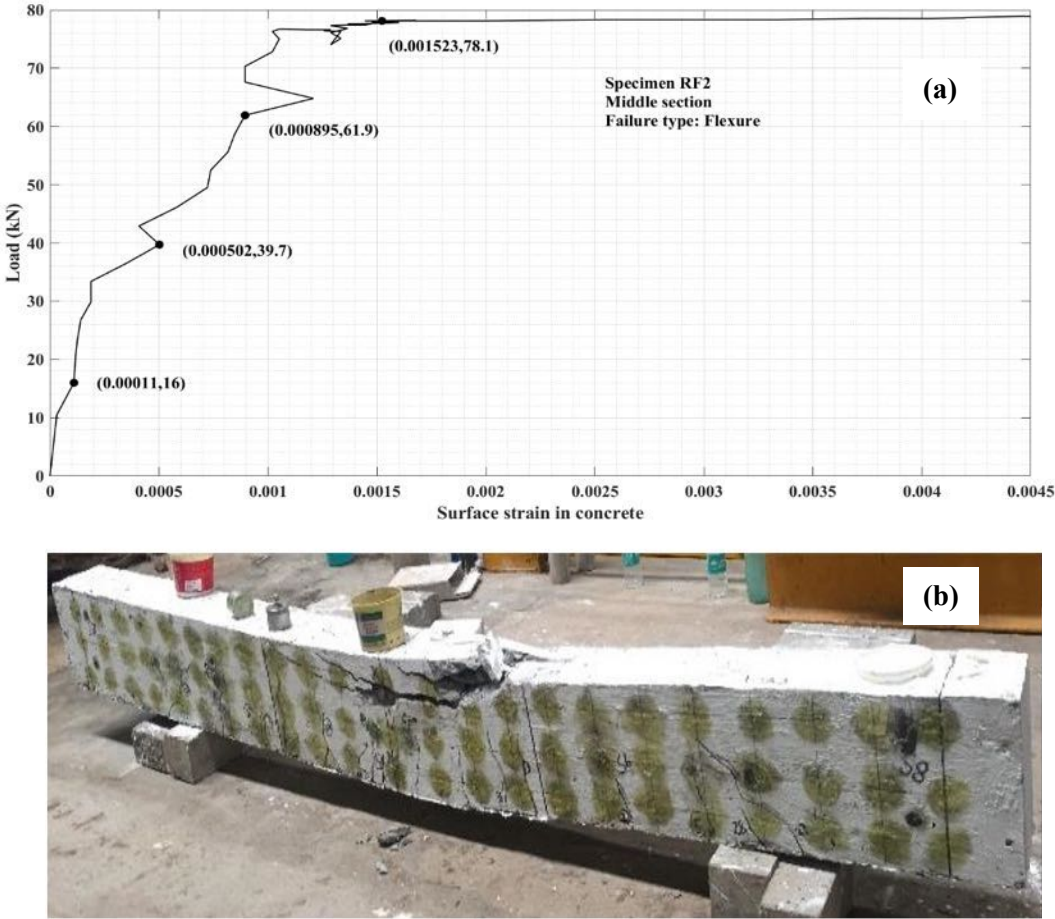


Fig. 9. (a) Variation of load with surface strain for RF2; (b) RC beam RF2 after experiment.

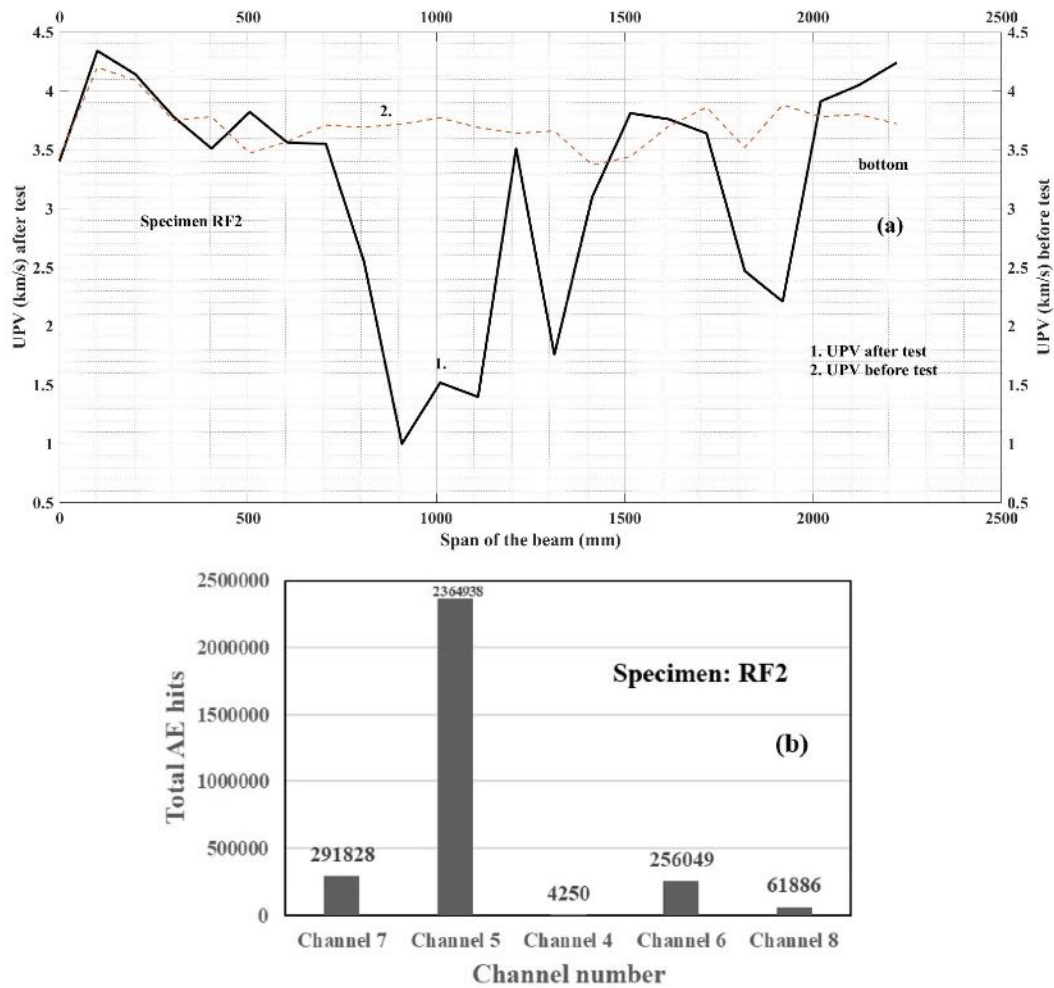


Fig. 10. (a) Variation of UPV along the span of the beam RF2; (b) AE hits recorded by sensors mounted on specimen RF2.

specimen RF2 before damage is approximately equal to 3.8 km/s and this reflects good quality of concrete as per IS: 516 (Part 5/ Sec 1): 2018: Hardened concrete - methods of test as shown in Fig. 10a [15]. Only the bottom row was chosen because the UPV values before testing did not show considerable fluctuation whereas the top and middle rows showed significant fluctuation in the UPV values before testing. The changes in UPV values along the span and the channel-wise AE hits recorded are shown in Fig. 10a and Fig. 10b respectively [16]. It is interesting to note that the channel location where maximum damage occurred, UPV decreased to a minimum value. The reason could be when an ultrasonic pulse travels through a concrete-air interface, there is negligible transmission of sound energy across this interface. Thus, any air-filled void or crack lying between ultrasonic pulse transmitter and receiver obstructs the transmission of ultrasonic pulse, when the projected length of the void/crack is greater than the width of transducer and the wavelength of the ultrasonic pulse in concrete [17]. When this happens, the first ultrasonic pulse to arrive at receiving transducer is diffracted around the periphery of the crack/void. It results in the increase of transit time. Hence UPV decreased due to development of crack. Figs. 11a-d shows the results of ISA of AE related to specimen RF1. Specimen RF2 was tested at a higher loading rate than specimen RF1. The in-service design load for beam RF1 is 58.25 kN [14]. Fig. 12 shows the surface strain at mid-span at mid height of the beam (Section - II). The strain at peak load is 0.0028 as can be seen from Fig. 12. The specimen started yielding when the surface strain reached 0.002823 at

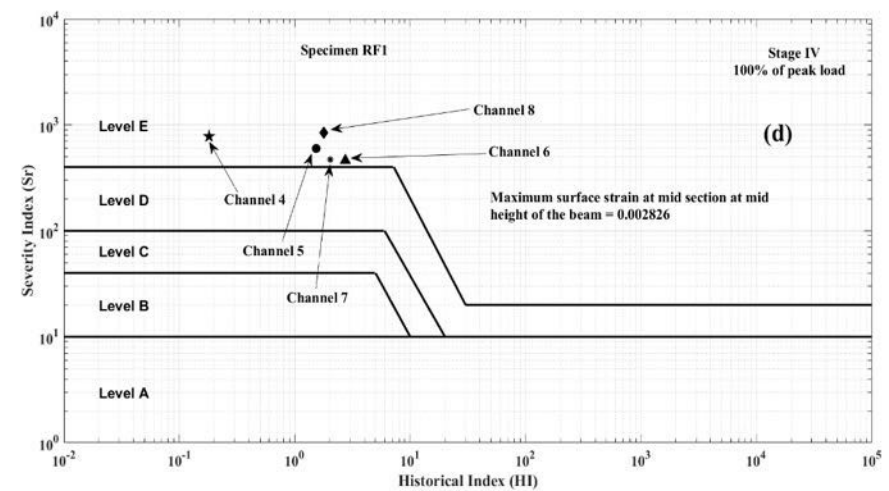
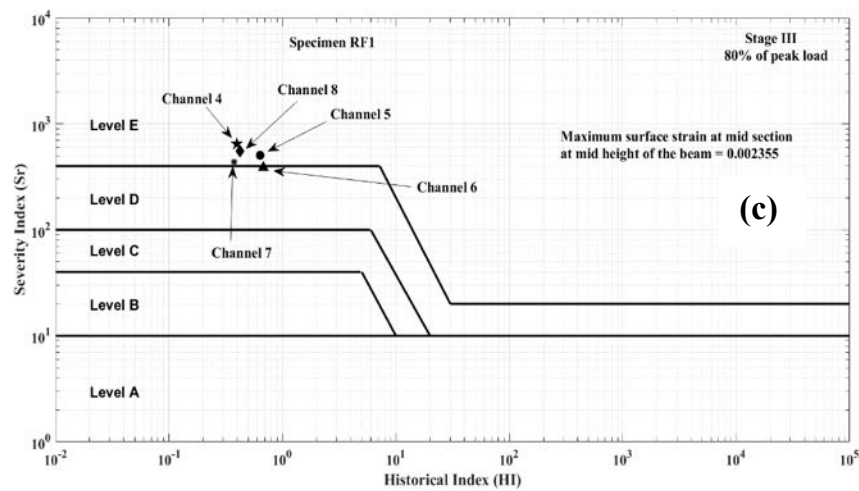
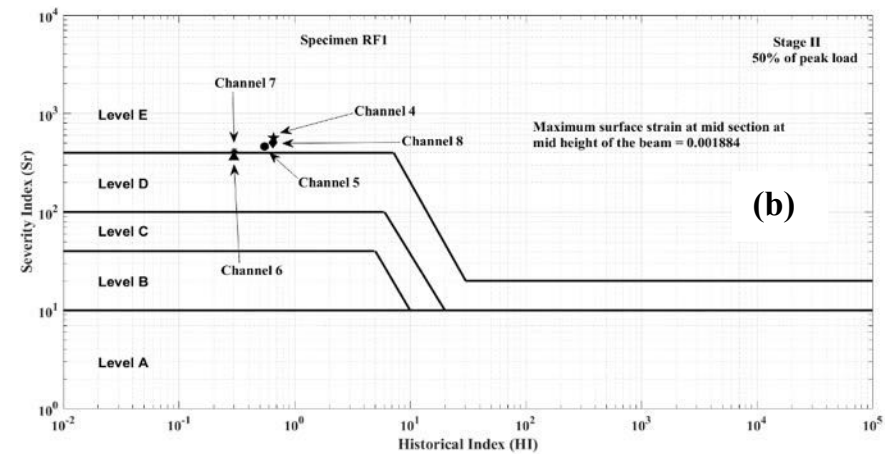
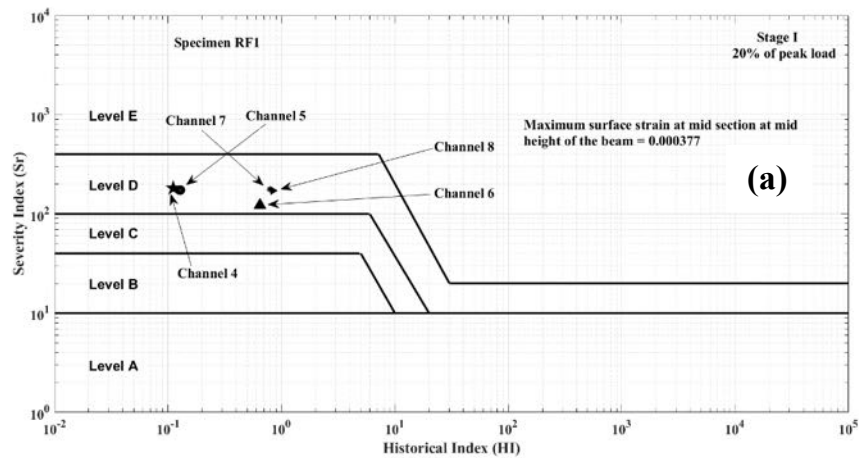


Fig. 11. Intensity signal analysis of AE up to (a) 20%; (b) 50%; (c) 80%; (d) 100% of peak load for specimen RF1.

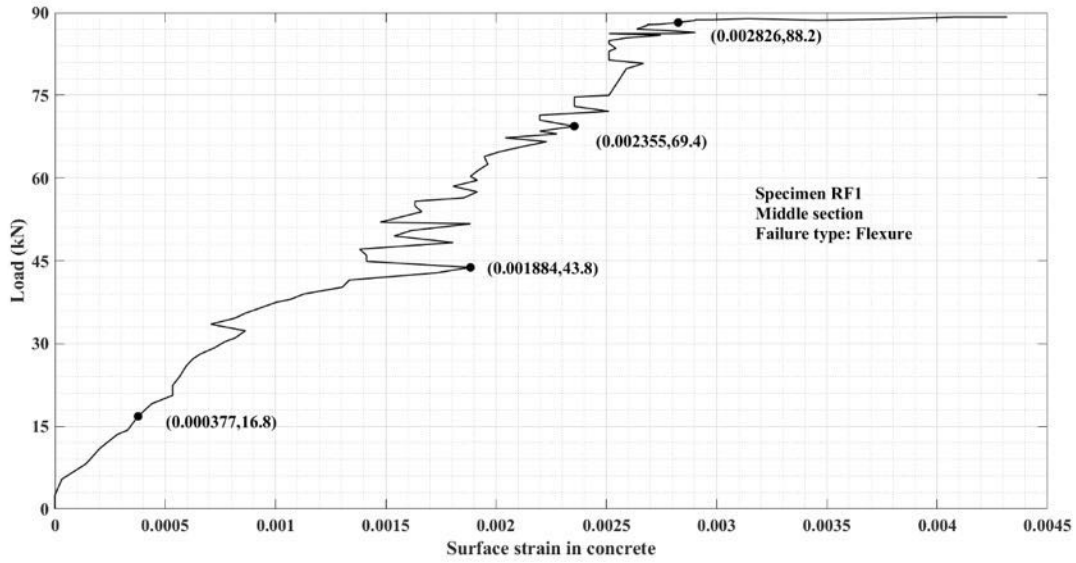


Fig. 12. Variation of load with surface strain for RF1.

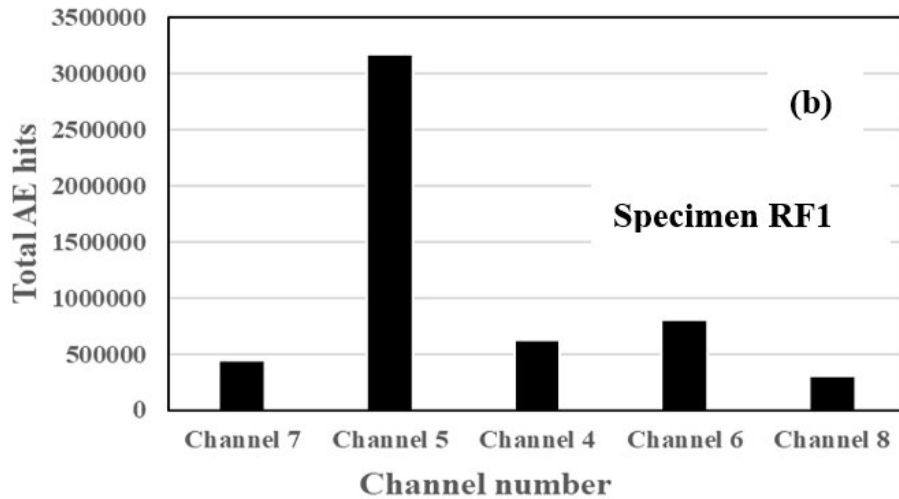
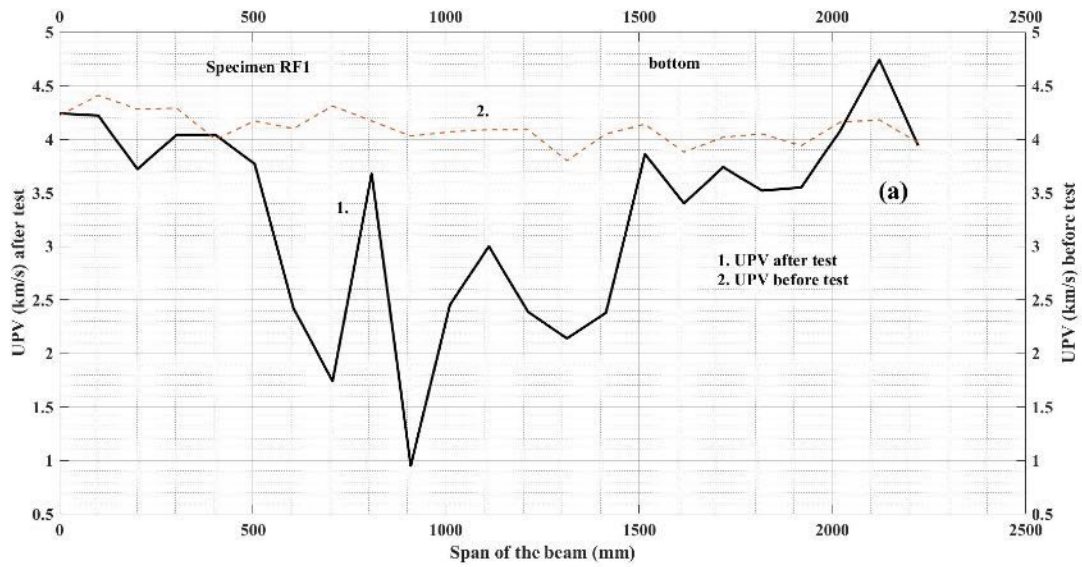


Fig. 13. (a) Variation of UPV along the span of the beam RF1; (b) AE hits recorded by sensors mounted on specimen RF1.

Section - II. In specimen RF1, the UPV along the span of the beam for the bottom row is 4 km/s before damage as shown in Fig. 13a. The UPV values before testing for top and middle rows showed high fluctuation. The UPV reduced considerably in the region near Channel - 5 as can be observed from Fig. 13a. This can be confirmed from Fig. 13b where it can be observed that maximum number of hits were also recorded by Channel - 5 and it reached Level - E as shown in Fig. 11d.

The surface strain in concrete is maximum at Section - II in case of specimens RF1 and RF2. The reason could be maximum bending moment takes place at Section - II. However, for specimens RS2 and RS1, the maximum surface strains were observed at Section - I and Section - III, respectively.

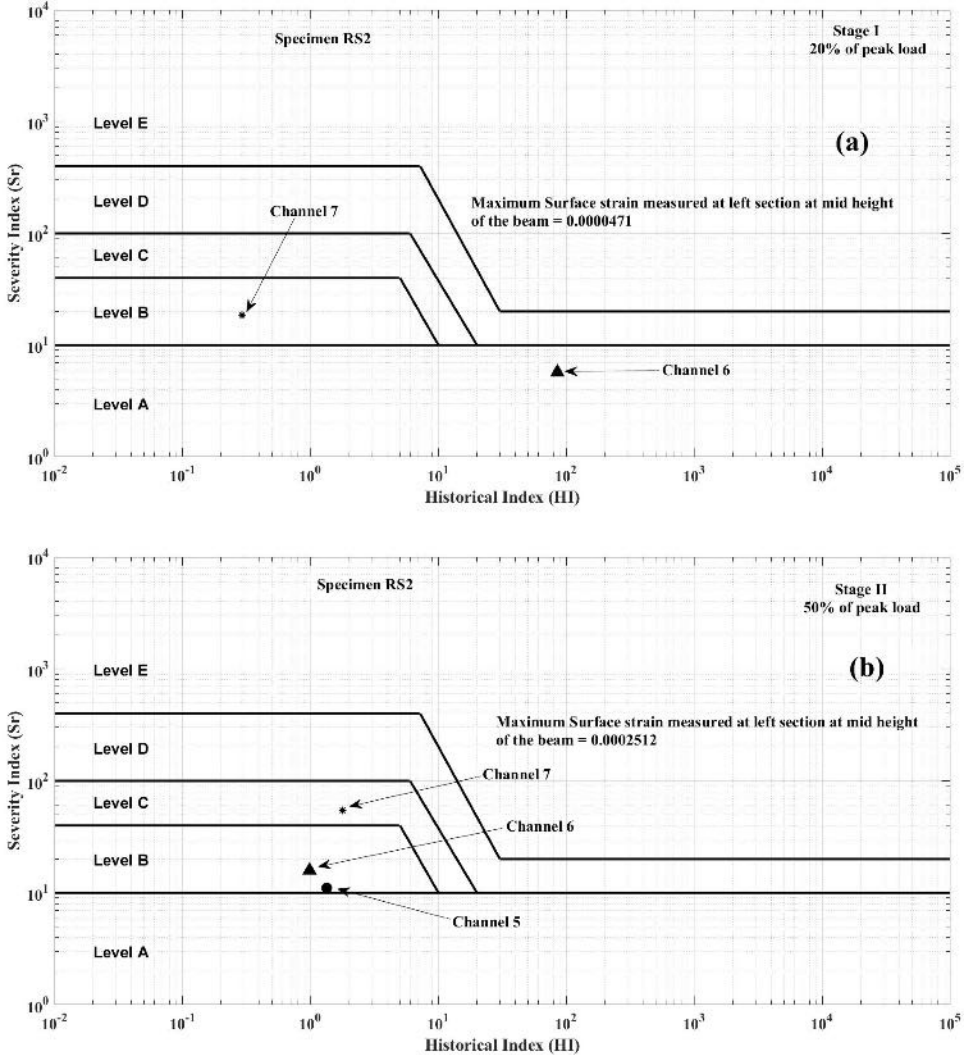


Fig. 14. Intensity signal analysis of AE up to (a) 20%; (b) 50% of peak load for specimen RS2.

3.2 Damage assessment in RC beams without shear reinforcement using ISA of AE

The total number of AE hits were separated channel-wise for specimen RS2 to implement ISA of AE. The in-service design load for beam RS2 is 53.4 kN [14]. From Fig. 14a, it can be observed that Channel - 7 falls in Level - B at 20% of peak load which indicates minor surface defects whereas Channel - 6 falls in Level - A indicating smaller number of AE hits recorded in that region.

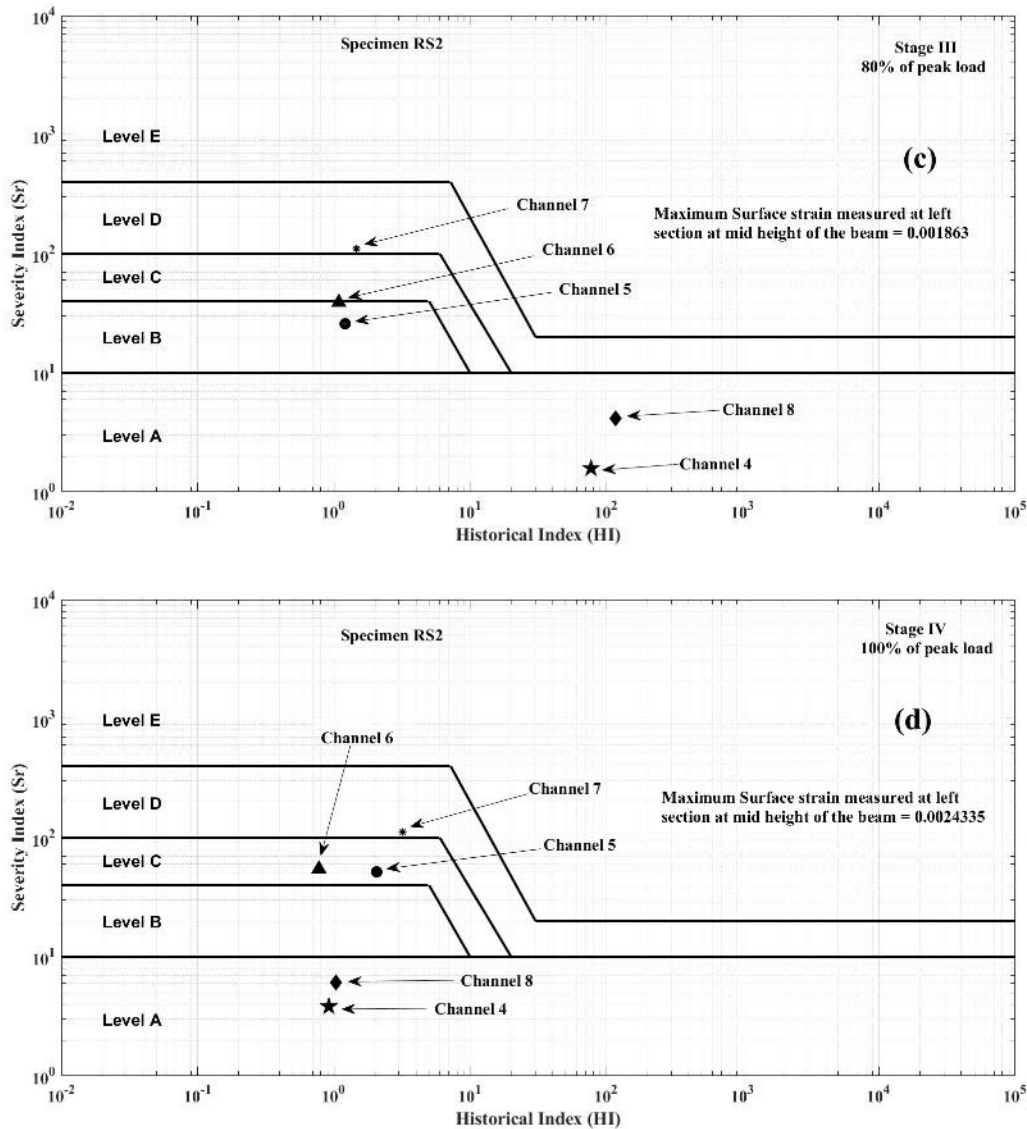


Fig. 14. Intensity signal analysis of AE up to (c) 80%; (d) 100% of peak load for specimen RS2.

At this level of loading only Channel - 6 and Channel - 7 recorded sufficient AE to compute HI and S_r . The other channels namely Channel - 8, Channel - 4, Channel - 5 have not recorded sufficient AE to compute HI and S_r . The reason could be because of negligible fracture process around those sensors. At 20% of peak load, the maximum strain at section near to left side support (Section - I) is 0.0000471 as shown in Fig. 14a. Upon increasing the loading level to 50% of peakload, Channel - 7 moved to Level - C as shown in Fig. 14b. Channel - 5 and Channel - 6 now fell in Level - B. The surface strain in concrete at this loading level at Section - I is 0.0002512. At 80% of peak load, Channel -7 just reached Level - D while Channel - 6 and Channel - 5 reached the upper reaches of Level - B as shown in Fig. 14c while Channel - 4 and Channel - 8 entered Level - A. The surface strain in concrete measured at Section - I was 0.001863 as shown in Fig. 15a. Upon reaching the peak load, Channel - 7 remained at Level - D whereas Channel - 5 and Channel - 6 reached Level - B. However, Channel - 4 and Channel - 8 remained at Level - A, indicating insignificant AE activity. The maximum surface strain in concrete measured at Section - I was 0.0024 and the specimen collapsed suddenly with the formation of a major diagonal crack

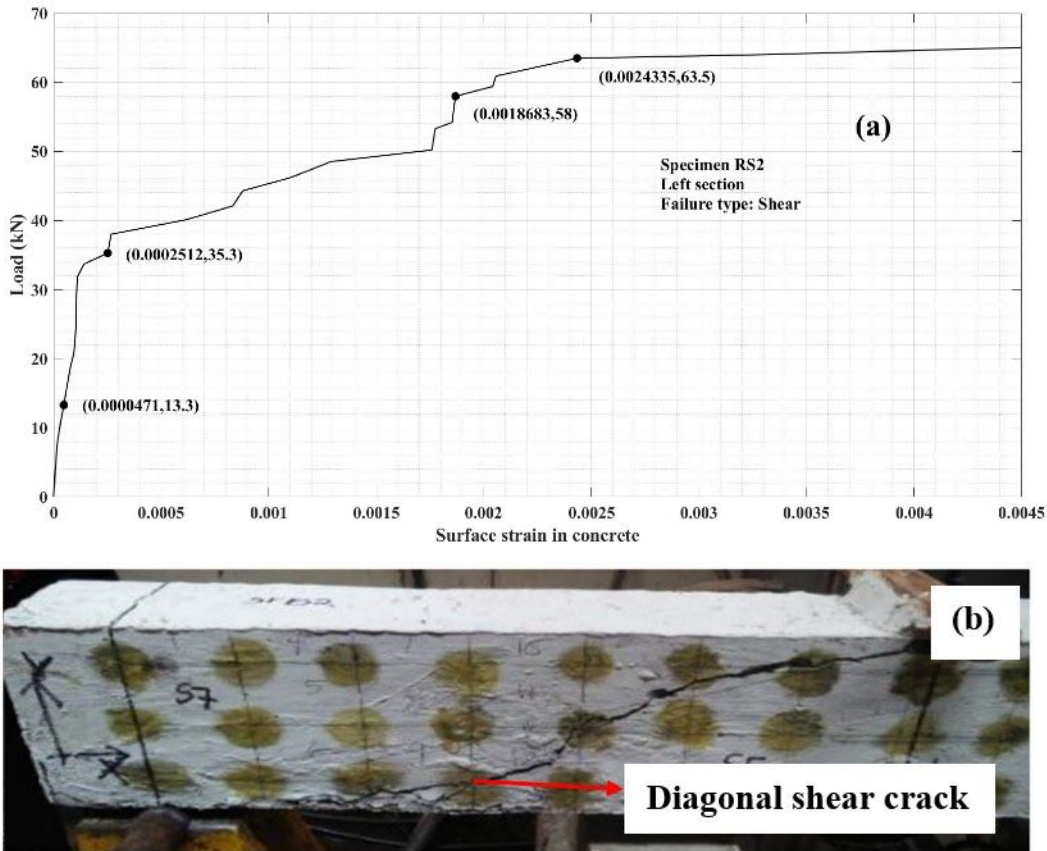


Fig. 15 (a) Variation of load with strain for specimen RS2; (b) Developed diagonal shear crack in Specimen RS2.

as shown in Fig. 15b. Also, the UPV suddenly decreased at the location where the major diagonal shear crack was formed as shown in Fig 16a. Only the middle row is shown because the UPV before test values showed very high fluctuation for the other two rows. Due to the presence of crack near to Channel - 5, AE activity was high as shown in Fig. 16b. At the same location, UPV attained its minimum value.

Figure 17 shows ISA of AE plots for specimen RS1. The in-service design load for beam RS1 is 47.6 kN [14]. Specimen RS1 was tested under displacement control at a rate of 0.04 mm/s. However, Specimen RS2 was tested at a lower rate of 0.005 mm/s. From the beginning of the experiment till 20% of peak load, sufficient AE was not recorded to compute HI and S_r indices as the rate of loading was relatively higher. From Fig. 17a, it can be observed that Channel - 4, Channel - 6 and Channel - 8 fall in Level - B at 50% of peak load whereas Channel - 7 and Channel - 5 fall in Level - C. From Fig. 17b, upon increasing loading level to 80% of peak load, it can be observed that Channel - 4, Channel - 6, and Channel - 8 move to Level - C whereas the other channels remained at Level - C. Upon reaching peak load, Channel - 6 and Channel - 8 move to Level - E which indicates propagation of a macro crack and indicates severe damage in the RC beam as shown in Fig. 17c. The remaining channels fell in Level - D which indicates significant damage in the regions around those channels. It is known that irreversible changes are the cause behind generation of AE during fracture process in solids [1-5]. In case of RC structures, the changes are micro cracking initiation, coalescence of microcracks, propagation of crack, debonding between steel bar and surrounding concrete. The fracture process of concrete is a

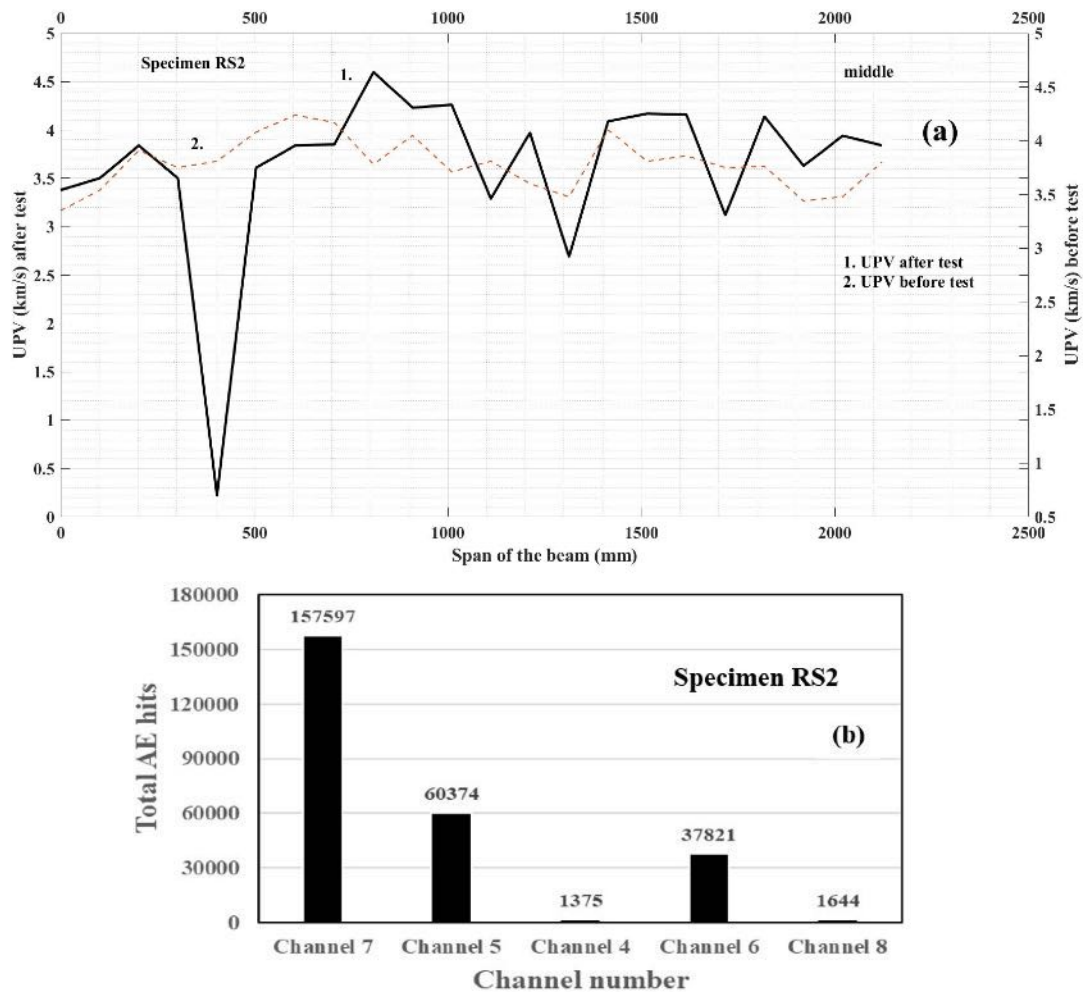
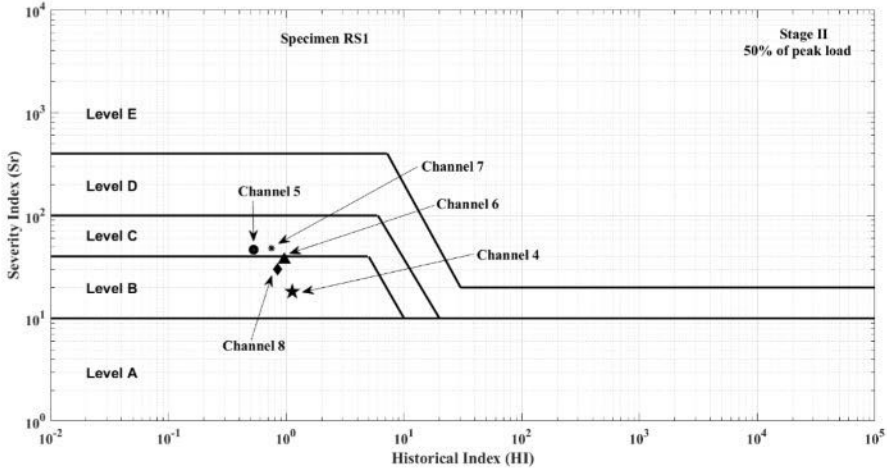
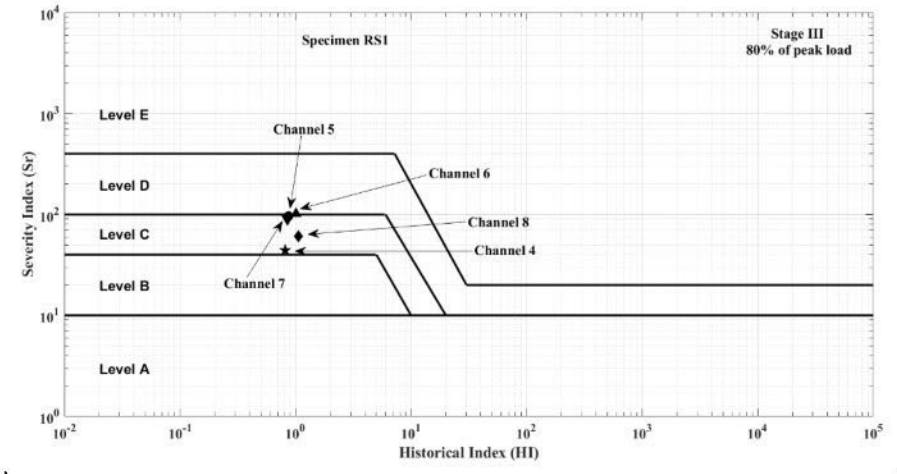


Fig. 16 (a) Variation of UPV along the span of the beam RS2; (b) AE hits recorded by sensors mounted on specimen RS2.

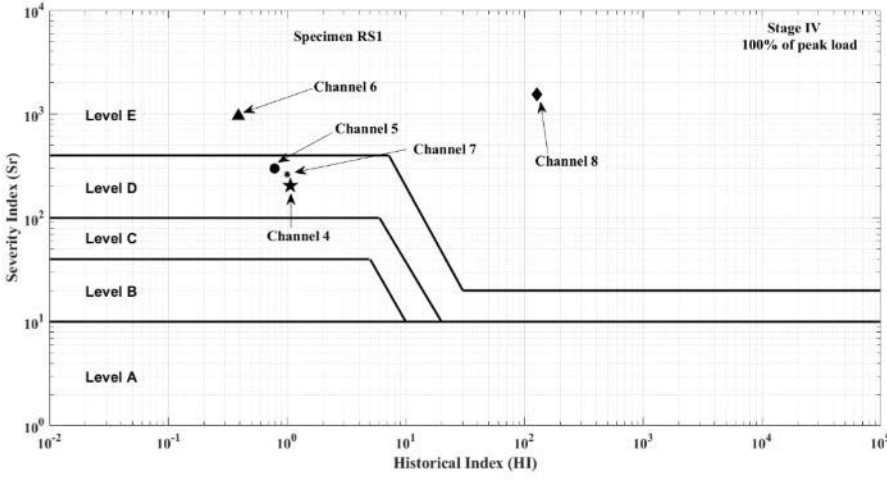
complex phenomenon and depends on several parameters [18]. In case of hardened concrete, fracture process depends on tensile stresses developed in concrete. The tensile stresses vary from point to point in concrete medium. In the present case, in specimen RS1, diagonal crack developed near the right support (Section - III). At the same location where major diagonal crack developed, Channel - 6 was present. It is interesting to note that UPV value is nearly 4 km/s along the span of the beam before damage occurred in the specimen. Due to the damage in the beam after the fracture process, values in the top and middle rows could not be recorded properly and hence only the bottom row values are shown. However, the UPV drastically reduced at same location as shown in Fig. 18a where diagonal crack developed. Even though Channel - 4 recorded maximum number of AE hits, the amplitude of those hits is low as shown in Fig. 18b. It is also observed that a greater number of low amplitude AE hits are recorded than high amplitude hits during the fracture process in specimens which reflects the Gutenberg - Richter empirical relation [19, 20]. The diagonal shear crack that was developed in the specimen RS1 is shown in Fig. 18c. Although this observation is known, it confirms previous researchers' observation [16]. The observations provide a reference for conducting non-destructive testing of RC structures in laboratory.



a)



b)



c)

Fig. 17. Intensity signal analysis of AE up to (a) 50%; (b) 80%; (c) 100% of peak load for specimen RS1.

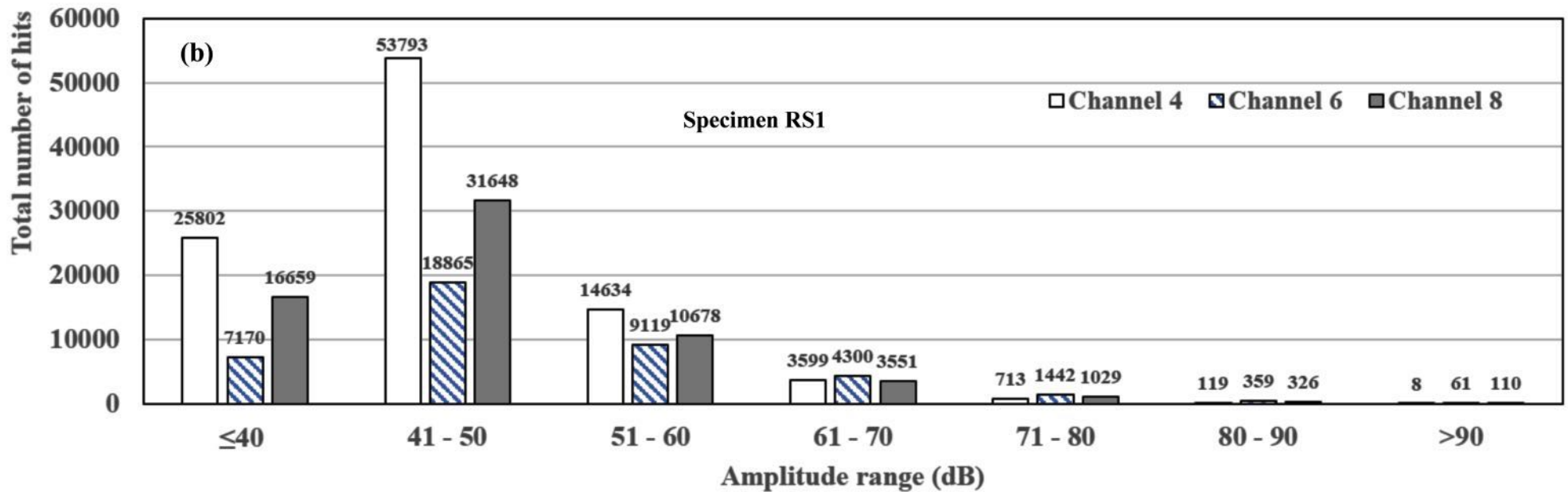
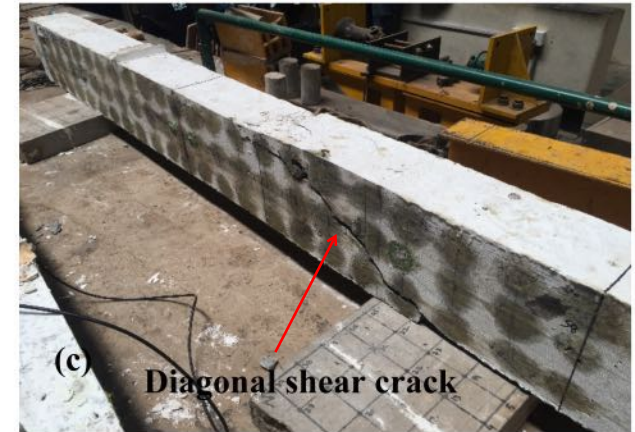
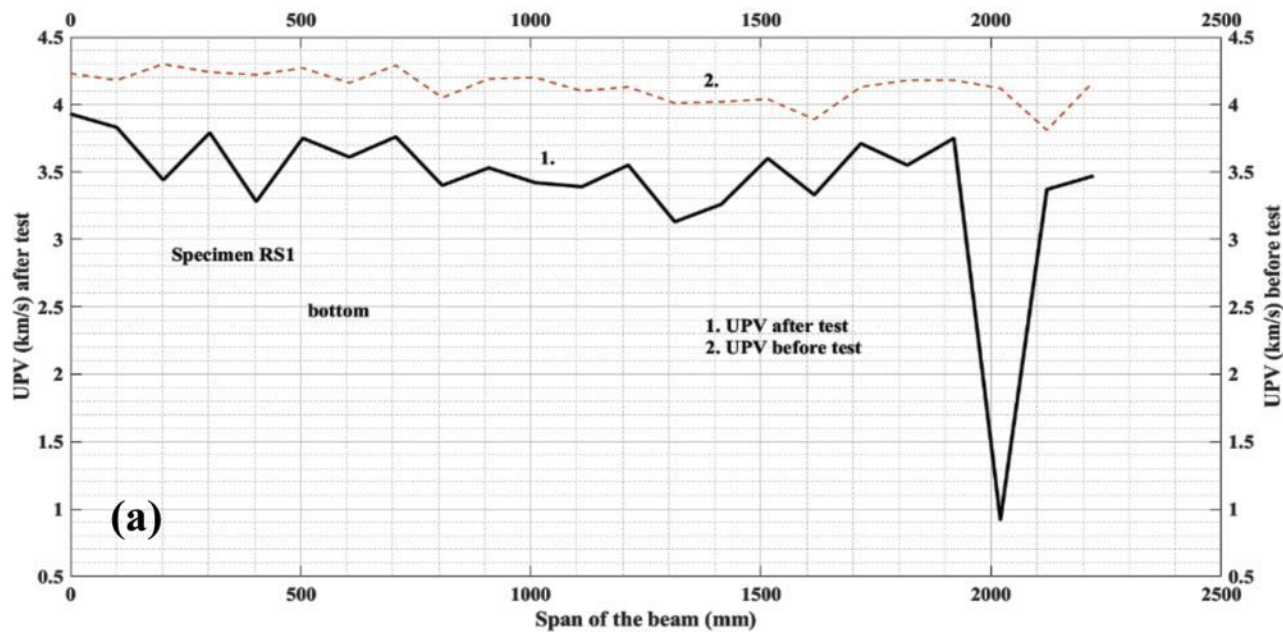


Fig. 18. (a) Variation of UPV along the span of the beam RS1; (b) Number of hits recorded and corresponding amplitude distribution for Channels 4, 6 and 8 related to Specimen RS1; (c) Developed diagonal shear crack in Specimen RS1.

3.3 Practical Significance

Generally, in a RC structure, beams transfer the loads along their length from floors and slabs to columns. The damage assessment of these structural elements is important as cracking affects structural performance such as serviceability and durability. After few years of service, in these RC structural members, damage takes place due to aging, environmental conditions, and heavy loads. The ISA of AE is a suitable NDT method to assess damage in existing RC structures. By connecting surface strain in concrete with damage level assessed using ISA of AE, the confidence level on this method increases.

4. Conclusions

The above experimental study primarily focused on ISA of AE to understand the damage which developed in the presence and absence of shear reinforcement in the RC beams. The major conclusions are given below.

1. At collapse, higher energy AE signals are released for the RC beams without shear reinforcement than the beams with shear reinforcement. The reason could be due to sudden development of major diagonal shear crack due to lack of shear reinforcement.
2. More AE is generated in RC beam specimens with shear reinforcement and less in RC beam specimens without shear reinforcement. RC beam specimen without shear reinforcement failed quickly. But RC beam specimen with shear reinforcement failed gradually and exhibited elasto-plastic behaviour.
3. As surface strain in concrete increased during the fracture process, the damage reached higher levels. At the location where the UPV value reduced significantly, the AE sensor present near the same location recorded maximum AE hits.

By connecting the surface strain in concrete of the RC beams and the damage level, the results of ISA method can be relied upon. Hence, ISA of AE is a useful method for assessing the safety and integrity of RC structures in a laboratory.

References

1. C.U. Gross, M. Ohtsu, eds. (2008), *Acoustic Emission Testing*, Springer-Verlag, Berlin, Germany.
2. M. Ohtsu (1998) Basics of acoustic emission and applications to concrete engineering, *Mater. Sci. and Res. Int.*, 4, 131-140.
3. RILEM TC 212-acd (2010a), Acoustic emission and related NDE techniques for crack detection and damage evaluation in concrete, Measurement method for acoustic emission signals in concrete, *Mater. and Struct.*, 43, 1177-1181.
4. RILEM TC 212-acd (2010b), Acoustic emission and related NDE techniques for crack detection and damage evaluation in concrete, Test Method for damage qualification of reinforced concrete beams by AE, *Mater. and Struct.* 43, 1183-1186.
5. RILEM TC 212-acd (2010c), Acoustic emission and related NDE techniques for crack detection and damage evaluation in concrete, Test method for classification of active cracks in concrete structures by acoustic emission, *Mater. and Struct.* 43, 1187-1189.
6. A. Behnia, H. K. Chai, T. Shiotani (2014). Advanced structural health monitoring of concrete structures with the aid of acoustic emission. *Constr. Build. Mater.* 65, 282-302.

7. T.J. Fowler, J.A. Blessing and P.J. Conlisk, New directions in testing, Proc. 3rd International Symposium on AE from Composite Materials, Paris, France, 1989.
8. J. A. Blessing, T. J. Fowler and F. E. Strauser. Intensity analysis. In: Proc., 4th International Symposium on AE from Composite Materials, Seattle, Washington, USA, 27 - 31 July 1992, ASNT, Columbus, Ohio, USA.
9. L. Golaski, P. Gebiski and K. Ono (2002). Diagnostics of reinforced concrete bridges by acoustic emission, *J. Acoust. Emiss.* 20, 83-98.
10. A. Nair and C.S Cai (2010). Acoustic emission monitoring of bridges: Review and case studies., *Eng. Struct.*, 32, 1704-1714.
11. S. Shahidan, R. Pullin, M.N. Norazura and K. Holford (2013). Damage classification in reinforced concrete beam by acoustic emission signal analysis, *Constr. Build. Mater.*, 45, 78-86.
12. A. Panjsetooni, N.M. Bunnori, A.H. Vakili, Z. Shirkhani, Z. Shirkhani (2013). Fracture formation evaluation of reinforced concrete structure using acoustic emission technique, *Chin. J. Eng.*, Volume 2013, Article ID 126509, doi.org/10.1155/2013/126509.
13. A.A. Pollock (2014). AE signal features: energy, signal strength, absolute energy and RMS. TN-103-22-9/11, MISTRAS Group, Princeton Junction, NJ, USA.
14. BIS (Bureau of Indian Standards). July 2000. *Plain and Reinforced Concrete- Code of Practice*. IS:456. New Delhi, India.
15. BIS (Bureau of Indian Standards). 2018. *Ultrasonic Pulse Velocity Testing*. IS:516 (Part 5/ Sec 1). New Delhi, India.
16. T. Shiotani, D.G. Aggelis and O. Makishima (2009). Global monitoring of large concrete structures using acoustic emission and ultrasonic techniques: case study, *ASCE J. of Brid. Eng.*, 14(3), 188-192. [https://doi.org/10.1061/\(ASCE\)1084-0702\(2009\)14:3\(188\)](https://doi.org/10.1061/(ASCE)1084-0702(2009)14:3(188)).
17. V.M. Malhotra and N. J. Carino (2004). *Handbook on Nondestructive Testing of Concrete*, CRC Press/ASTM International, PA, USA.
18. B.L. Karihaloo (1995). *Fracture Mechanics and Structural Concrete*, Longman Scientific and Technical, NY, USA.
19. A. Carpinteri, G. Lacidogna and N. Pugno (2006). Richter's laws at the laboratory scale interpreted by acoustic emission, *Magazine of Concrete Research*, 58(9), 619-625.
20. R. Vidya Sagar (2018). Acoustic emission signal 'peak amplitude-distribution' analysis related to concrete fracture under uniaxial compression, *Challenge J. Concrete Research Letters*, 9 (3), 85–102. <https://doi.org/10.20528/cjcr.2018.03.003>.



E-GLEA 10

ACTAS de Trabajos Completos

GRUPO LATINOAMERICANO
de
EMISION ACUSTICA **GLEA**

Décimo Encuentro Internacional del
Grupo Latinoamericano de Emisión Acústica

14-16 de agosto de 2019

Facultad de Ingeniería, Universidad Nacional del Comahue

UnCo, Neuquén

NEUQUÉN, ARGENTINA

ISBN 978-987-1323-65-4



COMISIÓN NACIONAL
DE ENERGÍA ATÓMICA

Selected Papers from the Proceedings of E-GLEA-10

Basgall A., Ferrari, G., and Gómez, M.P., Neural Networks applied to the monitoring of drilling processes in geological material samples, *J. Acoust. Emiss.* **37**, 2020, S1-S10

Bonelli Toro, A. G., Gómez M. P., Machine learning applied to acoustic emission for tool wear classification during milling of composite materials, *J. Acoust. Emiss.* **37**, 2020, S11-S20

Groth, E. B., Shumacher, G., Idzi J., Rojo Tanzi, B. N., Clarke, T. G. R., Lima, T. R. S. and Jacques, R. C., Acoustic emission numerical analysis applied to structural health monitoring of laminar structures (Guided waves), *J. Acoust. Emiss.* **37**, 2020, S21-S29

da Silva, D.S., Groth, E.B., Walter, J.S., Lutckmeier, F., Zuglian, G. F., Jaques, R. C., de Lima, T.R.S. and Clarke, T.G., Study of fiber Bragg gratings (FBG) as acoustic emission sensor to inspect and monitoring fiber-glass reinforced polymers (FGRP) degradation, *J. Acoust. Emiss.* **37**, 2020, S30-S37

Veca, A. C., Valesse, N., Ruzzante, J., Albalat, A., Marino, A., and Reyes Reyes, M. V., Autonomous acoustic system for passive acoustic monitoring of cetaceans, *J. Acoust. Emiss.* **37**, 2020, S38-S54.

Zitto, M.E., Sassano, M.P., Muszkats, J.P., Filipussi, D.A., and Piotrkowski, R., Energy and shannon entropy in acoustic emission signals for damage evaluation in andesite rock, *J. Acoust. Emiss.* **37**, 2020, S55-S64

López Pumarega, M. I., Ruzzante, J. E., and Gómez, M. P., La Emisión Acústica, su Historia en la Argentina, *J. Acoust. Emiss.* **37**, 2020, S65-S76. (in Spanish)

Contents of the Proceedings of E-GLEA 10 (Índice)

Topical Editors

José Ruzzante and Antolino Gallego

Neural Networks applied to the Monitoring of Drilling Processes in Geological Material Samples

Basgall, A.^a, Ferrari, G.^a, Gómez, M.P.^{a,b}

^a Grupo de Emisión Acústica, Facultad Regional Delta, Universidad Tecnológica Nacional, San Martín 1171, Campana, Buenos Aires, ARGENTINA.

^b Grupo de Ondas Elásticas – Proyecto ICES, Comisión Nacional de Energía Atómica, Av. Gral. Paz 1499, San Martín (1650), Buenos Aires, ARGENTINA. e-mail: angelbasgall@hotmail.com

ABSTRACT

An Artificial Neural Network (ANN) is a mathematical computational model that, in a limited way, attempts to mimic the structure and functioning of biological neurons which, broadly speaking, take electrical input signals and produce an output signal called “response”. By combining many artificial neurons, they can have the ability to “learn” specific patterns in signal analysis and predict results. These networks can be used in a wide range of applications such as object or signal classification, function approximation, autonomous driving, speech recognition, image or text analysis and processing, etc. Self-Organized Map (SOM) or Kohonen ANN perform a weighted summation of multidimensional input data, which are individually affected by a numerical value called weight. Then, in a competition between neurons, a winner is selected, and a neighborhood weight is adjusted to generate an output more similar to the input. This generates a two-dimensional map where the information is shown organized in areas that have similar characteristics. The weights of each neuron are modified continuously and in different ways during several “epochs” (epoch is the name given to each step of weighting adjustment) until the response error is minimized. This process is called training, where specifically for this network, it is an unsupervised type of learning. In this work, SOM ANNs are used to study acoustic emission (AE) signals from a drilling process of geological materials arranged in layers bonded with cementitious material. With these elements, Laboratory size specimens (320x320x400 mm) were made. Drilling was carried out with 62 mm diameter drills, with single-wire tungsten carbide inserts, making four holes per multilayer specimen, and the AE was measured during each drilling. After a detailed training process and rigorous data selection, this ANN showed the ability to recognize the different layers of each specimen from the processing of the AE signals obtained during the drilling process.

Keywords: Artificial Neural Network, acoustic emission, Drilling, geological materials.

1. INTRODUCTION

An Artificial Neural Network (ANN) is a modest mathematical computational model based on its biological homologues, which receive electrical impulses in their dendrites (input) which are then processed in the body (body of the neuron) and produce an electrical impulse that travels through the axon (output) and connects with nearby neuron dendrites through chemical neurotransmitters (weight) that modulate the signal. [Beale et al. 2020] [Zupan and Gasteiger, 1993].

Once a mathematical model that models the basic functions of an individual biological neuron is established, we can combine a large number of these until we acquire the ability to “learn” specific patterns and infer results. These networks can be used in applications such as autonomous conduction [Yáñez-Badillo H., 2017] [Faheem, 2013], image analysis and treatment [Su, 2019], and others [Boldsaikhana, 2011] [Fratini, 2009].

In the present study, a self-organized map or Kohonen ANN was used [Kohonen, 2001]. This network is characterized by an unsupervised learning, which means that the network automatically adjusts to the input values without any type of positive or negative stimulation by the user. This type of network results in a two-dimensional map independent of the number of input parameters. A Kohonen neural network performs multidimensional to two-dimensional scaling. The resulting map shows the neurons that determine areas of similarity,

of which the topology, i.e. the distribution of information with similar characteristics, can be analysed. In this way, a form of easier interpretation is reached for an observer.

This type of ANN contains many parameters to be defined, with the aim of achieving correct learning of the existing patterns in the data set. Important aspects to consider when "designing" and optimizing Kohonen ANN include the kind of learning, the number of neurons (expressed as an $M \times N$ matrix), weight correction, the topology, the geometry of the network, and the training epochs.

One of the ways to define an information learning rule is by comparing the outputs of all the neurons with the input data and defining as "winning neuron" the one with the weight closest to the input data. Once the winning neuron has been selected, the weights of that neuron and its neighbors are adjusted so that they are more similar to that type of data. The correction function of the neuron weights and its neighbors is the way in which an adjustment factor is distributed in each neuron, generally this value has a high correction in the winner and decreases as it moves away from it. The most common adjustment functions can be constant, Gaussian, linear, etc.

Topology is defined as the way in which each neuron interacts with its neighbors, defining the amount of individual communications. This can be seen in Fig. 1 where different arrangements are represented with different number of neuron neighbors are represented.

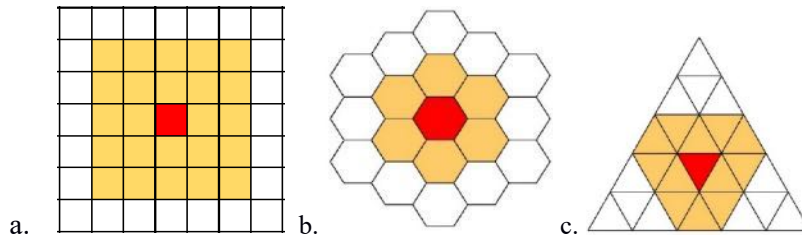


Fig. 1. a. Orthogonal distribution, b. Honeycomb Distribution, c. Triangular Distribution.

The network geometry establishes the behavior of the neighborhood when it is within the boundaries. It can be modelled in plane, tubular or toroid form (Fig. 2 a, b, c) which is then represented on a two-dimensional map as shown in the planar view of Figure 3 for a tubular and a toroidal geometry.

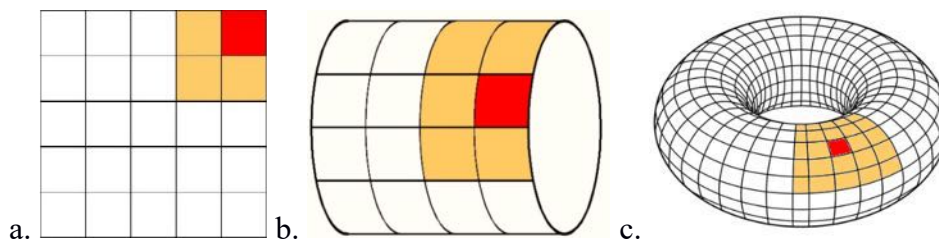


Fig. 2. a. Plane Geometry, b. Tubular Geometry, c. Toroid geometry.

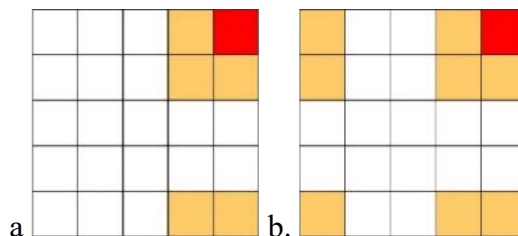


Fig. 3. Planar view of a. Tubular, b. Toroid geometry

Finally, an epoch is defined when the entire batch of data has been entered into the network. Usually many training epochs must be required to adjust the weights, taking care not to overtrain the network. In each epoch the error is measured as vectorial distances, whether

Euclidean, Minkowski, Tanimoto, Mahalanobis, etc; which express the difference between the input and output values of the net. Additionally, the mixing error can be calculated, which is produced when a data from one class is classified by a neuron that previously recognized a data from another class. The latter can only be done if the data of the different classes were previously labelled.

The technique of Acoustic Emission (AE) is based on the monitoring of elastic waves produced in a material and propagate through that physical medium. Generally, is produced by a material excitation. This wave can be detected and acquired by a piezoelectric transducer that transforms the material surface movement into a proportional voltage signal. In this process, the AE signal is digitized, parameterized and finally analyzed. In order to save computational resources, the most relevant information is extracted from the waves, using characteristic parameters to describe it. These, in general, are defined from the first and last crossing of a threshold defined by the operator to separate the interesting signal from the noise. This portion of the signal is called an AE hit. Some of the characteristic parameters of the AE are amplitude (expressed in dB), number of counts, duration, RMS, rise time, absolute energy, and others. The RMS is a measure of the energy contained in the signal and has the advantage of smoothing out small changes in the gain of the electronics or the coupling of the transducer. It is calculated by the equation:

$$V_{ef} = \sqrt{\frac{1}{T} \int_{t_0}^{t_0+T} v^2(t) dt} \quad (1)$$

The absolute energy is the time integral of the square of the AE signal, divided by the input resistance of the preamplifier. This parameter calculates the electrical energy at the sensor output which will be related to the elastic energy generated by the heard phenomenon.

$$E_e = \frac{1}{R} \int [V(t)^2] dt \quad (2)$$

The number of counts is the number of times the signal crosses the threshold during the duration of the hit. The rise time is the time from when the signal crosses the threshold until the hit reaches its maximum amplitude. The amplitude is the maximum modulus value of the AE signal voltage. This value is related to the magnitude of the source and material properties. Generally, it is expressed in decibels (dB_{AE}) since the variation in mV is of several orders.

It is calculated by the equation:

$$A(dB_{AE}) = 20 \log \frac{V_p}{V_{ref}} \quad (3)$$

These parameters or AE descriptors can be defined as information vectors that can eventually be used as input information to train and simulate an ANN with the ability to recognize the different AE signals during the monitoring of any process.

It has been demonstrated that some acoustic emission parameters are effective to evaluate tool wear in metal drilling [Gómez M., 2012], rock fracture [Lockner D., 1993], rock drilling [Ferrari G., 2015 and 2018], behaving of reinforced concrete beams [Xargay H., 2018], and others .

There is literature relating the use of ANNs and AE signals in different fields of application such as tool condition classification, as well as the final roughness obtained in grinding processes [Kwak, 2004], characterization of friction welding processes [Jiménez Macías, 2013], monitoring in additive manufacturing processes [Shevchik, 2018], monitoring of tool wear [Sick, 2002][Ferrari G., 2014], prediction of mechanical characteristics in rock drilling processes [Kumar, 2013], prediction of production stress of failure in composite material [Kumar, 2017], inference of rock abrasion index [Perez, 2015], monitoring in roughing processes, among many others.

In the present case, a Kohonen ANN was used to classify the characteristic patterns of AE corresponding to a drilling process on rocky materials. After selecting AE parameters and designing the ANN architecture, classification maps were obtained allowing to recognize the different geological materials layers.

2. EXPERIMENTAL DEVELOPMENT

2.1 Laboratory specimen's construction

Laboratory specimens were made by depositing different rocks bonded with cement. All the test pieces have the same external dimensions and the thickness and type of rock of each intermediate layer can vary.

The rock structure is then designed to allow four holes to be drilled in a single test specimen (see Fig. 4).

The rocks used for this work are sandstone and lutite (limestone). The cementitious element is made up of 3 parts of sand, 0.8 of cement and 0.2 of lime.

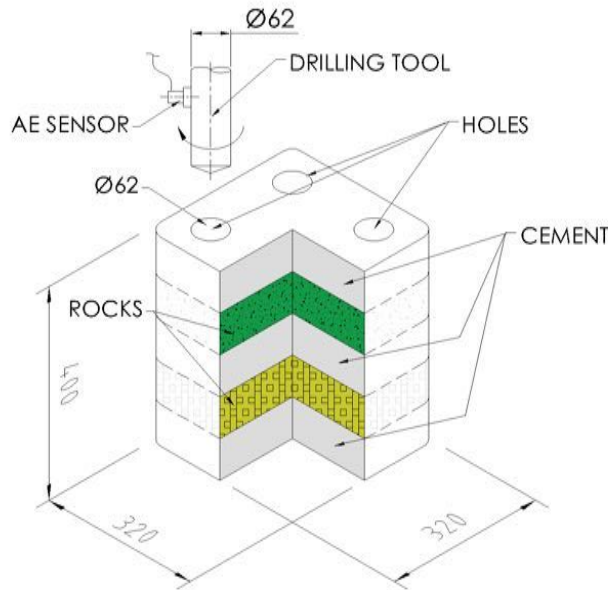


Fig. 4 Experimental set-up (specimen H2SL2 see Table 1).

Specimens with the compositions detailed in Table 1 were used to carry out this test.

Table 1 – Summary of specimen conformation.

TEST NAME	H1L1			H2SL2			H2LP1			H3S1					
	Cem.	Rock 1	Cem.	Rock 2	Cem.	Cem.	Rock 1	Cem.	Rock 2	Cem.	Cem.	Rock 1	Cem.	Rock 2	Cem.
Sandstone						S							S		S
Limestone		L		L			L		L						
Slate										P					

*H1L1, H2SL2, H2LP1 and H3S1 are internal codifications that identify each hole number, composition and specimen number. For example, H3S1 is hole number 3 (A3), has a double layer of Sandstone (S) and is the specimen number 1 from this composite. H2SL2, is hole number 2 (H2), with the first layer of Sandstone (S), second layer of Limestone (L) and is the specimen number 2 of this composite.

**P is from slate rock, but the information from this layer is not used in the present paper.

2.2 Equipment

For the acquisition of AE data, a four-channel PAC model DISP-4 acquisition board and a WD model broadband sensor of the same brand with a 2/4/6 preamplifier with 20 dB gain were used. The equipment was operated with the PAC AEWIN Version E4.6 software.

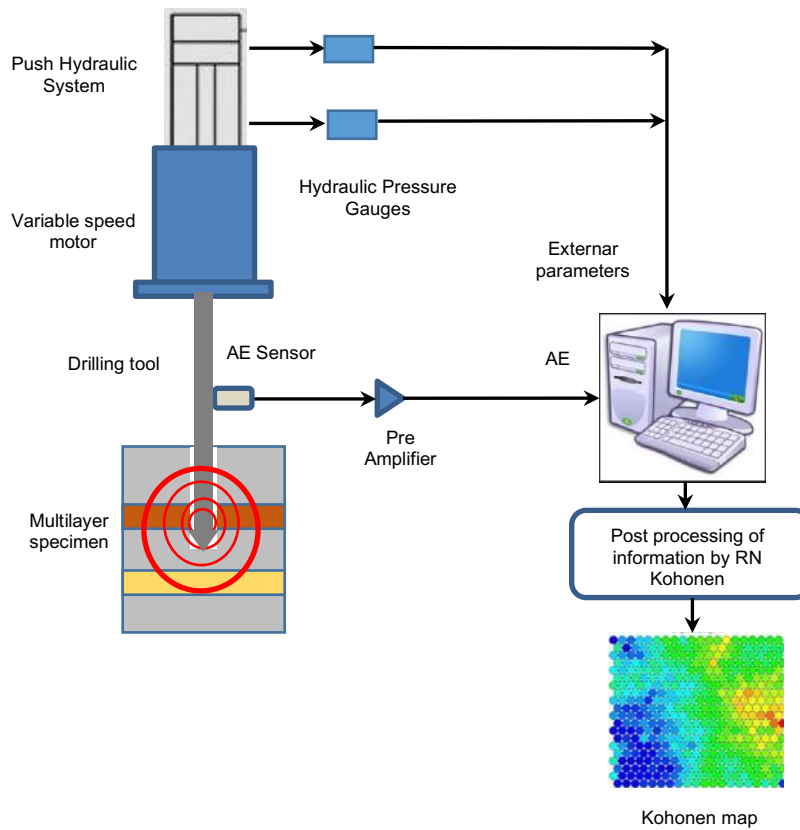


Fig. 5. Block diagram of the experiment.

To perform the penetration of the specimens, a 62 mm rotary tool was used, mounted on a vertical trolley, driven by a hydraulic cylinder, which is controlled by a system that allows to regulate the advance of the rotary tool (Fig. 5).

2.3 AE parameters used

In the acquisition, 19 AE parameters were taken: Rise Time (RISE), Count (COUNTS), Energy (ENER), Duration (DUR), Amplitude (AMP), Average Frequency (AFRQ), RMS, Average Signal Level (ASL), PCNTS, Reverberation Frequency (RFRQ), Initial Frequency (IFRQ), Signal Strength (SIG STRENGHT), Absolute Energy (ABS ENE), First Frequency Quadrant (FREQ PP1), Second Frequency Quadrant (FREQ PP2), Third Frequency Quadrant (FREQ PP3), Fourth Frequency Quadrant (FREQ PP4), Frequency Centre (CFRQ), Peak Frequency (PFRQ).

It was decided to use RMS, ABS ENERGY, COUNTS, RISE and AMP as input parameters for the neural network.

The selection of AE parameters is based on Pearson's correlation see Eq. (4), which is a statistical value that tells us the linear dependence between two variables, similar to covariance, but with normalized value scales between 0 and 1

$$\rho_{a,b} = \frac{\sigma_{ab}}{\sigma_a \cdot \sigma_b} \quad (4)$$

Where: σ_{ab} is the covariance of a and b
 σ_a is the standard deviation of a.
 σ_b is the standard deviation of b.

The minor variables correlated to each other should be used

As an example, Table 2 shows the results obtained from Pearson's correlation for the H2L1 test.

Table 2 – Pearson's correlation coefficients.

A 2 C 1	A B S E N E R G Y	A F R Q	A M P	A S L	C F R Q	C O U N	C Y C L E S	D U R A T I O N	E N E R	F R E Q P P 1	F R E Q P P 2	F R E Q P P 3	F R E Q P P 4	I F R Q	P A R A 1	P A R A 2	P C N T S	P F R Q	R F R Q	R I S E	R M S	S I G S T R E N G T H
ABSENERGY	1.00	-0.03	0.24	0.13	-0.01	0.69	NaN	0.36	0.80	-0.01	-0.01	0.04	0.05	-0.05	0.01	-0.01	0.29	-0.01	0.05	0.09	0.32	0.88
AFRQ	-0.03	1.00	-0.26	-0.15	0.10	-0.11	NaN	-0.20	-0.11	0.04	0.16	0.03	0.01	0.67	0.05	0.06	-0.16	0.06	-0.19	-0.22	-0.10	-0.10
AMP	0.24	-0.26	1.00	0.63	0.06	0.37	NaN	0.22	0.43	0.18	-0.21	0.03	0.09	-0.38	0.04	-0.14	0.43	0.14	0.26	0.19	0.51	0.38
ASL	0.13	-0.15	0.63	1.00	-0.15	0.21	NaN	0.14	0.27	-0.06	-0.37	-0.09	-0.03	-0.22	-0.09	0.01	0.25	-0.08	0.16	0.13	0.80	0.24
CFRQ	-0.01	0.10	0.06	-0.15	1.00	-0.06	NaN	-0.13	-0.04	0.92	0.56	0.22	0.13	0.10	0.12	0.01	-0.06	0.89	-0.02	-0.11	-0.12	-0.04
COUN	0.69	-0.11	0.37	0.21	-0.06	1.00	NaN	0.74	0.90	-0.06	-0.04	0.05	0.05	-0.16	-0.03	0.00	0.54	-0.05	0.10	0.28	0.33	0.91
CYCLES	NaN	NaN	NaN	NaN	NaN	NaN	NaN	NaN	NaN	NaN	NaN	NaN	NaN	NaN	NaN	NaN	NaN	NaN	NaN	NaN	NaN	NaN
DURATION	0.36	-0.20	0.22	0.14	-0.13	0.74	NaN	1.00	0.67	-0.14	-0.08	0.01	0.02	-0.21	-0.07	0.03	0.40	-0.13	0.00	0.42	0.19	0.63
ENER	0.80	-0.11	0.43	0.27	-0.04	0.90	NaN	0.67	1.00	-0.03	-0.06	0.02	0.04	-0.15	-0.02	-0.02	0.51	-0.03	0.08	0.27	0.41	0.97
FREQPP1	-0.01	0.04	0.18	-0.06	0.92	-0.06	NaN	-0.14	-0.03	1.00	0.26	0.06	0.03	0.01	0.11	-0.09	-0.05	0.85	0.02	-0.10	-0.07	-0.03
FREQPP2	-0.01	0.16	-0.21	-0.37	0.56	-0.04	NaN	-0.08	-0.06	0.26	1.00	0.27	0.14	0.20	0.12	0.14	-0.07	0.52	-0.07	-0.09	-0.23	-0.05
FREQPP3	0.04	0.03	0.03	-0.09	0.22	0.05	NaN	0.01	0.02	0.06	0.27	1.00	0.68	0.04	0.00	-0.01	0.04	0.13	0.00	0.00	-0.03	0.02
FREQPP4	0.05	0.01	0.09	-0.03	0.13	0.05	NaN	0.02	0.04	0.03	0.14	0.68	1.00	0.00	0.00	-0.02	0.05	0.08	0.01	0.00	0.00	0.03
IFRQ	-0.05	0.67	-0.38	-0.22	0.10	-0.16	NaN	-0.21	-0.15	0.01	0.20	0.04	0.00	1.00	0.05	0.08	-0.26	0.05	-0.30	-0.35	-0.16	-0.13
PARA1	0.01	0.05	0.04	-0.09	0.12	-0.03	NaN	-0.07	-0.02	0.11	0.12	0.00	0.00	0.05	1.00	-0.03	-0.04	0.12	-0.01	-0.07	-0.06	-0.01
PARA2	-0.01	0.06	-0.14	0.01	0.01	0.00	NaN	0.03	-0.02	-0.09	0.14	-0.01	-0.02	0.08	-0.03	1.00	-0.01	-0.01	-0.03	0.01	0.01	-0.02
PCNTS	0.29	-0.16	0.43	0.25	-0.06	0.54	NaN	0.40	0.51	-0.05	-0.07	0.04	0.05	-0.26	-0.04	-0.01	1.00	-0.04	0.16	0.63	0.30	0.45
PFRQ	-0.01	0.06	0.14	-0.08	0.89	-0.05	NaN	-0.13	-0.03	0.85	0.52	0.13	0.08	0.05	0.12	-0.01	-0.04	1.00	0.02	-0.10	-0.08	-0.03
RFRQ	0.05	-0.19	0.26	0.16	-0.02	0.10	NaN	0.00	0.08	0.02	-0.07	0.00	0.01	-0.30	-0.01	-0.03	0.16	0.02	1.00	0.12	0.12	0.07
RISE	0.09	-0.22	0.19	0.13	-0.11	0.28	NaN	0.42	0.27	-0.10	-0.09	0.00	0.00	-0.35	-0.07	0.01	0.63	-0.10	0.12	1.00	0.12	0.23
RMS	0.32	-0.10	0.51	0.80	-0.12	0.33	NaN	0.19	0.41	-0.07	-0.23	-0.03	0.00	-0.16	-0.06	0.01	0.30	-0.08	0.12	0.12	1.00	0.38
SIGSTRENGTH	0.88	-0.10	0.38	0.24	-0.04	0.91	NaN	0.63	0.97	-0.03	-0.05	0.02	0.03	-0.13	-0.01	-0.02	0.45	-0.03	0.07	0.23	0.38	1.00

Once the parameters to be used were selected, the tests were fractioned to obtain all the signal sections belonging to the cut condition of each kind of rock, then a reduction of the data was made to reduce the training time of the network.

Each section was reduced to 500 data per variable.

The start and end times for each rock layer, indicator (label) and amount of data from each section is shown in Table 3.

When the experiment was performed, the thicknesses of each layer and driller position were related to the test time, so it was possible to locate in time the physical position of each one (times from table 3 were selected by this way).

In Figures 6, 7, 8 and 9 the correlation between distance measurements and acoustic emission signals can be seen using the RMS parameter where the difference between each layer of rock and cement can be appreciated.

Table 3 - Summary of times and data quantities

Summary Table - Time and Data							
Test	Rock	Indicator	T. Start	T. End	Original data	Reduced Data	Selected total data
H1L1	Limestone	L	161.31	273.61	4807	480	3779
	Limestone	L	508.81	623.21	2554	510	
H2SL2	Sandstone	S	338.5	734	18681	518	
	Limestone	L	787.78	977.1	1548	516	
H2LP1	Limestone	L	378.01	430.372	675	675	
	Unused						
H3S1	Sandstone	S	280.55	437.44	5798	579	
	Sandstone	S	629.034	844.1	24075	501	

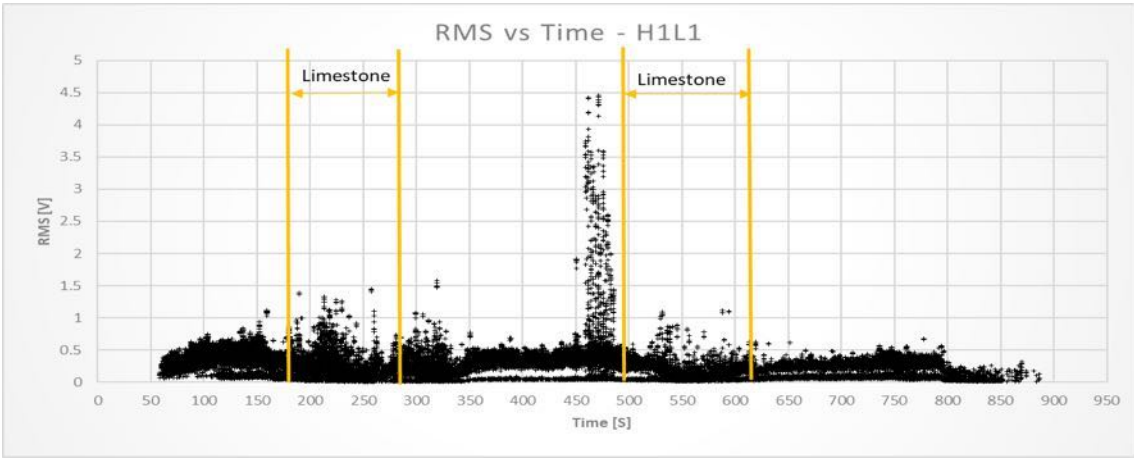


Fig. 6. RMS vs. Time from test H1L1.

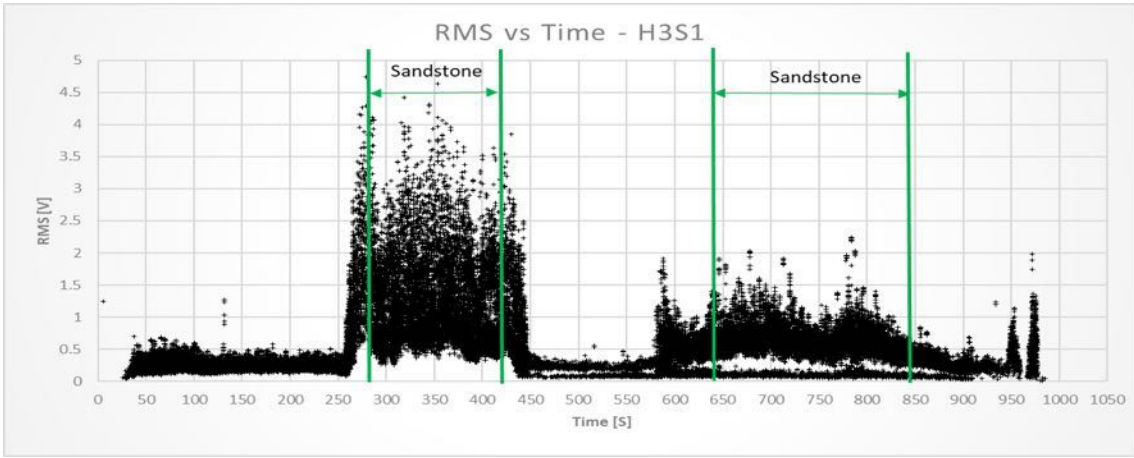


Fig. 7. RMS vs. Time from test H3S1.

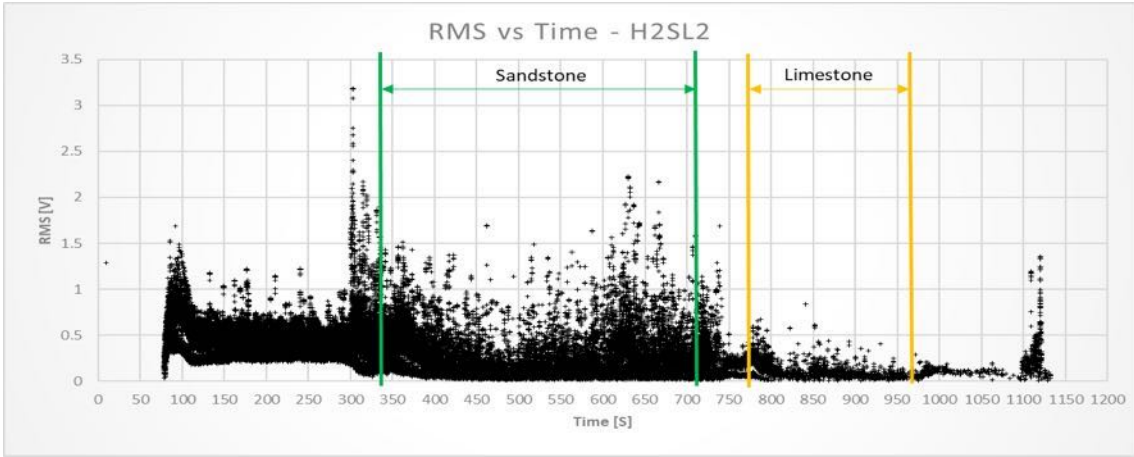


Fig. 8. RMS vs. Time from test H2SL2.

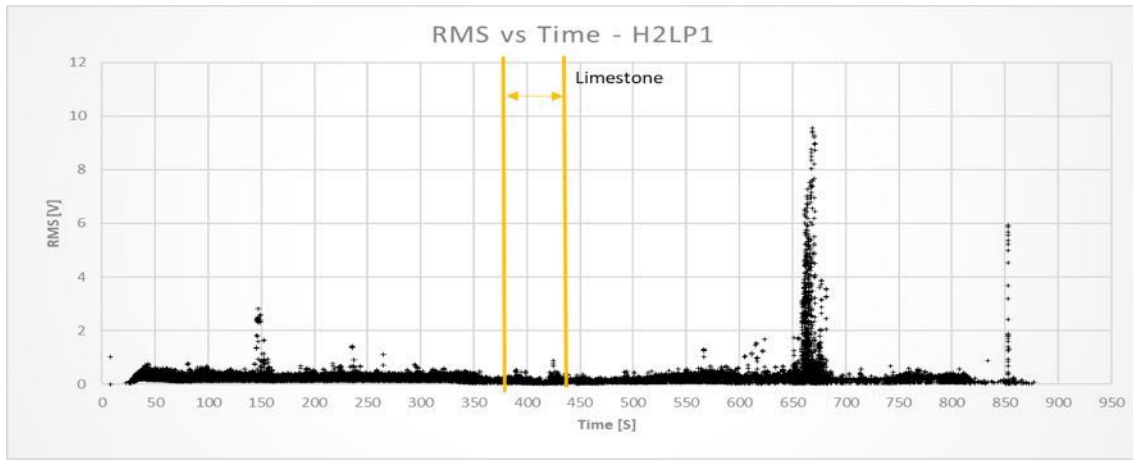


Fig. 9. RMS vs. Time from test H2LP1.

2.4 Final Kohonen neural network architecture

The parameters determined for the final network architecture after several iterations until acceptable results are obtained are summarized in Table 4.

Table 4. Summary of Network Parameters Used.

Network size	25x25
Geometry	Toroid
Correction function	Gaussian
Number of neighbours	5
Correction factor	Max: 0.6 - Min: 0.01
Training epochs	500

Training and prediction process

The selected data is scaled between 0 and 1, then joined forming a 3779 x 5 matrix (where the rows are the measurements and the columns are the 5 parameters previously selected). A scaling is made so that all parameters are in the same order of magnitude, allowing to make an effective error measure and an optimal weight adjustment.

The data are labeled to easily identify the resulting network. An "A" was used to identify the sandstone and a "C" to identify the limestone.

Data is randomly arranged so that the order of training is not initially preferential to a particular class.

Finally, 70% of the data is separated for training and 30% for prediction, data introduced in this prediction, never participated in the training process or adjustment of their weights; they are located in the zone where their vector distance is similar to that kind of data.

3. RESULTS

The results obtained from the training and prediction are shown in Fig. 10 in parts a and b, respectively.

Training shows that there is a zone where preferably the sandstone data is located (green "S") and another large zone where the limestone data is located (yellow "L"). considering that this is a toroidal geometry so the information in the edges is similar. There is also a dispersion where some of the data of "S" is located within the zone of "L".

In the prediction, a similar pattern can be observed, so the classification is made in an acceptable way, remembering that these data did not participate in the adjustment of the weights of the neurons, they are located in the zones where the data are the most similar.

The error control according to the number of epochs is found in Fig. 11, the results are 0.05 in standard error and 11.45% in the mixing error.

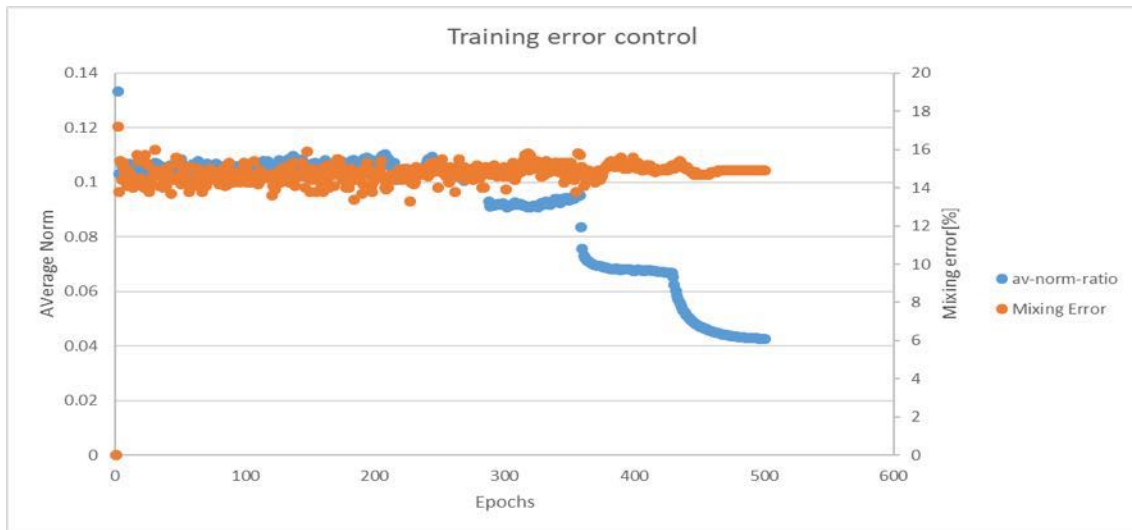
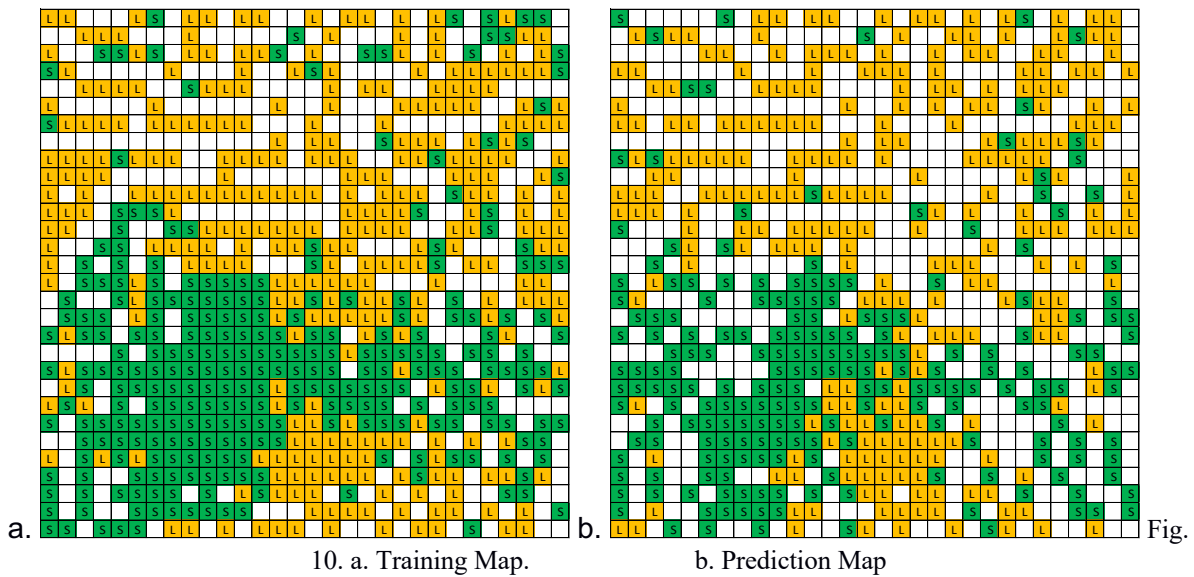


Fig. 11. Training Error control.

4. CONCLUSIONS

It was possible to observe the capacity of Kohonen neural networks to classify information, from a large amount of data, through easily recognizable patterns expressed in a user-friendly way. This could be improved using multilayer networks with a more complex architecture, further optimizing network parameters and using a larger amount of data. This last point leads to optimizing the programming of the network source code to take advantage of the resources of a modern computer.

We can also conclude that it is possible to use the AE parameters to describe the different types of drilled rocks.

It should be clarified that the parameters selected are effective for this particular case, for the error achieved expressed in the results, so that if similar networks were used for another purpose, satisfactory results might not be produced.

REFERENCIAS

Beale M., Hagan M., Demuth H., Neural Network Toolbox User's Guide. MathWorks, 2010
 Zupan J., Gasteiger J., Neural Networks for Chemists. VHC, 1993.

- Yañez-Badillo H., Control Neuronal en Línea para Regulación y Seguimiento de Trayectorias de Posición para un Quadrotor - *Revista Iberoamericana de Automática e Informática industrial* 14 (2017) 141–151.
- Faheem., A Survey of Intelligent Car Parking System- *Journal of Applied Research and Technology* 2013;11:714-26
- Hang Su., Pixel-Adaptive Convolutional Neural Networks - *Computer Vision and Pattern Recognition (CVPR)*, 2019:05:16
- Boldsaikhana E., The use of neural network and discrete Fourier transform for real-time evaluation of friction stir welding - *Applied Soft Computing* 11 (2011) 4839–4846.
- Fratini L., Using a neural network for predicting the average grain size in friction stir welding processes - *Computers and Structures* 87 (2009) 1166–1174.
- Kohonen T., *Self-Organizing Maps*. Springer 2001.
- Kwak J., Neural network approach for diagnosis of grinding operation by acoustic emission and power signals - *Journal of Materials Processing Technology* 147 (2004) 65–71.
- Jiménez Macías E., Emisión Acústica y Redes Neuronales para Modelado y Caracterización del Proceso de Soldadura por Fricción Agitación - *Revista Iberoamericana de Automática e Informática industrial* 10 (2013) 434–440.
- Shevchik S.A., Acoustic emission for in situ quality monitoring in additive manufacturing using spectral convolutional neural networks - *Additive Manufacturing Volume 21*, May 2018, Pages 598-604.
- Sick B., On-line and indirect tool wear monitoring in turning with artificial neural networks: a review of more than a decade of research - *Mechanical Systems and Signal Processing* (2002) 16(4), 487–546.
- Rajesh Kumar B., Regression analysis and ANN models to predict rock properties from sound levels produced during drilling - *International Journal of Rock Mechanics & Mining Sciences* 58 (2013) 61–72
- Suresh Kumar C., Failure strength prediction of glass/epoxy composite laminates from acoustic emission parameters using artificial neural network - *Applied Acoustics* 115 (2017) 32–41.
- Gómez M.P., Hey A.M., D'Attellis C.E. and Ruzzante J.E., “Assessment of cutting tool condition by acoustic emission”, *PROCEDIA MATERIALS SCIENCE*, 1, 321–328, Elsevier (2012) ISSN: 2211-8128. DOI: 10.1016/j.mspro.2012.06.043
- Perez S., A preliminary study on the role of acoustic emission on inferring Cerchar abrasivity index of rocks using artificial neural network – *Wear* 344-345 (2015) 1–8.
- Ferrari G., Magallanes J., Migliori J., Gómez M. P., “Clasificación de la condición de brocas en taladrado a partir del análisis de la Emisión Acústica mediante Redes Neuronales”, *Proceedings del Congreso Internacional de Metalurgia y Materiales*, S19 4418, UNL, Santa Fe (2014) ISBN 978-987-692-043-8 E-book.
- Ferrari G., Gómez M.P., “Correlation Between Acoustic Emission, Thrust and Tool Wear in Drilling”, *PROCEDIA MATERIALS SCIENCE* 8. 693 – 701. Elsevier (2015) ISSN 2211-8128. DOI: 10.1016/j.mspro.2015.04.126
- Hernán Xargay, Paula Folino, Nicolás Núñez y Martín Gómez, "Monitoreo mediante Emisión Acústica de vigas de hormigón de alta resistencia con y sin fibras expuesto a alta temperatura", *REVISTA MATERIA*, vol.23, n.2, e12074 (2018), ISSN 1517-7076. doi: 10.1590/s1517-707620180002.0410.
- Lockner D., The role of acoustic emission in the study of rock fracture, *International Journal of Rock Mechanics and Mining Sciences & Geomechanics Abstracts Volume 30*, Issue 7, December 1993, Pages 883-899. DOI: 10.1016/0148-9062(93)90041-B
- Ferrari G., Basgall A., Gómez M., Análisis de la emisión acústica en perforado de materiales geológicos con diferente granulometría, *Libro de resúmenes extendidos del 18º Congreso Internacional de Metalurgia y Materiales SAM-CONAMET 2018*, 1275-1277, 1ra Edición, CNEA (2018), Buenos Aires. ISBN: 978-987-1323

Machine Learning Applied to Acoustic Emission for Tool Wear Classification during Milling of Composite Materials

Bonelli Toro, A. G.^a, Gómez, M. P.^{b,c}

^aDMA, Gerencia de Materiales, Centro Atómico Constituyentes, CNEA, San Martín, Argentina.

^bGOE, GDTyPE, Centro Atómico Constituyentes, CNEA, San Martín, Argentina.

^cGEA, FRD, UTN, Campana, ARGENTINA. e-mail: abonellitoro@gmail.com

ABSTRACT

In the last decades, the use of composite materials was increased in aerospace and aeronautical industries. The tolerances of manufactured components are decisive in its acceptance. In this way, tool monitoring is an instrument to control the precision of the cutting processes. The drilling/milling process involves a 60% of the rejections of manufactured composite components. Tool wear is one of the main reasons for faulty milling as it achieves a poor termination and inaccurate size of the holes. In the present work, milling tools used in machining (milling or drilling) of sandwich structure panels for aerospace applications were studied for different wear stages. Elastic waves generated during the cutting action were measured by the method of acoustic emission. Three tools with different degree of wear were selected and different machine learning algorithms were implemented PCA and t-SNE for dimensionality reduction and random forest and Kohonen maps to identify the tool condition. The first results are encouraging to carry on these applications to online tool wear classification.

Keywords: acoustic emission, machining, composite materials, machine learning

INTRODUCTION

Monitoring and control methods for machining processes in manufacturing are essential in high-technology industries such as aerospace and aeronautics. With the purpose of improving efficiency of the manufacturing, these methods are continuously evolving. Drilling and milling are the most used operation for structure assembly of composite components. About 60% of these holes made in composites are rejected due to its bad termination [1], because it can severely degrade the mechanical properties of the component made and one of the main reasons is tool wear. Several ways to monitor tool condition are implemented, and can be classified as direct or indirect methods. The direct methods are those that assess the condition employing visual inspection of the tool geometry using techniques based on cameras and microscopes. The indirect methods allow us to infer the status of the tool based on parameters related with the process, for example, mechanical vibrations, current consumed by the machine, torque, forward force, or acoustic emission signals generated during the machining process. The advantage of the indirect methods is the applicability on line in the cutting process. Typically, direct methods are applicable while the process is stopped.

In the present work, the feasibility of acoustic emission applied on tool monitoring during composite machining is studied. Several machine learning algorithms such as Principal Component Analysis, t-Stochastic Neighbor Embedding, Kohonen maps and Random Forest are implemented to explore and classify the data. The specimens used are sandwich structures with reinforced carbon fiber polymer faces and an aluminum honeycomb core.

1. Acoustic Emission

Acoustic Emission (AE) is a Non-Destructive Testing (NDT) method that detects the propagation of elastic waves on the surface of a given material, usually using piezoelectric sensors in the range of 20 kHz to 1 MHz [2]. The most common AE sources are mechanical, electro-magnetic and chemical stresses. This is a passive method because it doesn't need an external active emitter [3], as opposed to other NDT methods (Ultrasound, X-Ray, etc.).

AE allows the analysis of different machining operations such as drilling, milling and turning, and was widespread used in metallic components [4, 5]. The increased usage of composite materials in recent decades demands the study of each associated manufacturing process. On

the one hand, the study of mechanical behavior in tensile, flexion and fatigue tests, seeking to understand the mechanical properties of composite materials. On the other hand, in the characterization and assessment of machining processes. The complexity of studying AE in composite materials is based in the high degree of anisotropy of the material and the dispersive nature of the propagated waves.

2. Sandwich structure

The sandwich structure is a structural composite material, commonly seen in aerospace industry. It has superior properties than other materials, such as high strength-to-weight and stiffness-to-weight ratios [6]. The hardness and strength are given by its faces (or face sheets) and in the core there is a thick lightweight material which gives flexural strength combined with the two faces. Fig. 1 shows a diagram of sandwich structure. The manufacture is complex and requires various stages. The faces are usually made of multi-laminate fiber-reinforced composite material (carbon or glass) which already has several stages to be made and then added to the core [7].

Drilling, milling and sawing and are the most common machining operations on composite sandwich structures, where the specimen must rigidly support the cut and the tool moves on the part to be removed. The matrix is completely independent of the cutting parameters [8]. These parameters will depend on the kind of fibers being machined, regardless of the type of matrix used. Tools with physical vapor deposition (PVD) are commonly used because of its high wear resistance.

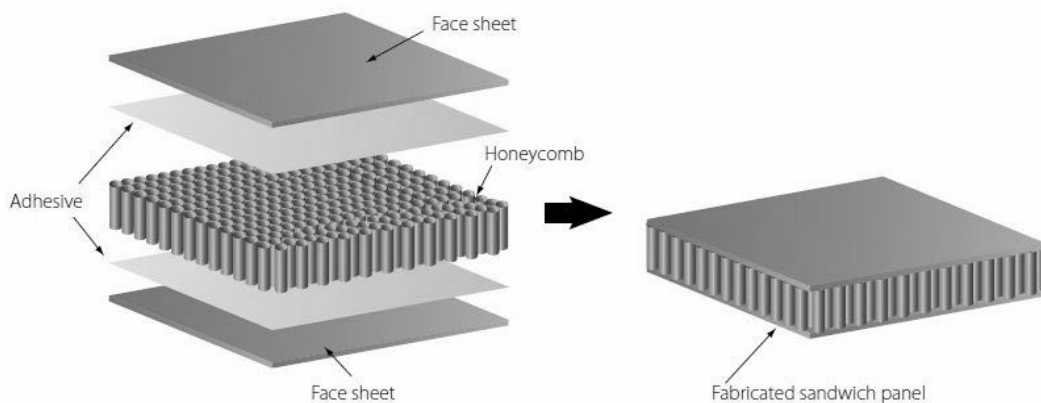


Fig. 1 Sandwich structure diagram.

To achieve a good quality of the machined workpiece, the tool must prevent the edge from attacking the multilaminate perpendicular to the plane. This is unavoidable, but the strategy is to use tools with a diameter smaller than the desired hole and then perform a concentric milling path, shown in Fig. 2.

1. Dimension reduction and classifying algorithms

Dimensionality reduction algorithms were developed in order to visualize the results of a high dimensionality dataset. This type of algorithms can also enhance the data processing time. One of the fundamental pillars is to preserve the characteristics of the original dataset in the new space.

Classification algorithms categorize the data in different classes and can be divided in two subclasses: supervised and unsupervised learning. Supervised algorithms need a target vector to match each element of a vector. On the other hand, unsupervised algorithms need no target to perform classification

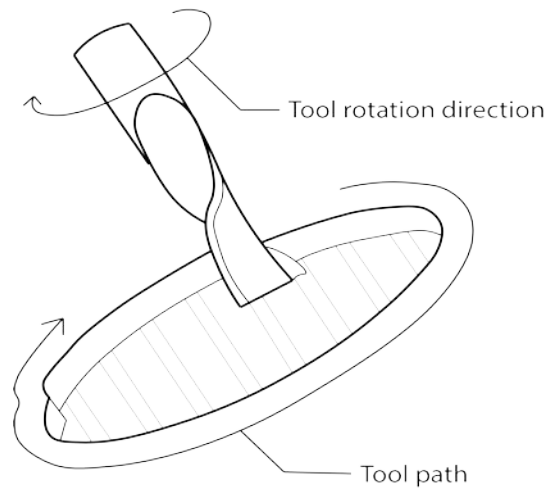


Fig. 2 Typical machining operation of sandwich panel structure.

i. Principal Component Analysis

Principal Component Analysis (PCA) is one of the simplest multivariate analyses based on auto-vectors and auto-values. The main idea is to reveal the internal structure of the data by displaying their variance. PCA provides the user a smaller dimensional dataset, a projection which is a complementary perspective than the original dataset [9].

ii. t-Stochastic Neighbor Embedding

Another dimensionality reduction method is t-Stochastic Neighbor Embedding (t-SNE). Unlike PCAs, t-SNE does a better analysis of non-linear behavior in a dataset by converting a high dimensional dataset into a low dimensional space, allowing data exploration [10]. The dataset is called a map, and its low dimensional points are called map points. The objective of this algorithm is to be able to maintain the data structure of the multidimensional space and its neighborhoods in the low dimensional space.

iii. Kohonen Map

The self-organizing map (SOM) or Kohonen map is an unsupervised single layer neural network. This implies that the dataset is given by the user in the input layer and there is no ideal user-supplied output. The SOM learns to group or map its data into a specific number of classes [11]. This means that the network will not take into account the relationship between each object and the true response, but that the network works completely independently [12]. Like PCA and t-SNE, the SOM also does a dimensional reduction which helps interpretation. It classifies arranging the elements in a grid, putting similar data close to each other.

iv. Random Forest

Random Forest is a supervised ensemble classification algorithm that is essentially a collection of Decision Trees (DT) [13]. DT are built on an entire dataset, using all the characteristics, while Random Forest randomly selects specific variables to build multiple Decision Trees and then averages the results. After building a large number of trees using this method, each tree "votes" or chooses the class, and the class that receives the simplest majority votes is the "winning" or predicted class.

EXPERIMENTAL

1. Tools selection

The Sandvik Coromill Plura (2P460-OA) with $(Ti,Al)N_2$ were used. Its diameter is about 8mm and the length is 63.5 mm. A set of tools was inspected with a scanning electron microscope to qualitative analyze each wear and three were selected. Fig. 3a shows the most worn tool (named H1); Fig. 3b shows the one with intermediate wear (H2); and H3 is a new tool, shown in Fig. 3 c.

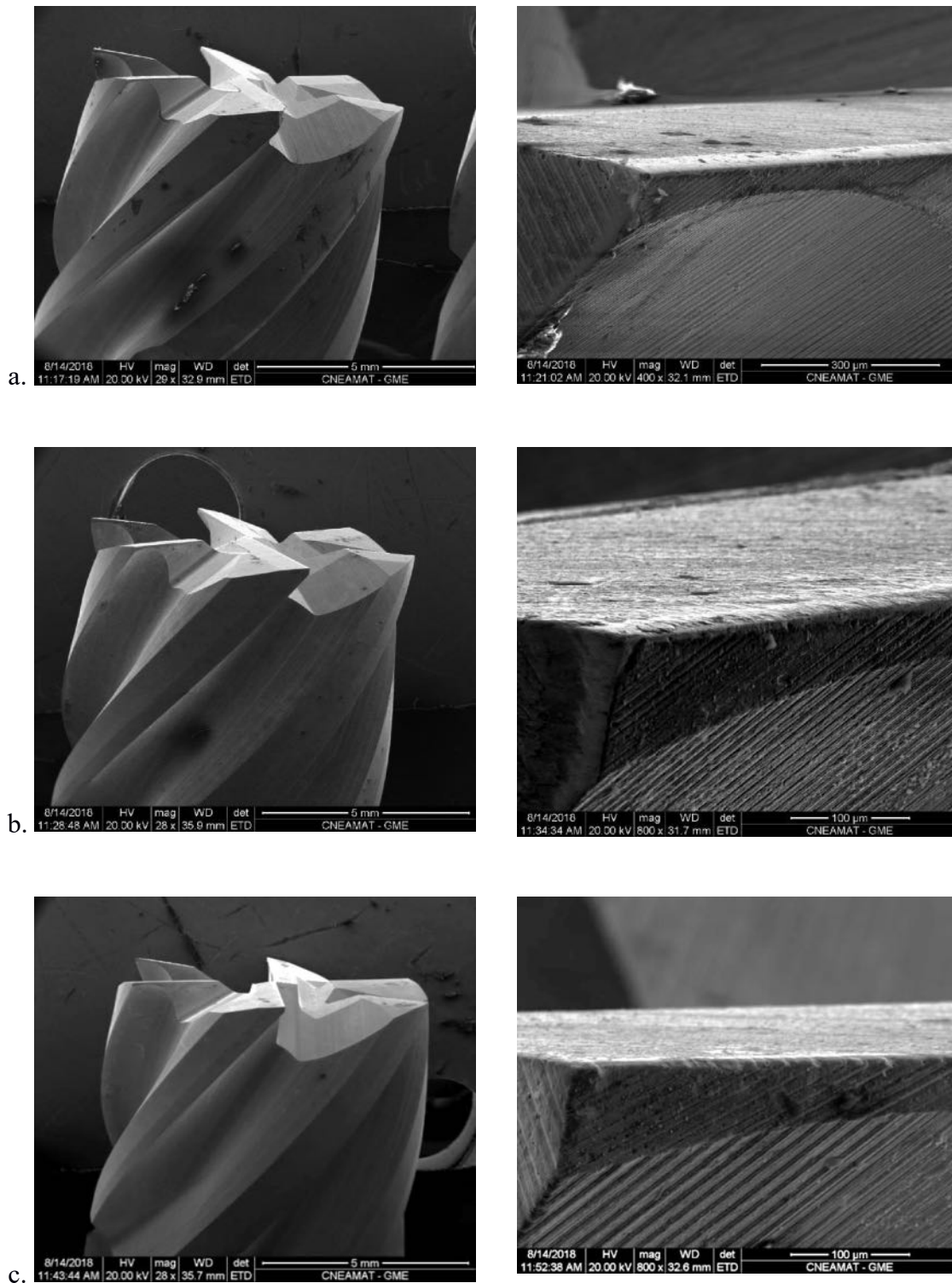


Fig. 3 SEM inspection (left) and cutting-edge detail of the tools H1 (a), H2 (b) y H3 (c)

Comparing the three tools, the most worn (H1) has rounded and soft cutting edges. The cause may be the interaction between the tool and the chip.

2. Specimens and machining procedure

Two sandwich structure panels with aluminum honeycomb core and CFRP composite laminate plates were the specimens for the machining process. Each laminate plate has 24 layers with a laminate orientation $[0, 30, 60, 90, -30, -60]_{2S}$. The size of each specimen is 620 mm length and 180 mm width. Eight blind holes in the top face were made in each specimen as shown in Fig. 4. In the first specimen, H1 milling tool was used in the left side of the specimen panel and H3 in the right side. In the second specimen, H2 and H3 in the left and the right side of the panel, respectively. The machining process was performed with an industrial CNC machine with a feed rate of 250 mm / min and spindle speed of 8000 RPM. Two AE sensors were positioned in the center of the width at 50 mm from the edge. The distance between the holes is 50 mm. First, a drilling stage was performed to make 8 mm diameter and then, a spiral milling was performed to increase the diameter to 10 mm.

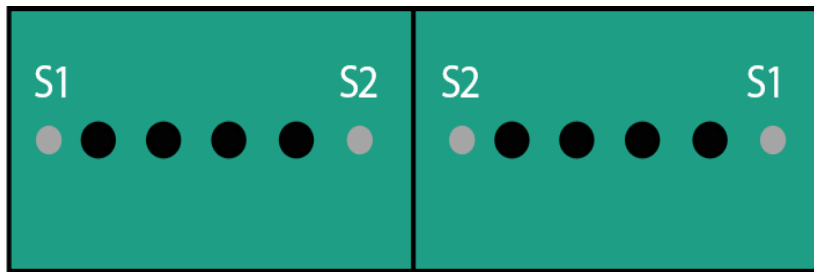


Fig. 4 Hole (black) and sensor (gray) placement in the test panels.

3. AE Measurement

Two Physical Acoustic Corporation (PAC) wideband sensors and 2/4/6 preamplifiers were used. The couplant was solid vaseline. Data was measured and acquired with an 18-bit resolution PAC PCI-2 AE system with a sampling frequency of 5 MHz and a 1 MHz LPF. The 15 parameters given by the equipment were registered.

RESULTS AND DISCUSSION

1. Tool inspection

After the measurement, an inspection under a magnifying glass was performed. It can be seen that as the tool wears, more chips are accumulated in the tool edges. Fig. 5a and 5b shows the difference between H1 and H3, respectively.

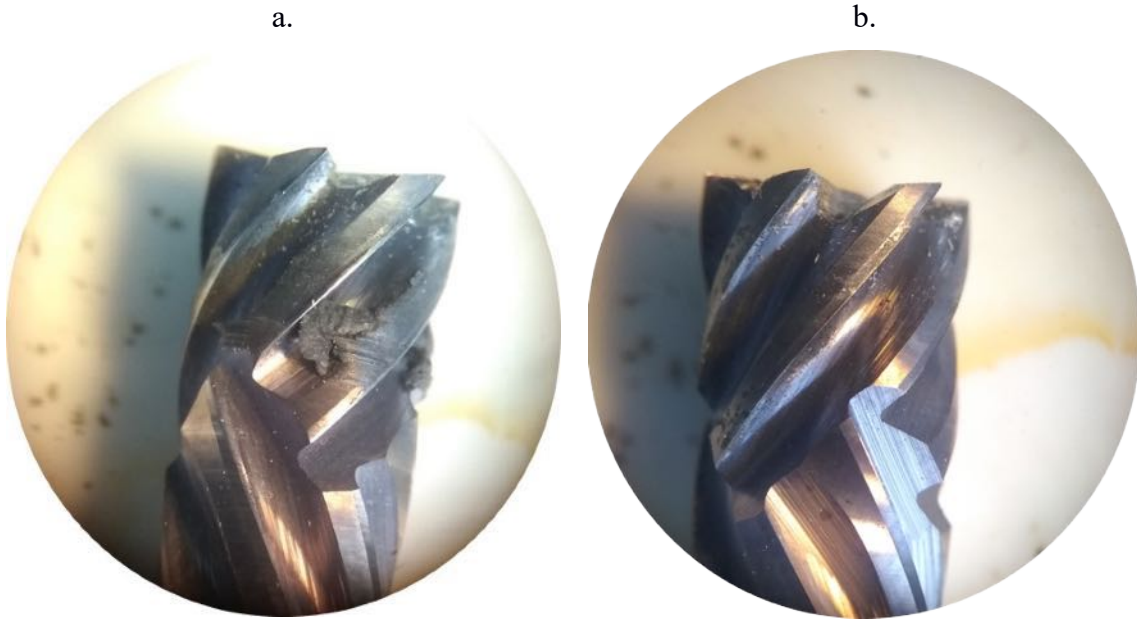


Fig. 5 (a) H1 and (b) H3 after panel machining.

2. Pre-processing

The AE measured during the machining operation was parametrized and analyzed. For each measured feature, data was filtered based on MARSE energy parameter at 70 aJ to remove background noise. Fig 6 shows the MARSE energy parameter to visualize the drilling and milling stage and its transition stages (stationary and exit). The transition stages were discarded because there is no machining involved.

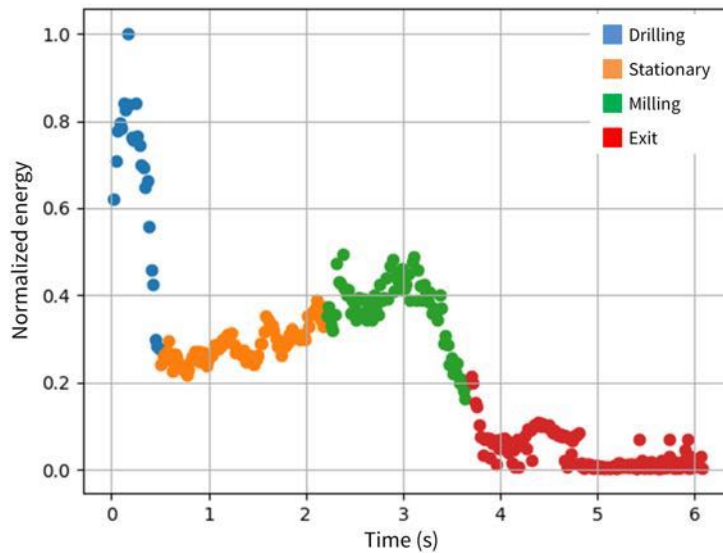


Fig. 6 MARSE energy vs time to show machining stages involved in the experiment.

Also, a time filter was used to select only the milling stage as it determines the quality of the hole's termination. Then, the data was normalized and all the measurement were concatenated in a single dataset. Finally, it was splitted into training (80%) and test (20%) dataset for classification algorithms evaluation.

A correlation between the different parameters and the target was made. Centroid frequency, RMS and average frequency were the most correlated variables.

3. Dimensionality reduction algorithms

i. PCA

The PCA algorithm was implemented and it's shown in Fig. 7. The non-linear nature of the mechanic waves involved in AE impedes this type of algorithm from maximizing its ability to discriminate between clusters. However, there are three zones with a clear predominant class.

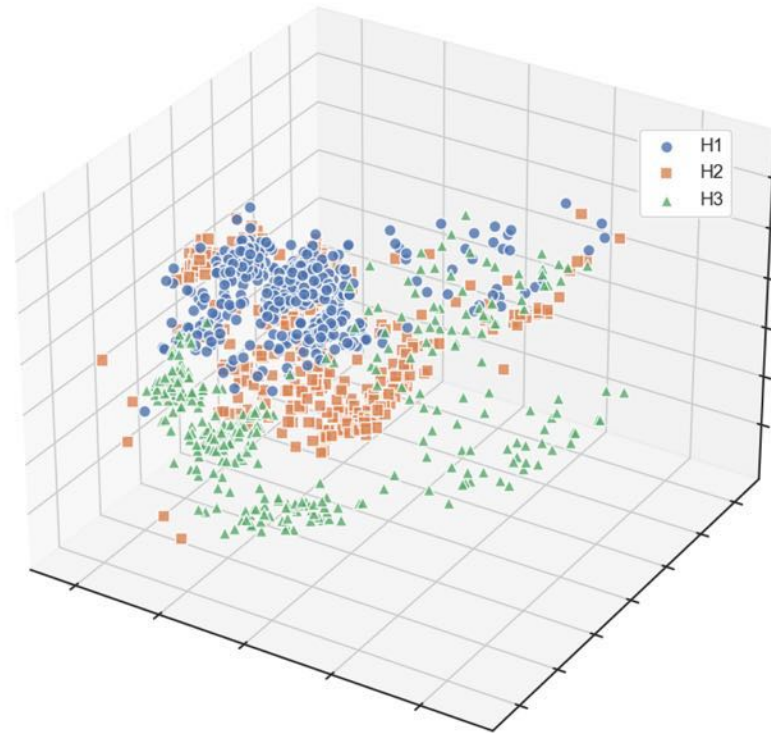


Fig. 7 3D PCA plot for the milling stages.

ii. t-SNE

In the t-SNE method, there are three zones were clearly prevail one of the tools above the others (Fig. 8). There is a mix of H2 data points in the H1 and H3 clusters. The reason is that the algorithm is nonlinear and works better for this kind of datasets supposing an advantage for a later classification.

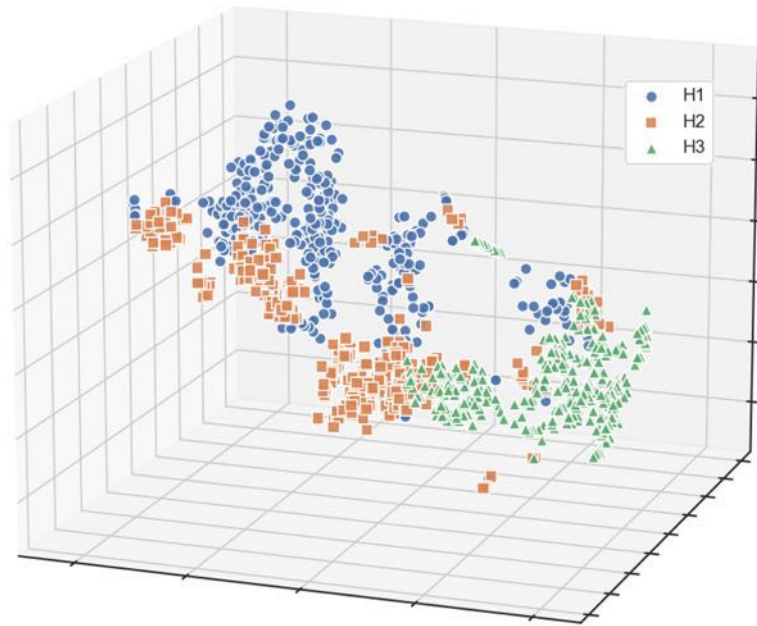


Fig. 8 3D t-SNE plot for the milling stage.

iii. Kohonen map

As mentioned above, SOM does a dimensionality reduction and a classification simultaneously. An implementation in Python named MiniSOM was used [14]. In this case Fig. 9 shows 3 topological zones, corresponding to the three different tools wear. In this case, there is also a certain mix in the classes. H2 is mixed in the clusters of the other tools.

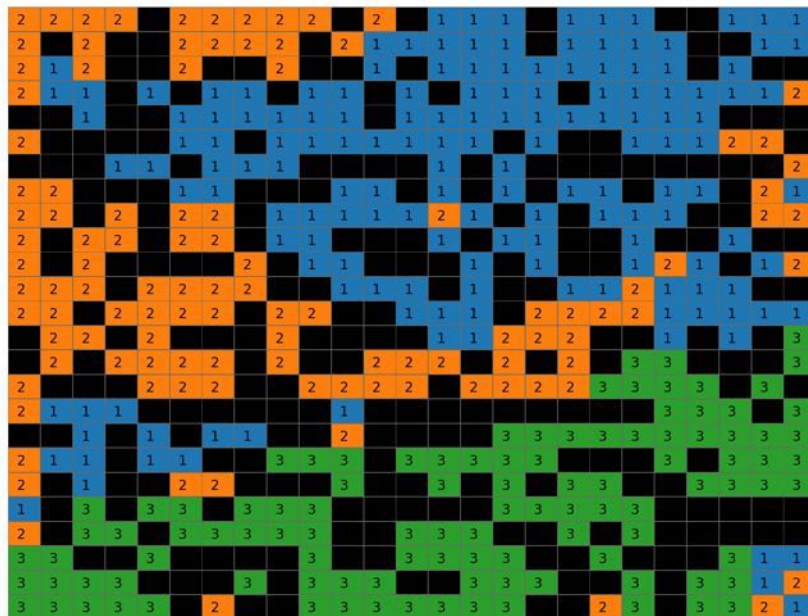


Fig. 9 Train self-organizing map for the milling stage.

The test set was used to perform the classification on unknown samples and the accuracy of this algorithm was 90%.

iv. Random Forest

The Random Forest algorithm was implemented to perform the wear classification on the original, the PCA and the t-SNE dataset. Table 1 shows that the most efficient dataset is the

original. However, the two dimensionality reduction algorithms work very well too. The application of this algorithms can be thought in a really large-scale implementation as an intermediate stage.

Table 1. Comparison between Random Forest implementation in the three datasets

Dataset	Training accuracy	Test accuracy
Original	0.99	0.97
PCA	0.97	0.94
t-SNE	0.98	0.95

CONCLUSIONS

In this work, different dimensionality reduction and classification algorithms were applied for the analysis of tool wear in composite materials machining. Three PVD tools and two specimens were analyzed in this study.

To achieve the desired size hole in the laminate composite plate, drilling and milling operations were performed. The focus of this work, the milling stage, was mainly studied because milling is the process that controls the hole quality termination. In this process it was possible to differentiate the three different tool conditions in each algorithm carried out.

For dimensionality reduction methods of PCA and t-SNE, the algorithms differentiated areas where one tool clearly predominates over the others, although with a certain mixing of H2 part over the others.

The tool wear analysis, performed using SOM, allowed the observation of areas where one tool prevailed over the others with an accuracy of 90%.

The Random Forest algorithm was used on the original, PCA and t-SNE datasets. In all the situations the results were above 95% of accuracy which is a very good result for this kind of experiments.

ACKNOWLEDGEMENTS

Special thanks to Nicolás Belinco, Martín González Fuster, Gerardo Fernández, Federico Antico, Pablo Vogt, Adriana Domínguez, Nicolás Núñez and Hernán Sánchez.

REFERENCES

1. Liu, D., Tang, Y., & Cong, W. L. (2012). A review of mechanical drilling for composite laminates. *Composite Structures*, 94(4), 1265–1279. <https://doi.org/10.1016/j.compstruct.2011.11.024>
2. Gómez, M. P. (2015). *Fundamentos de la Emisión Acústica*. UTN-FRD.
3. Grosse, C. U. (2008). *Acoustic Emission Testing*. Acoustic Emission Testing. Springer. <https://doi.org/10.1007/978-3-540-69972-9>
4. Gómez, M. P., Hey, A. M., D'Attelis, C. E., & Ruzzante, J. E. (2012). Assessment of Cutting Tool Condition by Acoustic Emission. *Procedia Materials Science*, 1, 321–328. <https://doi.org/10.1016/j.mspro.2012.06.043>

5. Ferrari, G., & Gómez, M. P. (2015). Correlation Between Acoustic Emission, Thrust and Tool Wear in Drilling. *Procedia Materials Science*, 8, 693–701. <https://doi.org/10.1016/j.mspro.2015.04.126>
6. Davies, J. M. (2001) *Lightweight sandwich construction* (MPG Books). Manchester: Blackwell Science.
7. Bitzer, T, (1997) *Honeycomb Technology: Materials, Design, Manufacturing, Applications and Testing*. Springer Science.
8. Zenkert, D. (1997). *An Introduction To Sandwich Construction*. Emas Publishing, London.
9. Einasto, M., Saar, E., Einasto, J., Tempel, E., & Tago, E. (2011). SDSS DR7 superclusters. *Astronomy & Astrophysics*, 1–13. Hinton, G., & Roweis, S. (2002). Stochastic Neighbor Embedding. *Advances in Neural Information Processing Systems*, 15, 833-840.
10. Heaton, J. (2012). *Introduction to the math of neural networks*. (WordsRu.co, Ed.). Chesterfield: Heaton Research Inc.
11. Magallanes, J., et al. (2011). Kohonen classification applying ‘missing variables’ criterion to evaluate the p -boronophenylalanine human-body- concentration decreasing profile of boron neutron capture therapy patients. *Journal of Chemometrics*, 340–347.
12. Géron, A. (2017). *Hands-on machine learning with Scikit-Learn and Tensor Flow: concepts, tools, and techniques to build intelligent systems*. Sebastopol, CA: O'Reilly Media. ISBN: 978-1491962299
13. Vettigli G., *MiniSom: minimalistic and NumPy-based implementation of the Self Organizing Map*. Available: <https://github.com/JustGlowing/minisom/>

Acoustic Emission Numerical Analysis Applied to Structural Health Monitoring of Laminar Structures (Guided Waves)

Groth, E. B.^a, Shumacher, G.^b, Idzi J.^c, Rojo Tanzi, B. N.^b, Clarke, T. G. R.^a,
Lima, T. R. S.^a and Jacques, R. C.^a

^a Laboratório de Metalurgia Física LAMEF, Universidade Federal do Rio Grande do Sul, BRASIL

^b Grupo de Mecânica Aplicada GMAP, Universidade Federal do Rio Grande do Sul, BRASIL

^c UIDET Ingeniería Aplicada en Mecánica y Electromecánica (IAME), Facultad de Ingeniería, Universidad Nacional de La Plata, La Plata, ARGENTINA e-mail:eduardo.groth@ufrgs.br

ABSTRACT

Structural health monitoring of critical components such as bridges, pipes, aircraft bodies is regarded with great interest by the industry and researchers nowadays. The development of these evaluation techniques is strictly connected to the development of new materials, with new properties, behaviors, and other characteristics, allowing the design of new transducers. This includes works in the propagation of mechanical waves, which is a phenomenon highly studied in non-destructive testing (NDT). Acoustic emission testing is a technique that uses mechanical wave propagation to monitor structural integrity by analyzing the sound waves produced by small increments in size of defects present in a sample. This type of test is challenging because the acoustic emission event cannot be repeated, and techniques such as averaging of multiple readings to increase signal to noise ratios cannot be thus employed. In this context, the present work suggests a numerical model of the acoustic emission phenomenon for better understanding of the generated signal, which allows for better designing of resonant sensors with a high sensitivity.

Keywords: Monitoring, acoustic emission, DEM, natural frequency, guided waves.

1. INTRODUCTION

Crack propagation is a well-known and evaluated phenomenon mainly due to recurrence in civil structures of different scales and applications (Sengupta et. al). Whenever a crack advances, microstructural ruptures release kinetic energy in the material medium. This energy that disperses and propagates from the crack is a typical acoustic emission and might take place in structures such as bridges, pressure vessels, etc. Monitoring of this type of event allows control of structural integrity, remaining life estimations and safe operation of the component at the current location. Acoustic emission technique has been widely applied to monitor structures such as pipelines, (Jacques et. al; Clarke et. al), pressure vessels (Tirbonod and Hanacek) and concrete structures (Paresh et. al; Chao et. al).

One of the great challenges in acoustic emission monitoring is the environmental noise detected by the sensors. In several occasions one event might exhibit a displacement amplitude below the background noise, depending on the distance between source and sensor, and the acoustic emission will be undetected. Also, the monitored component might be placed in an environment subject to diverse noise sources, such as rotating machines, fluid flow, impacts and even rain, the latter being a considerable agent that might mask/hide acoustic emission, and disqualify the method (Eagle et. al).

In this context, this present work proposes to introduce a method that, through the use of numerical analysis, allows the development of sensors with a high sensitivity to acoustic emission and low response to background noise, thus increasing acoustic emission performance in monitoring the integrity of structures and components.

2. DEVELOPMENT

Fracture numerical modelling is a non-trivial theme which conventional finite element method is not capable of reproducing. The adopted alternative in this work is a model based on discrete elements (LDEM), initially proposed by Riera in 1984. This finite element method discretizes the domain in cubic elements formed by beams that only support axial loads. Figure 1 presents a single element and the internal beam configuration (Groth 2016).

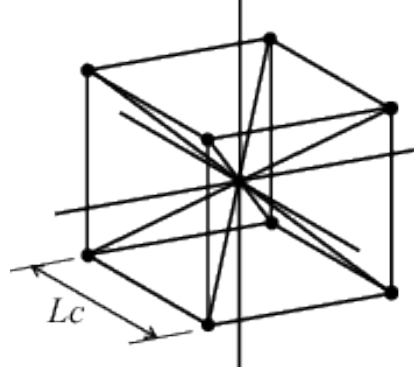


Figure 1: Unit finite element characteristic of the LDEM method

The mass is placed in the nodes, and each node has three degrees of freedom, corresponding to node displacement in the three orthogonal directions. The equations that relate element properties to the elastic constants of the isotropic medium are:

$$\eta = \frac{9\nu}{4 - 8\nu}, \quad EA_n = EL_c^2 \frac{(9 + 8\eta)}{2(9 + 12\eta)}, \quad EA_d = \frac{2\sqrt{3}}{3} A_n$$

where E is the Young Modulus, ν is the Poisson coefficient, A_n and A_d are the areas of the normal and diagonal elements and L_c is the length of the side in the basic cube. The resulting movement equations obtained from this spatial discretization can be written in the following form:

$$M\ddot{x}(t) + C\dot{x}(t) + F_r(t) - P(t) = 0,$$

where x represents a node displacement vector, M is the diagonal mass matrix, C is the damping matrix, F_r is the vector of internal forces acting on the node masses and P is the external forces vector. The integration at the domain is carried out through addition of the central finite differences which allow large deformations.

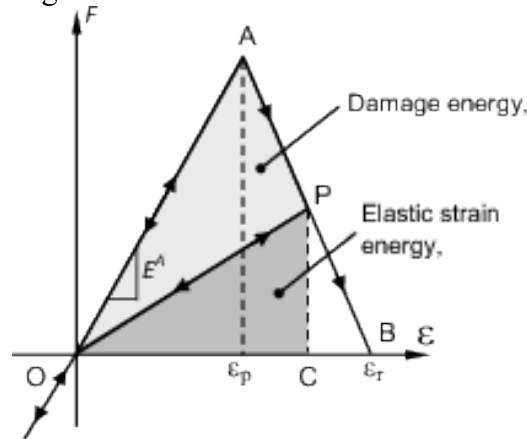


Figure 2: Bilinear constitutive model with material damage.

In this work, the LDEM implemented a relation between the axial force and axial deformation in the internal beams of the element based on the bilinear law proposed by Hillerborg in 1978 and presented in Figura 2. The specific fracture energy, G_f , is directly proportional to the area below the triangle formed by the meeting of the two straight lines with the x -axis in the geometric analysis of the law. An important characteristic of this model is the random distribution of the G_f value of each beam within a pre-established range of values. In

order to obtain randomness of the mechanical property, a Weibull distribution is applied, which in practical terms is the effect of the metal grain size among other microstructural characteristics which are found to vary within a domain. The deformation associated to the maximum load supported by each beam (ϵ_p) was also randomly varied.

2.1 Hybrid model DEM + FEM

A model solely built in LDEM to analyze mechanical wave propagation might lead to an unfeasible computational cost to most ordinary computers. In this work, a fusion between a LDEM and a FEM model was implemented. The aim was to adapt the LDEM characteristics for crack propagation and a sufficient quantity of modelled material medium to allow the acoustic emission produced by the crack to exhibit a natural propagation manner and also allowing frequency analysis of this perturbation.

The approach consists in transferring the displacements produced in LDEM to the modeled geometry in the FEM model, as presented in Figure 4. Three simulations were used to validate the method: a pure LDEM, a FEM and the mixed model. The subject chosen for this test was a rectangular beam made of low carbon steel (SAE 1020) with $E = 210 \text{ GPa}$, $\rho = 7850 \text{ kg/m}^3$, $\nu = 0,25$, and sample dimensions of $15 \times 5 \times 1500 \text{ mm}^3$. The loads are applied in the excitation area (see Figure 3) in the longitudinal direction of the wave guide (z-direction). Readings were taken from a control point located at a distance of 400 mm away from the frontal side of the sample.

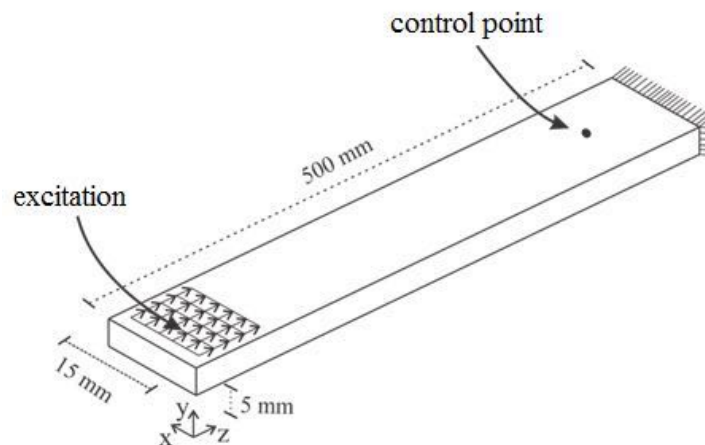


Figure 3: Model used to evaluate the hybrid model technique.

As previously mentioned, three distinct models were studied: the first was built only with discrete elements (DEM), the second used only finite elements (FEM) and the third was a hybrid model, where half of the sample (which contains the excitation region) was modeled with DEM and the other half modeled with FEM (see Figure 4).

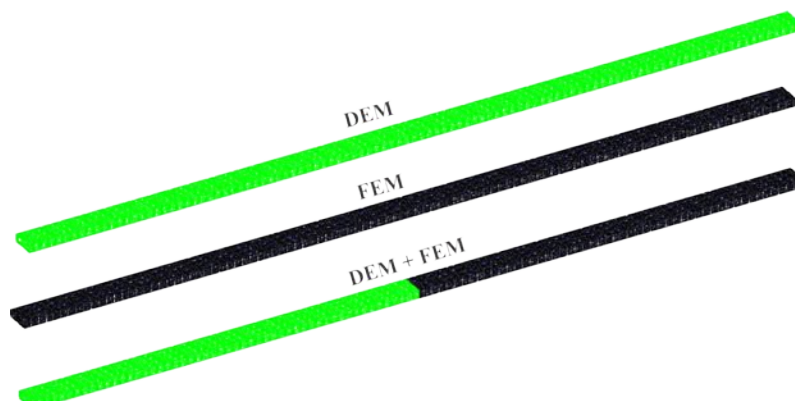


Figure 4: Three models designed to compare different model approaches.

Because the meshes of the two models (DEM and FEM) were not exactly the same, coupling between them was carried out in two different manners: (a) only in the nodes at the edge; (b) in the inner nodes of the interface (Figure 5). This resulted in two solutions for the hybrid model.

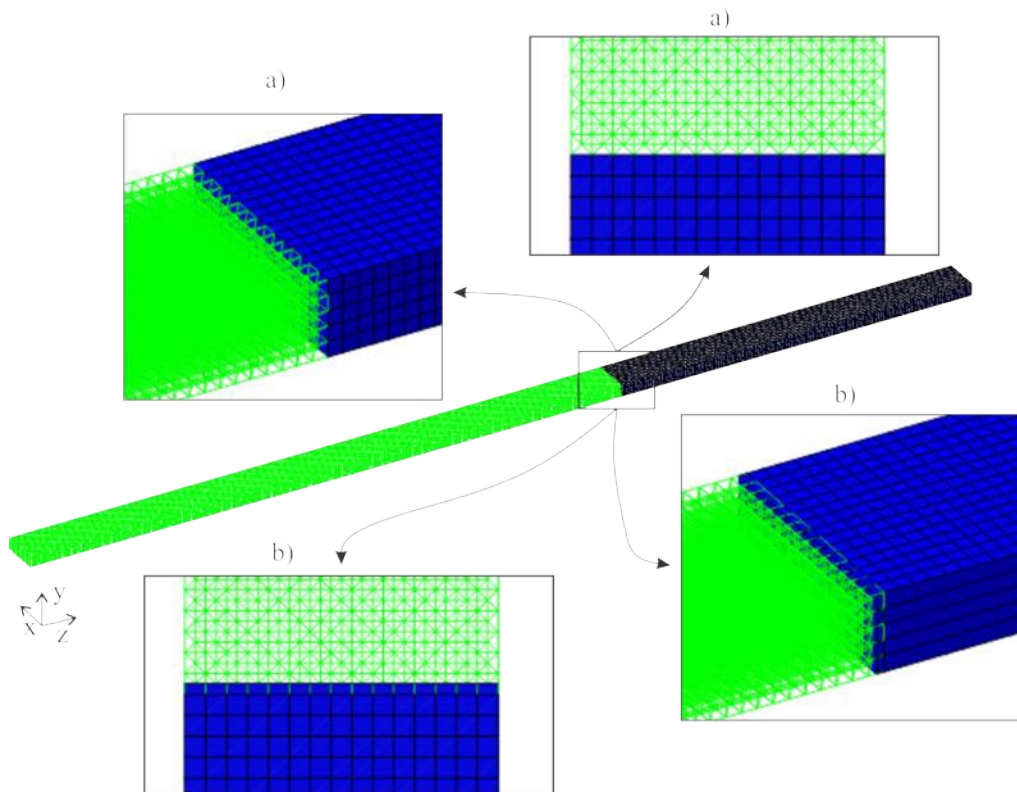


Figure 5: Models of coupling between DEM and FEM domains of the body: a) in the edge nodes and b) in the internal nodes of the common face.

2.1.1 Results of the mixed model validation

The results found for the displacement in the waveguide direction (z -axis) for the three models are presented in Figure 6. It is noticeable that the methods are perfectly applicable for the elastic wave propagation study, since an excellent superposition of the curves was achieved.

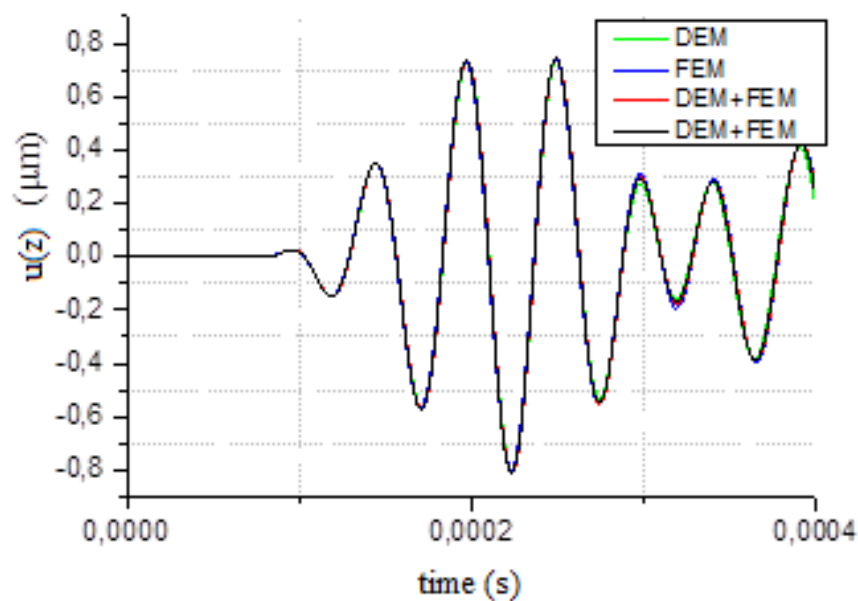


Figure 6: Responses to the z -shift at the pickup point for the DEM, FEM models and the two types of DEM + FEM models.

3. APPLICATION

After validation of the mixed model (LDEM + FEM), a numerical study of the acoustic emission produced by a crack opening in the three possible modes (Figure 7) is presented.

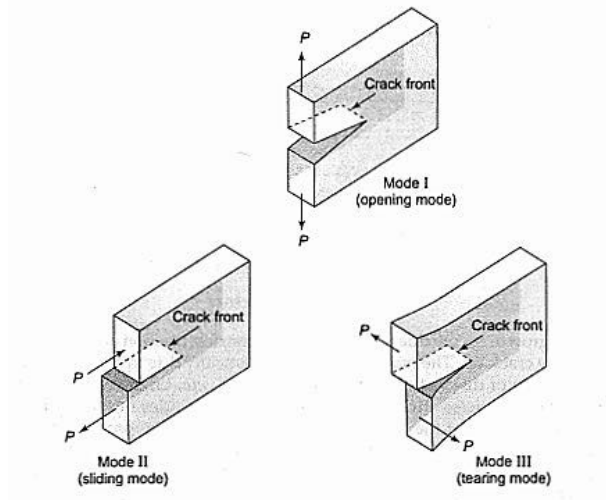


Figure 7: Crack breaking modes

The details of the model are presented in Figure 8: the DEM/FEM interface and the loads to augment the crack for the three possible modes shown in Figure 7.

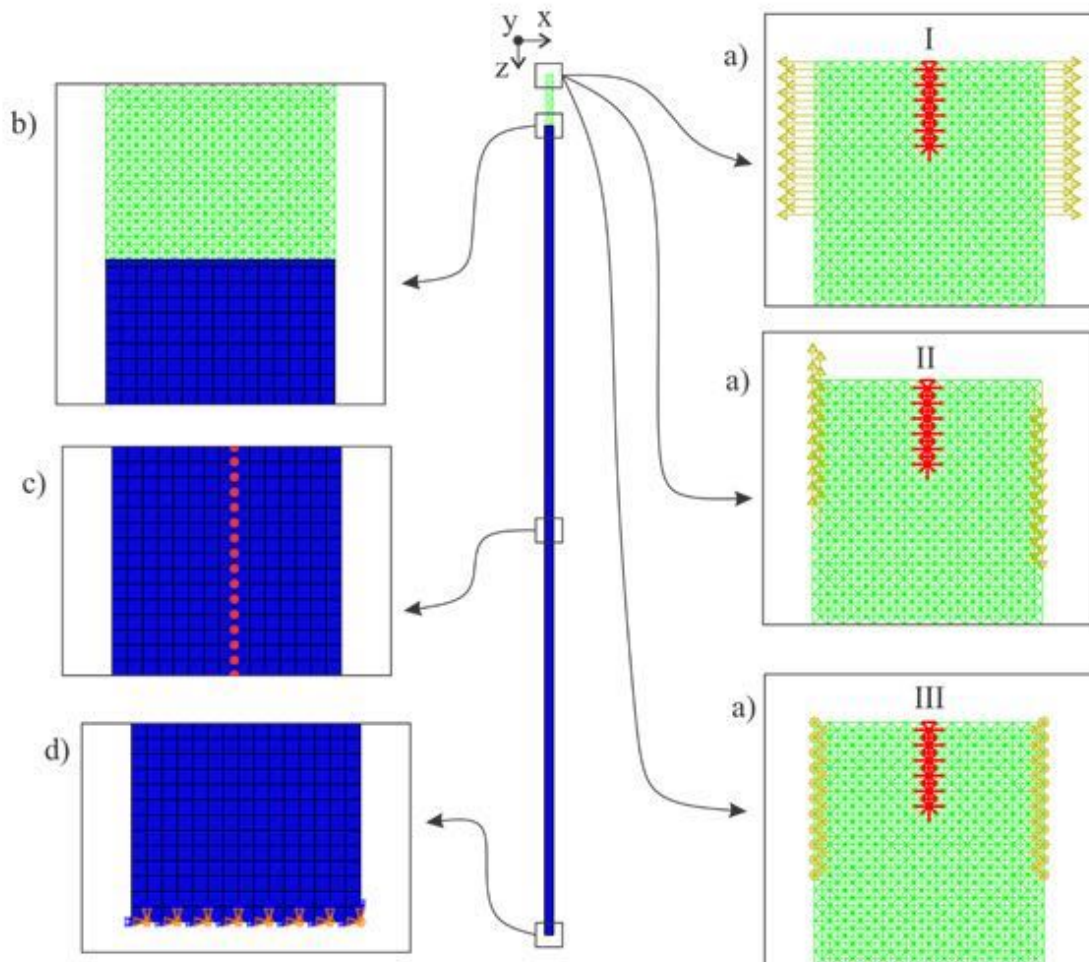


Figure 8: DEM/FEM hybrid model. (a) different load directions for each cracking mode; (b) DEM/FEM interface; (c) monitoring nodes; (d) boundary condition.

4. RESULTS

Monitoring of a line of nodes equally spaced allows the application of a 2-way Fourier Transform (FT). This method allows analysis of the existing frequencies and wavelengths in the propagations produced by the increase in crack size. Initially the analysis considered only the monitoring node, and later the 2-way FT was implemented.

The signal observed (three directions) in one of the monitoring nodes is presented in Figure 9. In this case, the crack is breaking in mode I and clearly the longitudinal movement is the most activated. The circle to the left indicates waves of the pressure (P) type originated from the crack growth. A more detailed analysis of the regions marked with circles will now follow.

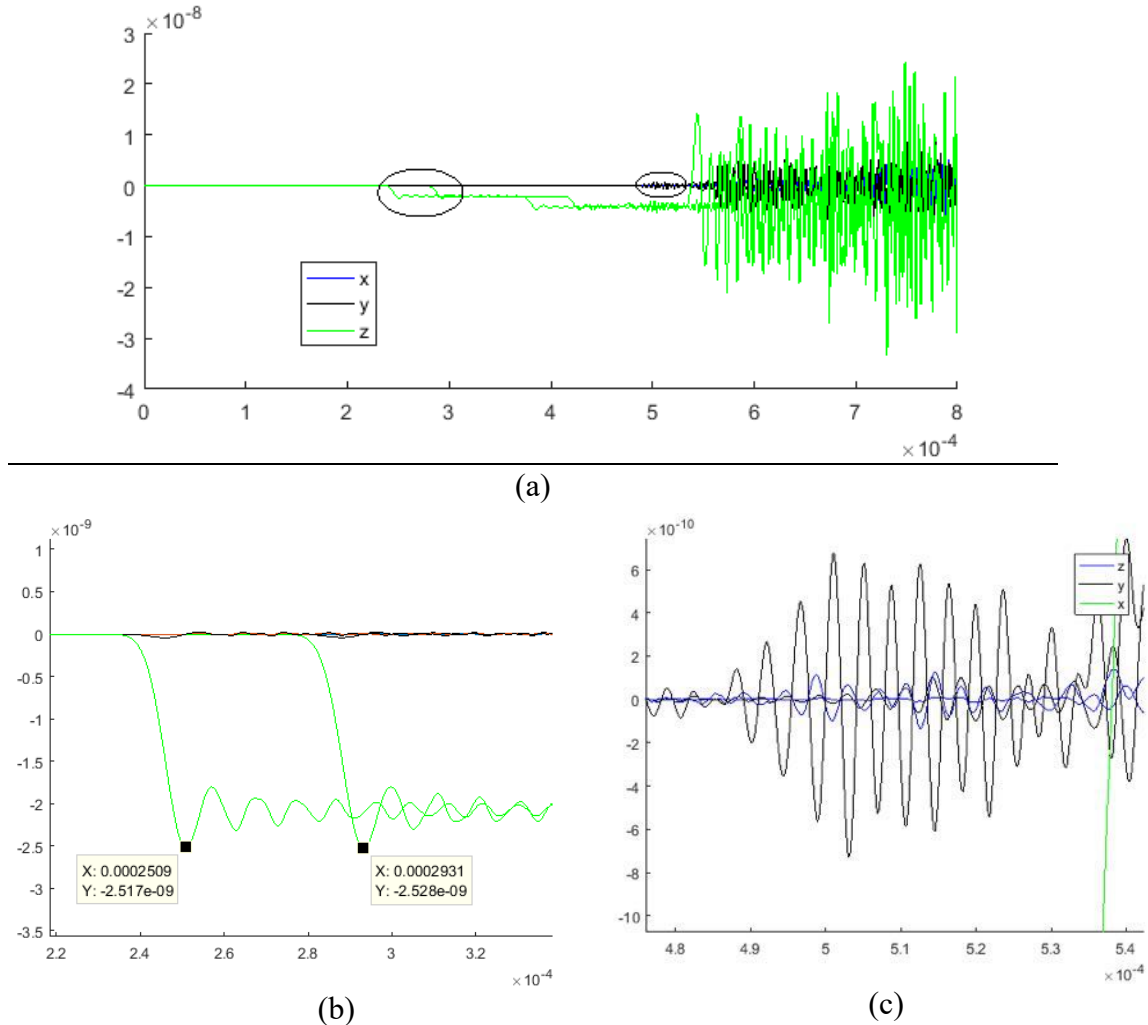


Figure 9: Sign at one of the monitoring points, in the three directions, z (green), y (black) and x (blue).

The detail, Figure 9 (b), shows the arrival of a typical compression wave, the points are at a distance of 190 [mm], and with the observed times, a velocity of propagation of 4500 m/s for this pulse can be calculated. Figure 8 (c) shows a zoom in of the second circled region in the signal. An energy packet (Figure 9, $t = 0.25$ milliseconds) is noticeable, which apparently assumes the form of a L propagation mode. This information can be used in the design of sensors customized for this type of signal.

The FFT (Fast Fourier Transform) of the acquired signal during crack growth in mode I, when compared to the dispersion curves of the waveguide (simulated beam) where the acoustic emission propagates, shows predominately generation of the longitudinal mode. This proves that the most prominent displacements happen in the direction of the mechanical wave propagation (Alleyne 1992).

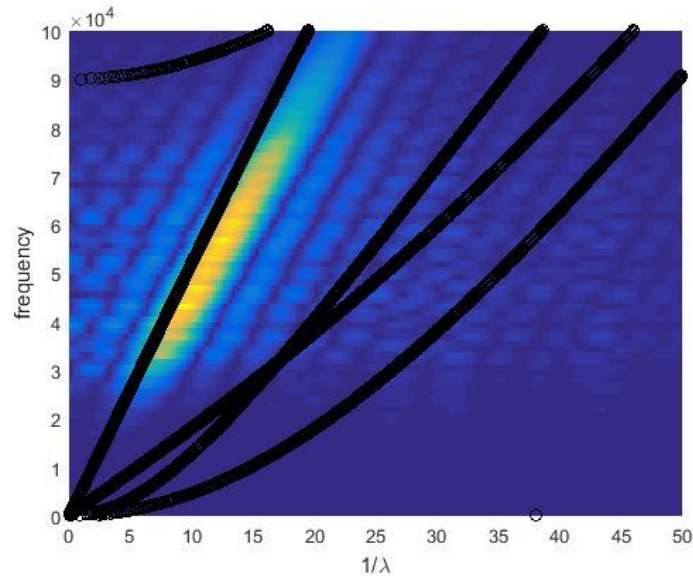


Figure 10 z direction displacements.

In Figure 10, the superposition of the dispersion curves found for the rectangular beam (Groth et al) is presented over the fft of the signal generated by the crack growth. The energy is concentrated in the curve which represents the longitudinal mode (P wave excitation) when the cracks grows in tensile mode. The signal exhibits a bit of noise in a large range of frequencies.

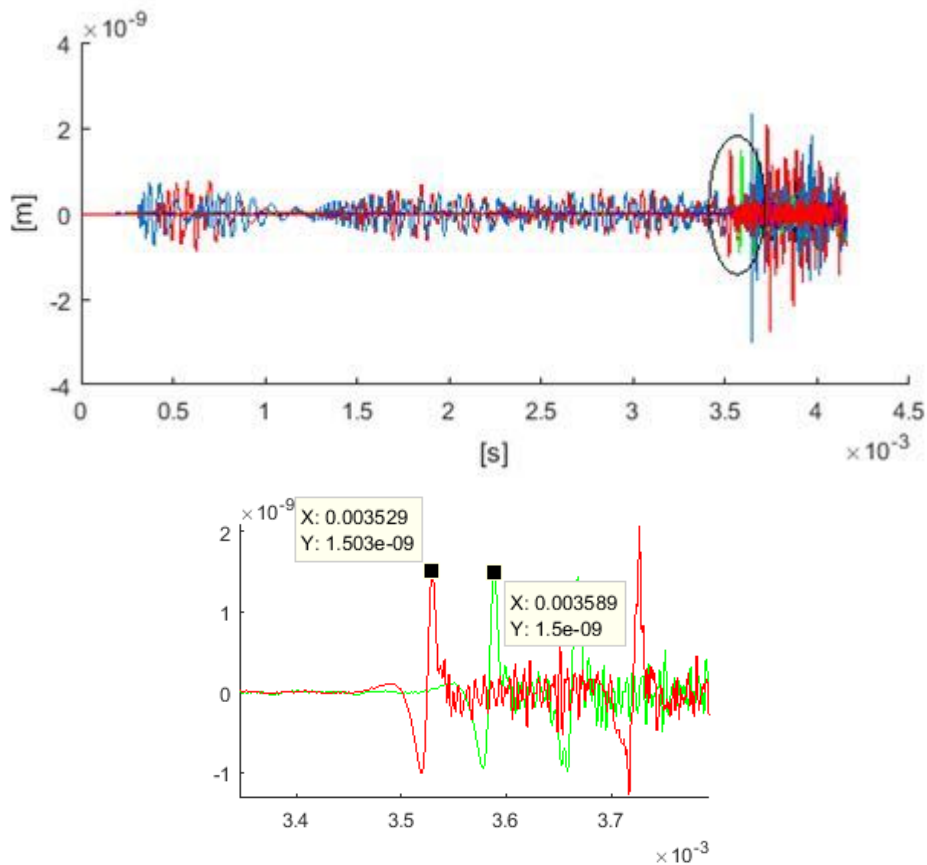


Figure 11: Analysis of the emission by the crack advance in mode 2 in the monitoring of a point. X, y and z shifts after signal processing (20-1500 kHz filter window).

Figure 11 shows the acoustic emission analysis of the crack growth in mode II. The signal exhibits movements preferably in the x and y directions, which indicates that the energy is propagating in mostly shear displacement. However a longitudinal pulse may also be generated (shown by the circle in Figure 11), with a velocity of 5000 m/s.

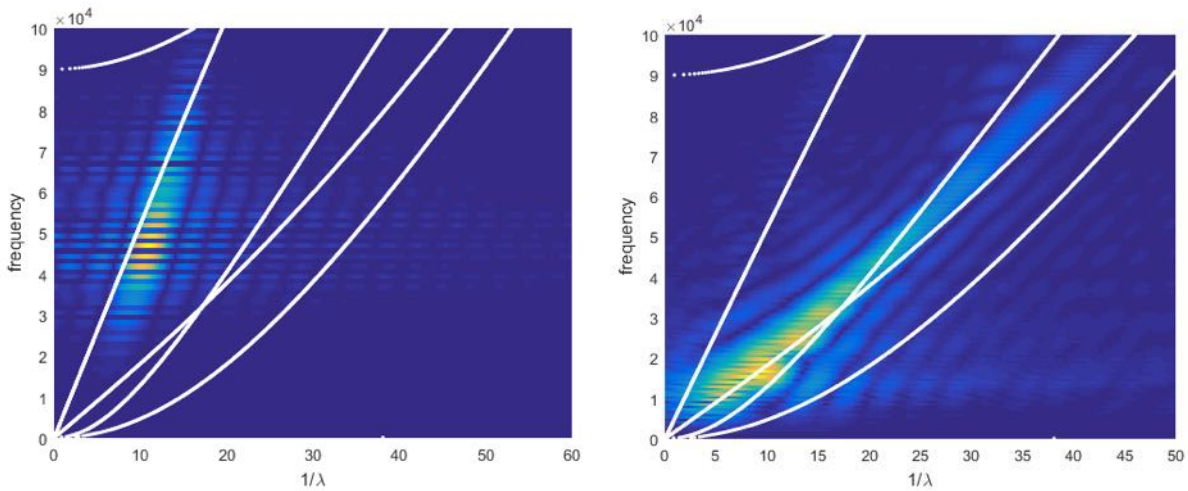


Figure 12: (Left) FFT of the emission produced by the crack in mode 2 (sliding); (right) FFT of the emission produced by the crack in mode 3 (tearing).

Figure 12 (right hand side) shows the FFT of the signal obtained through the propagation of the crack in mode 3 (tearing). In this analysis, it is also possible to notice the energy mainly in the torsional mode.

5. DISCUSSION

The idea of modeling the phenomenon is the understanding of the frequencies and preferable movements activated by the acoustic emissions in order to use this data in the design of high sensitivity sensors. One hypothesis of this work is that the energy released by the crack growth will assume some guided wave propagation mode in the beam where the crack is present. The geometry tested was a beam with a cross-section of 15 x 5 mm with a crack placed at the edge of the model. Loads applied to this edge caused the crack to advance in modes I, II and III.

Through the analysis of the results, the method is thought to produce a result that corroborates the hypothesis that the propagating modes are activated by the growth of cracks in wave guides. Simulations produced a wide range of information which can be used in the design and project of acoustic sensors.

Experimental validation should follow in the future in order to verify the technique and ensure it can be used to help advance the area of acoustic emission.

6. CONCLUSIONS

In this present work, a proposal of numeric modeling for crack propagation (which encompasses the acoustic emission produced in the direction of the crack growth) was presented

It was possible to use the hybrid approach to induce the crack growth and to analyze the propagation of wave mechanics in the same model. These two ideas were possible due to matching of two numerical techniques: traditional finite element method and discrete element method, the later allowing the rupture of the domain. The technique of the hybrid model is promising and produced a reasonable result with a wide range of information, which can be used in projects and in the understanding of the phenomenon, as long as the model is solid and reliable.

REFERENCES

- Alleyne D., Cawley P., (1990) A two-dimensional Fourier transform method for the measurement of propagating multimode signals. *JASA* 89:1159-1168
- Clarke, T. G. R.; Jacques, R. C.; Bisognin, A.; Camerini, C.; Damasceno, S.; Strohaecker, T.R. Monitoring the structural integrity of a flexible riser during a full-scale fatigue test, *Engineering Structures*, Volume 33, Issue 4, 2011, Pages 1181-1186, ISSN 0141-0296, <https://doi.org/10.1016/j.engstruct.2010.12.039>.
- Chao Xie, Linjuan Yuan, Min Zhao, Yinghui Jia, Study on failure mechanism of porous concrete based on acoustic emission and discrete element method, *Construction and Building Materials*, 235, 2020, 117409, ISSN 0950-0618, <https://doi.org/10.1016/j.conbuildmat.2019.117409>.
- Eagle DM, (2005) *Fundamentals of Acoustic Emission Testing: Wave Propagation*. In: Moore PO, et. al. *NDT Handbook* Vol. 6, 3rd ed.
- Groth E.B., Iturrioz I., Kostas L.E., Birck G., Silva G.S., and Clarke T.G.R., Acoustical Emission propagation in a prismatic wave guided: Simulations using truss like discrete element method. *PROGRESS IN ACOUSTIC EMISSION XVIII*. 2016
- Groth E. B. The dispersion curve applied in guided wave propagation in prismatic rods. *Latin American Journal of Solids and Structures*. 2018 doi: 10.1590/1679-782545274
- Jacques, R.; C.; Clarke T. G. R.; Morikaw, S.; Strohaecker T.R. Monitoring the structural integrity of a flexible riser during dynamic loading with a combination of non-destructive testing methods, *NDT & E International*, 43, 2010, 501-506, <https://doi.org/10.1016/j.ndteint.2010.05.005>.
- Jacques, R C; Flores, J V; Strohaecker, T R; Reguly, A. Acoustic emission testing in wires from the tensile armour of flexible risers under load. *Insight - Non-Destructive Testing and Condition Monitoring*, 51, 2009, pp. 504-507, 511, <https://doi.org/10.1784/insi.2009.51.9.504>.
- Paresh Mirgal, Joy Pal, Sauvik Banerjee, Online acoustic emission source localization in concrete structures using iterative and evolutionary algorithms, *Ultrasonics*, 108, 2020, 106211, ISSN 0041-624X, <https://doi.org/10.1016/j.ultras.2020.106211>.
- Rose JL (2014) *Ultrasonic guided waves in solid media*. Cambridge University Press, New York.
- Sengupta, Sanjay; Datta, Alope Kumar And Topdar, Pijush. Structural damage localisation by acoustic emission technique: A state of the art review. *Lat. Am. J. Solids Struct*. 2015, 12, 1565-1582. <https://doi.org/10.1590/1679-78251722>.
- Tirbonod, B.; Hanacek, L., Acoustic emission measurements during the local monitoring of a defect in the ZB2 pressure vessel, *NDT & E International*, 24, 1991, 3-14, [https://doi.org/10.1016/0963-8695\(91\)90676-T](https://doi.org/10.1016/0963-8695(91)90676-T).

Study of Fiber Bragg Gratings (FBG) as Acoustic Emission Sensor to Inspect and Monitoring Fiber-Glass Reinforced Polymers (FGRP) Degradation

da Silva, D.S., Groth, E.B., Walter, J.S., Lutckmeier, F., Zuglian, G. F., Jaques, R. C.,
de Lima, T.R.S. and Clarke, T.G.

Laboratório de Metalurgia Física, LAMEF, Universidade Federal do Rio Grande do Sul, BRASIL
e-mail: saraiva.silva@ufrgs.br

ABSTRACT

Fiber-glass reinforced polymers (FGRP) exhibit characteristics such as excellent chemical resistance and low weight which make their use specially attractive for a series of industrial applications, which include pressure vessels and pipes. However, a considerable inconvenience for the application in critical components is the lack of inspection and monitoring methods that allow structural integrity evaluation in a reliable and efficient manner. The objective of this work is the development of a method capable of inspection and monitoring based on acoustic emission (EA) using Fiber Bragg Grating (FBG) to be applied in the detection of failure and degradation of composite components made of FGRP. This new method has advantages over conventional acoustic emission methods: there is no risk of explosion in classified environments, immunity to magnetic field noise, low attenuation of the light pulses even for long distances and multiplexing capabilities. The first stage of this work consisted in the development, manufacture of the FBG sensors and characterization. After approval, the sensors were used to monitor the damage progression in a pipe segment under fatigue loading and results were compared to the data obtained with conventional EA sensors. The proposed method proved to be viable with great potential although further studies are required for sensibility optimization.

Keywords: Composite material, FGRP, monitoring, acoustic emission, Fiber Bragg grating.

1. INTRODUCTION

Technological advances in new materials create a demand for new inspection and monitoring techniques that can guarantee safe operation for critical structures and processes. In this context, composite materials and specifically fiber-glass reinforced polymers (FGRP) stand out due to properties such as high chemical resistance and low weight.

Among the techniques and inspection methods currently used to monitor damage and degradation of this type of material, acoustic emission (AE) is a promising alternative (Maggi, 2018). In this method, material degradation is associated to row of events of energy release which leads to acoustic emissions in the material; those acoustic emission events can be describe as transitory elastic waves generated by the rapid redistribution of strain inside the material during loading (Assarar, 2016).

Current standards and codes determine the use of piezoelectric transducers (PZT) as acoustic emission sensors (ABNT, 2005). However, this type of sensor has disadvantages such as coupling difficulties and large number of cables for signal acquisition, which imparts higher loads to the structure if a large number of sensors is used.

As an alternative, bragg gratings in optical fibers (FBG) can be used as EA sensors (Rajan et al, 2017). This type of sensor is largely used as a strain sensor due to its rapid response and great sensitivity to longitudinal stresses (Campanella et al, 2018). Studies have shown the EA monitoring capability of FBG if interrogating systems with high sampling rates for signal acquisition are employed. (Xia et al, 2015).

The use of optical fiber as a sensor has a number of advantages over conventional sensors, such as: smaller size and weight, multiplexing capabilities (more than one sensor in a single fiber), immunity to electromagnetic noise, low signal attenuation (readings can be taken kilometers away from the measuring point, and the possibility of instalation in classified environments with risk of explosion. (Rajan, 2015; Allil, 2010; Gomez et al, 2017).

The objective of this work is the development of an inspection and monitoring method based on acoustic emission with FBG sensors to be applied in the detection of failures and

degradation of components produced by FGRP composites. For this purpose, different tests were carried out for FBG sensor evaluation. The first stage consisted of monitoring the acoustic events produced in a controlled manner in a FGRP pipe segment. Piezoelectric sensors were used to allow comparison between data results. Later, the FBG sensor was used for damage and degradation monitoring in a FGRP pipe in a fatigue loading test.

2. FIBER BRAGG GRATING (FBG) AS ACOUSTIC EMISSION SENSOR (AE)

Fiber Bragg grating sensors are manufactured through techniques divided in two categories: interferometer techniques and non-interferometer techniques, through periodic exposition of the fiber to UV radiation. The most common non-interferometer technique uses phase masks, a diffractive optical element which spatially modulates the UV beam emitted by a laser. This technique was demonstrated for the first time in 1993 by K. O. Hill. (Hill et al, 1993).

Bragg grating in optical fibers can be described as a periodic modulation of the refraction index in the core of the fiber. This periodic modulation is perpendicular to the longitudinal axis of the fiber and exhibits constant spacing between each period. The functioning principle of this sensors involves the use of an optic interrogator, which is responsible for emitting a light pulse through the fiber and is also responsible for acquiring the reflected signal. The light pulse emitted by the interrogator interacts with the Bragg grating and is reflected in the opposite direction. This reflection is centered in a specific wavelength, called Bragg wavelength (λ_b). (Rajan, 2015). λ_b is a function of the effective refraction index of the optical fiber (n_{eff}) and the grating period (Λ_b), according to equation 1:

$$\lambda_b = 2 * n_{eff} * \Lambda_b \quad (1)$$

The signals obtained by the FBG sensors are associated to variations of the grating period in the Bragg sensor due to longitudinal stresses or temperature variations. This correlation of the Bragg wavelength with strain and temperature is described by equation 2:

$$\frac{\Delta\lambda}{\lambda_0} = (1 - p) * (\epsilon_m + \alpha_{sp} * \Delta T) + \alpha_\delta * \Delta T \quad (2)$$

Where p is the photo-elastic coefficient (0.22), ϵ is the strain, α_{sp} is the thermal expansion coefficient of the material, α_δ is the fiber refraction index variation and ΔT is the temperature variation.

3. METHODOLOGY

The methodology used in this work is divided in three distinct stages: development and manufacture of the Bragg gratings, evaluation of sensor response to acoustic events generated in a controlled manner and evaluation of performance in dynamic testing (fatigue).

3.1. FBG Sensors Development and Production

In the stage of sensor development and production, the FBG sensors were produced by using the technique with phase masks and were later encapsulated. The laser equipment used for fabricated the Bragg gratings on to the fibers was a Braggstar M from Coherent company. This laser is operated with energy pulses that emit ultraviolet radiation with a wavelength of 248 nm, and a variable operating frequency up to 100 Hz.

The procedure of sensor manufacturing consisted in exposing the core of the fiber (10mm area), which becomes the active length of the sensor. This area is positioned behind the phase mask, which is a diffraction optical element with carefully controlled engravings on one of the faces. This spacing is called Bragg grating period (Λ_{pm}), and each masks has a specific Λ_{pm} which will originate a specific FBG sensor.

In this work, the phase mask had a $\Lambda_{pm} = 1063$ nm, which resulted in a FBG sensor with a $\lambda_b = 1550$ nm. The phase mask was chosen to allow λ_b of the sensor to be inside the measuring range of the optical interrogator, which is from 1530 nm to 1558 nm.

In Figure 1 the production of the FBG is illustrated. The laser emits UV light pulses which hits on the reflective mirrors. These mirrors redirect the UV lightbeam to a cylindrical lens positioned in front of the phase mask that collimates the beam and concentrates the energy. At last, the beam goes through the phase mask and is diffracted, reaching the core of the fiber that was positioned behind the mask, which originates the FBG sensor.

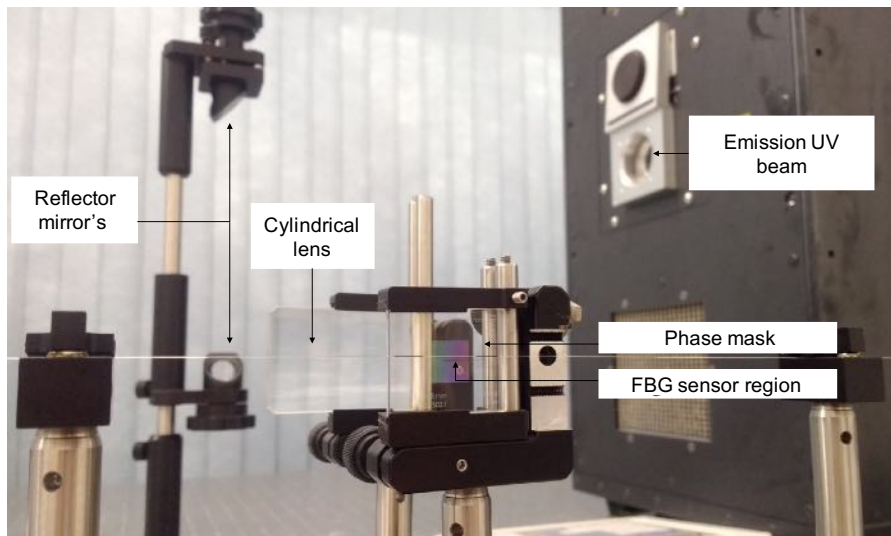


Figure 1 – Manufacturing of FBG sensors with the phase mask technique.

Due to the frailty of the fiber, it was necessary to develop a proper encapsulating method to allow manipulation and installation of the FBG sensor. The sensor is initially glued to a polyimide substrate, which is responsible for transferring the deformation of the surface to the sensor.

3.2. Evaluation of The Response to Acoustic Events Generated in A Controlled Manner

In this stage, the response of the FBG sensors to static tests consisting of lead break acoustic emissions was compared to signals obtained with piezoelectric sensors. The interrogator used for the acquisition of the acoustic emission signals was a FI3200, from Fiberpro company, with an acquisition capacity of up to 100 kHz. The equipment used for the piezoelectric sensors was an AMSY-5, from Vallen, and VS-30 sensors without any pre-amplification.

The static test for technique comparison (FBG vs piezo sensors) is presented in Figure 2, which shows the sensors attached to a GFRP pipe segment. The FBG sensor was glued to the sample with a rapid cure cyanoacrylate resin. The piezoelectric sensors were coupled with vaseline grease and held in place with adhesive silver tape. The spacing between the sensors was 300 mm.

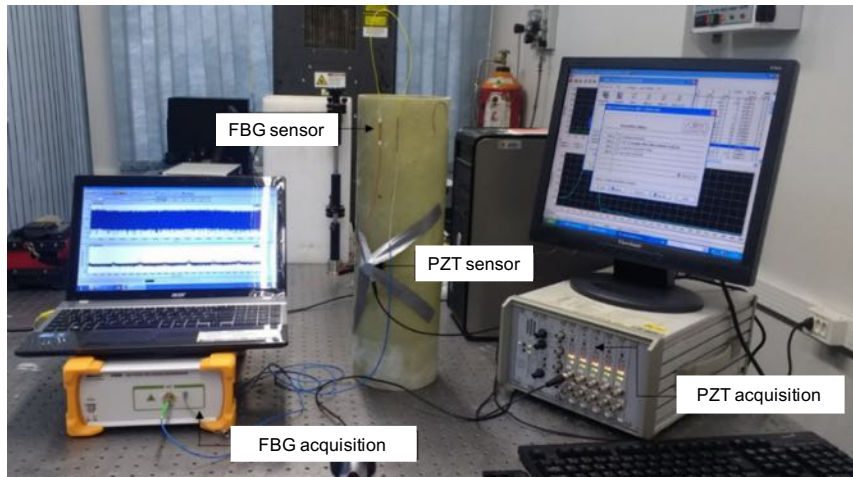


Figure 2 – Setup of static test.

3.3. Performance Evaluation in Dynamic Tests

The performance of the FBG sensors in dynamic tests was evaluated during fatigue loading (5000 loading cycles) of a GFRP pipe segment. Figure 3 shows the test setup. A FBG sensor was positioned at the center of the pipe, longitudinal direction, with cyanoacrylate resin. Signal acquisition was carried out with a FI3200 equipment.



Figure 3 – Setup dynamic test.

4. RESULTS

4.1 FBG Sensor Development and Production

The methodology chosen for sensor production and encapsulation was proven to be efficient. It was possible to obtain sturdy sensors with good reflectivity. In Figure 4, the optical response of the FBG sensor with $\lambda_b = 1050.60$ nm is presented. The sensor after encapsulation is presented in Figure 5.

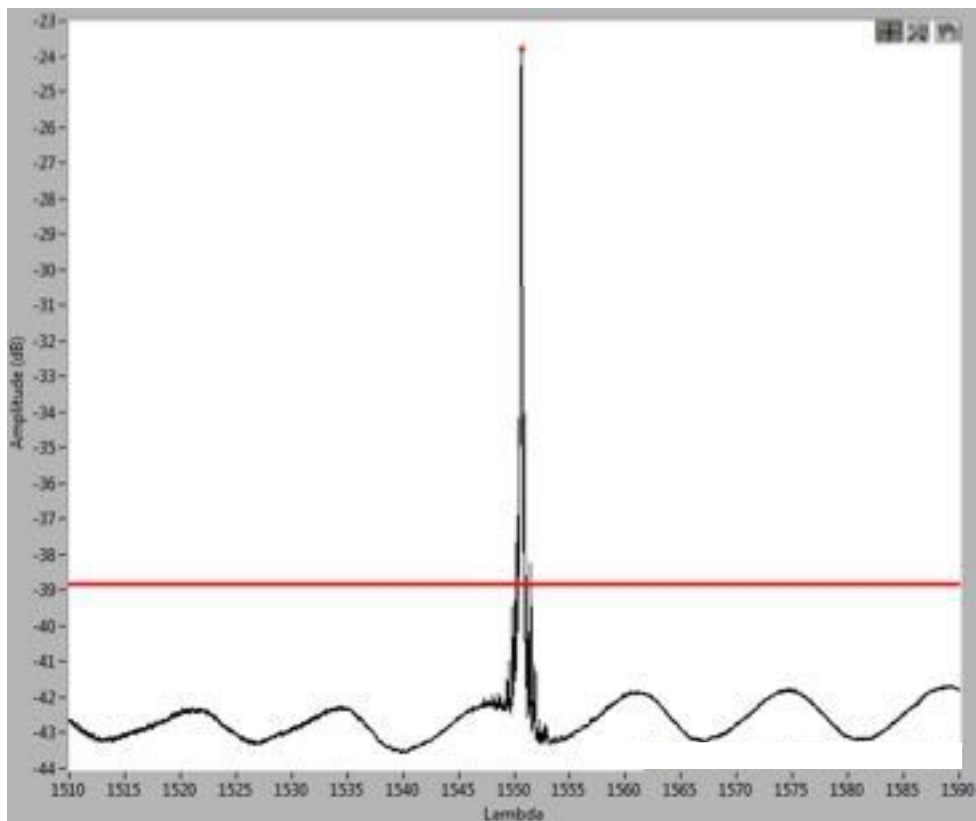


Figure 4 – Optical spectrum of the FBG.

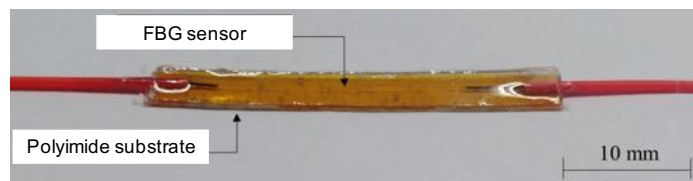


Figure 5 – Encapsulated FBG.

4.2 Evaluation of The Response to Acoustic Events Produced in A Controlled Manner

Results obtained in the lead break test for performance evaluation of the FBG sensors compared to commercial piezoelectric sensors were satisfactory, since it was possible to detect the acoustic events with both sensors. In Figure 6 (a) a waveform of the signal captured by the piezoelectric is presented, and Figure 6 (b) shows the result of the FBG sensor to the same event.

In Figure 6 (b) it is possible to see the signal to noise ratio for the FBG sensor is approximately 7.6x (maximum signal amplitude 0,01629 nm and background noise with an amplitude of 0,00214 nm).

A comparative analysis of the signal amplitudes (in dB) obtained for each sensor is presented in Figure 7. Three events were generated with the lead breakings, always in at the same position. The amplitude of the signals acquired with the PZT sensor is considerably higher than the signals obtained with the FBG sensors. It was also more constant. An amplitude variation for the FBG signal is noticeable on the third event (higher than 10dB). No significant amplitude variations were detected with the PZT sensor.

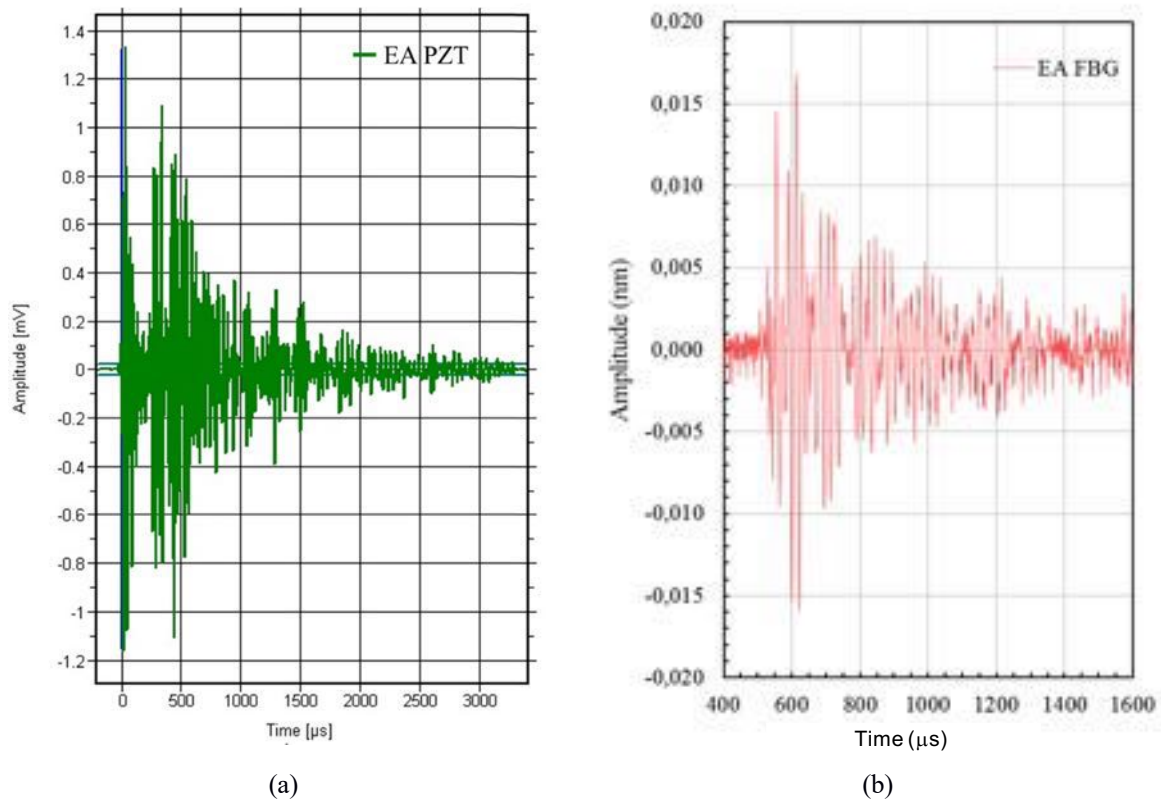


Figure 6 – Evento acústico adquirido com sensor (a) PZT and (b) FBG.

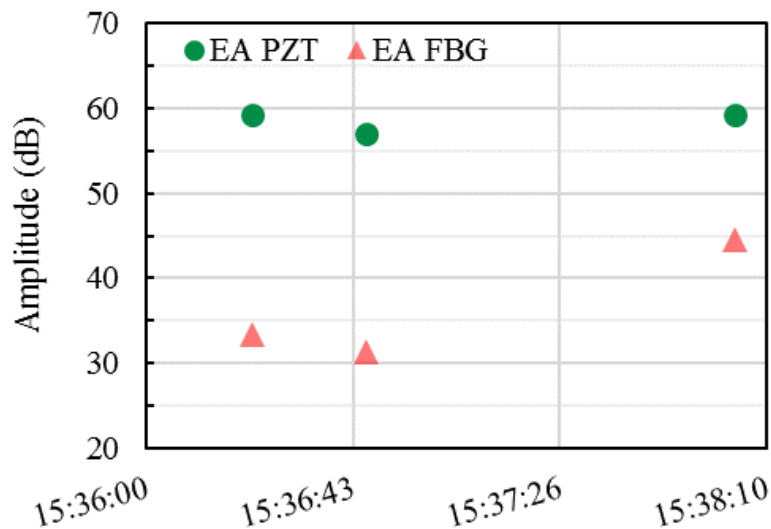


Figure 7 – Comparative amplitude of the signals acquired by the FBG and PZT sensors in dB.

4.3 Performance Evaluation in Dynamic Fatigue Test

The acoustic emission events were monitored during the fatigue load testing. In this work will be presented the results of the beginning of the 5.000 cycle fatigue load. Figure 8 shows the acoustic emission events detected by the FBG sensor. Three events can be identified that have amplitudes higher than the threshold.

Figures 9 (a) and 9 (c) show the data related to the events detected above 50 dB, at time instants 11:38:51 and 11:39:59, whereas Figure 9 (b) and 9 (d) show a zoom-in of the areas of the respective events.

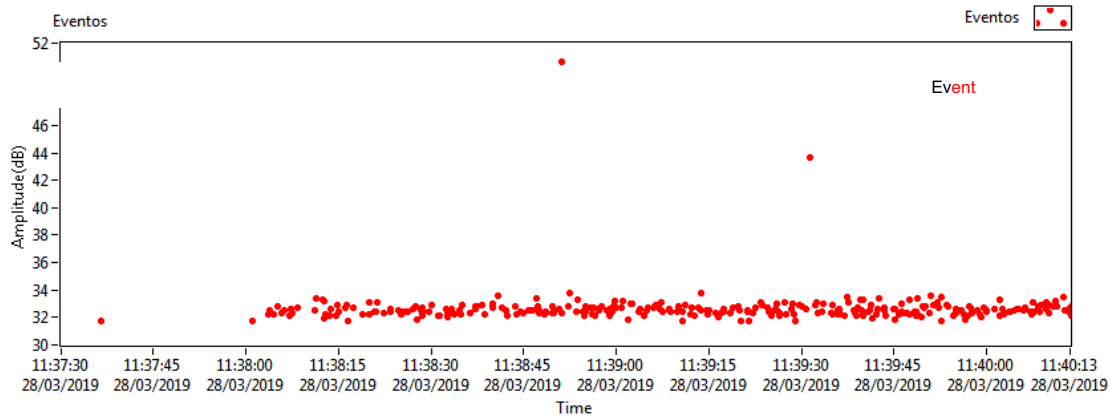


Figure 8 – Acoustic emission events detected during fatigue loading test.

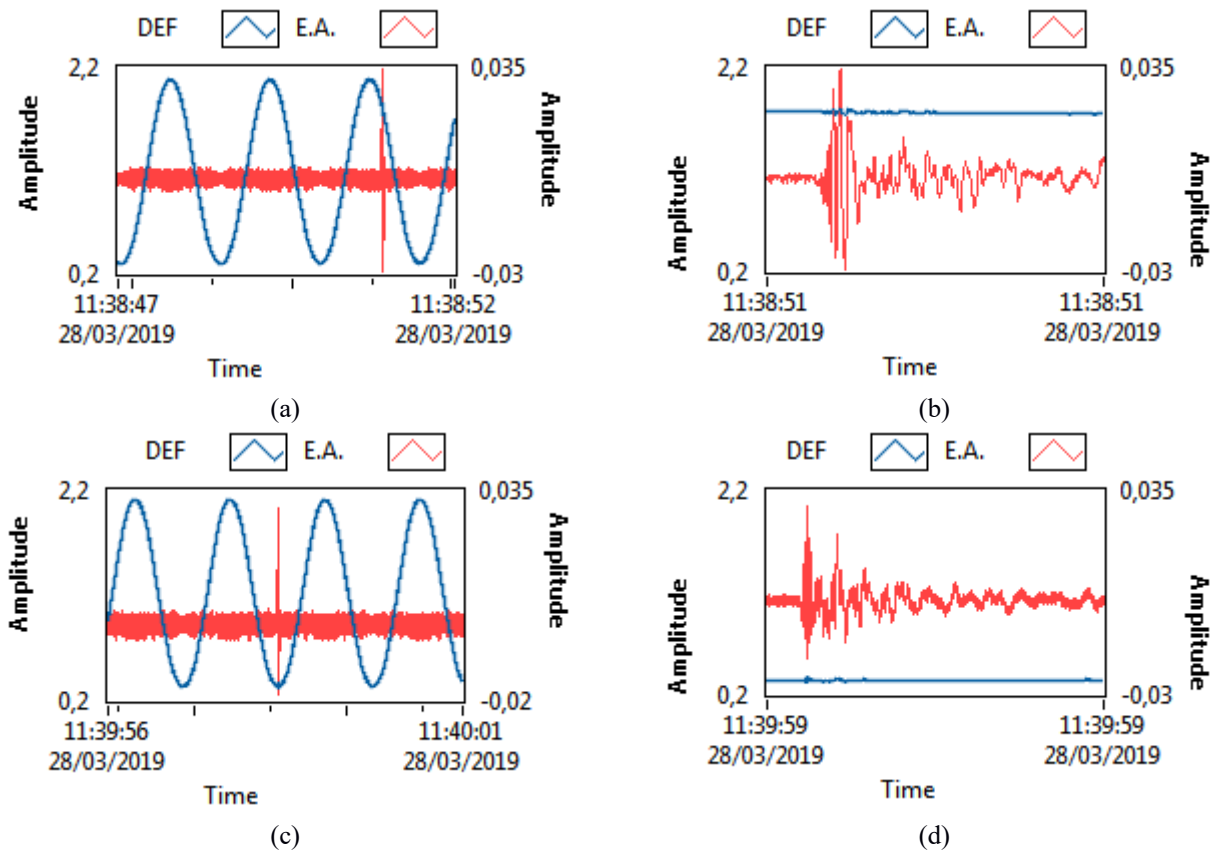


Figure 9: (a) event detection; (b) stress signal (DEF) and acoustic emission (E.A.) in the detected event; (c) increase in the region of the event.

The acoustic emission events detected with the FBG sensor presented an acceptable signal to noise ratio, and the amplitude of the highest event was 0.035 nm.

Even though it is not possible to correlate these events to the GFRP composite damage or degradation, it is evident that the FBG sensors are capable of detecting acoustic emission events of the material, and further investigations should be carried out in the future.

5. CONCLUSIONS

In this work, the development of an inspection method based on acoustic emissions captured with fiber Bragg grating sensors for composite materials of the GFRP type was presented.

The methodology for sensor fabrication was proven to be efficient and allowed the production of FBG sensors with a wavelength λ_b within the expected range. The procedure for the FBG

sensor encapsulation was successfully applied and increased the resistance of the sensor during handling.

The FBG sensors detected acoustic emission events generated in a controlled manner through lead breakings with a signal amplitude of 0.0165 nm, 7.6x above the background noise. In comparison, the average amplitude of the PZT sensor was 58 dB whereas the average signal amplitude for the FBG sensor was 36 dB.

In the dynamic test the FBG sensors detected acoustic emission events with an amplitude of 0,035 nm. It was not possible, though, to correlate such events to any damage associated to material degradation.

Results obtained in this work are promising and serve as an illustration of the evident capacity of the FBG sensors to detect acoustic emission and monitor composite materials of the GFRP type, both for static and dynamic tests.

REFERENCES

- ABNT - Associação Brasileira de Normas Técnicas. NBR 15269 – Ensaios não destrutivos – Monitoração contínua por emissão acústica – Procedimento. 2005.
- Allil R. C., “Sensores a fibra óptica com tecnologia FBG para medida de temperatura e alta tensão”, Tese (Doutorado) – Universidade Federal do Rio de Janeiro, CPPE, Programa de Engenharia Elétrica. 209 f, 2010, Rio de Janeiro, Brasil.
- Assarar, M., Scida, D., Zouari, W., Saidane, E., Ayad, R. Acoustic emission characterization of damage in shorthemp-fiber-reinforced polypropylene composites. *Polymer composites* 2016. 1101-1112.
- Campanella, C., Cuccovillo, A., Campanella, C., Yurt, A., Passaro, V., Fibre Bragg grating based strain sensors: review of technology and applications. *Sensors* 2018, 18, 3115;
- Gomez, J., A., Ozdagali, A., I., Moreu, F., Reference-free dynamic displacements of railroad bridges using low-cost sensors. *Journal of intelligent material systems and structures* 2017. v. I, n. 15.
- Hill, K. O., Malo B., Bilodeau F., Johnson D. C., Albert J., Bragg gratings fabricated in monomode photosensitive optical fiber by UV exposure through a phase mask, *Appl. Phys. Lett.* 1993. 62, 1035–1037.
- Maggi, A. Aplicação da técnica da emissão acústica em análise de dano em estruturas reforçadas com fibras. Monografia - Universidade Federal do Rio Grande do Sul. 25 f. 2018.
- Rajan G. “Optical Fiber Sensors Advanced Techniques and Applications”, Taylor & Francis Group, LLC, 2015, pág. 207.
- Rajan, G., Vinod, J., Moses, T., Prusty, B., Xi, J., Ballast breakage analysis using fbg acoustic emission measurement system. *Geotech Geol Eng* 2017; 35:1239–1247.
- Xia, M., Jiang, M., Sui, Q., Jia, L., Theoretical and experimental analysis of interaction from acoustic emission on fiber Bragg grating. *Optik* 2015. 126. 1150–1155.

Autonomous System for Passive Acoustic Monitoring of Cetaceans

Veca, A. C.^a, Valse, N.^b, Ruzzante, J.^{c,d}, Albalat, A.^b, Marino, A.^b, Reyes Reyes, M. V.^b

^aInstituto de Automática, Facultad de Ingeniería, Universidad Nacional de San Juan, ARGENTINA; e-mail: aveca@inaut.unsj.edu.ar

^bGrupo de Investigación en Acústica Subacuática, Universidad Nacional de Tres de Febrero – Fundación Cethus, ARGENTINA

^cLaboratorio de ensayos no destructivos, Universidad Tecnológica Nacional, Facultad Regional Delta, ARGENTINA

ABSTRACT

This paper describes the development of an autonomous system for passive acoustic monitoring of cetaceans in the Argentine Sea. The system consists of an omnidirectional hydrophone with a piezoelectric transducer designed and built for this purpose, which record signals in a frequency range up to 200 kHz. The signals are processed by a digital algorithm based on pattern identification to extract the data of interest and store it in a temporary memory. Once the memory capacity is full, the data is sent through WiFi to a land-based station located 6 km away, for its analysis. The system will be anchored at a depth of 40 m and submerged 5 m below the surface, with autonomy for 2 months. To date, tests in laboratory using patterns of sounds produced by cetaceans in the wild, show that the system is capable of fulfilling the proposed objective.

Keywords: cetaceans, emission pattern, underwater acoustics.

1. INTRODUCTION

In nature, many species of animals use sound as the main way of communication (fig. 1). In particular, bats in air and odontocetes in water have developed a biosonar or echolocation system to detect obstacles and to search and locate their prey. For this purpose, they use the pulse-echo technique with frequencies above 20 kHz (Veca *et al*, 2019).

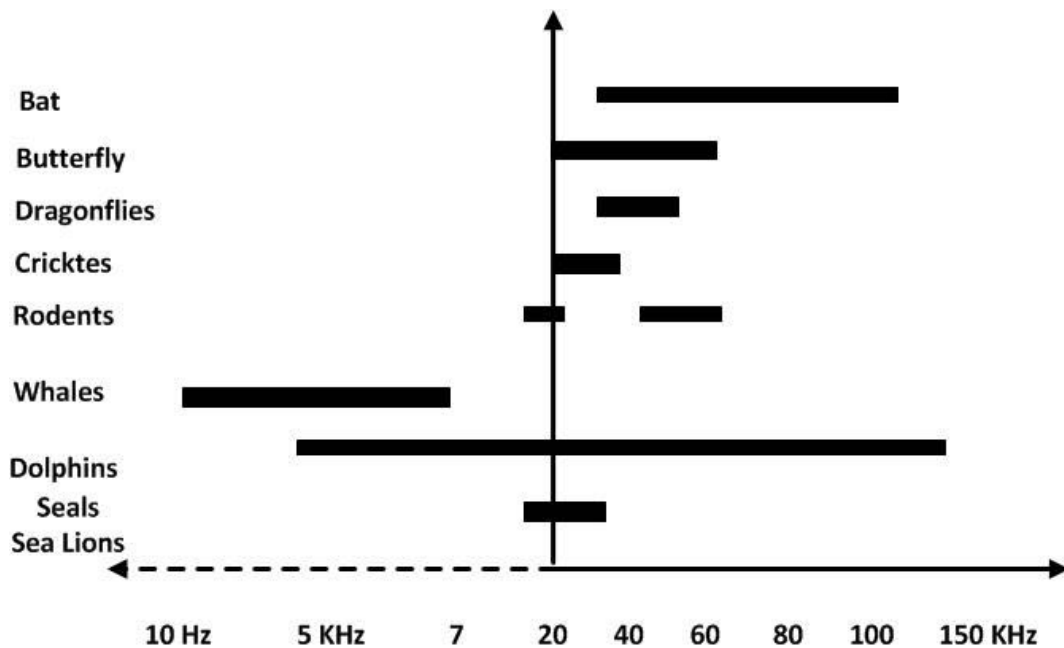


Fig. 1. Acoustic spectrum in nature

As light does not penetrate too deep into the ocean, cetaceans rely on sounds as their primary sensorial sense. They produce a variety of sounds that can be recorded for long or short periods

of time as well as in real time using passive acoustic monitoring tools, such as autonomous hydrophones that store the information inside. In general, the acoustic signals emitted by cetaceans are unique to each species, which allows getting relevant ecological information of each species through non-invasive studies using passive acoustics. One reason to this is the fact that propagation speed of acoustic waves in water is five times higher than in air. These characteristics allow acoustic energy to propagate over long distances with reduced attenuation. As disadvantages, sound transmission is affected by the frequency of the signal, the absorption loss and the noise present in the medium.

This paper presents preliminary results of the development of an electronic prototype system for the recognition of sounds emitted by cetaceans and transmission to a station located on the coast for further analysis. The main objective is the development of an acoustic system for passive acoustic monitoring of cetaceans in the Argentine sea.

A particular objective is to gain experience in the development of automatic systems for recording signals in a hostile environment and transmitting data to an autonomous station located on the coast. The general scheme of the system is shown in fig. 2. The data-acquisition zone will be submerged 5 m below the surface and contains an omnidirectional hydrophone and a built-in pre-amplifier.

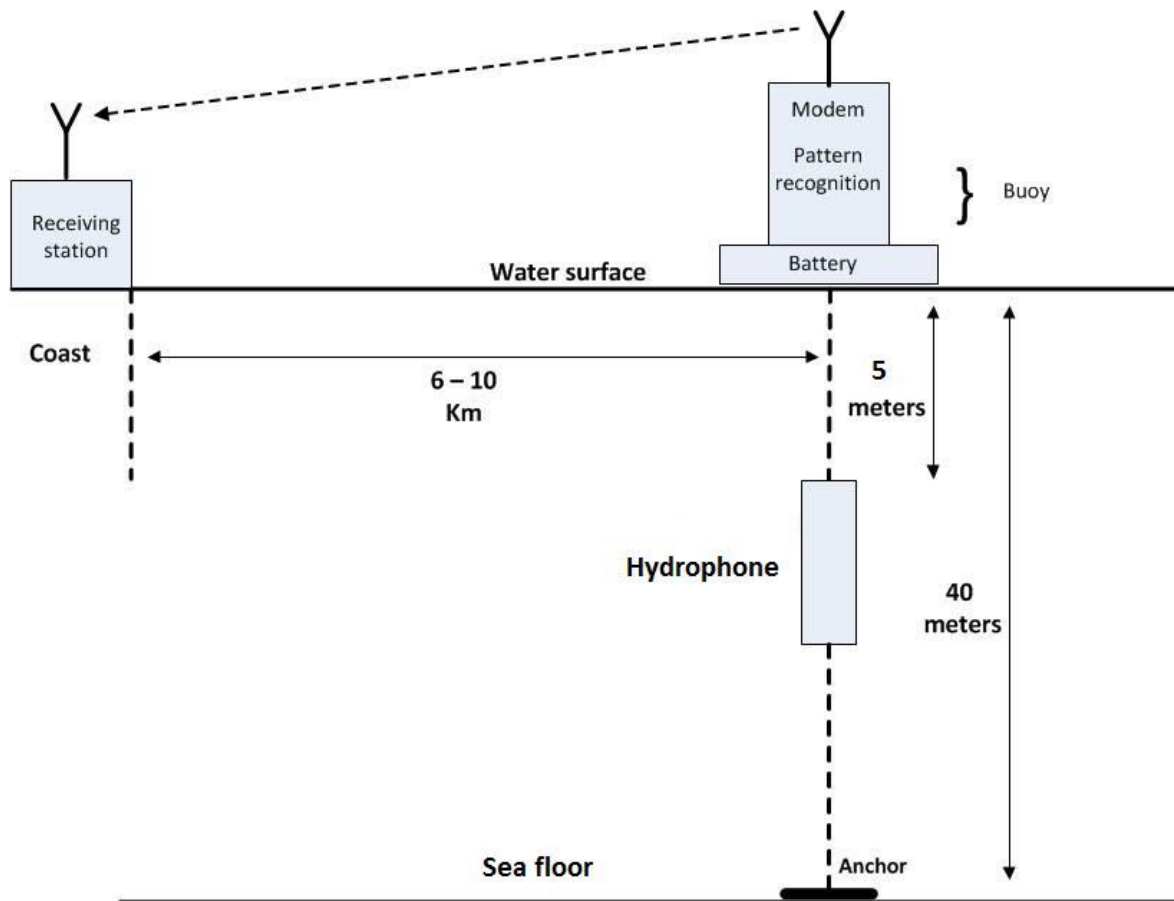


Fig. 2. Scheme of the system

The buoy contains the electronic system for the recognition of the acoustic signals captured by the hydrophone, an analog to digital converter ADC with its corresponding memory, the batteries and a modem with an antenna for the transmission of the signals to the land-based station.

2. CHARACTERISTICS OF THE WORK ENVIRONMENT

Sound Speed

As already mentioned, the sound propagation of the marine environment is characterized by the speed, absorption loss and noise presence. The sound velocity profile shown in fig. 3 (Kinsler *et al.*, 1980) is divided into four zones, being the upper layer (surface layer) the one of interest in this case as the hydrophone will be submerged 5 m deep. This layer is influenced by local environmental variables. The speed of sound decreases with a soft negative gradient, taking an approximate value of 1,495 m/s. The surface layer presents characteristics of isothermal water mixed by the action of the wind at the surface of the ocean. Sound tends to be trapped by reflections on the surface and refractions upwards from the bottom due to the change in acoustic impedance (fig. 4).

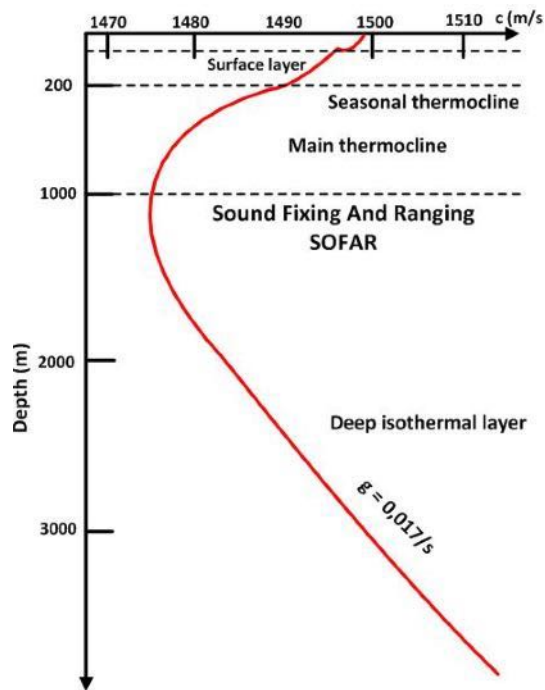


Fig. 3. Sound speed profile in the ocean.

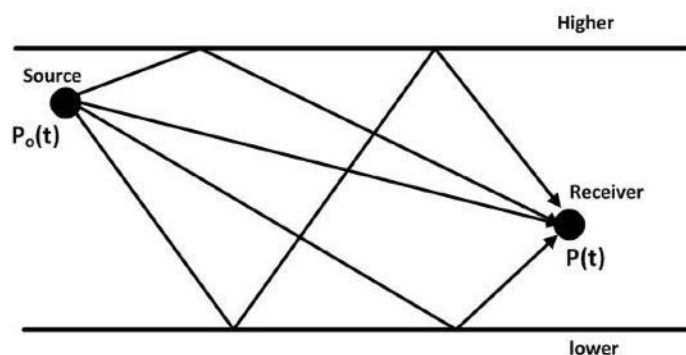


Fig. 4. Sound reflections and refractions within the surface layer

Transmission Loss

If the wave front is considered spherical, then absorption loss can be modelled by (Agost González, 2015):

$$TL(dB) = 10 * \log(r) + \alpha r * 10^{-3} \quad (1)$$

where r is the distance from the source to the receiver in km and α is the absorption coefficient in dB/km. α is a function of frequency (f):

$$\alpha = 0,11 \frac{f^2}{1+f^2} + 44 \frac{f^2}{(4100+f^2)} + 0,000275f^2 + 0,0003 \quad (2)$$

Given that the signals of interest, further described below, have all their energy above 100 kHz, the absorption attenuation, α , is about 30 dB/km. Assuming a source-receiver distance of 10 km, the transmission loss would be about 10 dB, which shows the reduced attenuation of the acoustic wave front in the water.

Noise

Soundscapes, or acoustic environment in the ocean are composed of three different acoustic sources: 1) the geophony comprised sources from the physical ambient such as water currents, bubbles due to non-linear processes, the movement of waves, earthquakes, etc; 2) the biophony composed by sounds produced by marine life, such as schools of fish, cetaceans, among others; and 3) anthropophony, which includes noise produced by human activities at sea, such as shipping, naval exercises with sonars, etc. Fig. 4 shows the time series (bottom left), spectrogram (top left), and the noise density spectrum (right) of a fragment of a recording. The spectrogram and the noise levels are referred to 1 μ Pa. As observed, the low frequencies present a higher relative level in the spectrum, 110 dB in the vicinity of 1 Hz due to the low attenuation at low frequencies, while the average is in the order of 80 dB.

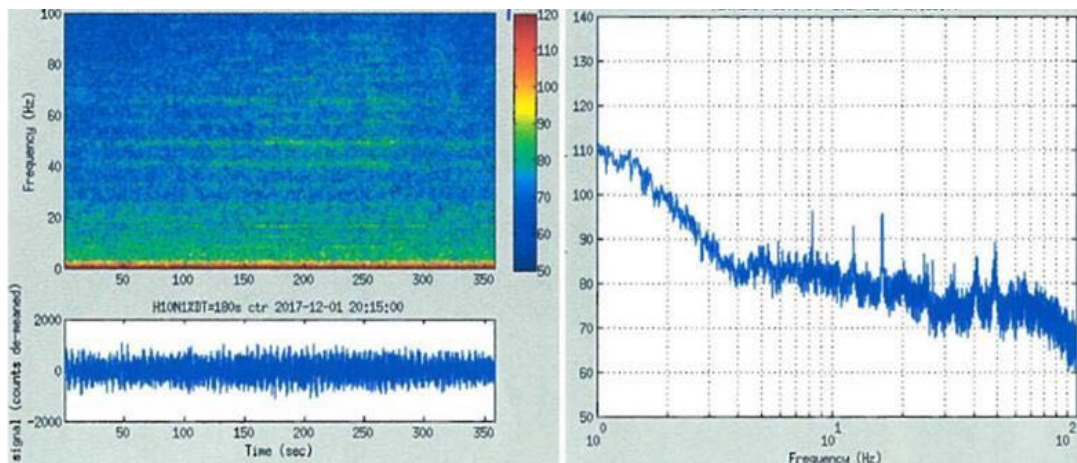


Fig. 4. Ocean noise levels

From this analysis, it is concluded that the average noise level belongs to frequency bands much lower than the frequency range emitted by the dolphins, presenting a salvable influence. Furthermore, the profile of the seabed at the distance where the hydrophone will be located is similar to that indicated in fig. 5, presenting low-pass filter characteristics (Medwin, 1998).

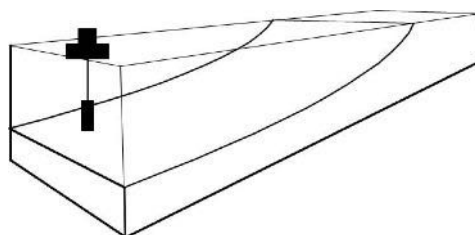


Fig. 5. Seabed profile where the hydrophone will be located.

3. EMITTED ACOUSTIC SIGNAL

A specific type of signals that could be present in the designated recording area is the Narrow Band High Frequency (NBHF) click. These clicks have been previously described and assigned to several species of porpoises and small dolphins (Reyes *et al.* 2018, Melcón *et al.* 2012, Kyhn *et al.* 2009) as well as the pygmy sperm whale (Madsen *et al.* 2005). These acoustic signals are often stereotyped, presenting a peak frequency around 120-130 kHz, no energy below 100 kHz, 3 dB bandwidth around 15 kHz (Reyes *et al.* 2018, Madsen *et al.*, 2005) and durations of around 300 μ s. Due to the high frequency content of NBHF clicks, these result to be highly directional (Martin *et al.* 2018, Kyhn *et al.* 2010), making them difficult to record when being emitted away from the axis between the hydrophone and the animals head.

Clicks are normally produced within click trains, in which a regular inter click interval (ICI) between 5-50 ms (Reyes *et al.* 2018) separates one click from another. Figure 6 shows a fragment of a recording including a series of NBHF clicks recorded at the location where the currently described autonomous system will be deployed.

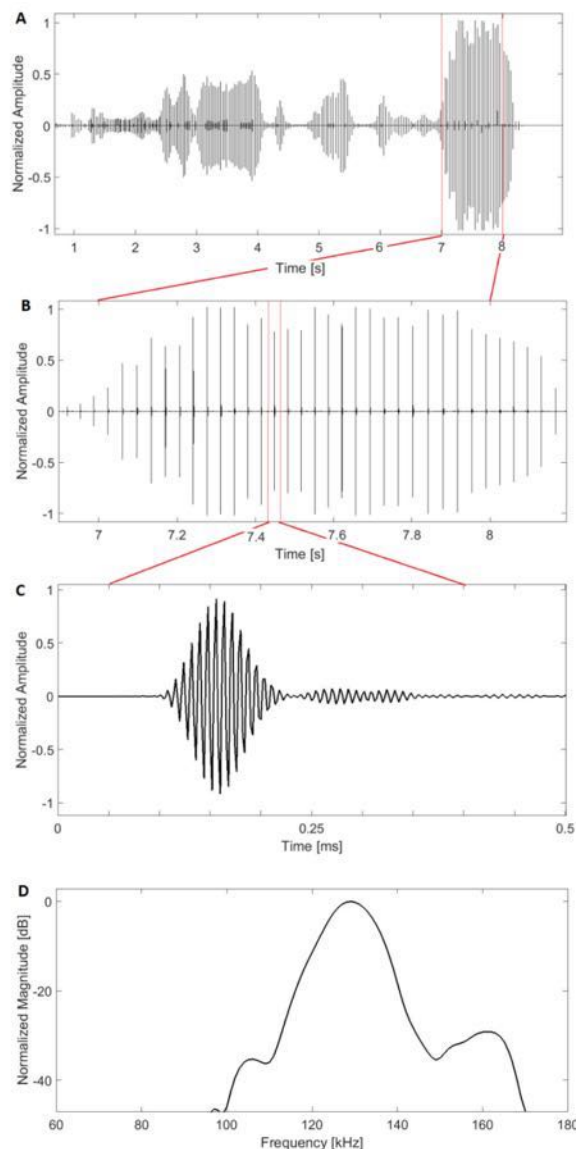


Fig. 6. Acoustic recordings from Peale's dolphins (*Lagenorhynchus australis*) in Argentinean Patagonia. a) Series of click trains; b) zoomed fragment of single click train; c) zoomed single click within a click train; d) 512 FFT points normalized power spectrum of click in (c) (Marino 2017)

If the system transmits to the land-based receiving station, all the sounds recorded by the hydrophone, the transmitting modem should always be active. Taking into account the technical specifications of the modem, the consumption of 1 Amp/h would make it impossible

to achieve a reasonable autonomy of the system. Added to that, the consumption of the rest of the electronic systems should be considered. To overcome this limitation, it was decided to develop a simple criterion for the recognition of the signal of interest. The criterion used in acoustic emission (Ruzzante & Pumarega 2017) and in the determination of threshold transit time for ultrasound signals (Veca, 2019) was chosen. That is to use a decision threshold above the noise level present in the signal and a time window that takes into account the average ICI, as shown in fig. 7.

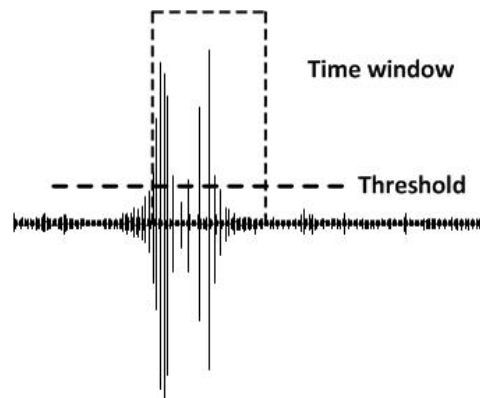


Fig. 7. Threshold and temporal window

4. SYSTEM IMPLEMENTATION

This project comprises three fundamental components: the reception of acoustic signals emitted by cetaceans, their discrimination with respect to other signals present in the marine environment and the transmission of recorded data to a receiving station located on the coast. Below the development of the hydrophone is presented, then the recognition and recording system of the received signals, and finally the data transmission is explained.

4.1 Hydrophone

The design of the hydrophone considered different parameters related to its future implementation for research studies:

- The temperature of the aquatic environment does not affect the functioning of the piezoelectric ceramic.
- The equipment is resistant to the environment in which it will work.
- The sensitivity and frequency response of the hydrophone are adequate for the study signals.
- The cable length is adequate for the depth in which the hydrophone will be placed during measurement.

Design and manufacturing are separated into three main parts. In the first instance, the transducers were characterized and measured under different circumstances in order to optimize the following stages. Secondly, the preamplifier circuit was designed contemplating the values obtained in the previous stage, and finally, the housing where all the electronics are mounted together with the transducer was designed and built.

4.1.1 Transducer

In order to choose the type of transducer for this application, it is necessary to take into account that water impedance ($1.54 \times 10^6 \text{ Pa}\cdot\text{s}/\text{m}^3$) is much higher than that of air ($412 \text{ Pa}\cdot\text{s}/\text{m}^3$), therefore the transducer must be robust and capable of generating a great force (Rossing *et al.*, 2004) In this work it was decided to implement two piezoelectric ceramics as a transducer element since its firmness makes it capable of supporting or producing great efforts.

The working frequency range that is intended to be covered goes from 10 Hz up to 200 kHz. Taking this into account, it was decided to use piezoelectric ceramics as they are the electroacoustic transducers that best fit the needs of this study. Two different types of ceramics were implemented in order to cover the entire frequency range of interest. The first one presents a hemispherical geometry (fig. 8) in order to obtain a broader directionality in its receiving pattern.



Fig. 8 – Hemispherical piezoelectric of Sonox P53 material, CeramTec

The ceramic belongs to the CeramTec brand and it is made of a material that is a registered design called Sonox P53 (CeramTec, Germany). The characteristics of this hemisphere PZT ceramic is shown together with its resonance frequency in table 1.

Table 1 – Characteristics of the hemispherical crystal.

<i>Parameter</i>	<i>Measurement</i>
Internal radius	5.25 mm
External radius	6.25 mm
Width	1.00 mm
Resonance frequency	172 kz

Secondly, a cylindrical piezoelectric ceramic was implemented to omnidirectionally cover the low frequency bandwidth of interest. Fig. 9 shows this PZT ceramic and its dimensions and resonance frequency are shown in table 2.



Fig. 9 – Cylindrical piezoelectric, Steminc SMC32D30H10410.

Table 2 – Characteristics of the cylindrical crystal.

<i>Parameter</i>	<i>Measurement</i>
Internal radius	30 mm

External radius	32 mm
Height	10 mm
Resonance frequency	29.5 kHz

These piezoelectric elements were analyzed under different circumstances in order to estimate the impedance curve in each of them (fig. 10). This measurement is important since, based on the maximum impedance value obtained, the input impedance value of the signal preamplifier circuit is determined. To ensure maximum voltage transfer across the spectrum of interest, correct impedance matching is required between the transducer and the preamplifier input. Furthermore, the resonance frequency of the ceramics can be deduced from the impedance curve, which shows which part of the spectrum presents the highest sensitivity.

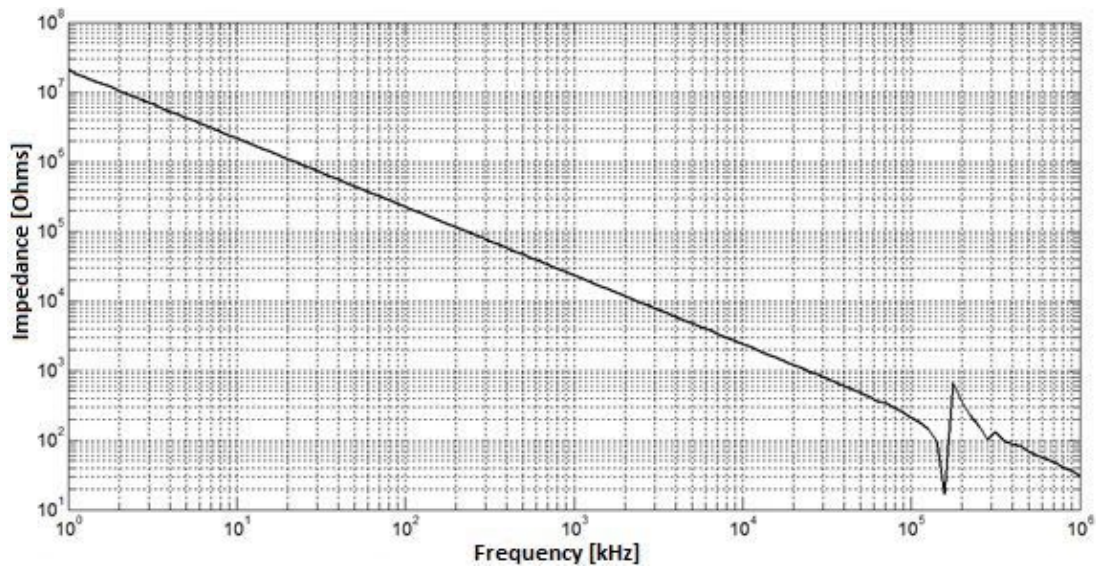


Fig. 10 – Impedance variation with frequency for the hemispherical piezoelectric ceramics.

The ceramics set was assembled using a piece designed in 3D printing software where each hemispherical ceramic points to the opposite side in order to cover a wide reception angle (fig. 11). The cylindrical ceramic is located below the hemispheres at a distance of approximately 1 cm.

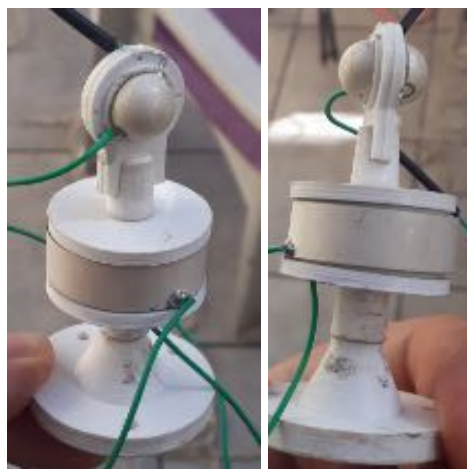


Fig. 11 – Piezoelectric ceramics assembled in the 3D structure.

4.1.2 Preamplifier circuit

The signal preamplifier is placed inside the housing, as close as possible to the structure that holds the ceramics. This decision was made in order to shorten the path of the signal without

amplification to reduce noise induction and improve signal to noise ratio (fig. 12). This implementation has advantages from other kind of electronic topology as a charge amplifier.

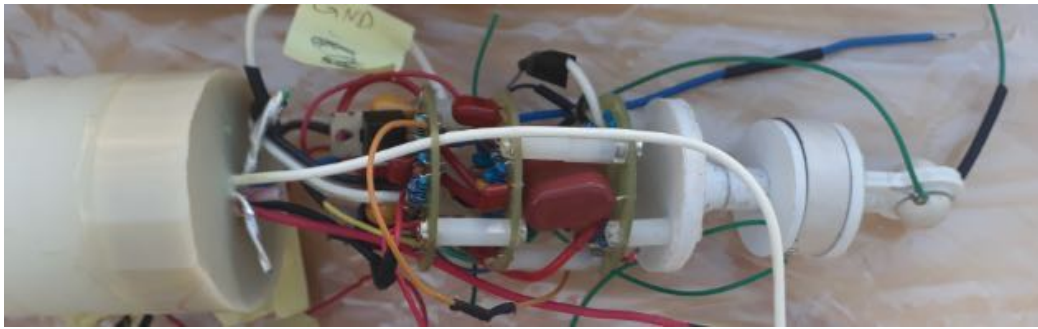


Fig. 12 – Preamplifier circuit at the assemblage stage with the piezoelectric crystals.

At the first stage of the circuit the signal is amplified with an approximated gain of 32 dB. This gain was determined according to the typical gain values used in amplifiers for hydrophones of similar characteristics. Also, this type of circuit lowers the high impedance of the sensors, improving the SNR of all the system. At the input of the circuit two diodes were placed to discharge any voltage peak caused by the sensors. The most important feature in this first stage is the implementation of a DC voltage servo to decouple the DC voltage at the circuit output. This circuit was used both for the signal coming from hemispherical ceramic and for the signal coming from the cylindrical ceramic, in parallel. Then the outputs of both parallel stages are added (fig. 13).

At the circuit output, an asymmetric balancing system was implemented in order to protect the signal from any type of unwanted interference that may be induced along the path from the hydrophone output to the monitoring station.

This balancing system ensures the same impedance value in each output, which implies equivalent noise induction in each of them. Thus, by unbalancing the signal, a greater cancellation of the noise induced in common mode is obtained. Also in this implementation it doubles the signal level. Figure 14 shows the frequency response of the preamplifier circuit.

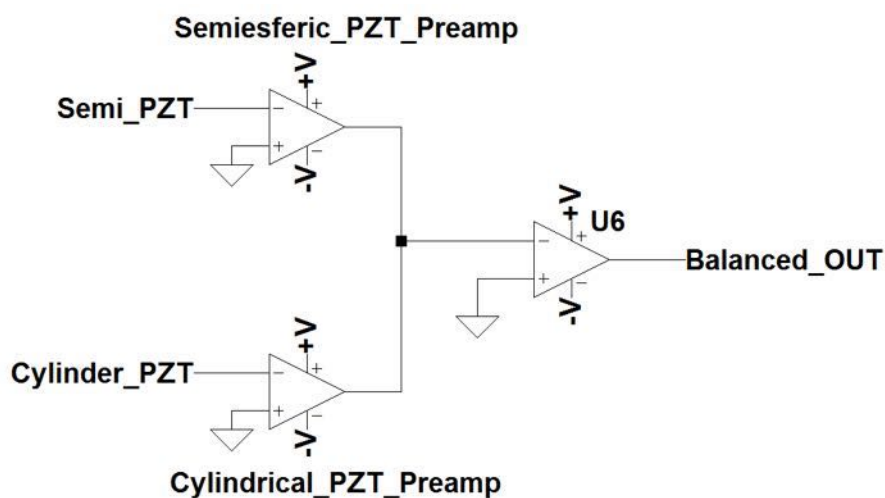


Fig. 13 – Block diagram of the preamplifier circuit.

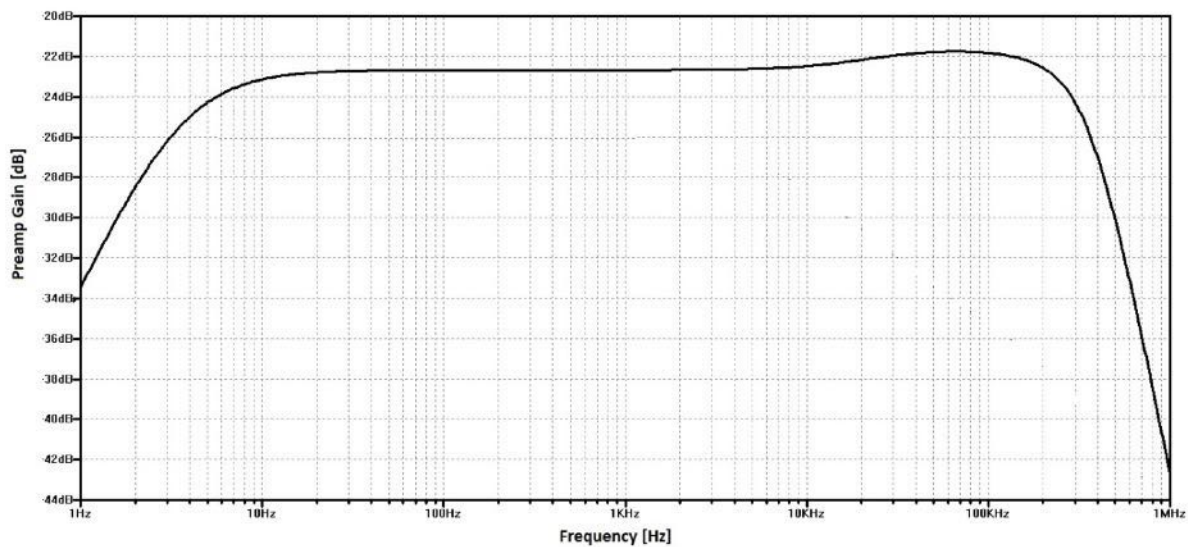


Fig. 14 – Frequency response of the preamplifier

4.1.3. Hydrophone housing

The design of the hydrophone housing is a fundamental part of the design process. This must meet certain requirements that ensure the durability and correct operation of the hydrophone under the environmental work conditions. Ideally, it should have a minimal impedance change regarding the aquatic medium and behave as an attenuator for unwanted signals such as noise. In addition, the materials used for its construction must have negative buoyancy.

Fig. 15 shows the components assembled inside the hydrophone housing. It is made up of two turned solid PVC tips and a PVC tube-shaped cylinder.



Fig. 15 – Assembled hydrophone within its housing.

The hydrophone will be subject to noise sources with varying relative intensities depending on the signal frequency, the speed of the current, the location of the hydrophone, the effectiveness of both external and internal decoupling materials and the size of the hydrophone. The current and movement generate a fluctuation in the pressure outside the housing that contains the hydrophone, exciting vibrations in its surface and in the other components of the hydrophone.

As only one hydrophone is used, for this study it was not possible to implement the gain control method of an array to achieve the reduction of ambient noise by combining several transducers. However, sea current noise can be reduced by certain design features, as the use of a dielectric mineral oil that has a density as close as possible to water density (1000g/m³) filling the hydrophone housing in order to ensure a minimum impedance change for the acoustic signal of interest.

4.2. Recognition and recording system

Given that the hydrophone will be submerged at 5 m depth, 6 to 10 km far from the coast, reasonable operation autonomy of at least 1 month must be ensured. The autonomy depends exclusively on the available energy source, the batteries. Based on this limitation, it was decided to:

1. Consider only acoustic signals exceeding the decision threshold between a certain temporal window.
2. The decision threshold will be set above the average background noise level recorded in the area.
3. The temporal window will be determined by the mean duration of the acoustic signals of interest.

The signal recorded by the hydrophone will follow two paths (fig. 16). On one hand, it will enter to a stage called "decision-making" and on the other hand, it will be digitized with a 16-bit analog-to-digital converter (ADC) with a sampling rate of 500 kHz (ADS8322)(Analog Devices, MA, USA), which allows an amplitude resolution of $76 \mu\text{V}$. The digitized signal will enter a circular buffer (FIFO stack). If the decision-making stage recognizes that it is a signal of interest, the information contained in the buffer will be stored on a solid state hard disk. When its capacity is complete, all stored signals will be transmitted to the station located on the coast through the modem for further analysis.

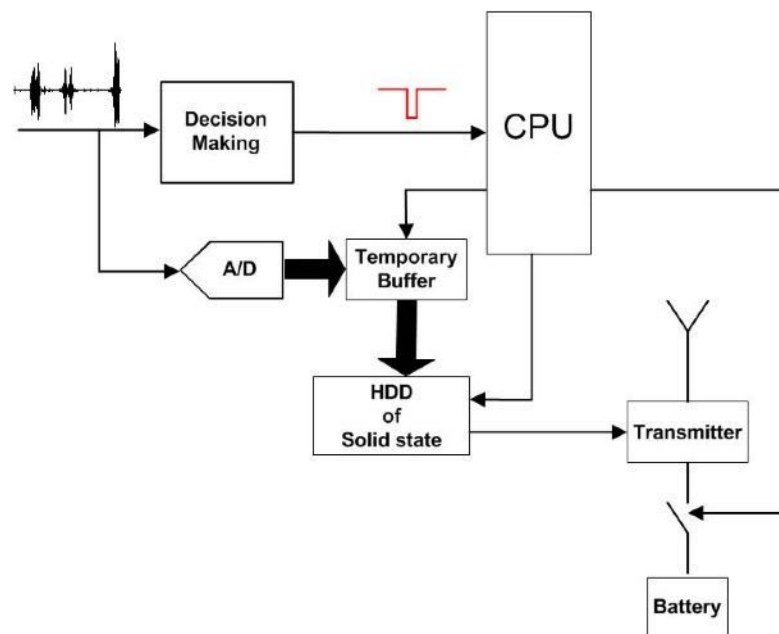


Fig. 16. Block diagram of the recognition, recording and data transmission system.

During the decision-making stage the signal recorded by the hydrophone is rectified and its envelope is calculated using of a low pass filter. Then it is compared with the threshold and temporal window. If the signal meets both conditions (logical condition Y), it is stored in the hard disk (fig. 17) (Veca, 2019).

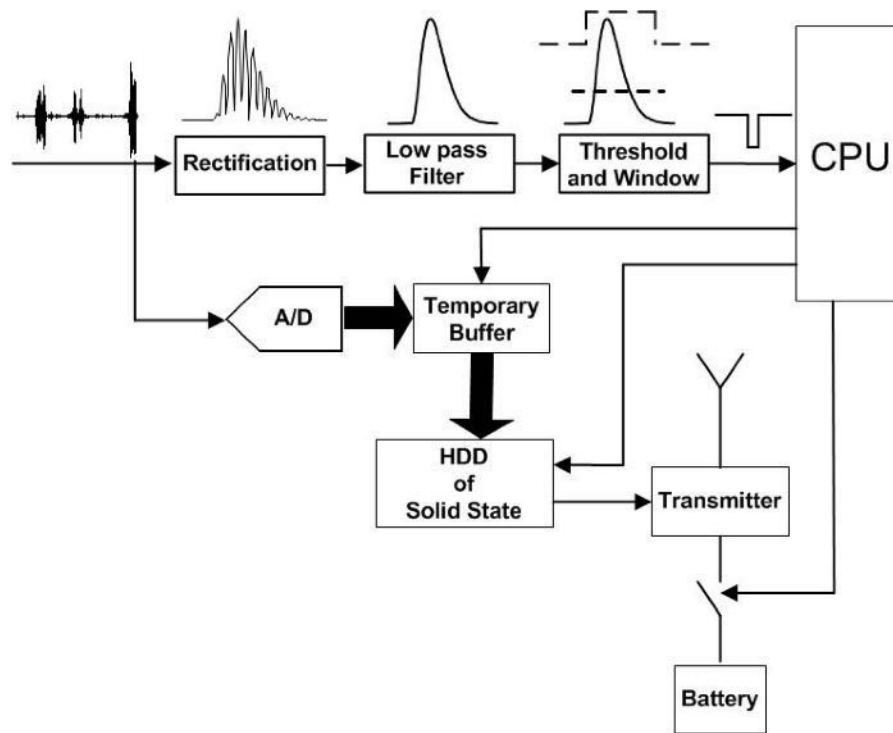


Fig. 17. Decision-making stages.

The rectifier was implemented with a LM318 operational amplifier and two 1N4148 diodes. The LM318 integrated circuit IC has high gain per bandwidth ($GB = 15 \text{ MHz}$) and high slew-rate ($SR = 70V/\mu s$), which are necessary to perform with the diodes, the complete rectification of the input signal with the minimum deformation. Once the signal is rectified, it goes through a second order low pass filter based on the Sallen Key topology with a cutoff frequency of 10 kHz, using a TL081 IC. The threshold comparator is based on a LM311 and the temporal window on a LM555 in monostable configuration. The "AND" function is performed with the output of the LM555 and the output of the LM311 by means of NAND gates using a CD4011 IC. The diagram is shown in figure 18. The CPU is based on an Arduino DUE system (Arduino, 2018).

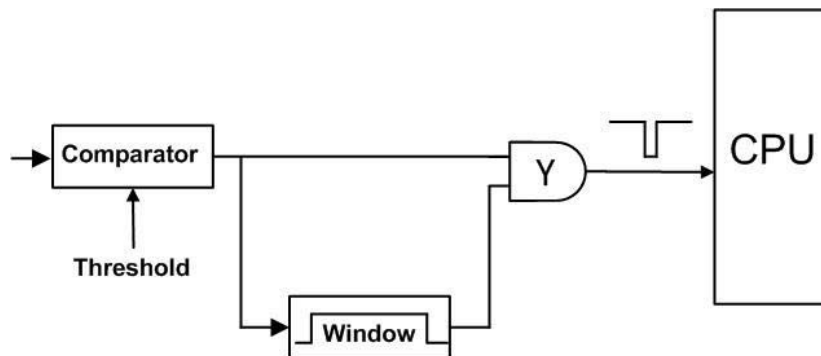


Fig.18. "And" function.

4.3. Data transmission

For the purpose of this paper, a FS1000A module that transmits at a frequency of 433 MHz, and its respective XDRF5V receiver, were used to transmit and receive the data (fig. 19). These devices work at that frequency because it is within the free use bands, and are compatible with the Arduino UNO system. For the final system, it is planned to implement transmission-reception with a "rocket M5 (Ubiquity networks, NY, USA) system with TCP/IP protocol that supports a transfer speed of the order of 150 Mbps with a bandwidth between 2 to 40 MHz. It

can operate in environments with temperatures between - 70 °C and + 75 °C and it has protection against static discharges in the order of +/- 24 kV. The transmitting antenna is omnidirectional due to the movements of the buoy.

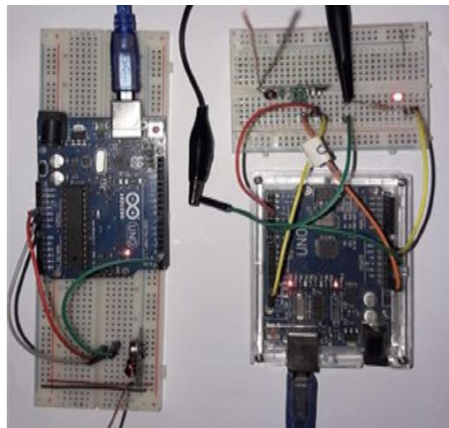


Fig. 19. Transmitter (located in the buoy) and receiver (located at the coast)

5. LABORATORY SIMULATION TESTS

A series of laboratory tests were carried out to test the developed system. They consisted of emulating the surroundings of the hydrophone and the signals emitted by the species of cetaceans in the area. A fish tank was used to simulate the marine environment (fig. 20) (Gimenez *et al.*, 2018, Julian *et al.*, 2018, Bustos *et al.*, 2018). Inside, a piezoelectric disk is connected to the emulator of the sounds emitted by cetaceans. The sounds were generated by means of an electronic synthesizer, programmable by software (fig. 21). On the opposite side, there is a piezoelectric receiver that simulates the hydrophone.

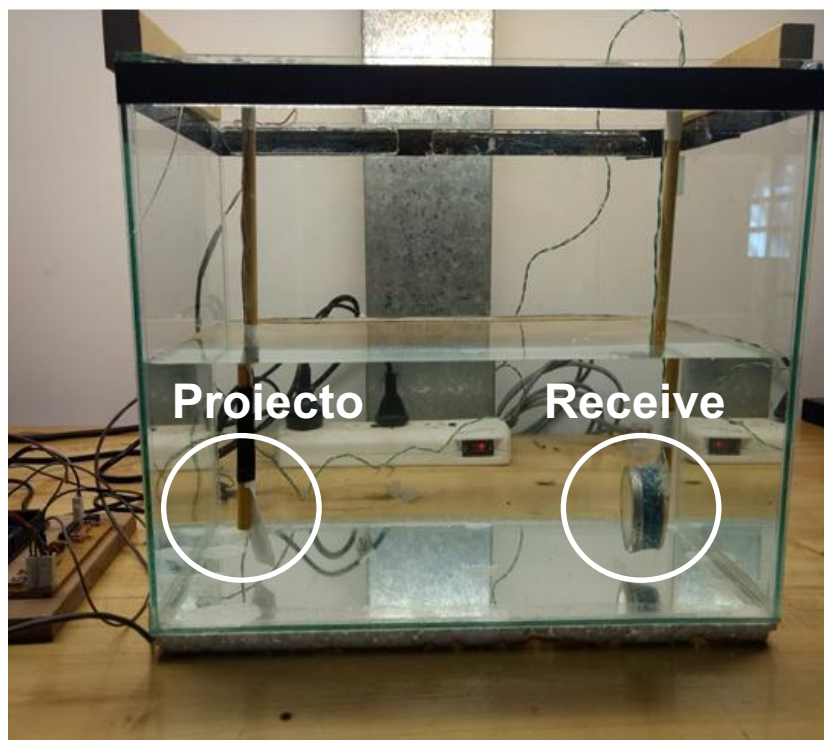


Fig. 20. Emulation of the marine environment.

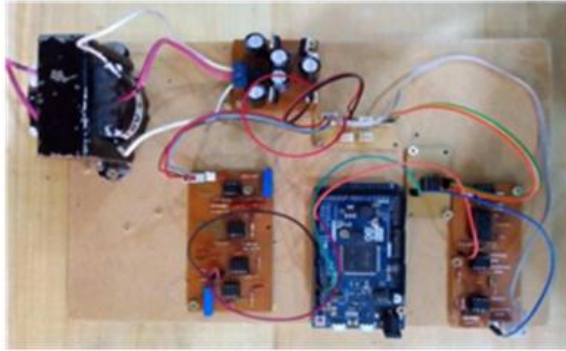


Fig. 21. Sound generator system.

The acoustic signal detector consists of the envelope extractor, the decision threshold and the temporal window (fig. 22). The transmitter that emulates the modem and the receiver that simulates the land-based station is shown in fig. 19.

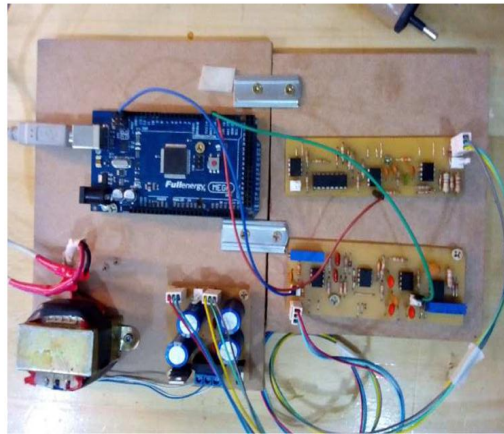


Fig. 22. Receiving system.

Finally, figure 23 shows a top view of the fish tank and the modules mentioned above.

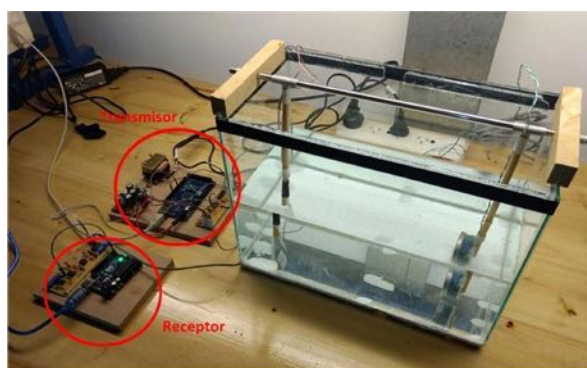


Fig. 23. Whole system

6. RESULTS

Two tests were carried out. The first one used commercial buzzer-type disks with working frequency of 5 kHz excited with a square wave as transducers. The process of modulation, reception, rectification and the comparator output can be seen in fig. 24. In this case, the window and the "AND" function were not implemented. A higher background noise level than expected was recorded due to the dimensions of the tank and the working frequency, since the

acoustic wave front travels through the water and through its walls, causing interference and beating. A FLUKE 281 programmable generator was used to generate the signals, and a Tektronix TDS2002C dual channel oscilloscope with a 70 MHz sampling frequency was used to record the signals.

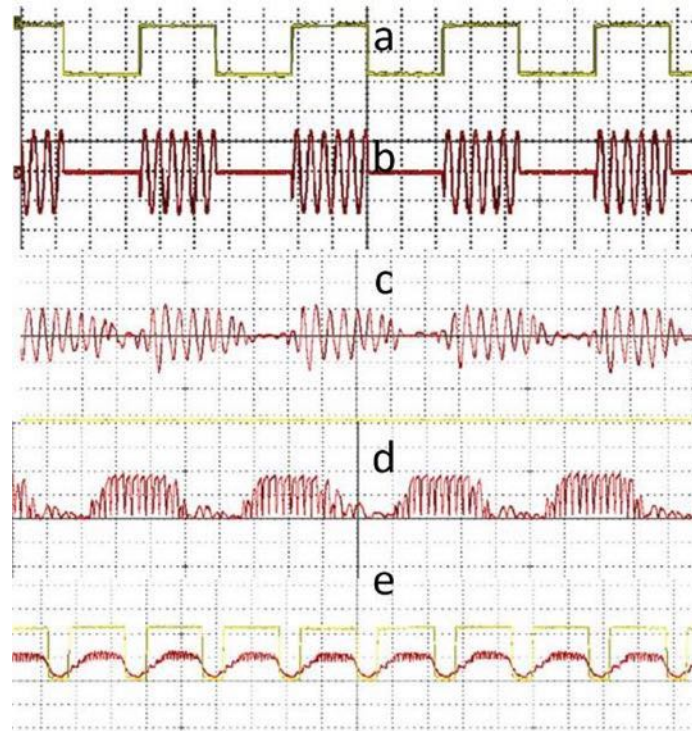


Fig. 24. Test with 5 kHz ceramics. a) Modulator. b) Modulated sinusoid. c) Received signal. d) Rectified signal. e) Filtered signal (red) and comparator output (yellow).

The second test used MASA E-180/220 ultrasound transducers (Massa, 2000) operating at 220 kHz. In this case, the detection and decision system was tested in air, from a reflective surface 40 cm from the transducer. The reason for using these transducers is that the working frequency is similar to that used by signals of interest emitted by dolphins, being able to test all the electronics in conditions close to reality. Fig. 25 shows the echo signal, the rectifier signal, the comparator response, the window signal and the "AND" function signal. To record the signals, a PC-based OWON VDS3102 oscilloscope with a 100 MHz sampling rate was used. In this case, the signal-to-noise ratio was in the order of 30 dB since there was no noise caused by reflections and interference.

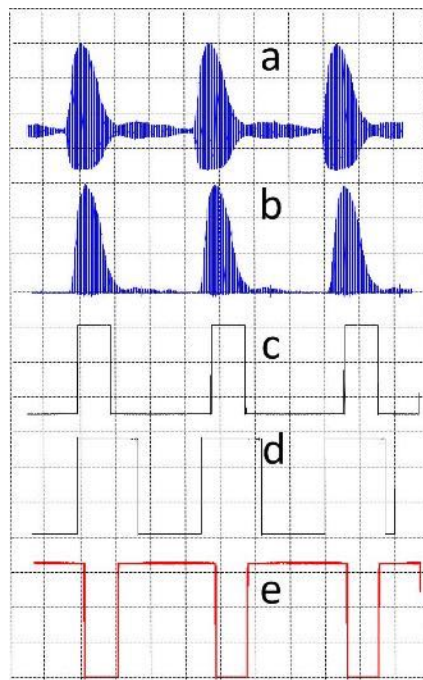


Fig. 25. Test with a 220 kHz ultrasound transducer. a-Echo signal. b-Rectified signal. c-Comparator output, d-Temporal window and e- “AND” function.

7. CONCLUSIONS

This paper presents preliminary studies of the development of a system for reception of signals generated by cetaceans in order to study their activity. First, the physical characteristics of the marine environment that influence the recording of acoustic signals were analyzed. Then, a typical emission sequence was analyzed from the point of view of the power density spectrum, verifying the expected bandwidth.

Taking into account the energy limitations at the buoy, it was decided to use the threshold and temporal window technique to recognize the signals of interest and to proceed to record it for its subsequent transmission to the receiving station on the coast.

Using a fish tank, a simulation was performed to test the designed detection system that consisted of generating a low frequency sequence, detecting it and transmitting it to a receiver that emulated the receiving station.

Finally, the detection and decision system was tested with a generated high-frequency ultrasound signal, verifying that it meets the expected conditions.

The system can support other low consumption sensors in order to transmit complementary information, such as water temperature, relative humidity, salinity, UV radiation, and geostationary data (GPS), among others.

REFERENCES

- C. A. Agost González (2015), Transmisión de Datos Mediante una Conexión por Ultrasonidos en un Medio Sub-acuático. Cátedra: Aplicaciones Industriales del Ultrasonido, Curso 2015 Departamento de Electrónica y Automática Facultad de Ingeniería de la Universidad Nacional de San Juan. <http://www.fi.unsj.edu.ar/Ultrasonido>.
- A. Albalat. (2018), “Diseño y construcción de un amplificador de carga multipropósito”. Engineering thesis, Universidad Nacional de Tres de Febrero, Argentina.
- Arduino (2018) DUE. <http://arduino.cc>
- E. Bustos, J. Carrizo, L. Ferreyra, M. Ortiz, G. Santander, E. Vallejo (2018), “Transmisión Acústica Inalámbrica entre Robots Submarinos y Boyas de Superficie Parte II,” Course:

- Aplicaciones Industriales del Ultrasonido, Departamento de Electrónica y Automática, Facultad de Ingeniería Universidad Nacional de San Juan.
<http://www.fi.unsj.edu.ar/Ultrasonido>.
- R. Gimenez, G. Papparelli, N. Ruiz (2018), “Comunicación Acústica Halfduplex entre Vehículos Submarinos,” Course: Aplicaciones Industriales del Ultrasonido., Departamento de Electrónica y Automática, Facultad de Ingeniería, Universidad Nacional de San Juan.
<http://www.fi.unsj.edu.ar/Ultrasonido>.
- J. M. Julian., S. Mateo, D. Quinteros, P. Pelaez, S. Jalil, L. Saldivar (2018), “Comunicación Acústica Inalámbrica entre Robots Submarinos y Boyas de Superficie Parte I”. Course: Aplicaciones Industriales del Ultrasonido. Departamento de Electrónica y Automática Facultad de Ingeniería Universidad Nacional de San Juan.
<http://www.fi.unsj.edu.ar/Ultrasonido>.
- L. E. Kinsler, A. B. Frey, A. B. Coppens, J. V. Sanders (1980), “Fundamentals of Acoustics”, Fourth Edition, John Wiley & Sons, Inc.
- L. A. Kyhn, J. Tougaard, F. Jensen, M. Wahlberg, G. Stone, A. Yoshinaga, K. Beedholm, P.T. Madsen (2009), “Feeding at a high pitch: Source parameters of narrow band, high-frequency clicks from echolocating off-shore hourglass dolphins and coastal Hector’s dolphins,” *J. Acoust. Soc. Am.* 125(3): 1783-1791. doi: 10.1121/1.3075600
- L.A. Kyhn, F.H Jensen, K. Beedholm, J. Tougaard, M. Hansen, P.T. Madsen (2010), “Echolocation in sympatric Peale’s dolphins (*Lagenorhynchus australis*) and Commerson’s dolphins (*Cephalorhynchus commersonii*) producing narrow-band high-frequency clicks,” *J. Exp. Biol* 213: 1940-1949. doi: 10.1242/jeb.042440
- P. T. Madsen, D.A. Carder, K. Bedholm. S.H. Ridgway (2005), “Porpoise clicks from a sperm whale nose - convergent evolution of 130 kHz pulses in toothed whale sonars?,” *Bioacoustics* 15(2):195-206.
- A. Marino (2019), “Detección de Clicks para Implementación de Monitoreo Acústico Pasivo de Delfines”, Engineering thesis, Universidad Nacional de Tres de Febrero, Argentina.
- M. Martin, T. Gridley, S. Elwen, F. Jensen, (2018), “Heaviside's dolphins (*Cephalorhynchus heavisidii*) relax acoustic crypsis to increase communication range,” *Proceedings of the Royal Society B: Biological Sciences.* 285. 10.1098/rspb.2018.1178.
- Massa Sonic E-188/220 (2017) <https://www.massa.com/wp-content/uploads/2017/08/E-188-220-Datasheet-170510.pdf>
- H. Medwin, C. S. Clay (1998), “Fundamentals of Acoustical Oceanography,” Academic Press.
- M. L. Melcón, M. Failla M. A. Iñíguez (2012), “Echolocation behavior of franciscana dolphins (*Pontoporia blainvillei*) in the wild,” *J. Acoust. Soc. Am.* 131(6): EL448–EL453. doi: <http://dx.doi.org/10.1121/1.4710837>
- M. V. Reyes Reyes, A. Marino, N. Dellabianca, M. Hevia, M. Torres, A. Raya Rey, M.L. Melcón (2018), “Acoustic signals of Burmeister’s porpoises (*Phocoena spinipinnis*) in Tierra del Fuego, Argentina,” *NOTES. Marine Mammal Science.* 34. 10.1111/mms.12489.
- T. D. Rossing, N. H. Fletcher (2004), “Principles of Vibration and Sound”, 2nd Edition, Springer, New York.
- J. E. Ruzzante, M. I. López Pumarega (2017). “Emisión Acústica, un diálogo con los materiales”, <https://www.ciencias.org.ar>
- L. N. Vales (2017), “Diseño, Construcción y Caracterización de un Hidrófono Orientado a la Transducción de Señales Emitidas Por Cetáceos”. Engineering thesis, Universidad Nacional de Tres de Febrero, Argentina.
- A. C. Veca, J. E. Ruzzante, M. I. López Pumarega, E. Accolti, (2016), “Ultrasonido y Emisión Acústica para Ingenieros y Estudiantes de Ingeniería”. 1st Edition.
<http://www.fi.unsj.edu.ar/Ultrasonido>.
- A. C. Veca (2019), “Arquitecturas Circuitales para la Emisión y Recepción de Ultrasonido, orientadas a la determinación de tiempo de transito”, <http://www.fi.unsj.edu.ar/Ultrasonido>.

Energy and Shannon Entropy in Acoustic Emission Signals for Damage Evaluation in Andesite Rock

Zitto^a, M.E., Sassano^{a,b}, M.P., Muszkats^{a,c}, J.P., Filipussi^{d,e}, D.A., and Piotrkowski^{a,e}, R

^a Grupo de análisis de series temporales no estacionarias y no lineales, Facultad de Ingeniería, Universidad de Buenos Aires, ARGENTINA. series.nsnl@fi.uba.ar

^b Ingeniería de sonido, Universidad Nacional de Tres de Febrero, ARGENTINA

^c Universidad Nacional del Noroeste de la Provincia de Buenos Aires, ARGENTINA

^d Gerencia Desarrollos Tecnológicos y Proyectos Especiales, CNEA, ARGENTINA

^e Escuela de Ciencia y Tecnología, Universidad Nacional de San Martín, ARGENTINA

ABSTRACT

Andesite rock samples were subjected to uniaxial compression tests monitored by Acoustic Emission (AE) for the assessment of the brittle fracture process. The identification and evolution of different fracture regimes were based on the application of methods suited for non-stationary and nonlinear time series: Wavelet Transform (WT); Empirical Mode Decomposition (EMD); Hilbert-Huang Transform (HHT) and Shannon Entropy (SE). The jumps of accumulated AE energy, which indicate where the greatest damage due to macro fractures occurs, were preceded by minimum entropy values of the EMD components, which would indicate that they act as precursors to catastrophic damage.

Keywords: Wavelet Transform, Hilbert Huang Transform, Shannon Entropy, Andesite Rock, Fracture.

1. INTRODUCTION

The Acoustic Emission (AE) technique allows obtaining information about different processes that occur inside a material subjected to stress by analyzing the non-stationary elastic waves generated, dispersed, and finally detected. At a microscopic level, natural flaws act as stress concentrators in rock, favoring brittle fracture. This nucleation process continues with an interplay of microcrack growth and coalescence into macrocracks, leading to the final rupture when the accumulation of energy dissipated in fractures reaches a critical level (Lockner, 1993). Thus, crack propagation is characterized by wideband AE (Rodriguez, 2019). The generation and propagation of the elastic waves imply different spatial and temporal scales ranging from the breakdown of atomic bonds to seismic failures, which makes the characterization with AE of fractures be an important complement in seismology (Filipussi, 2015).

The generated AE signals are of very low amplitude (10 μV) and high frequency (50 kHz to 1 MHz) and are characterized by discrete oscillating pulse events (hits) that reach a maximum amplitude in a rise time of the signal and are then damped (Grosse, 2008). It is possible to assess damage by computing the characteristic parameters of hits: energy, root mean square (RMS), amplitude, rise time, duration. Due to the essential connection between AE and seismology, some authors (Zhang, 2018; Carpinteri, 2009; Rao, 2005; Shiotani, 2001) evaluate damage through the b-value, which means the accumulated frequency distribution of AE amplitudes. The linear relationship in log-log scale rules in AE resembling the seismic Gutenberg-Richter law.

Under the hypothesis that it is possible to associate characteristic frequencies to the different damage processes, the authors of this work have performed previous studies, analyzing and applying the Wavelet Transform (WT) to AE signals in specimens of andesite rock subjected to uniaxial compression. A frequency band associated with the propagation and advance of fractures in the material was selected through the determination of the maximum coefficients

of the WT and the minimum of Shannon Wavelet Entropy (SWE) (Muszkats, 2019; Sassano, 2017).

Following previous work, and taking account of the non-linearity of AE signals, an alternative analysis was here performed: the Empirical Mode Decomposition (EMD). The method consisted in searching characteristic modes, associated with the advance of dangerous cracks with the application of the Shannon Mode Entropy (SME).

2. EXPERIMENT AND ANALYSIS METHODS

2.1 Experiment

Four cylindrical specimens were tested, 75 mm diameter and 150 mm length, coming from an andesite core extracted in the rock location of Cerro Blanco, Province of San Juan, Argentina. These specimens were subjected to simple uniaxial compression tests, up to breakage. A hydraulic servo type and closed-loop CGTS machine was used, with 100 tons capacity and 0.12 mm/min actuator travel speed. Fig. 1 shows the experimental setup. The andesite specimen is instrumented with AE sensors.

AE was monitored with three piezoelectric sensors. Two of them were attached to the surface of the specimen, tuned respectively to 60 kHz and 150 kHz. The third one, which was broadband, was attached to the lower loading plate taking into account the ability of the metal as a wide waveguide. The AE equipment, also shown in Fig. 1, was completed with a two-channel board *PCI-2 PAC*, (Physical Acoustic Corporation). The commercial software *AEWIN* was used for the analysis and determination of the characteristic parameters of signals.

We present results obtained with specimen 3, whose signals corresponded to the broadband sensor channel, 100 kHz - 1 MHz. This selection was to avoid the pre-filtering provided by the resonant sensors. The test lasted approximately 15 minutes, the sampling time was $t_s = 1 \mu s$, and 75385 hits were obtained.



Fig. 1 Experimental setup and AE equipment.

2.2 Analysis methods

a) *Wavelet Transform*

WT is a widely used method for non-stationary time series analysis. This method allows analyzing the data in a time-frequency plane from its decomposition taking a fixed basis, which is obtained by scaling and displacing a mother wavelet, with different scales and temporal displacements. The time-frequency resolution obtained with this method exceeds that obtained with the windowed Fourier Transform. (Bogges, 2009; Torrence, 1998).

In (Muszkats, 2019), we adopt the Continuous Wavelet Transform (CWT) that allows us working with frequency bands of variable width that we formally define in Eq. 1

$$Wf(u, s) = \int_{-\infty}^{\infty} f(t) \psi_{u,s}^*(t) dt \quad (1)$$

Where $\psi_{u,s}(t)$, displayed in Eq. 2, is the wavelet corresponding to scale s and time displacement u .

$$\psi_{u,s}(t) = \frac{1}{\sqrt{s}} \psi\left(\frac{t-u}{s}\right), \quad s > 0 \quad (2)$$

Taking discrete values for u and s (associated with a frequency), the squared coefficients of $Wf(u, s)$ give us the power content of the signal at time $u_n = nt_s$ and scale s .

The complex Morlet wavelet was used as the mother wavelet, which provided an improved capture of the oscillatory character of the signal.

b) *Empirical Mode Decomposition (EMD)*

WT uses an a priori basis, which in general is unsuitable to analyze non-linear signals, and the difficulty is usually saved with mathematical tricks, adding non-meaningful terms to the analysis to fit the data.

At the beginning of the century, Norden Huang developed the EMD method for time series analysis based on locally decomposing the series with a basis obtained from data. This allows splitting the series into modes (Intrinsic Mode Functions, IMFs). An IMF must meet two conditions: i) the number of zeros has to be equal to the number of local extremes, or at most differ in one; and ii) the mean value of the upper and lower envelopes must be null at all points. The first condition means that modes are oscillatory functions. The second condition means that the local mean value is zero. Data fitting improves. Additionally, the Hilbert transform applied to IMFs leads to obtain instantaneous frequencies associated with each of them. The entire process of calculating IMFs and then applying the Transform of Hilbert constitutes the Hilbert-Huang Transform (HHT). (Huang, 1998; Huang, 2014).

The procedure for obtaining IMFs consists of first determining the upper and lower envelopes of the series. Secondly, the local mean value of both envelopes is calculated and then subtracted from the original series points. If the resulting function meets the conditions i) and ii) previously stated, the result constitutes the first IMF. If not, the procedure, called sifting, is reinitiated. The first IMF corresponds to the most tiny detail, i.e. the largest frequency. The first IMF is subtracted from the original data and the first residue is obtained. The procedure is repeated on the first residue and the second IMF is obtained. The iteration permits to obtain the successive IMFs. It finishes when it is not possible to extract more oscillations, which is when the corresponding residue is a monotonous function or it has at most one local extreme.

Thus, the decomposition of $x(t)$ results in Eq. 3

$$x(t) = \sum_{i=1}^N f_i(t) + r(t) \quad (3)$$

where $r(t)$ is the series trend, N is the number of modes and f_i is the i -mode. By definition, the Hilbert transformations of the f_i s are well behaved, so it is possible to calculate the

instantaneous frequencies corresponding to each mode as a function of time (Huang, 2008; Huang, 2014).

c) Shannon entropy

The Shannon Entropy (SE) is a measure of the intrinsic order of the signal, and the presence of minima suggests a more organized behavior, for example, an impulsive response, due to abrupt advancement of fractures, different from phenomena such as friction, fracture closure and noise in general that can be associated with high entropy values. (Shannon, 1948). SE was applied by the authors in previous AE and WT work (Piotrkowski, 2009; Sassano, 2017; Muszkats, 2019b).

If we have the discrete values of a hit, $x(t)$, measured with a certain sampling time t_s and we call them $x_j, j = 1, \dots, M$, we can define the hit energy in arbitrary units (a.u.), (Eq. 4).

$$E = \sum_{j=1}^M (x_j)^2 \quad (4)$$

We can define the fraction of energy corresponding to time jt_s as in Eq. 5

$$p_j = \frac{(x_j)^2}{E} \quad (5)$$

hence we can define the SE of $x(t)$ as in Eq. 6

$$SE = -\sum_{j=1}^M p_j \log(p_j) \quad (6)$$

3 RESULTS

a) Continuous Wavelet Transform (CWT)

In this section, we first recap some of the main results presented in (Muszkats, 2019), to compare them with the EMD decomposition. Following the results of some of the authors of this work (Zitto, 2015; Sagasta, 2018) it is possible to assign certain frequency bands to the different processes that lead to a final break in brittle materials. To determine the band of frequencies associated with incipient damage due to fractures we use the CWT, which allows us to filter the hits around a certain frequency. At the beginning of tests, crack nucleation occurs; the damage mainly consists of a large number of small cracks. The coalescence of these micro-cracks results in larger cracks of dangerous rapid advance, new micro-cracks emerge from the macro-cracks, and the whole process repeats until the final collapse occurs.

Since the selected t_s in the AE tests was $1 \mu s$ the highest frequency we could detect was 500 kHz. Our study focused on frequencies ranging from 100 to 500 kHz. The CWT of all the hits corresponding to the test was calculated. The frequency (scale) band corresponding to the highest absolute CWT values was identified around 240 kHz. A few of these maxima occurred at the beginning of the test, and the occurrence increased after 4 minutes when fractures began to appear in the sample. For other frequency bands, either a few maximum coefficients appeared, or they appeared with equal density throughout the test. Therefore, the 240 kHz frequency band could be assigned to damage connected with macro fractures in the specimen (Muszkats, 2019).

The evolution of AE accumulated energy was compared with those of each frequency band. It can be observed in Fig. 2 that energy evolution curves are similar in shape, but do not explain the whole energy of hits. Besides, the band with the highest energy content corresponds to a frequency of 121 kHz.

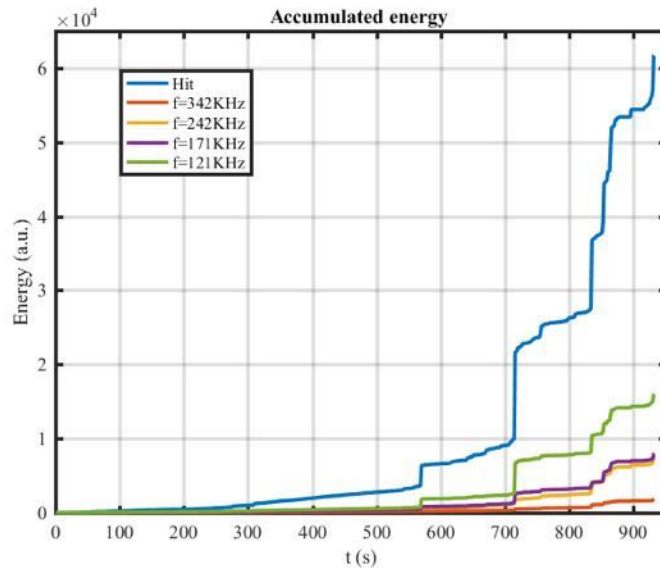


Fig 2 Evolution of the accumulated AE energy and the accumulated CWT energy of the different bands.

b) Empirical Mode Decomposition (EMD)

The EMD and the instantaneous frequency evolution (HHT) were calculated for each hit, to associate the different modes in the decomposition with different mechanisms that generate AE. Five to six modes were obtained, depending on each particular hit. Fig. 3 shows the first three IMFs that correspond to characteristic hits. The amplitude of the first mode is similar to the amplitude of the full hit; for the second mode, the amplitude is 25% of the amplitude of the first mode; and overall, the amplitude decreased in the successive modes, becoming negligible.

Fig. 4 shows HHT results for the same hits graphed in Fig. 3. The instantaneous frequencies of modes 1 and 2 are within the sensor bandwidth. Frequencies of mode 1 correspond to the 200-300 kHz interval, and the intensity is appreciable only during a minor interval of the hit, especially at the beginning. The frequencies for mode 2 are in general lower than 170 kHz and their intensities extend throughout the entire hit. These results would suggest that we could associate the impulsive mode 1 to the rapid advance of macro fractures. This agrees with the results obtained with CWT.

Then we calculated the accumulated energy for each mode comparing it with the AE energy. Results are in Fig. 5. We can observe that mode 1, with instantaneous frequencies ranging between 200 and 300 kHz, contains approximately 90% of the AE energy, which is otherwise negligible for modes 3 and onwards. Contrarily, with the filtering performed with CWT, the energy in the 240 kHz band is much lower than the energy of hits. This constitutes a goal of the EMD decomposition, which takes into account the nonlinearity of the signal. Due to the adaptive basis employed, more precision and conciseness are achieved, and the severe fracture process could be more confidently assigned to mode 1.

c) Shannon Mode Entropy (SME)

Finally, we calculated the SME for all the hits, studying their evolution throughout the entire test. Since entropy is very variable from hit to hit, we performed a moving average smoothing involving 700 hits. Fig. 6 compares the SME of modes 1 and 2 with the accumulated AE energy for the second half of the test. The graph shows that the SME for modes 1 and 2 exhibits a very similar shape. The jumps of accumulated energy indicate where the greatest damage due to macro fractures occurs. Noticeably, these energy jumps are preceded by minimum entropy values, which would indicate that they are precursors to catastrophic damage.

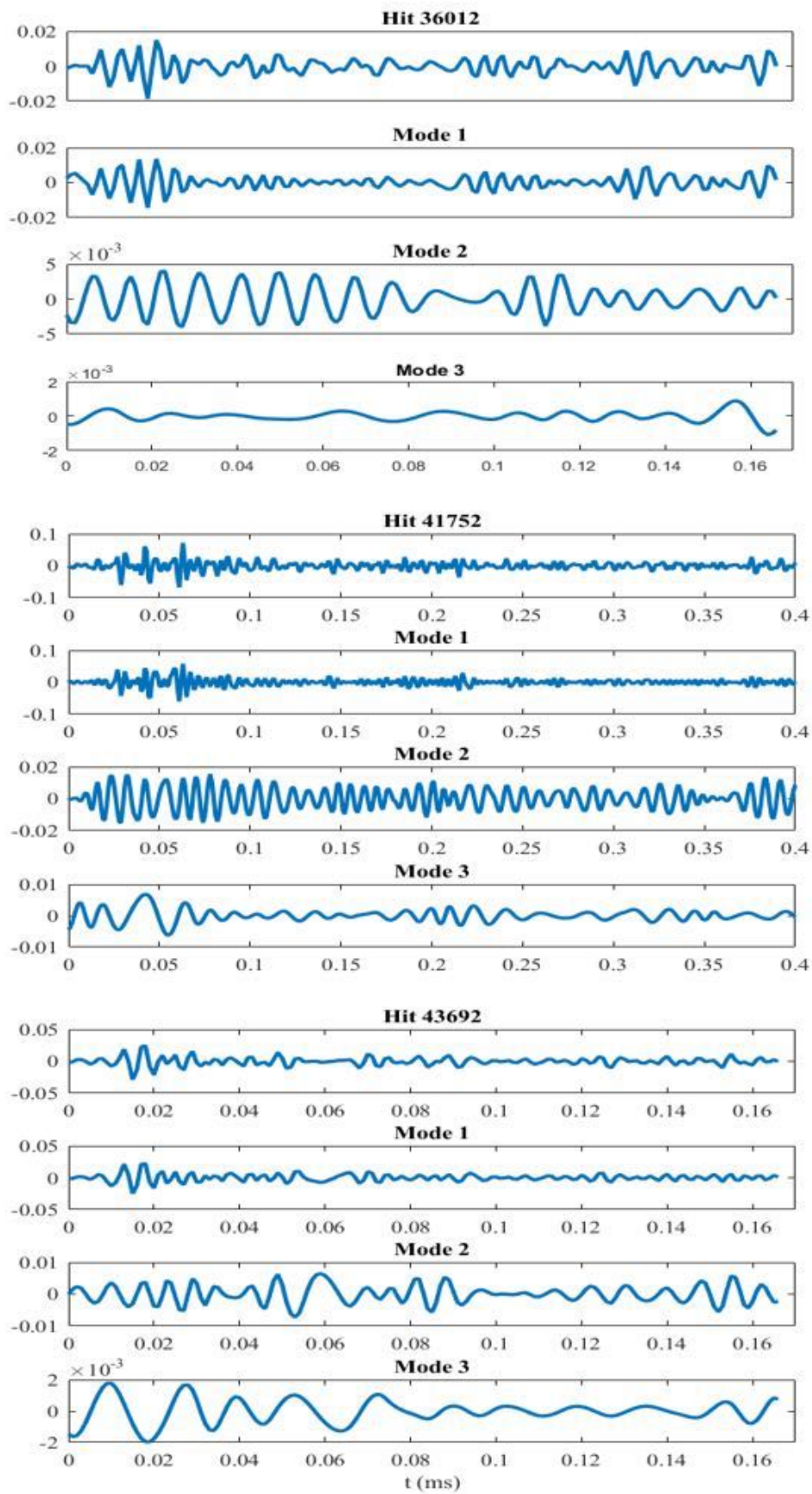


Fig. 3 Three characteristic hits with their corresponding first three modes of the EMD decomposition.

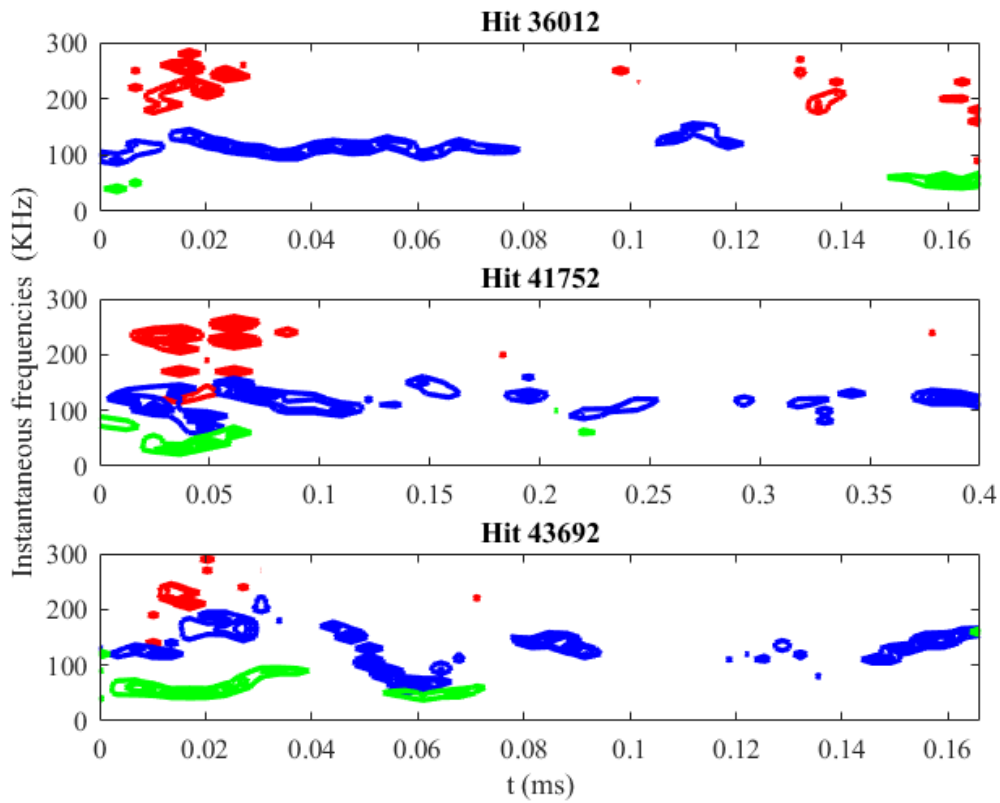


Fig. 4 Instantaneous frequency for the hits in figure 3. Red: mode1, blue: mode 2 and green: mode 3.

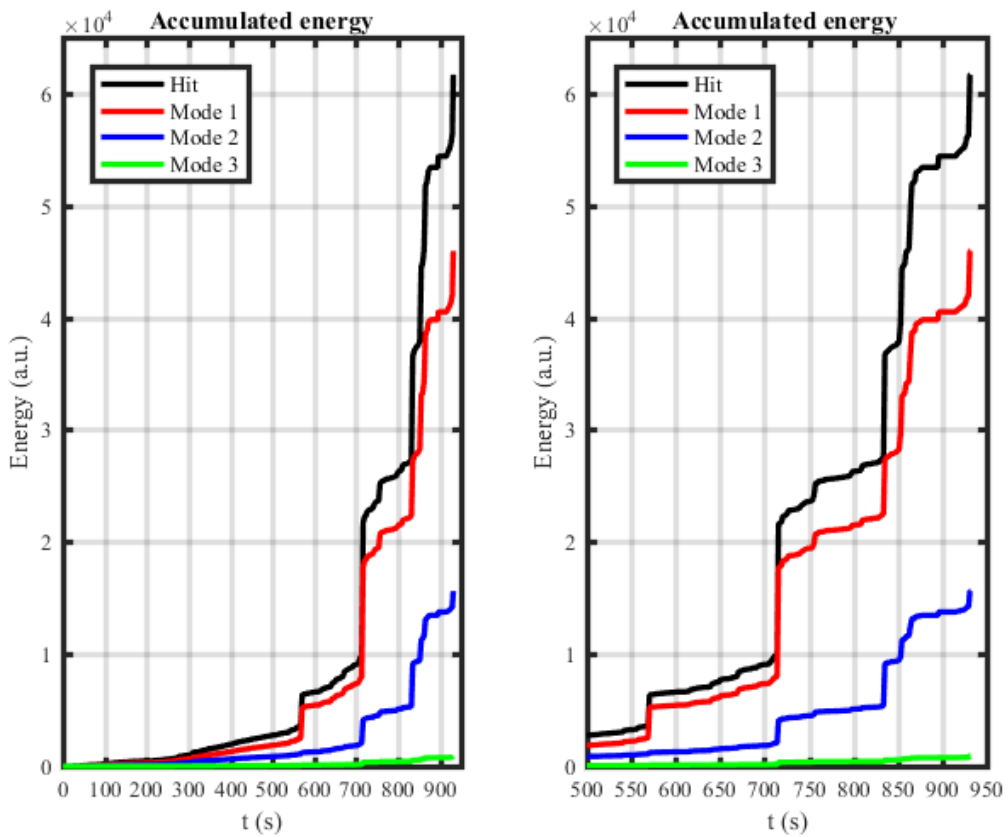


Fig. 5 Accumulated energies of the first three modes in the EMD decomposition compared with the accumulated AE of hits during the whole test (left) and in the last half part of the test (right).

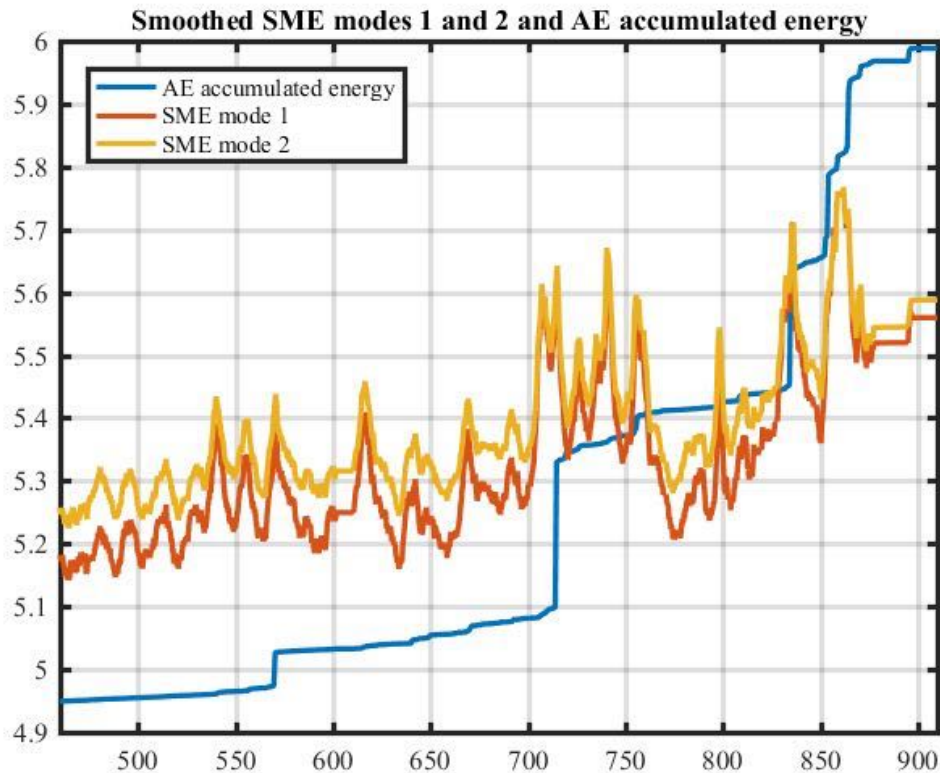


Fig. 6 Smoothed SME modes 1 and 2 compare with the AE accumulated energy AE energy scale is different from that of Fig. 5 for clarity reasons.

4 CONCLUSIONS

AE signals from uniaxial compression tests on Andesite rock previously analyzed with WT were analyzed in the present paper with EMD and SE. With both WT and EMD analysis methods, the frequency of around 240 kHz could be assigned to the mechanisms of formation and rapid advancement of macro fractures. However, the energy dissipated in that band could not be quantitatively determined with the WT. In this sense, the EMD showed its potential for analyzing signals from non-stationary and non-linear processes. Comparison of the Shannon entropy of modes (SME) and AE energy throughout the test showed that the minimum entropy values are precursors to abrupt jumps of energy that identify severe fracture damage.

REFERENCES

- A. Boggess, F.J. Narcowich (2009), *A First Course in Wavelets with Fourier Analysis* (second Edition), John Wiley & Sons, ISBN 9780470431177.
- A. Carpinteri, G. Lacidogna, S. Puzzi (2009), *From criticality to final collapse: Evolution of the “b-value” from 1.5 to 1.0*. *Chaos, Solitons and Fractals*. 41(2), pp. 843– 853. <https://doi.org/10.1016/j.chaos.2008.04.010>
- D.A. Filipussi, C.A. Guzmán, H.D. Xargay, C. Hucauluk, D.N. Torres (2015), *Study of Acoustic Emission in a Compression Test of Andesite Rock*, *Procedia Materials Science*, 9, pp. 292–297. <https://doi.org/10.1016/J.MSPRO.2015.04.037>
- C. Grosse, M. Ohtsu (2008), *Acoustic Emission Testing*. Springer Berlin Heidelberg, Berlin, Heidelberg, ISBN 978-3-540-69895-1.

- N.E. Huang, Z. Shen, S.R. Long, M.C. Wu, H.H. Shih, Q. Zheng, N.C. Yen, C.C. Tung, H.H. Liu (1998), "*The Empirical Mode Decomposition and the Hilbert Spectrum for Nonlinear and Nonstationary Time Series Analysis*", Proceedings of the Royal Society of London A., 454 (1971), pp. 903–995.
- N.E. Huang, Z. Wu (2008), *A review on Hilbert-Huang transform: Method and its applications to geophysical studies*, Rev. Geophys., 46, RG2006. doi:10.1029/2007RG000228.
- N.E. Huang (2014), *Hilbert-Huang transform and its applications* (Vol. 16), World Scientific.
- D. Lockner (1993), *The role of acoustic emission in the study of rock fracture*, International Journal of Rock Mechanics and Mining Sciences, 30 (7), pp. 883–899.
- J.P. Muszkats, D.A. Filipussi, M.E. Zitto, M.P. Sassano, R. Piotrkowski (2019), *Detection of fracture regimes in andesite rock via the energy evolution of acoustic emission signals in relevant frequency bands*, In Proceedings VII Congreso de Matemática Aplicada, Computacional e Industrial (MACI).
http://asamaci.org.ar/wp-content/uploads/2019/08/actas_edicion-vii_maci2019.pdf.
- J.P. Muszkats, M.E. Zitto, M.P. Sassano, D.A. Filipussi, R. Piotrkowski (2019b), *Assessment of different fracture regimes in Andesite rock via acoustic emission, wavelet transform and energy b value*, Mecánica Computacional (Vol XXXVII), pp. 529-538.
- R. Piotrkowski, E. Castro, A. Gallego (2009), *Wavelet power, entropy and bispectrum applied to AE signals for damage identification and evaluation of corroded galvanized steel*, Mechanical systems and signal processing, 23(2), pp. 432-445.
<https://doi.org/10.1016/j.ymsp.2008.05.006>.
- M.V. Rao, K.J. Prasanna Lakshmi (2005), *Analysis of b-value and improved b value of acoustic emissions accompanying rock fracture*, Current Science, 89(9), pp. 1577–1582.
<https://doi.org/10.2307/24110936>.
- P. Rodriguez, T.B. Celestino (2019), *Application of acoustic emission monitoring and signal analysis to the qualitative and quantitative characterization of the fracturing process in rocks*, Engineering Fracture Mechanics, 210(1), pp. 54-69.
<https://doi.org/10.1016/j.engfracmech.2018.06.027>.
- F. Sagasta, M.E. Zitto, R. Piotrkowski, A. Benavent-Climent, E. Suarez, A. Gallego (2018), *Acoustic emission energy b-value for local damage evaluation in reinforced concrete structures subjected to seismic loadings*, Mechanical Systems and Signal Processing, 102, pp. 262–277.
- M.P. Sassano, M.E. Zitto, R. Piotrkowski (2017), *Shannon wavelet entropy and acoustic emission applied to assess damage in concrete in dynamical tests* (abstract). Mecánica Computacional, XXXV, pp. 2563–2563. ISSN 2591-3522.
- C.E. Shannon (1948), *A mathematical theory of communication*, Bell system technical journal, 27 (3), pp. 379-423.
- T. Shiotani, S. Yuyama, Z.W. Li, M. Ohtsu, (2001), *Application of AE improved b value to quantitative evaluation of fracture process in concrete materials*, Journal of Acoustic Emission, 19, pp. 118–133.

C. Torrence, G.A. Compo (1998), *Practical Guide to Wavelet Analysis*, Bulletin of the American Meteorological Society, 79(1), pp. 61–78. ISSN 00030007.

J. Zhang (2018), *Investigation of Relation between Fracture Scale and Acoustic Emission Time-Frequency Parameters in Rocks*. Shock and Vibration, pp. 1–14.
<https://doi.org/10.1155/2018/3057628>

M.E. Zitto, R. Piotrkowski, A. Gallego, F. Sagasta, A. Benavent-Climent (2015), *Damage assessed by Wavelet scale bands and b-value in dynamical tests of a reinforced concrete slab monitored with acoustic emission*, Mechanical Systems and Signal Processing, 60-61, pp. 75-89.

LA EMISIÓN ACÚSTICA, SU HISTORIA EN LA ARGENTINA

López Pumarega M. I.^{a, b}, Ruzzante J. E.^{b, c, d}, Gómez M. P.^{b, c, e}

^a *Proyecto Centro Internacional para Estudios de la Tierra (ICES), Comisión Nacional de Energía Atómica y Universidad Nacional de Cuyo, Mendoza, Argentina.*

^b *Grupo Latinoamericano de Emisión Acústica GLEA.*

^c *Fac. Reg. Delta, Universidad Tecnológica Nacional, Campana, Buenos Aires, Argentina.*

^d *Universidad Tres de Febrero, Caseros, Buenos Aires, Argentina.*

^e *Dpto. ICES y Ondas Elásticas, Gerencia de Área Investigaciones y Aplicaciones No Nucleares, Comisión Nacional de Energía Atómica, Centro Atómico Constituyentes, San Martín, Buenos Aires, Argentina.*

e-mail: ilopezpumarega@gmail.com

La Emisión Acústica (EA) es un método de Ensayo No Destructivo (END) que es ampliamente utilizado para estudios e investigaciones en ciencias de los materiales. Los inicios de esta técnica en el mundo se remontan al siglo XX con Kishinoue en la década del 30 en Japón y a Obert en Estados Unidos de América en la década del 40, pero como referencia científica fundacional del tema, se puede mencionar la Tesis Doctoral de Joseph Kaiser en Alemania en 1950. Kaiser abordó el problema concreto de las ondas elásticas producidas por los metales durante su deformación y lo estudió a partir de registrarlas mediante instrumentación electrónica. Con el avance tecnológico de las últimas décadas, los equipos y sistemas de EA han alcanzado altos desempeños y bajos costos en relación a sus antecesores, permitiendo ampliar y diversificar sus posibilidades de aplicación. Actualmente la EA es utilizada en ensayos industriales para evaluar la integridad de grandes estructuras y componentes, y también en una amplia variedad de líneas de investigación en materiales, como metales, plásticos, concreto, rocas, maderas, compuestos, etc. En este trabajo se resumen las actividades de la EA en la Argentina desde sus orígenes en la década del 60, hasta nuestros días, incorporando una breve reseña de los avances en su Normalización a nivel nacional (IRAM), regional (MERCOSUR) e internacional (ISO). Se presentan también la creación del Grupo Latinoamericano de Emisión Acústica (GLEA) en 1997 y una breve reseña histórica desde 1999 de los Encuentros científico-tecnológicos llamados E-GLEA.

Palabras Clave: Emisión Acústica, GLEA, Normalización, Argentina.

1. INTRODUCCIÓN

La detección temprana de daño en los materiales de componentes y estructuras industriales, es un tema de enorme importancia económica y de seguridad ambiental, ya que permite disminuir los costos de fabricación y mantenimiento, y los riesgos para los trabajadores y para el público en general. En ese sentido, la Emisión Acústica (EA), que forma parte de los Ensayos No Destructivos (END), es una herramienta fundamental. Las técnicas de END, y en particular la EA, son valiosas para la caracterización de materiales y la identificación y cuantificación de los distintos procesos físico-químicos que ocurren en los mismos. La particularidad de la EA es su capacidad para detectar “on line” las modificaciones en el estado de tensiones de los materiales y por ende detectar la aparición de procesos de falla incipientes, posibles precursores de cambios catastróficos aún en

regiones alejadas de una estructura. Incluso la técnica se utiliza desde hace unos 30 años en minas y en el estudio de la corteza terrestre, apuntando a la predicción de sismos y erupciones volcánicas.

La EA, que es el nombre tanto del proceso como de la técnica, está constituida por ondas elásticas generadas por la redistribución repentina del campo de tensión-deformación en materiales o estructuras sometidos a carga externa. La EA es un fenómeno dinámico. Ocurre en el inicio o crecimiento de fisuras, en apertura y cierre de fracturas, deformación, movimiento de dislocaciones, formación de cavidades, corrosión, rotura de ligaduras en materiales compuestos, etc. Estas ondas se propagan a través del material y eventualmente llegan a la superficie donde producen pequeños desplazamientos temporarios. Son ondas de baja amplitud y alta frecuencia, normalmente ultrasónicas. Por esta razón, se requiere para su detección transductores piezoeléctricos muy sensibles. Las fuentes de EA están generalmente relacionadas con “daño”. Por ello, la detección y el análisis puede ser usado para evaluar el comportamiento dinámico del material bajo condiciones de carga y de este modo predecir su falla.

La diferencia principal con otros métodos de END tales como Rayos X, Ultrasonido, etc., es su capacidad de detectar cambios en tiempo real. De este modo, usando un sistema de EA, podemos monitorear “in situ” el comienzo y el desarrollo de daño en el material o la estructura, aun cuando ello no sea posible por medio de la inspección visual.

2. ORÍGENES DEL MÉTODO DE EA

Históricamente los antecedentes del uso de la EA se remontan a tiempos muy remotos, ya que seguramente pudo ser escuchada en forma directa en diversos fenómenos naturales como, por ejemplo, en los movimientos sísmicos, el congelamiento del agua al formarse hielo, la fractura de rocas y árboles, etc. Es posible, según los antropólogos, que los primeros alfareros que horneaban cerámicas, también percibieran los sonidos emitidos durante el enfriamiento de las mismas, para evaluar el proceso. También, al alcanzar el grado de pureza necesario del estaño, se podrían haber producido las primeras experiencias del “grito del estaño”, sonido audible que se genera cuando se provoca deformación plástica por maclado, ya que las piezas más antiguas conocidas de ese metal puro, datan del año 2650 a.C. En la edad media ya se había documentado la existencia de ruidos originados cuando un acero es templado, detectándose con esos sonidos la transformación martensítica. (Drouillard, 1996). Históricamente la EA ya figura en textos escritos durante el siglo IIX en el actual Irak, tal como lo cita Ruzzante J. et al (2016), relacionada con el sonido producido al deformar el estaño, y en Latinoamérica en el siglo XVII, referido al enfriamiento del hierro.

En las ciencias médicas, también los sonidos que produce el cuerpo humano han contribuido ampliamente para el estudio de la salud y la enfermedad, primero en forma directa con el oído del médico y luego mediante el invento del estetoscopio (Palacios T., 2001). También hay antecedentes históricos del uso de dispositivos similares por Leonardo da Vinci para detectar barcos cercanos a la costa. Hasta acá se está considerando la EA como un fenómeno ondulatorio en la parte audible del espectro de frecuencias.

En la primera mitad del siglo XX, hay documentos que muestran primeros estudios sistemáticos basados en la medición de la producción de ondas elásticas, como por ejemplo en Japón, adonde Kishinoue estudió la fractura de una varilla de madera sometida a una tensión flexural, utilizando como transductor (sensor) una cápsula de fonógrafo.

En los Estados Unidos de América, Robert J. Anderson en 1925, informo en su Tesis que, durante los ensayos de tracción de una aleación de aluminio, entre el punto de fluencia y cerca de la carga de rotura, los incrementos de carga producían una serie de

deslizamientos que daban lugar a una serie de líneas aserradas o bandas de Lüders, que eran acompañados por una serie de "clics o sonidos audibles" que dependían del espesor de la chapa, siendo más agudos para una chapa delgada. Se observa así, cómo a lo largo del tiempo se amplió el conjunto de materiales donde se detectaba el fenómeno de la EA. (Drouillard, 1996).

La etapa científico-tecnológica de la EA se inicia en Alemania durante 1950 con la primera Tesis Doctoral de Joseph Kaiser (1950): "Estudio del Fenómeno Acústico en los Ensayos de Tracción", en la Universidad Técnica de Múnich, relacionada con el comportamiento de los metales ante la tracción.

Luego el método y las técnicas de aplicación de la EA han evolucionado rápidamente, y hasta la actualidad se han publicado miles de trabajos.

3. LA EA EN LA ARGENTINA

En el Centro Atómico Bariloche de la Comisión Nacional de Energía Atómica (CNEA), el Dr. Roberto Pascual durante el año 1971 inició las actividades de EA en Argentina. Entre ese año y 1980 se realizaron trabajos de investigación en diversas aleaciones de cobre y de aluminio que produjeron varias publicaciones y una Tesis de Doctorado. Luego se formó otro Grupo en la Universidad de Córdoba, que también realizó publicaciones y una Tesis de Doctorado (Palacios T., 2001).

En el Centro Atómico Constituyentes de la CNEA, en 1979 el Dr. José. Ruzzante formalizó las actividades de un Grupo de Trabajo dedicado íntegramente a la investigación científico-tecnológica y la promoción de desarrollos en EA. Dicho grupo continúa en la actualidad dirigido por el Dr. Martín Gómez, habiéndose publicado numerosos trabajos científico-tecnológicos y Tesis de Grado, Maestría y Doctorado. Sus áreas de trabajo relacionadas con la EA y las ondas elásticas, se aplican en varios temas diferentes: metales, plásticos, cementos, materiales compuestos, concreto, materiales odontológicos, rocas, ciencias de la tierra, emisión magneto acústica, adherencia de recubrimientos ("scratch test") y aplicaciones en geofísica. Se realizan también desarrollos tecnológicos de equipos especiales.

Asimismo, se formó otro Grupo relacionado con las aplicaciones de la EA en el Instituto de Matemática, Astronomía y Física, I.M.A.F. de la Universidad Nacional de Córdoba y otro en la Facultad de Ingeniería de la Universidad de Buenos Aires. En ambos casos hubo varias publicaciones internacionales y Tesis de Doctorado (Palacios T., 2001).

En 1997 comenzaron los trabajos en el Instituto de Materiales y Suelos de la Facultad de Ingeniería de la Universidad Nacional de San Juan de la mano del Ing. M. A. Sabio Montero. En ese mismo año, el Dr. Horacio Lescano incluye la EA entre las tareas del grupo de Vibraciones mecánicas (GVM) de la Facultad Regional Delta de la Universidad Tecnológica Nacional, a partir del cual se nuclea el Grupo de Emisión Acústica (GEA) que actualmente dirige el Dr. Martín Gómez.

En el ámbito científico académico existen otros Grupos que trabajan o han trabajado en los últimos 15 años en investigación y desarrollo en EA, o que la aplican como método de evaluación en diversos procesos: Entre estos se pueden mencionar los Grupos de Daño por Hidrogeno y de Corrosión, ambos de la Gerencia de Materiales de la CNEA; el Grupo de Materiales Compuestos del ITPN (CONICET-FI UBA), la Facultad de Ingeniería de la Universidad Nacional de Río Cuarto, provincia de Córdoba; la Facultad de Ingeniería de la Universidad Nacional de Misiones UNaM en Oberá, Misiones; en la Carrera de Ingeniería en Sonido, Universidad Nacional de Tres de Febrero UNTREF, en Caseros, Buenos Aires; y el DME-FAIN de la Facultad de Ingeniería de la Universidad Nacional del Comahue en Neuquén, donde se realiza este E-GLEA 10.

4. LA COMUNIDAD DE EA EN EL MUNDO

Pocos años después del inicio de los estudios e investigaciones de la nueva técnica de EA, sus especialistas, técnicos y usuarios, comenzaron a organizarse en varias partes del mundo. Así en EEUU se creó en 1967, el “Acoustic Emission Working Group, AEWG”, para centralizar la información, compatibilizar la terminología y las técnicas experimentales, y compilar e intercambiar experiencias. Su primer Encuentro fue en 1968. En Japón comenzó a reunirse en 1969 el “Japanese Committee on Acoustic Emission (JCAE)”. Por otro lado, Europa comenzó la organización de la comunidad usuaria de la EA en 1972, con la “Physics Conference on Acoustic Emission” en Londres, allí se creó el “European Working Group on Acoustic Emission, EWGAE” (Ruzzante J. et al, 2016).

En Asia el primer grupo de trabajo nacional en EA fue el de la India, creado en 1985. El grupo nacional de Sud África denominado "South African Working Group for Acoustic Emission" se creó en 1989. En Corea se creó en 1990 el "Korean Working Group on Acoustic Emission, KWGAE" (Palacios T., 2001).

Todos estos Grupos periódicamente organizan Congresos Internacionales donde se presentan los últimos trabajos de investigación, desarrollo y aplicaciones de la EA.

5. LA COMUNIDAD DE EA EN LATINOAMÉRICA

En Argentina, con la necesidad de vincular a los especialistas, técnicos y usuarios relacionados con la EA, el 4 de abril de 1997, se creó en la CNEA el **Grupo Latinoamericano de Emisión Acústica, GLEA** Los miembros fundadores por Argentina son: Dr. J. E. Ruzzante (CNEA), Dra. M. I. López Pumarega (CNEA), Téc. M. Armeite (CNEA), Dr. C. E. D'Attellis (CNEA), Ing. T. A. Palacios (CNEA); Dra. R. Piotrkowski (Universidad Nacional de San Martín); Ing. M. A. Sabio Montero (Universidad Nacional de San Juan), y el Ing. P. Feres Filho de Brasil (López Pumarega M. I. et al., 2002; Ruzzante J. et al, 2004).



Figura 1. Miembros Fundadores del GLEA: R. Piotrkowski, T. Palacios, J. E. Ruzzante, M. I. López Pumarega, M. Armeite, P. Feres Filho, M. A. Sabio Montero.

Los objetivos del GLEA son puramente científicos y tecnológicos: promover, desarrollar, investigar, realizar reuniones, en temas de EA, y fomentar la incorporación de nuevos adherentes interesados en estos temas. La participación en el GLEA es absolutamente gratuita.

El GLEA dispone de una página web y un correo electrónico (<https://www.cnea.gov.ar/cac/glea/>). En la Fig. 1, se puede ver una fotografía de los miembros fundadores del GLEA. Con posterioridad se fueron incorporando más de 200 especialistas, técnicos y usuarios de Sudamérica y de España.

5.1. ENCUNTROS E-GLEA

Para promover las actividades y generar un espacio de discusión de temas, desde 1999, y cada dos años, el GLEA organiza Encuentros Internacionales, denominado E-GLEA, ya habiéndose realizado 9 ediciones del mismo. El primero de estos Encuentros, el E-GLEA 1, se realizó en el Centro Atómico Constituyentes de la CNEA, en Buenos Aires, del 10 al 14 de septiembre de 1999. En esa ocasión se invitó al especialista Prof. Dr. Kanji Ono, de la Universidad de California, EEUU, uno de los más reconocidos investigadores en EA, creador y editor de la revista especializada “Journal of Acoustic Emission”. A través de esa publicación se difundieron las actividades realizadas durante el E-GLEA 1 a la comunidad internacional (ver Fig.2).

Los E-GLEA son un ámbito de encuentro, discusión y difusión de los nuevos trabajos de investigación y aplicaciones de la EA. Año por medio, se fueron realizando los distintos Encuentros internacionales del GLEA de acuerdo con el siguiente resumen:

- E-GLEA 1: Buenos Aires, Argentina, 6-10 de septiembre de 1999.
- E-GLEA 2: Buenos Aires, Argentina, 10-14 de septiembre de 2001.
- E-GLEA 3: Río de Janeiro, Brasil, 2-6 de junio de 2003.
- E-GLEA 4: Taormina, Italia, 16 al 19 de octubre de 2005.
- E-GLEA 5: Universidad Nacional de Misiones, Oberá, Misiones, Argentina, durante este Encuentro se celebraron los 10 años del GLEA, 29 de agosto al 1 de septiembre de 2007.
- E-GLEA 6: Universidade de Rio Grande Do Sul, Porto Alegre, Brasil, 16 de septiembre de 2009.
- E-GLEA 7: Universidad Tecnológica Nacional, Regional Mendoza, Mendoza, Argentina, 25-27 de agosto de 2011.
- E-GLEA 8: Universidad Nacional de Tres de Febrero, UNTREF, Caseros, Buenos Aires, Argentina, 10-12 de septiembre de 2013.
- E-GLEA 9: Facultad de Ingeniería, Universidad Nacional de Misiones, Oberá, Misiones, Argentina, celebrándose los 20 años del GLEA, del 29 al 31 de agosto de 2017.
- E-GLEA 10: Facultad de Ingeniería, Universidad Nacional del Comahue, Neuquén, Provincia de Neuquén, Argentina 14 al 16 de agosto de 2019, donde se presenta este trabajo.

Como se puede ver, en 6 ocasiones se pudieron privilegiar como lugares de realización de los Encuentros, los ámbitos universitarios afines a la EA, pudiéndose así fomentar la participación de los estudiantes. En todos los E-GLEA participaron en promedio más de 60 especialistas, investigadores, técnicos y usuarios de la EA.

Desde sus inicios, los Encuentros contaron con la colaboración de varias instituciones extranjeras y argentinas, incluida la Agencia Nacional de Promoción Científica y

Tecnológica a través del Fondo para la Investigación Científica y Tecnológica (FONCYT) y sus subsidios para Reuniones Científicas.

En las Fig. 2 a 4 y 7 a 12, se muestran fotografías de los participantes en los encuentros E-GLEA. Las fotos de la Figuras 5 y 6 se insertan en orden cronológico a las antes mencionadas y corresponden a unas Jornadas de Emisión Acústica y Estructuras Geofísicas, auspiciadas por el GLEA, la primera en San Juan, Argentina en 2003 y la siguiente en Malargüe, Mendoza, Argentina, en 2004. En esas reuniones comenzaron a sentarse las bases de lo que luego sería el “International Center of Earth Sciences” (ICES) fundado entre la CNEA y la Universidad Nacional de Cuyo, en conjunto con investigadores del Consiglio Nazionale delle Ricerche (CNR) e importantes instituciones científicas de Italia.

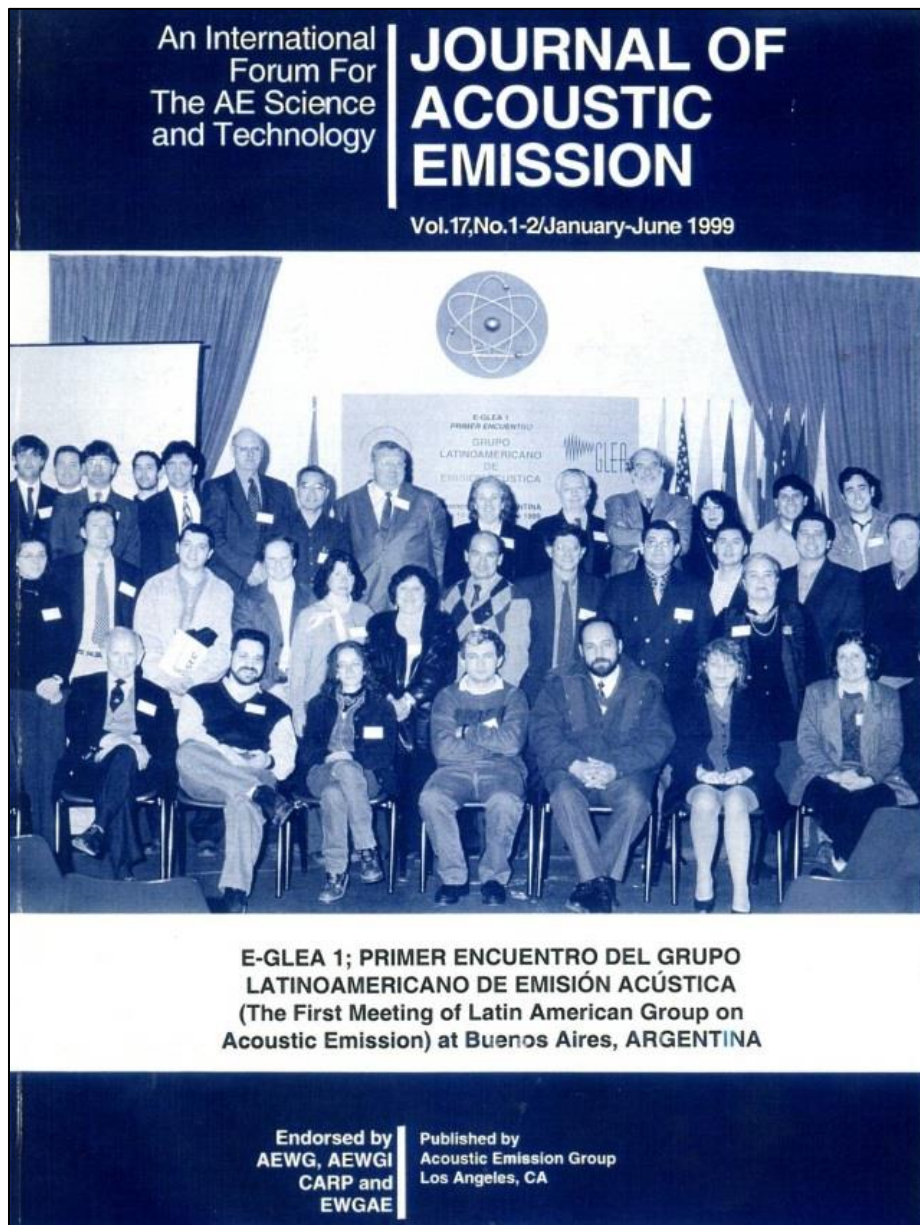


Figura 2. E-GLEA 1, Portada de la revista “Journal of Acoustic Emission, Vol. 17, No. 1-2/January-June 1999”, gentileza Prof. Dr. Kanji. Ono, Centro Atómico Constituyentes, Buenos Aires, Argentina, 6-10 de septiembre de 1999.



Figura 3. E-GLEA 2, Centro Atómico Constituyentes, Buenos Aires, Argentina, 10-14 de septiembre de 2001.



Figura 6. 1^{as.} Jornadas de Emisión Acústica y Estructuras Geofísicas, Malargüe, Mendoza, Argentina, 20-21 de diciembre de 2004.



Figura 4. E-GLEA 3, en el marco del "3^{rd.} Pan-American Conference for Nondestructive Testing (3 PANNDT)", Río de Janeiro, Brasil, 2-6 de junio de 2003.



Figura 7. E-GLEA 4, Taormina, Italia, 16-19 de octubre de 2005.



Figura 5. Jornada sobre Emisión Acústica en Estructuras (Geofísicas y de Ingeniería Civil), Instituto Nacional de Prevención Sísmica INPRES, San Juan, Argentina, 5 de diciembre de 2003.



Figura 8. E-GLEA 5 y Celebración de los 10 años del GLEA. Universidad Nacional de Misiones, Oberá, Misiones, Argentina, 29 de agosto al 1 de septiembre de 2007.



Figura 9. E-GLEA 6, Universidad Federal de Rio Grande do Sul (UFRGS), Porto Alegre, Brasil, 16 de septiembre de 2009.



Figura 10. E-GLEA 7, Facultad Regional Mendoza, Universidad Tecnológica Nacional, Mendoza, Argentina, 25-27 de agosto, 2011.



Figura 11. E-GLEA 8, Universidad Nacional de Tras de Febrero UNTREF, Caseros, Buenos Aires, Argentina, 10-12 de septiembre de 2013.



Figura 12. E-GLEA 9 y Celebración de los 20 años del GLEA, Facultad de Ingeniería, Universidad Nacional de Misiones, Oberá, Misiones, 29 al 31 de agosto de 2017.

6. LA NORMALIZACIÓN EN EA

Desde hace más de 30 años, en la Argentina existen varias empresas, subsidiarias de otras extranjeras y también algunas nacionales, que realizan ensayos de EA en el ámbito industrial e inclusive algunas que diseñan y fabrican equipos especiales.

A medida que avanzaban el uso y las aplicaciones de la EA en Argentina y con el fin de obtener un nivel de ordenamiento tecnológico mínimo, fue necesario poder crear disposiciones, protocolos o documentos específicos. Así surgió la necesidad de comenzar a trabajar en la “Normalización” de las actividades de EA.

Una Norma es un documento, que, aprobado por consenso en un organismo reconocido, establece reglas y criterios para usos comunes y repetidos. Las Normas están en todas partes y nos protegen a todos. Los productos elaborados conforme a Normas son más aptos, más seguros y de mejor calidad. Aseguran la compatibilidad de los productos y la disponibilidad de repuestos que prolongan la vida útil del objeto, facilitando el comercio y colaborando con la regulación del mercado, permitiendo la transferencia de tecnología.

La actividad de “Normalización” es llevada a cabo, en cada país, por un Organismo de Normalización: entidad reconocida a escala nacional, regional o internacional. Cada nación del mundo tiene su propio Organismo Nacional de Normalización. En Argentina es el Instituto Argentino de Normalización y Certificación IRAM. Este Instituto lleva adelante las actividades de Normalización desde el año 1935, y fue reconocido en 1994 por el Poder Ejecutivo Nacional, como el Organismo de Normalización de la República Argentina. Es un ente privado, no estatal, en el que participan representantes de consumo, producción, usuarios, gobierno, comunidad científico-técnica, fabricantes de productos, etc. Desarrolla, estudia y publica Normas argentinas en todos los campos de actividad. Se debe destacar que el IRAM fue el primer Organismo de Normalización creado en América Latina, llevando elaboradas más de 13000 Normas aplicables en muy diversos ámbitos.

El proceso de elaboración de Normas se hace a través de los Organismos de Estudio (Comisiones), con la participación de representantes de distintas organizaciones que pertenecen a los tres sectores involucrados en su creación: los productores, los consumidores y los responsables de velar por el interés general y el bien común. Todos, excepto el personal del IRAM, tienen carácter honorario

En Argentina, debido a los altos estándares de calidad y seguridad que se deben aplicar en la industria nuclear, a iniciativas de la CNEA, en 1969 se creó en el IRAM el Subcomité de Ensayos No Destructivos, con competencia específica en todas las áreas de este tipo de ensayos. Recién en junio de 2000, también a pedido de la CNEA, se creó en el IRAM la Comisión de EA. Esta Comisión funciona desde entonces en forma autónoma y continua, reuniendo en promedio 5 personas en cada convocatoria mensual.

En la década de los 90, debido a la creciente regionalización latinoamericana, se creó la Asociación MERCOSUR de Normalización (AMN). Es el único organismo responsable por la gestión de normalización voluntaria en el ámbito del MERCOSUR. En junio de 2004, a propuesta de la Comisión de EA del IRAM, junto con su equivalente de Brasil (Associação Brasileira de Normas Técnicas, ABNT), se creó en ese ámbito el Comité Sectorial MERCOSUR 24 (CSM 24) con competencia específica en el tema de los END, estableciéndose también el Subcomité de Emisión Acústica. En la actualidad existen más de 12 Normas de EA publicadas en el IRAM y/o en el MERCOSUR (Catálogo de Normas IRAM y Asociación Mercosur de Normalización).

A nivel internacional también las actividades en la creación y adopción de Normas de EA, ha ido progresando rápidamente. En la “International Organization for Standardization ISO”, existía el “Technical Committee TC135” para todos los END, pero

en el año 2007 el CSM 24, propuso la creación de un grupo específico para el estudio de la EA, el “Sub Committee SC9”. Su Secretaría en la actualidad pasó de Brasil a China. En este Subcomité participan activamente 14 países y otros 5 más son “Observadores”. A su vez, cada Subcomité crea Grupos de Trabajo (“Working Groups, WG”) para tratar temas específicos, convocando a reconocidos especialistas internacionales. En esos Grupos de Trabajo, participan por Argentina, varios reconocidos especialistas de CNEA.

En Europa además existe el “European Committee for Standardization” CEN, que reúne a los Institutos de Normalización nacionales de 33 países europeos, desarrollando y publicando Normas europeas. Desde octubre de 1991, se aprobó formalmente un Acuerdo de Cooperación Técnica entre la ISO y el CEN, tratando así de no duplicar las tareas.

De acuerdo a una revisión internacional realizada por una empresa alemana fabricante de equipos de EA, existen a nivel internacional, más de 100 Códigos y Normas relacionadas con este método de END (Vallen–Syteme GmbH, Release September 2013). En la cita de la referencia, las Normas, Códigos y Prácticas están ordenadas por institución productora (ISO, ASNT, CEN, API, EPRI, ASME, IEEE, etc.), actualizadas al año 2013, con su correspondiente codificación, título, fecha de edición y comentarios. Las Normas desarrolladas en Latinoamérica no han sido incorporadas en ese documento aún, pero pueden ser consultadas en la página web de la AMN, CS24.

La Agencia Internacional de Energía Atómica (OIEA por sus siglas en inglés), dependiente de las Naciones Unidas, también desarrolla el tema de la EA en su Documento Técnico: IAEA-TECDOC 628/Rev.1. La Sección V del Código ASME, en su Artículo 12 describe el proceso de examinación por EA, de recipientes metálicos durante la prueba de presurización (ASME Code, Section V, ARTICLE 12). El Artículo 13, describe los requerimientos a usarse durante la monitorización continua por EA, en contornos de recipientes a presión metálicos y no metálicos usados en servicio, en la industria nuclear y no nuclear, (ASME Code, Section V, ARTICLE 13). En la Publicación No. 322 del “American Petroleum Institute, API”, se hace una evaluación ingenieril del método de EA para la detección de pérdidas en tanques sobre tierra, para almacenamiento.

Gran parte de la actividad de personas en el área de los END está reglamentada a escala nacional e internacional, a través de las Normas específicas para cada Método de END, y en la Norma de Calificación y Certificación de Personal, que se dedica a la aplicación de los END en la industria. Es ésta la Norma NM-ISO 9712 para la Calificación y Certificación de Personal de END. Allí están comprendidas todas las actividades industriales de EA, con los requisitos, competencias y obligaciones para los Operadores e Inspectores de EA, en sus tres posibilidades: Nivel 1, Nivel 2 y Nivel 3.

El IRAM está acreditado por el Organismo Argentino de Acreditación (OAA) para la Certificación de Personas y éste a su vez, delega la facultad de la Calificación de Personas en los Organismos de Calificación Acreditados (OCA), certificando sus acciones. En la Argentina existen pocos OCAs, entre ellos se pueden citar: la CNEA, la Universidad Tecnológica Nacional (UTN) Facultad Regional Delta y la UTN Facultad Regional Mendoza. Todos ellos están habilitados para la Calificación de Personas en los métodos de END en los que cada uno es competente, desempeñándose conforme a las indicaciones de la NM-ISO 9712.

Teniendo como marco Norma NM-ISO 9712, en la Argentina, aún no se ha podido establecer definitivamente el Sistema de Calificación de Personas que operan con la técnica de EA. En el año 2007, desde la CNEA y a través del IRAM, se pudo completar en forma provisoria el esquema de Certificación para el Nivel 1 de EA, llegando a dictarse también el primer Curso de Nivel 2, pero luego por diversas circunstancias fortuitas este proceso fue interrumpido. Por las particularidades del método de EA, la tarea de la Normalización de las actividades que profesionales y técnicos desarrollan dentro del

ámbito de los END, es muy importante y compleja de realizar, siendo ésta una tarea todavía no concretada que debe encararse seriamente entre todos los involucrados con este método.

A nivel nacional existen al menos 8 documentos gubernamentales nacionales y provinciales que nombran específicamente a la EA (Ruzzante J. et al, 2016). La documentación en el ámbito nacional y provincial donde se menciona la EA pueden encontrarse en el portal de “*Información Legislativa y Documental Oficial*”, especificando el tipo de documento y el año de su publicación.

De todo lo escrito anteriormente, se desprende la enorme importancia del uso de la EA en el mundo y en particular en la Argentina, estando presente inclusive en la documentación legal nacional y provincial.

7. CONCLUSIONES

Se han mostrado el avance y los logros más importantes de todos los colegas que han dedicado su trabajo y su esfuerzo a profundizar la comprensión de la EA, difundir su uso, ampliar sus posibilidades y potencialidades de aplicación, y obtener un nivel de ordenamiento tecnológico mínimo a través de la tarea de la Normalización.

Una prueba fehaciente de esos frutos es la realización de este Décimo Encuentro del Grupo Latinoamericano de Emisión Acústica E-GLEA 10, en el ámbito de la Universidad Nacional del Comahue en la ciudad de Neuquén, con la presentación Oral de más de 30 Trabajos de diversos campos de aplicación de la EA.

La presentación de este Trabajo, se ha realizado como tributo de homenaje a toda la comunidad de los investigadores, profesionales, técnicos y usuarios de la EA en América del Sur y especialmente en Argentina. Todos ellos, desde hace muchos años han sabido unirse para profundizar el conocimiento en esta área de la ciencia, compilar e intercambiar sus experiencias en fraterna comunidad que potencia y aumenta la sinergia de sus trabajos individuales. Parte de esa tarea ha sido posible gracias a la creación y funcionamiento del Grupo Latinoamericano de Emisión Acústica GLEA y de todos sus integrantes.

REFERENCIAS

- Acoustic Emission Examination of Metallic Vessels During Pressure Testing, *ASME Code, Section V, ARTICLE 12*.
- Acoustic Emission Working Group, AEGW, <http://www.aewg.org/>
- An Engineering Evaluation of Acoustic Methods of Leak Detection in Aboveground Storage Tanks, *API Publication Number 322*.
- Asociación Mercosur de Normalización, AMN, <https://www.amn.org.br/>
- Asociación Mercosur de Normalización:
https://www.amn.org.br/Content/Documentos/ptCartilha_AMN_FINAL2.pdf
- Catálogo de Normas IRAM, <http://www.iram.org.ar/index.php?id=Catalogo-de-normas>
- Code, Standards, Practices, and Guidelines related to Acoustic Emission (AE), *Vallen-Syteme GmbH, Release September 2013*.
- Continuous Acoustic Emission Monitoring, *ASME Code, Section V, ARTICLE 13*.
- Drouillard, T.F., A History of Acoustic Emission, *Journal of Acoustic Emission, vol. 14, N°1*, pp. 1-34, 1996.
- European Committee for Standardization, <https://www.cen.eu>
- European Working Group on Acoustic Emission (EWGAE), <http://www.ewgae.eu/>
- Grupo Latinoamericano de Emisión Acústica (GLEA),
<https://www.cnea.gob.ar/cac/glea/>
- Información Legislativa y Documental Oficial INFOLEG, www.infoleg.gov.ar

- Instituto Argentino de Normalización y Certificación IRAM,
<http://www.iram.org.ar/index.php>
- International Standard Organization ISO, <https://www.iso.org/standards.html>
- Kaiser J. Untersuchung über das Auftreten von Geräuschen beim Zugversuch, *Dr.-Ing. Dissertation, Fakultät für Maschinenwesen und Elektrotechnik der Technischen Universität München (TUM)*; 1950.
- López Pumarega M. I., Piotrkowski R., Ruzzante J. E., The history of the Latin American Acoustic Emission Group (GLEA), *NDT.net, Vol. 7 No.09*, September 2002.
- Normas MERCOSUR de END, <https://www.amn.org.br/Paginas/NormasGeral>
- Palacios T., Antecedentes históricos de la Emisión Acústica en Latinoamérica, *Primer Encuentro del Grupo Latinoamericano de Emisión Acústica, E-GLEA 1*,
<http://www.cnea.gov.ar/cac/glea/trabajos/palacios.pdf>, 2001.
- Ruzzante J. E., López Pumarega M. I., Piotrkowski R., The status of Acoustic Emission in Argentina, *Insight, ISSN: 1354-2575, Vol. 46, No. 12*, pp.733-735, 2004.
- Ruzzante J., López Pumarega M. I., *Emisión Acústica, un diálogo con los Materiales*,
<https://www.ciencias.org.ar/user/Ruzzante.pdf>, 2016.
- Training guidelines in non-destructive testing techniques, *IAEA-TECDOC 628/Rev.1*.
- Vallen–Syteme GmbH, Code, Standards, Practices, and Guidelines related to Acoustic Emission (AE), Release September 2013,
http://www.vallen.de/zdownload/pdf/AE_Standards_1309.pdf

Índice

RESULTADOS PREMILINARES DE UNA CONSTRUCCIÓN DE SENSORES ULTRASÓNICOS	
<i>Albalat A.M., Ruzzante J.E., Carballal C.A., Cavalchini J., Elorriaga M. y Antunez M.E.</i>	1
INFLUENCIA DO SISTEMA DE CONTROLE DA CARGA EM ENSAIOS DE EMISSAO ACUSTICA: ESTUDO TEORICO EXPERIMENTAL	
<i>Almeida W.R., Rojo Tanzi B.N., Lacidogna G., De León D.M. y Iturrioz I.</i>	7
REDES NEURONALES APLICADAS AL MONITOREO DE PROCESOS DE PERFORACIÓN EN PROBETAS DE MATERIAL GEOLÓGICO	
<i>Basgall A., Ferrari, G., Gómez, M.</i>	18
ESTUDIO DE PROPIEDADES MECÁNICAS EN TUBOS DE CFRP	
<i>Bonelli Toro A., Podetti G., Arcone D., Daverio N., Hazarabedian A. y Gómez M.P.</i>	29
INTERFAZ PARA VISUALIZAR Y PROCESAR SEÑALES DE EMISIÓN ACÚSTICA	
<i>Bonelli Toro A.G., Iofrida M.J., y Gómez M.P.</i>	37
ESTUDIO DE LA CONDICIÓN DE HERRAMIENTAS DE MECANIZADO DE MATERIALES COMPUESTOS UTILIZANDO EMISIÓN ACÚSTICA	
<i>Bonelli Toro A.G., González Fuster M., Fernández G., Antico F., Vogt P. y Gómez M.P.</i>	46
PROPAGACIÓN DE ONDAS EN SÓLIDOS ANISOTRÓPICOS: PREDICCIÓN DE VELOCIDAD EN POLICRISTALES	
<i>Cowes D.A., Mieza J.I. y Gómez M.P.</i>	56
METODOLOGÍA PARA ESTIMAR LA INFLUENCIA DE EVENTOS ANÓMALOS EN LOS NIVELES DE RUIDO DEL TRÁNSITO RODADO DE LA CIUDAD AUTÓNOMA DE BUENOS AIRES	
<i>Crapa M.N., Masson F., Mansilla J., Zanardi E. y Lombera E.</i>	61
MONITORAMENTO DA DEGRADAÇÃO DE COMPÓSITO PRFV APLICANDO A TÉCNICA DE EMISSÃO ACÚSTICA (EA) COMBINADA COM SENSORES DE REDE DE BRAGG EM FIBRA ÓTICA (FBG)	
<i>Da Silva D.S., Groth E.B., Lutckmeier F., Zuglian G., Jaques R., de Lima T.S. y Clarke T.G.</i>	71
EMISIÓN ACÚSTICA APLICADA AL MONITOREO DE PROCESOS DE PERFORACIÓN EN PROBETAS DE MATERIAL GEOLÓGICO	
<i>Ferrari G., Basgall A., Gómez M.</i>	81
ANÁLISIS DE INCERTIDUMBRE PRODUCIDA POR EL CAUDAL VEHICULAR MEDIANTE EL USO DEL MÉTODO DE CÁLCULO NMPB-ROUTES-96	
<i>Galimberti J., Ruffa F. y Stasi A.</i>	88

ANÁLISIS MODAL BASADO EN MEDICIONES NO INVASIVAS CON UN ARREGLO DE MICRÓFONOS COMERCIAL	
<i>Garcia J. y Boelke O.</i>	101
ANÁLISE NUMÉRICA DA EMISSÃO ACÚSTICA APLICADA AO MONITORAMENTO DE INTEGRIDADE DE ESTRUTURAS	
<i>Groth E.B., Shumacher G., Rojo Tanzi B.N., Clarke T.G.R., Jacques R.C. y Iturrioz I.</i>	109
ACOUSTIC EMISSION MONITORING OF 16" PIPE SEGMENTS DURING HYDROSTATIC TESTING	
<i>Jacques R.C., Lima T. S., Soares S.D., Groth E.B. y Clarke T.G.R.</i>	120
ANALISIS DE VIBRACIONES EN UNA CAJA REDUCTORA DE UNA TURBINA	
<i>Klemplnow. A., Piñeyro J.J., Bello A. y Elfi F.</i>	132
MEDICIÓN DE RUIDO EN PEQUEÑAS TURBINAS EÓLICAS	
<i>Labriola C.L., Colón D.L., Lassig J. y Palesse C.</i>	141
ANALISIS PARA DETERMINAR UNA CLASIFICACIÓN CUALITATIVA DEL ESTADO DE FONDOS DE TANQUES A PARTIR DE ENSAYOS DE EMISION ACUSTICA Y SU RELACIÓN CON EL FENOMENO DE LA CORROSIÓN ACTIVA	
<i>Montenegro A.N.</i>	151
ESTUDIO DE LA TRANSFORMACIÓN MARTENSITICA EN UN ACERO AISI 321 MEDIANTE TÉCNICAS MAGNÉTICAS	
<i>Neyra Astudillo M.R., Gómez M.P. y Pardal J.</i>	158
PREDICCIÓN DE LA RESISTENCIA AL DESGASTE POR ABRASIÓN DE RECARGUES POR SOLDADURA A TRAVÉS DE EMISIÓN ACÚSTICA	
<i>Peix D.A., Ávila E., Molina G., Ferrari G., Folgueiras J. y Gómez M.P.</i>	175
ANÁLISIS, TRANSFORMACIÓN Y RESÍNTESIS DE SONIDO: UNA IMPLEMENTACIÓN DE LA TÉCNICA ATS COMO BASE PARA POSIBLES INTERRELACIONES ENTRE SEÑALES SONORAS Y AUDIO DIGITAL	
<i>Perna G.L., Paupy P.E. y Huggenberger D.</i>	185
ESTUDIO DE LA NORMA DE ENSAYO DE EMISIÓN ACÚSTICA PARA LA DETECCIÓN DE CORROSIÓN EN TANQUES LLENOS DE LÍQUIDO EN ARGENTINA	
<i>Semorile M., Montenegro A.N. y Tellería G.</i>	197
NORMAS TÉCNICAS DE EMISIÓN ACÚSTICA EN ARGENTINA Y MERCOSUR	
<i>Semorile M.</i>	205
A REDUCED ORDER MODEL OF WAVE PROPAGATION AND VIBRATIONS IN RODS AND TUBES OF UNIFORM CROSS SECTIONS	
<i>Suárez Antola R.</i>	221

ESTUDIO E IMPLEMENTACIÓN DE CUADRO DE CLASIFICACIÓN CUANTITATIVO PARA ENSAYOS DE EMISIÓN ACÚSTICA EN FONDOS DE TANQUES EN ARGENTINA

Tellería Gonzalo, Tellería Juan Manuel y Castillo Canache Argenis 233

ESTUDIO DE LA PROPAGACION DE FISURAS MEDIANTE EMISION ACÚSTICA

Vatcoff L. y Santarelli E. 241

SISTEMA AUTÓNOMO PARA MONITOREO ACÚSTICO DE CETÁCEOS

Veca A.C., Valesse N., Ruzzante J.E., Albalat A.M. y Marino A. 253

ENERGÍA Y ENTROPÍA WAVELET DE SHANNON EN SEÑALES DE EMISIÓN ACÚSTICA PARA EVALUACIÓN DE DAÑO EN ROCA ANDESITA

Zitto M.E., Sassano M.P., Muszkats J.P., Filipussi D.A. y Piotrkowski R. 262

LA EMISIÓN ACÚSTICA, SU HISTORIA EN LA ARGENTINA

López Pumarega M.I., Ruzzante J.E y Gómez M.P. 273